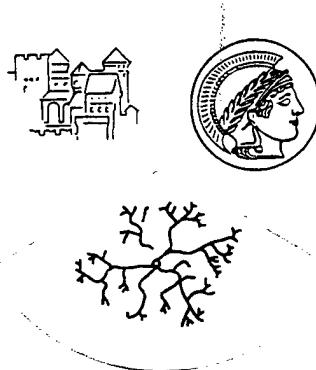# Interfacially Controlled Functional Materials: Electrical and Chemical Properties

Schloß Ringberg, Germany, March 8–13, 1998

Editors:

Joachim Maier
Harry L. Tuller

North-Holland

REPORT DOCUMENTATION PAGE

Form Approved OMB No. 0704-0188

1. AGENCY USE ONLY (Leave blank)	2. REPORT DATE 2000	3. REPORT TYPE AND DATES COVERED 8-13 March 1998 Final Report

4. TITLE AND SUBTITLE

International Workshop on Interfacially Controlled Functional Materials: Electrical and Chemical Properties. Held at Schloss Ringberg, Germany on March 8-13, 1998. Papers.

6. AUTHOR(S)

Joachim Maier and Harry L. Tuller, Editors

5. FUNDING NUMBERS

7. PERFORMING ORGANIZATION NAME(S) AND ADDRESS(ES)

8. PERFORMING ORGANIZATION REPORT NUMBER

ISSN 0167-2738

9. SPONSORING/MONITORING AGENCY NAME(S) AND ADDRESS(ES)

Office of Naval Research,
European Office
PSC 802 Box 39
FPO AE 09499-0039

10. SPONSORING/MONITORING AGENCY REPORT NUMBER

11. SUPPLEMENTARY NOTES

12a. DISTRIBUTION/AVAILABILITY STATEMENT

12b. DISTRIBUTION CODE

A

12. ABSTRACT (Maximum 200 words)

These are the proceedings of the International Workshop on Interfacially Controlled Functional Materials held at Schloss Ringberg, Germany on March 8-13, 1998. The workshop concentrated on the electrical and chemical properties of ionic materials. The emphasis was on systematically structured (both natural and artificial) ceramic materials in which properties are largely influenced or even completely controlled by interfaces (grain boundaries, surfaces and heterostructures). This workshop carries on the tradition of the meeting held four years ago in Ringberg on Interfaces in Ionic Materials in relation to the respective bulk phase. This conference is dedicated to the utilization of such effects to design materials and materials systems with respect to their overall properties (electrical and chemical). Important applications include sensors, fuel cells, catalysis, photoelectrochemistry and semiconducting devices.

13. SUBJECT TERMS

ONR, Foreign reports, Conference proceedings, Interfaces, Material science

15. NUMBER OF PAGES

16. PRICE CODE

17. SECURITY CLASSIFICATION OF REPORT UNCLASSIFIED	18. SECURITY CLASSIFICATION OF THIS PAGE UNCLASSIFIED	19. SECURITY CLASSIFICATION OF ABSTRACT UNCLASSIFIED	20. LIMITATION OF ABSTRACT UL

20011203 228

SOLID STATE IONICS

INTERFACIALLY CONTROLLED FUNCTIONAL MATERIALS: ELECTRICAL AND CHEMICAL PROPERTIES

Papers from the International Workshop held at
Schloß Ringberg, Germany, March 8–13, 1998

Editors:

Joachim Maier
Max-Planck-Institut für Festkörperforschung, Stuttgart, Germany

Harry L. Tuller
Massachusetts Institute of Technology, Cambridge, MA, USA

N·H

NORTH-HOLLAND
AMSTERDAM–LAUSANNE–NEW YORK–OXFORD–SHANNON–TOKYO

AQ F02-02-0280

CONTENTS

Interfacially Controlled Functional Materials: Electrical and Chemical Properties
Schloß Ringberg, Germany, March 8–13, 1998

Section 5. Applications

Preface

These are the proceedings of the *International Workshop on Interfacially Controlled Functional Materials,* with concentration on the electrical and chemical properties of ionic materials. Emphasis was placed on systematically structured (both natural and artificial) ceramic materials in which properties are largely influenced or even completely controlled by interfaces (grain boundaries, surfaces and hetero-structures). This workshop carries on the tradition of the meeting held four years ago in Ringberg on *Interfaces in Ionic Materials* (organized by J. Maier, M. Rühle) in which the changes of properties at interfaces were discussed in relation to the respective bulk phase. This conference is dedicated to the utilization of such effects to design materials and materials systems with respect to their overall properties (electrical and chemical). Important applications include sensors, fuel cells, catalysis, photoelectrochemistry and semiconducting devices.

In this context, the effects on the nano-scale are of special relevance. Here one deals with the transition regime between molecules and the solid state which includes the range in which many mesoscopic effects occur. On this scale, chemistry, biology and physics intermingle in an exciting way. Physicists typically devote themselves to the preparation and measurement of synthetic nano-structures, chemists to the supramolecular state, and biologists traditionally to the structuring on the nano-scale, as related to biological functions. There are important aspects of this field not covered by these disciplines but are critical to the field of functional ceramics and solid state electrochemistry. For example, contrary to biological and semiconducting systems, questions relating to morphological stability are particularly critical for ceramic systems commonly utilized at elevated temperatures.

This highly stimulating workshop surely contributed to the elucidation of this exciting field. The present proceedings are to confirm this. Some speakers felt that their contributions were already adequately described elsewhere and are thus not represented in this proceedings. The following references [1–6] deal with these topics.

Acknowledgements

References

[1] M. Trau, N. Yao, E. Kim, Y. Xiao, G.M. Whitesides, I.A. Aksay, Nature 390 (1997) 674.
[2] J.O. Carlsson, U. Jansson, Prog. Solid St. Chem. 22 (1994) 29.
[3] U. Bach, D. Lupo, P. Comte, J.E. Moser, F. Weissörtel, J. Salbeck, H. Spreitzer, M. Grätzel, Nature 395 (1998) 544.
[4] K. von Klitzing, in: Single-Electron Tunneling and Mesoscopic Devices, H. Koch, H. Lübig (Eds.), Springer Series in Electronics and Photonics, Vol. 31, Springer-Verlag, Heidelberg, 1992.
[5] S. Semancik, R. Cavicchi, Accounts of Chemical Research 31 (1998) 279.
[6] R. Waser, Integrated Ferroelectrics 15 (1997) 39.

J. Maier,
H.L. Tuller

From atoms to solids

T.P. Martin*

Max-Planck-Institut für Festkörperforschung, Heisenbergstr. 1, 70569 Stuttgart, Germany

Abstract

Under certain experimental conditions a periodic structure can be induced in the mass spectra of clusters of metal atoms. For example, if the clusters are heated with a laser beam, those with high stability resist evaporation. The resulting mass spectra reveal that clusters with closed electronic shells and clusters with perfect icosahedral symmetry are unusually stable. © 2000 Elsevier Science B.V. All rights reserved.

Keywords: Metal clusters; Mass spectrometry

1. Introduction

The properties of bulk metal are so different from those of a metal atom that it is sometimes hard to imagine how they might be related. However, a connection can be established by studying a succession of clusters containing 2, 3, 4, 5 . . . atoms. If the properties of the solid were found to evolve gradually and continuously with increasing cluster size, this type of investigation would not really be of much interest. But nature has presented us with a different situation. The properties of clusters change not continuously, but often periodically with cluster size. This is due to the formation of shells – shells of electrons and shells of atoms.

---
*Tel.: +49-711-689-1346; fax: +49-711-689-1010.
E-mail address: martin@vaxff3.mpi-stuttgart.mpg.de (T.P. Martin)

2. Shells of electrons

If it can be assumed that the electrons in metal clusters move in a spherically symmetric potential, [1–16] one must solve only a radial Schrödinger equation,

$$\left[\frac{-d^2}{dr^2} + \frac{l(l+1)}{r^2} + V(r) \right] P_{nl} = E_{nl}(r)$$
$$= E_{nl}P_{nl}(r) \tag{1}$$

where l is the angular momentum quantum number and $V(r)$ is the radial dependence of the potential in which the nucleons move. A further simplification can be made by assuming that $V(r)$ is a simple potential well. Some confusion can arise as we will use a slightly different definition for the principal quantum number n.

Throughout this paper we will use the principal quantum number from nuclear physics, i.e. n denotes

the number of extrema in the radial wavefunction. Subshells for large values of angular momentum can contain hundreds of electrons having the same energy. The highest possible degeneracy assuming cubic symmetry is only 6. So under spherical symmetry the multitude of electronic states condenses down into a few degenerate subshells. Each subshell is characterized by a pair of quantum numbers n and l, Fig. 1. Under certain circumstances the subshells themselves condense into a smaller number of highly degenerate shells. The reason for the formation of shells out of subshells requires more explanation.

The concept of shells can be associated with a characteristic length. Every time the radius of a growing cluster increases by one unit of this characteristic length, a new shell is said to be added. The characteristic length for shells of atoms is approximately equal to the interatomic distance. The characteristic length for shells of electrons is related to the wavelength of an electron in the highest occupied energy level (Fermi energy). For the alkali metals these lengths differ by a factor of about 2. This concept is useful only because the characteristic lengths are, to a first approximation, independent of cluster size.

3. Observation of electronic shell structure

Knight et al. [1] first reported electronic shell structure in sodium clusters in 1984. Electronic shell structure can be demonstrated experimentally in several ways: as an abrupt decrease in the ionization energy with increasing cluster size, as an abrupt increase or an abrupt decrease in the intensity of peaks in mass spectra. The first type of experiment can be easily understood. Electrons in newly opened shells are less tightly bound, i.e. have lower ionization energies. However, considerable experimental effort is required to measure the ionization energy of even a single cluster. A complete photoionization spectrum must be obtained and very often an appropriate source of tunable light is simply not available. It is much easier to observe shell closings in photoionization, TOF mass spectra. However, depending upon the intensity and wavelength of the ionizing laser pulse, the new shell is announced by either an increase or a decrease in mass peak height.

For high laser intensities, multiple-photon processes cause the mass spectra to be less wavelength sensitive and also cause considerable fragmentation of large clusters. The resulting mass spectrum re-

Fig. 1. The degeneracy of states of the infinitely deep spherical well on a momentum scale. The total number of fermions needed to fill all states up to and including a given subshell is indicated above each bar.
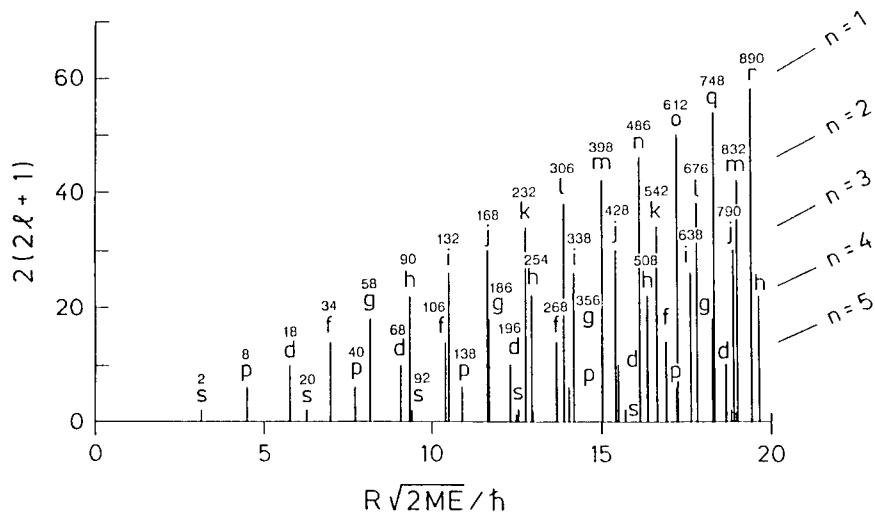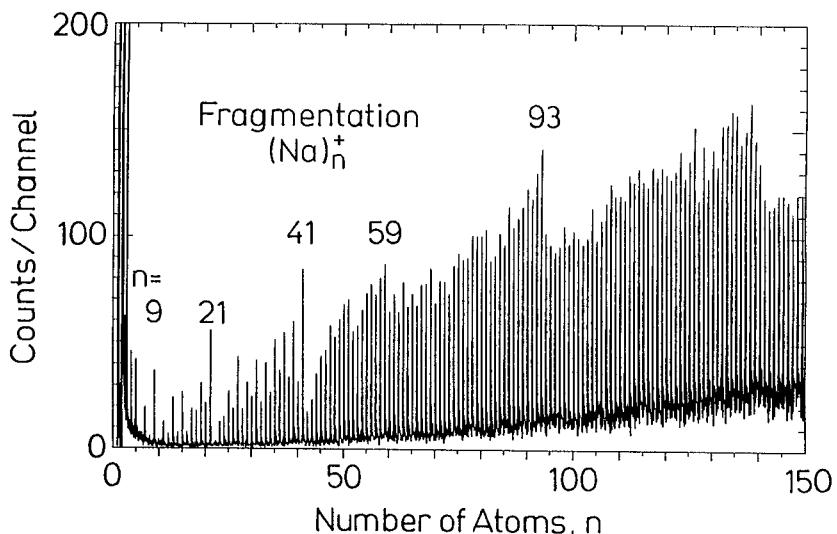
Fig. 2. Mass spectrum of $(Na)_n^+$ clusters ionized with high intensity, 2.53 eV light. The clusters are fragmented by the ionizing laser. Fragments having closed shell electronic configurations are particularly stable.

flects the stability of cluster ion fragments. Clusters with newly opened shells are less stable and are weakly represented in the mass spectra. Notice in Fig. 2 that as each new shell is opened there is a sharp step downward in the mass spectrum. Remember that cluster ions containing 9, 21, 41, 59, ... sodium atoms contain the magic number (8, 20, 40, 58, ...) of electrons.

4. Shells of atoms

One might think that the definition of a shell of atoms is straightforward – one layer of atoms arranged on the surface of a core such that the newly formed, larger unit has the same (overall) outer symmetry as the core itself. However, as one begins to construct examples, it becomes quickly clear that this definition might lead to confusion. For example, consider a cluster composed of atoms placed at the sites of a simple cubic lattice and having the overall outer shape of a cube. The first such cube that can be formed around a central atom contains 27 atoms, three atoms on a side; the next, 125 atoms, i.e. 5 atoms on a side, etc. But what happened to the 64 atom cube with 4 atoms on a side? It has no central

atom. That is, this simple example might be considered to describe two distinct shell sequences, one set of shells possessing a central atom; the other set has a central 8-atom cube. One way of getting around this difficulty is to combine the two sets into a single set. Each successive member of this combined set is obtained by adding atoms to only three of the six faces of the preceding member. We will see that it is useful to designate a set of such shells as irregular shells in order to distinguish them from, for example, the regular shells of an icosahedron where atoms must be added to all faces in order to complete the next shell.

5. Shells obtained from close-packed spheres

A limited number of symmetric clusters can be constructed from the close-packing of hard spheres; e.g. tetrahedra, octahedra, and their truncated forms. The truncated forms can have triangular, square or hexagonal faces. For example, the cuboctahedron, an octahedron truncated by a cube, Fig. 3, has 6 square faces and 8 triangular faces. Although this figure is constructed from close-packed layers, the cut form-
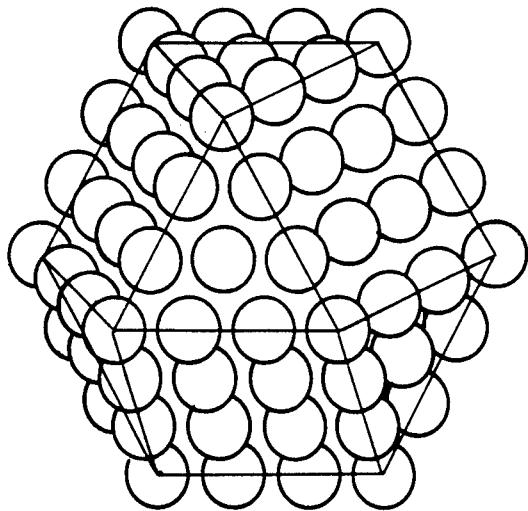
Fig. 3. A closed-shell 147 atom cuboctahedron. Notice that the atoms in the square faces are not close-packed.

ing a square face reveals a surface which is not close-packed. Such a surface is relatively unfavorable energetically and is a good candidate to accept the first atoms of a new shell.

6. Shell structures related to the bcc lattice

In a previous section we used the example of a cube-shaped cluster cut out of a simple cubic lattice. This was convenient to illustrate the concept of irregular shells, but is unrealistic in that elemental matter does not usually condense into a simple cubic structure. However, if such a cube is squeezed along a body diagonal, the cube deforms into a rhombohedron which can be cut out of a bcc lattice, Fig. 4. The bcc rhombohedron represents a set of irregular shells containing, of course, the same number of atoms as simple cubic shells. The bcc lattice contains also a set of regular shells. The first member in this set is shown in Fig. 4. The atoms of such clusters are contained within 12 rhombic faces.

7. Shell structures with five-fold symmetry

Until now we have discussed shell structure in clusters of close-packed atoms or of atoms on crystal lattice sites. Clusters in the form of icosahedra or decahedra are neither close-packed nor are they small pieces cut out of a crystal. A five-fold symmetry axis is not consistent with the crystalline requirement of translational symmetry. Icosahedra form a set of regular shells around a central atom, Fig. 5.

Fig. 4. A smaller geometric figure found in a bcc lattice is outlined with heavy lines. This figure can be found in shells of increasing size.
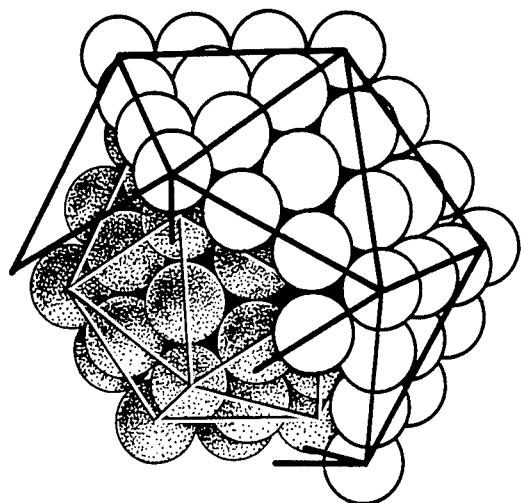
Fig. 5. A closed-shell 55 atom icosahedron and a portion of the next shell.
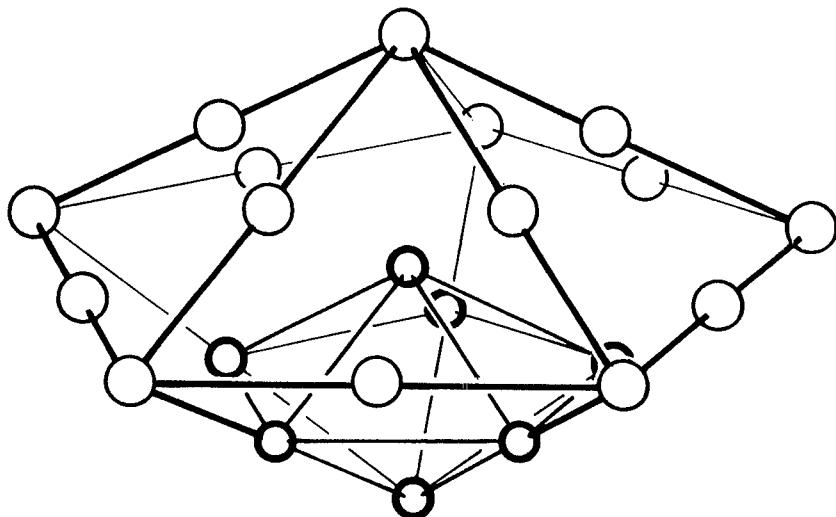
Fig. 6. Decahedra form a set of irregular shells. Successively larger shells are formed by adding an umbrella-shaped partial layer.

Nature has played a strange trick on us here. The number of atoms needed to complete icosahedral shells is exactly that needed to complete cuboctahedral shells. For this reason, the experimental observation of magic numbers corresponding to shell closings is not sufficient to allow us to distinguish between non-crystalline icosahedra and fcc cuboctahedra.

Decahedra represent a set of irregular shells. The shells possess alternately a central atom and a central 7-atom decahedron and are formed by placing a large overlapping 'umbrella' on top of the previous member of the set, Fig. 6.

8. Observation of shells and subshells of atoms

Both calculations and experiments [17–25] indicate that inert gas clusters containing from 13 to 923 atoms have icosahedral symmetry. These might be referred to as precrystalline structures since the inert gases are known to condense into fcc crystals. Precrystalline structures have also been observed for metallic materials in condensed units large enough to yield sharp electron diffraction patterns [26–28]. These quasicrystals present a fascinating challenge to scientists to develop methods for describing a regular but nonperiodic state of bulk matter. Smaller

icosahedral metal particles have been observed directly using the technique of high-resolution electron microscopy [29].

Additional evidence exists for icosahedral symmetry in metal clusters. Calculations predict that very small alkaline earth clusters prefer noncrystalline structures [30–34]. The pattern of NH_3 and H_2O binding energies with Co and Ni clusters has been interpreted as indicating icosahedral symmetry in metal clusters containing from 50 to 150 atoms [35,36]. Mass spectra of Ba and Ba–O clusters seem to indicate an icosahedral growth sequence in the size range from 13 to 35 atoms [37–39].

Recently we observed a slow modulation in mass spectra of Na clusters, Fig. 7, which we interpreted as evidence for the existence of shell structures, i.e. a highly symmetric, onion-like cluster structure [14]. The modulation appeared only if the energy of the ionizing photons was chosen to coincide with the ionization potential of the clusters and was found to be almost periodic when plotted on a cube root of mass scale. The cusp-like minima of the mass spectra pointed to characteristic masses or numbers of atoms. Within the accuracy of reading the minima, these magic numbers correspond to the number of atoms in complete Mackay icosahedra [40]. However, on the basis of such observations, it is not possible to conclude that the clusters have icosahedr-

Shell of Atoms
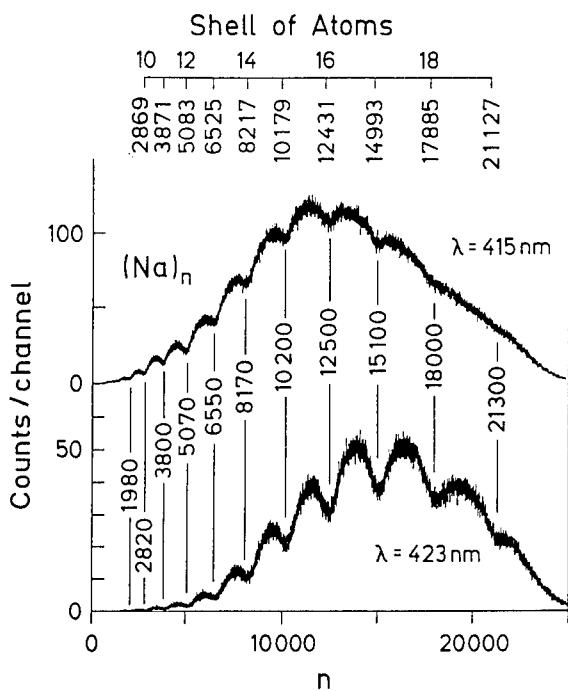
Fig. 7. Averaged mass spectra of (Na)$_n$ clusters photoionized with 2.99 and 2.93 eV light. Well-defined minima occur at values of n corresponding to the total number of atoms in close-packed cuboctahedra and nearly close-packed icosahedra (listed at top).

al symmetry because icosahedral shells and fcc cuboctahedral shells contain exactly the same number of atoms.

Fig. 8 shows a mass spectrum of pure Mg clusters containing up to 3000 atoms [41]. The choice of ionizing photon energy and laser intensity is important. We have used 50 mJ/cm^2 of 308 nm radiation per 10 ns pulse. With such high intensities massive fragmentation of the clusters is to be expected. For this reason we believe that strong peaks in the mass spectrum indicate cluster ion fragments with high stability. Even though we are using a high laser intensity, the signal is weak, about one cluster per laser shot. Over 200 000 shots at 50 Hz were required to obtain this spectrum. Because of the low signal, some averaging is necessary to bring out the spectral features. First, an average is made over 500 time channels. This, plus the fact that magnesium has three natural isotopes (79% ^{24}Mg, 10% ^{25}Mg, 11% ^{26}Mg), limits the mass resolution. In a next step the spectrum is averaged over 5000 time channels. The resulting curve contains no structure but is merely an envelope of the original data. Finally, we form the ratio of the slightly averaged spectrum to the strongly averaged (envelope) spectrum. The resulting ratio spectra are shown in Figs. 8 and 9.
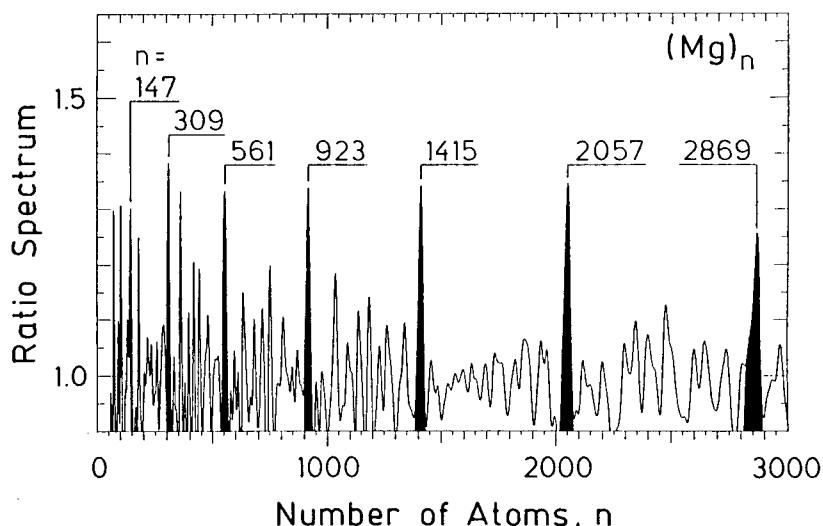
Fig. 8. Ratio spectrum (slightly smoothed mass spectrum divided by highly smoothed envelope spectrum) for Mg clusters. The filled mass peaks correspond to completely filled icosahedral shells.
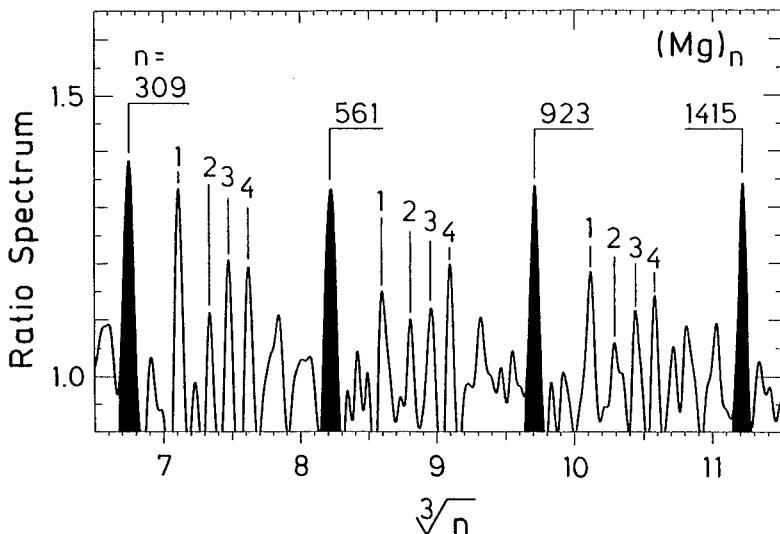
Fig. 9. Ratio mass spectrum of $(Mg)_n$ clusters. The filled mass peaks, corresponding to completely filled icosahedral shells, are nearly equally spaced on this $\sqrt[3]{n}$ scale. The four mass peaks observed between shell closings indicate highly stable partial shells.

The strongest mass peaks correspond to the number of atoms in closed shells having either icosahedral or cuboctahedral symmetry. The Mackay icosahedra can be constructed from nearly close-packed spheres. These structures might be called noncrystalline since they possess a point group which is not consistent with translational symmetry. Cuboctahedra on the other hand, can be constructed from close-packed spheres. In fact, cuboctahedra containing an arbitrary number of shells can be cut out of a fcc crystal. The main sequence of strong mass peaks does not allow us to distinguish between these two structures. We have to look elsewhere for decisive experimental data. We believe these data are contained in the weaker mass peaks between shell closings.

Fig. 9 shows a portion of the previous mass spectrum but now plotted against $n^{1/3}$. Notice that the four main peaks are equally spaced. This is a characteristic common to all types of shell structure. The reason for this can be seen in the following way. Every time the radius (proportional, of course, to $n^{1/3}$) of a growing cluster increases by one unit of a characteristic length, a new shell is said to be added.

Notice in Fig. 9 that the spectral features between complete shells repeat exactly within the statistical accuracy of the experiment. In particular, we will focus our attention on the repetitive peak structure labeled 1, 2, 3 and 4, and suggest below that this structure corresponds to partial icosahedral shells.

The clusters most probably grow by adding shells of atoms to a rigid core. The number of atoms contained in a growth shell is dependent on the preferred coordination and local symmetry of the atoms and on the overall symmetry of the shell. If we assume that the magnesium atoms are close-packed, or nearly so, and that the outer form is that of an cuboctahedron or an icosahedron, then the total number of atoms N_k in a cluster containing K shells of atoms is [41].

$$N_k = (10\,K^3 + 15\,K^2 + 11\,K + 3)/3. \qquad (2)$$

Clusters constructed of complete shells can be expected to be highly stable. For inert gas clusters both experiments and calculations indicate that partial icosahedral shells of atoms also show enhanced stability [19–23]. For example, one might expect that completely covered facets of a cluster surface represent intermediate structures of high stability. Since the facet structure of the icosahedron (20 triangular faces) and the cuboctahedron (8 triangular and 6 square faces) are quite different, a determination of

partial shell sizes should make it possible to dis-
tinguish between the two structures.

The square faces of the cuboctahedron would be
likely candidates to accept the first atoms of a newly
deposited layer because the atoms in these faces are

not close-packed. However, no arrangement of atoms
on these faces alone or in combination with other
cuboctahedral faces could be found which matched
the observed subshell magic numbers. Next, we
turned to the icosahedron for which subshell struc-
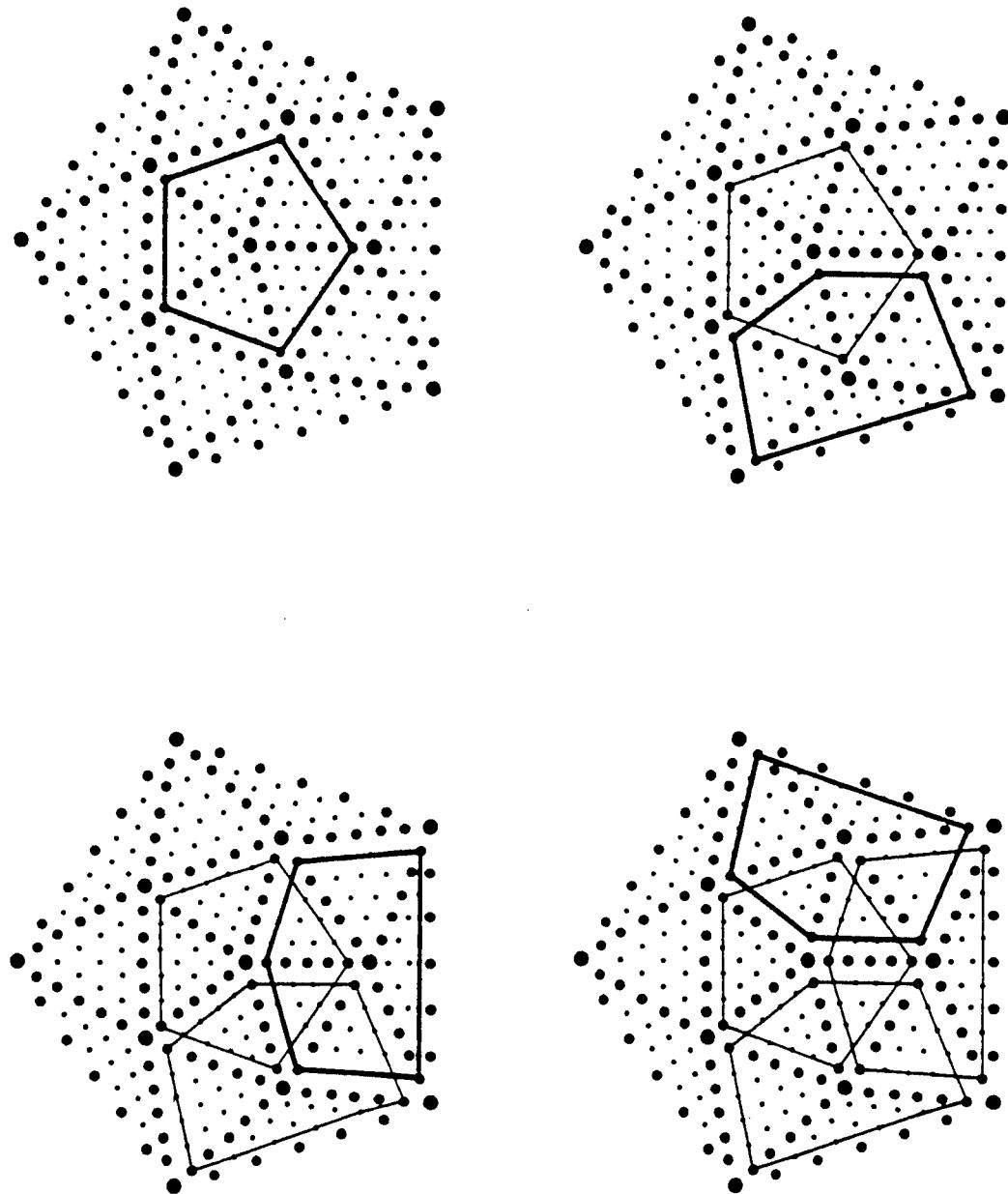
Fig. 10. The dots represent the atoms of the 7th shell of an icosahedron projected onto a plane. The bottom 76 atoms are not shown. The umbrella-shaped structures are identical, each containing 76 atoms. We suggest that the umbrellas represent highly stable partial shells of magnesium atoms.

ture had already been studied [19–23]. The first atoms to form a new shell on an inert gas icosahedron apparently do not immediately take their final positions. This would force atoms on the border between two triangular faces to have contact with only two substrate atoms. Instead, the triangular faces are first filled with a close-packed layer. Only after the shell is more complete do the atoms rearrange into their final icosahedral positions. This shell filling sequence, observed in inert gas clusters, although close, seems to deviate significantly from the observed magic numbers for Mg clusters. There-

fore, we would like to suggest an alternative sequence.

Assume that the atoms in the new shell take immediately their final positions. In Fig. 10 the positions of the atoms in the seventh shell have been projected onto a plane in the manner of Northby [20,21]. We suggest that umbrella-shaped intermediate groups have enhanced stability. Each of the umbrellas contains 76 atoms and each has the same shape (although they appear distorted in the projection shown in Fig. 10). Only 51 additional atoms are necessary to complete the second umbrella because it
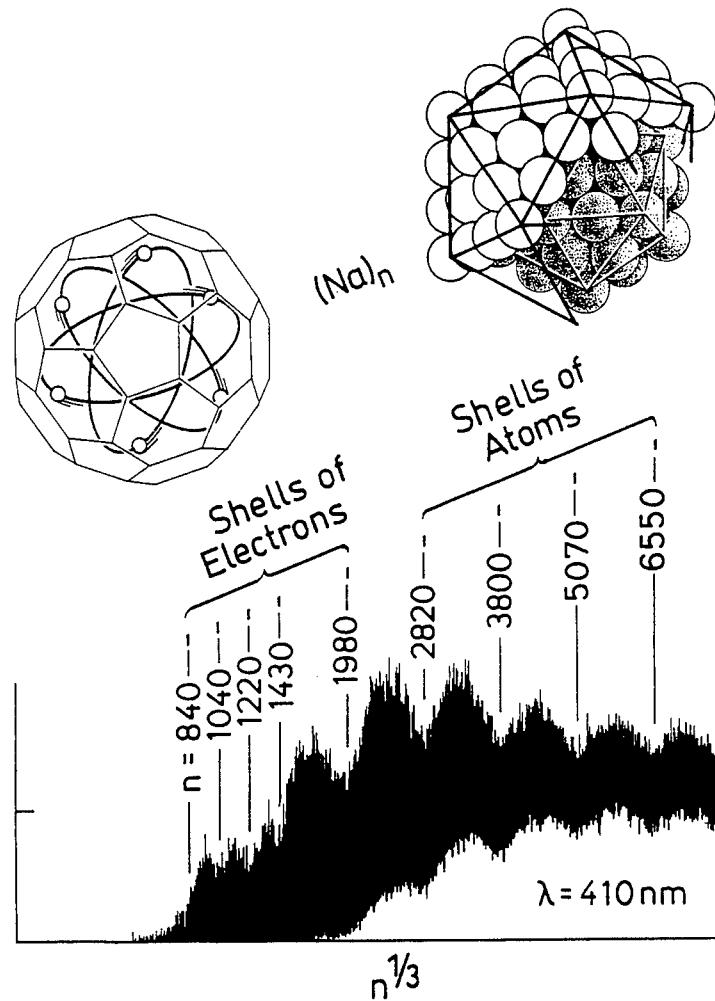
Fig. 11. Mass spectrum of $(Na)_n$ clusters photionized with 3.02 eV photons. Two sequences of structures are observed at equally spaced intervals on the $n^{1/3}$ scale – an electronic shell sequence and a structural shell sequence.

shares atoms with the first. The third and fourth umbrellas overlap two others. Therefore, they require only 36 additional atoms for completion.

9. Transition from shells of electrons to shells of atoms

Two types of shell structure have been observed in the same mass spectrum of large sodium clusters, Fig. 11. For small clusters ($n \leq 1500$) the pattern appears to be due to the filling of electronic shells. For large clusters the shells seem to be composed of atoms.

Why might one expect a transition from electronic shell structure to shells of atoms? For very small clusters the atoms are highly mobile. There is no difficulty for the atoms to arrange themselves into a sphere-like conformation if this is demanded by the closing of an electronic shell. At a size corresponding to about 1500 atoms under our experimental conditions, the clusters become rigid. Thereafter, each newly added atom condenses onto the surface and remains there. Further growth takes place by the accumulation of shells of atoms.

References

[1] W.D. Knight, K. Clemenger, W.A. de Heer, W.A. Saunders, M.Y. Chou, M.L. Cohen, Phys. Rev. Lett. 52 (1984) 2141.

[2] M.M. Kappes, R.W. Kunz, E. Schumacher, Chem. Phys. Lett. 91 (1982) 413.

[3] I. Katakuse, I. Ichihara, Y. Fujita, T. Matsuo, T. Sakurai, T. Matsuda, Int. J. Mass Spectrom. Ion Processes 67 (1985) 229.

[4] C. Brechignac, Ph. Cahuzac, J.-Ph. Roux, Chem. Phys. Lett. 127 (1986) 445.

[5] W. Begemann, S. Dreihofer, K.H. Meiwes-Broer, H.O. Lutz, Z. Phys. D 3 (1986) 183.

[6] W.A. Saunders, K. Clemenger, W.A. de Heer, W.D. Knight, Phys. Rev. B 32 (1986) 1366.

[7] T. Bergmann, H. Limberger, T.P. Martin, Phys. Rev. Lett. 60 (1988) 1767.

[8] J.L. Martins, R. Car, J. Buttet, Surf. Sci. 106 (1981) 265.

[9] W. Ekardt, Ber. Bunsenges. Phys. Chem. 88 (1984) 289.

[10] K. Clemenger, Phys. Rev. B 32 (1985) 1359.

[11] Y. Ishii, S. Ohnishi, S. Sugano, Phys. Rev. B 33 (1986) 5271.

[12] T. Bergmann, T.P. Martin, J. Chem. Phys. 90 (1989) 2848.

[13] H. Göhlich, T. Lange, T. Bergmann, T.P. Martin, Phys. Rev. Lett. 65 (1990) 748.

[14] T.P. Martin, T. Bergmann, H. Göhlich, T. Lange, Chem. Phys. Lett. 172 (1990) 209.

[15] S. Bjørnholm, J. Borggreen, O. Echt, K. Hansen, J. Pederson, H.D. Rasmussen, Phys. Rev. Lett. 65 (1990) 1627.

[16] E.C. Honea, M.L. Homer, J.L. Persson, R.L. Whetten, Chem. Phys. Lett. 171 (1990) 147.

[17] M.R. Hoare, Adv. Chem. Phys. 40 (1979) 49.

[18] O. Echt, K. Sattler, E. Recknagel, Phys. Rev. Lett. 47 (1981) 1121.

[19] J. Farges, M.F. de Feraudy, B. Raoult, G. Torchet, J. Chem. Phys. 84 (1986) 3491.

[20] J.A. Northby, J. Chem. Phys. 86 (1987) 6166.

[21] I.A. Harris, R.S. Kidwell, J.A. Northby, Phys. Rev. Lett. 53 (1984) 2390.

[22] P.G. Lethbridge, A.J. Stace, J. Chem. Phys. 91 (1989) 7685.

[23] W. Miehle, O. Kandler, T. Leisner, O. Echt, J. Chem. Phys. 91 (1989) 5940.

[24] The subject of icosahedral shells of atoms in inert gas clusters has a long and interesting history. For a recent starting point into this extensive literature see: Proceedings of Faraday Symposium on Large Gas Phase Clusters, J. Chem. Soc. Faraday Trans. 86 (1990).

[25] K.E. Schriver, M.Y. Hahn, J.L. Persson, M.E. LaVilla, R.L. Whetten, J. Phys. Chem. 93 (1989) 2869.

[26] D. Shechtman, I. Blech, D. Gratias, J.W. Chan, Phys. Rev. Lett. 53 (1984) 1951.

[27] C. Janot, J.-M. Dubois, J. Non-Crystalline Solids 106 (1988) 193.

[28] B.D. Hall, M. Flüeli, R. Monot, J.-P. Borel, Z. Phys. D 12 (1989) 97.

[29] C. Chapon, M.F. Gillet, C.R. Henry (Eds.), Proceedings: 4th Intl. Meeting on Small Particles and Inorganic Clusters, Springer, Berlin–Heidelberg–New York, 1989.

[30] E. Blaisten-Barojas, S.N. Khanna, Phys. Rev. Lett. 61 (1988) 1477.

[31] F. Reuse, S.N. Khanna, V. de Coulon, J. Buttet, Phys. Rev. B 41 (1990) 11743.

[32] G. Pacchioni, W. Pewestorf, J. Koutecky, Chem. Phys. 8 (1984) 201.

[33] C.W. Bauschlicher, P.S. Bagus, B.N. Cox, J. Chem. Phys. 77 (1982) 4032.

[34] J. Koutecky, P. Fantucci, Chem. Rev. 86 (1986) 539.

[35] T.D. Klots, B.J. Winter, E.K. Parks, S.J. Riley, J. Chem. Phys. 92 (1990) 2110.

[36] B.J. Winter, T.D. Klots, E.K. Parks, S.J. Riley, Z. Phys. D 19 (1991) 381.

[37] D. Rayane, P. Melinon, B. Cabaud, A. Hoareau, B. Tribollet, M. Broyer, Phys. Rev. A 39 (1989) 6056.

[38] R.L. Whetten, private communications.

[39] T.P. Martin, T. Bergmann, J. Chem. Phys. 90 (1990) 6664.

[40] A.L. Mackay, Acta Cryst. 15 (1962) 916.

[41] T.P. Martin, T. Bergmann, H. Göhlich, T. Lange, Chem. Phys. Lett. 176 (1991) 343.

**SOLID
STATE
IONICS**

Point-defect thermodynamics and size effects

Joachim Maier*

Max-Planck-Institut für Festkörperforschung, Heisenbergstraße 1, 70569 Stuttgart, Germany

Abstract

The introductory part reviews some basic aspects of bulk point-defect thermodynamics. It makes use of the fact that for the purposes under consideration, the real structure can be decomposed in a perfect ground structure and a superimposed defect structure. Then modifications of the point-defect concentration and distribution are considered occurring if interfaces are approached. A simple treatment is possible for the abrupt core-space charge situation in which the standard chemical potentials are assumed to change in a step-like way. Evidence is given that in very many cases this is a reasonable model. There, the adjustment at interfaces occurs solely via space charge regions. 'Trivial' size effects are brought about by the changed surface (i.e. core plus space charge layer) to volume ratio. A mesoscale size effect is expected if the width of the space charge layers is no longer small compared with the distance of neighbouring interfaces (Debye-length λ as scaling parameter). In some situations, e.g. if extremely small clusters are treated, distinct deviations in the ground structure also occur, affecting energetic and entropic standard terms. Since such modifications usually decay steeply with increasing interfacial distance (L), another scaling parameter (ℓ) defines a further mesoscopic regime. As examples, micro- and nano-sized particles, films, polycrystals and composites are discussed. © 2000 Elsevier Science B.V. All rights reserved.

Keywords: Point defects; Thermodynamics; Size effects; Interfaces; Space charges; Nanocrystallinity

1. Introduction

Point defects in solids are, on the one hand, analogous to the H_3O^+ and OH^- ions which play a central role in aqueous electrochemistry, and to excess electrons and electron holes, the decisive carriers in semiconductor physics, on the other. In both fields it is a matter of fact that boundary effects have a significant influence on the charge carrier concentrations and distributions.

In both fields, the importance of the nanoscale is also evident as exemplified by colloid chemistry, bio-electrochemistry [1–3] or by the emerging field of nano-electronics [4]. Beyond that, the nanoscale is the scale on which macroscopic and microscopic concepts meet, e.g. the transition between cluster chemistry and physics [5–7], and solid state science.

In this contribution, static interfacial effects are discussed for the field of Solid State Ionics in particular with respect to expected and observed nanosize phenomena (cf. also Refs. [8–10]).

The structure of the paper is as follows: After a brief overview on bulk defect thermodynamics (Section 2), the defect chemistry at interfaces embedded

*Tel.: +49-711-689-1720; fax: +49-711-689-1722.

E-mail address: weiglein@chemix.mpi-stuttgart.mpg.de (J. Maier)

in the infinite bulk is considered (Section 3). In Section 4 interfaces are successively brought closer to each other and the resulting size effects are studied.

2. Point-defect thermodynamics in the infinite bulk

In the classical treatment of defective materials, the real structure is decomposed into a perfect (ground) structure and a (chemically excited) defect structure:

Real structure = perfect structure + defect structure

$$(1)$$

the first one being invariant while the latter responds to changes in the state and control parameters, in particular temperature (T), doping content (C) and component potential (e.g. expressed by the oxygen partial pressure P in a binary oxide). In the infinite bulk, electroneutrality is usually an excellent assumption [11–13]. Global and local equilibrium at constant T and total pressure demands the minimisation of the Gibbs energy in terms of the particle numbers. If the defects are dilute, Boltzmann statistics can be applied and ideal mass action laws follow. If the electroneutrality condition can be condensed to a proportionality of two majority carrier concentrations, the power law form [14–16]

$$c_j = \alpha_j P^{N_j} C^{M_j} \Pi_r K_r^{\gamma_{rj}}(T) \qquad (2)$$

results, with the characteristic exponents N_j, M_j, γ_{rj} (simple rational numbers). The K_rs are the mass action constants of the defect reactions under regard. Representations of $\log c_j$ $vs.$ $\log P$ (Kröger–Vink plots), $\log c_j$ vs. $\log C$ as well as $\log c$ vs. $1/T$ (Arrhenius or better van't Hoff plots) yield straight lines with N_j, M_j and $\Sigma_r \ \gamma_{rj}\Delta_r H^\circ$ ($\Delta_r H^\circ$: standard enthalpy of reaction r) as slopes. A sensitive measure for c_j is the conductivity σ_j which also involves the T-dependent mobility.

Fig. 1 shows the defect chemistry of the Frenkel disordered material AgCl. Since ionic carriers are in majority, the electroneutrality equation is $[\mathrm{Ag}_i^\cdot] \cong [\mathrm{V}_{\mathrm{Ag}}']$. The important disorder reactions are the Frenkel reaction (r = F)
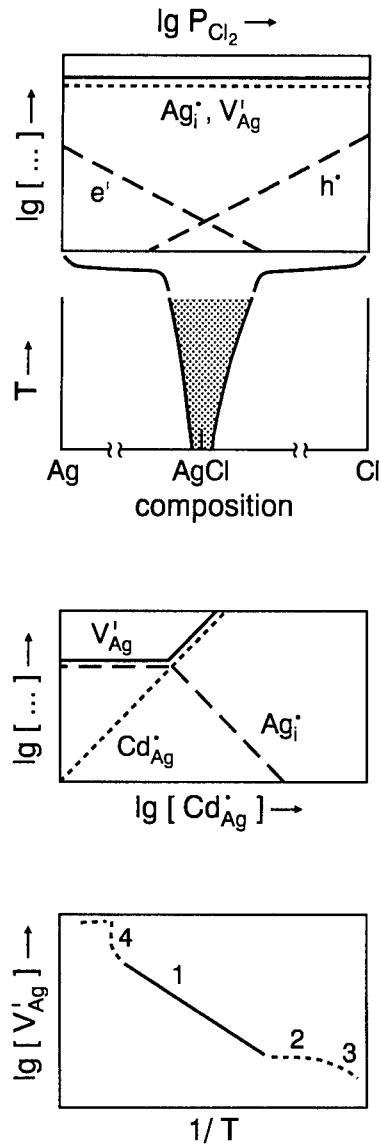
Fig. 1. Defect chemistry in the bulk of AgCl.

$$\mathrm{Ag_{Ag}} + \mathrm{V}_i \rightleftharpoons \mathrm{Ag}_i^\cdot + \mathrm{V}_{\mathrm{Ag}}' \qquad (3)$$

as well as the interaction with the component potential according to (r = Cl)

$$\frac{1}{2}\mathrm{Cl}_2(g) + \mathrm{Ag}_i^\cdot \rightleftharpoons \mathrm{AgCl} + \mathrm{V}_i + h^\cdot \qquad (4)$$
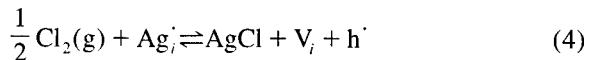
or in terms of Ag (g) (r = Ag)

$$\mathrm{Ag}(g) + h^\cdot + \mathrm{V}_i \rightleftharpoons \mathrm{Ag}_i^\cdot. \qquad (5)$$

Note that silver and Cl_2-partial pressures are related to the formation enthalpy according to

$$P_{Ag} \cdot P_{Cl_2}^{1/2} \simeq \text{const.} \exp - \Delta_f G_{AgCl}{}^{\circ}. \tag{6}$$

The inter-correlation of $[h^{\cdot}]$ with $[e']$ is provided by the band gap transfer $(r = B)$

$$\text{Nil} \rightleftharpoons e' + h^{\cdot}. \tag{7}$$

The interaction with the component potential is only relevant on the level of the electrons as minority carriers, while the majority carrier concentrations (ions) are approximately independent of P_{Cl_2} and P_{Ag}. Hence, $[Ag_i^{\cdot}] = [V_{Ag}'] = K_F^{1/2}$ as shown at the top of Fig. 1, while $[e'](\propto P_{Cl_2}^{-1/2})$ and $[h^{\cdot}](\propto P_{Cl_2}^{1/2})$ sensitively depend on the position in the phase diagram. In the van't Hoff diagram (bottom of Fig. 1), a straight line (1) results with the slope of $\Delta_F H^{\circ}/2$.

Irreversibly introduced aliovalent impurity traces (e.g. Cd^{2+} on Ag^{+}-site, i.e. $Cd_{Ag}^{\cdot}$) appear in the electroneutrality equation only. If $[Cd_{Ag}^{\cdot}]$ has been increased to values in the order of or greater than $K_F^{1/2}$ (see centre Fig. 1), $[V_{Ag}']$ increases $(\rightarrow [Cd_{Ag}^{\cdot}] \simeq [V_{Ag}'])$ as $[e']$ does, while $[Ag_i^{\cdot}](\rightarrow K_F/[V_{Ag}'])$ and $[h^{\cdot}]$ decrease (see centre of Fig. 1 and curve 2 in the bottom picture). At lower temperatures short range interactions become important. This short range interaction can, to a good extent, be taken into account by an association reaction (see curve 3 in the bottom picture, low T) [17,18].

$$Cd_{Ag}^{\cdot} + V_{Ag}' \rightleftharpoons (Cd_{Ag} V_{Ag})^{\times}. \tag{8}$$
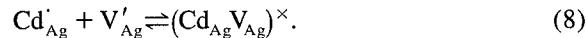
We now have three ionic species (free Cd^{2+}, free Ag^{+}-vacancy and associate) for which again, Boltzmann statistics can be applied with reasonable approximation.

Such a procedure does not work at high temperatures (usually below the melting point) at which so many native defects have been generated that (i) the restricted number of sites and (ii) the long-range interactions must be taken account of. The former can be done by using Fermi–Dirac type of statistics:

$$\mu = \mu^{\circ} + RT \ln \frac{c}{c_{max} - c} \tag{9}$$

the latter leads to the introduction of interaction coefficients (μ^{ex}) due to Coulomb interaction. These long-range Coulomb interactions lower the effective defect formation energy such that defect formation becomes successively more favourable leading to an over-Arrhenius increase of the ionic conductivity and eventually even to a phase transition (see curve 4 in the bottom picture, high T). The classical approach to describe long-range interactions is the Debye–Hückel theory [19] which fails at significantly high concentrations ($>0.1\%$). In Ref. [20] it was shown that, in such cases, a quasi-Madelung approach ($\mu^{ex} \propto c^{1/3}$) can yield a reasonable explanation of both the conductivity anomaly as well as the phase transition temperatures. The proportionality factor between the excess chemical potential and the cube root of the concentration is in line with a simple Madelung estimate as well as with recent MD-simulations [21].

3. Equilibrium point-defect distribution at interfaces

Now we investigate the modifications due to approaching interfaces. First of all we adopt a simplified picture which assumes (ground) structural invariance up to the core of the interfaces which itself is thought to be of a different but invariant (ground) structure. In other words we assume the chemical ground structure to behave as an ideal step function and allow only the point-defect concentration to vary and to contribute to the adjustment of the electrochemical potentials.

Real structure = Perfect bulk structure
+ perfect core structure
+ inhomogeneous defect structure

$$(10)$$

In particular, carrier mobilities and standard chemical potentials (and thus mass action constants) behave in a step-function way. In contrast to the perfect structure, the defect structure — and thus the carrier concentrations — does not vary in a step-function way but is smeared out around the interface.

We follow the core-space-charge model described in more detail in Ref. [22]. As a consequence of the abrupt change of structure and standard chemical potentials and as a consequence of the requirement

that the electrochemical potentials of all mobile species have to be homogeneous, changes of the chemical potentials occur at the expense of electrical potential changes, in other words, space charge regions with modified defect concentrations come into play. The complete treatment demands knowledge of defect chemistry of both bulk and core, to establish for each carrier j the relationship:

$$c_j = f_j(x; P, T, C; \mathbf{B}) \tag{11}$$

$\mathbf{B}$ denotes the parameter set additionally necessary to define the interface. Already in the case of an ideal grain boundary, $\mathbf{B}$ is at least a five-fold manifold[1] [24]. Owing to the kinetic constraints and the complexity of interfacial structure and composition, the core ground structure and composition ($\mathbf{B}$) is more pragmatically handled as a irreversibly introduced boundary condition and thus as a further controlling parameter similar to C in Eq. (2).

If two majority defects 1, 2 of equal absolute charge follow the space charge field we can write

$$c_j / c_\infty = \left(\frac{1 + \vartheta_j \exp - x/\lambda}{1 - \vartheta_j \exp - x/\lambda} \right)^2 . \tag{12}$$

ϑ, the degree of influence contains the boundary core chemistry, while c_∞ and $\lambda(c_\infty)$ contain the bulk chemistry. The conductance enhancement parallel to the interface follows as

$$\Delta Y^{\parallel} = \sum_{j=1,2} (2\lambda) F u_j \left(2c_\infty \frac{\vartheta_j}{1 - \vartheta_j} \right) \tag{13}$$

(u: mobility, $\vartheta_1 = -\vartheta_2$). For details see Ref. [25]. Besides grain boundaries, phase boundaries are of importance such as interfaces of a mixed conductor with an inert solid material, with a second mixed conductor (which includes grain boundaries) or with a gas phase. In Ref. [26] an extensive discussion of related conductivity effects is given. To mention a few examples, grain boundaries may exhibit conductive pathways along the enhancement layer while they may simultaneously block the transport by a

resistive core; surface active insulators can adsorb mobile ions and lead to enhanced vacancy conduction; in the miscibility gap of two conductors, conductivity anomalies can occur through a carrier redistribution, and at surfaces adsorbed gas molecules may lead to ionic space charge effects (see Fig. 2: CaF_2/BF_3). Analogous effects are known for electronic conductors. In mixed conductors usually the interaction of the majority carriers (e.g. ions) defines the space charge potential which is then perceived by the minority species (e.g. electrons [26]). Beyond that, the ratio of ionic and electronic conductivity may be varied [28–30]. In some cases, surface-interaction free energies may well be enough to lead to interfacial phase transitions [31,32]. They can, e.g. be thought to be formed via charge carrier interaction as discussed which can be different in the boundary regions, e.g. due to modified carrier concentration [26].

Fig. 3 shows the conductivity enhancement of heterogeneously doped AgCl. The effects can be quantitatively described by an ideal space charge model [26].

The conductivity enhancement in heterogeneously doped β-AgI [33] is qualitatively in agreement with the simple space charge theory (tendencies, slopes etc.) but the absolute values are too high by orders of magnitude to account for the effect quantitatively. It has been shown [34–36] that interfacial phase transitions occur which are not unexpected in view of the polymorphism of the AgI-structures and the statements given in the previous section. A more detailed explanation of the anomaly is given in Section 4.

In addition to the excess charge, pure core disorder may also be important in view of lowered defect formation energies and varied mobilities for core defects. For more details on this see Ref. [37]. Recent computer simulations [38,39] show that in CeO_2 oxygen vacancies and excess electrons are more stable at the surface than in the bulk.

The step-function behaviour of the structure, i.e. of $\mu°$, is of course an assumption. Structural models show that bond distances may vary over a certain range at boundaries in a more or less smooth way. From structure investigations it is known that the H_2O-structure of ice becomes water-like in the vicinity of surfaces [40], while the first layers of liquid water in contact with certain electrodes are

---

[1]Five is the number of macroscopic degrees of freedom determining the configuration of grain boundaries obtained by bringing together two single crystalline pieces. The additional microscopic degrees of freedom can usually not be controlled independently [23].
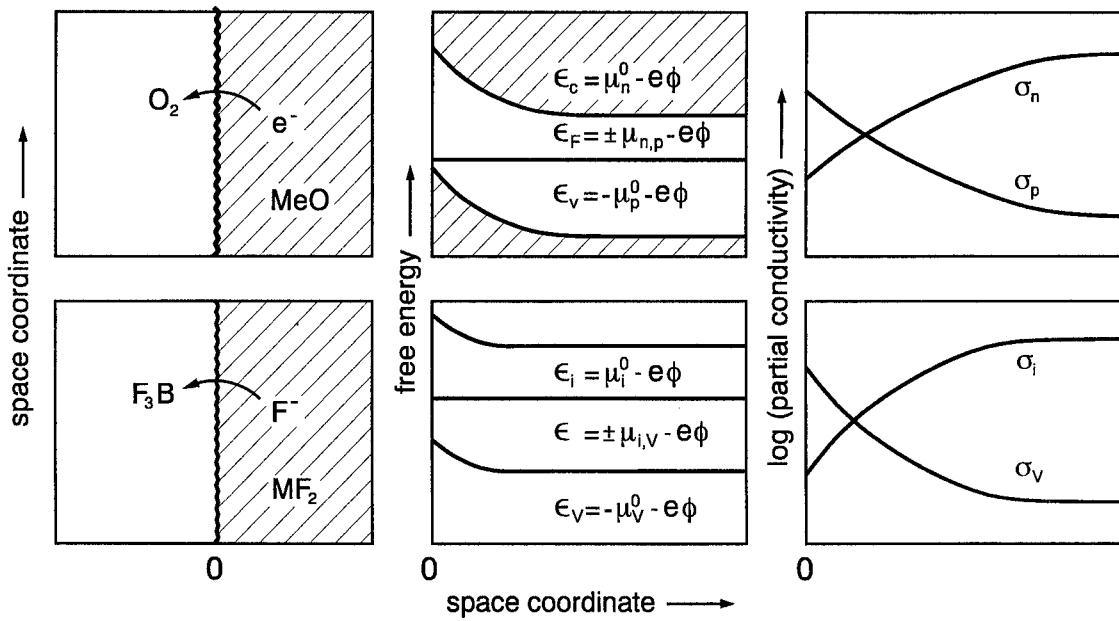
Fig. 2. The exposure of CaF_2 to the Lewis-acid BF_3 leads to an increase of the fluoride vacancy concentration (conductivity). The effect is analogous to the exposure of semiconducting oxides to O_2. This is shown by the potential diagrams in the central column (cf. Refs. [26,27]).
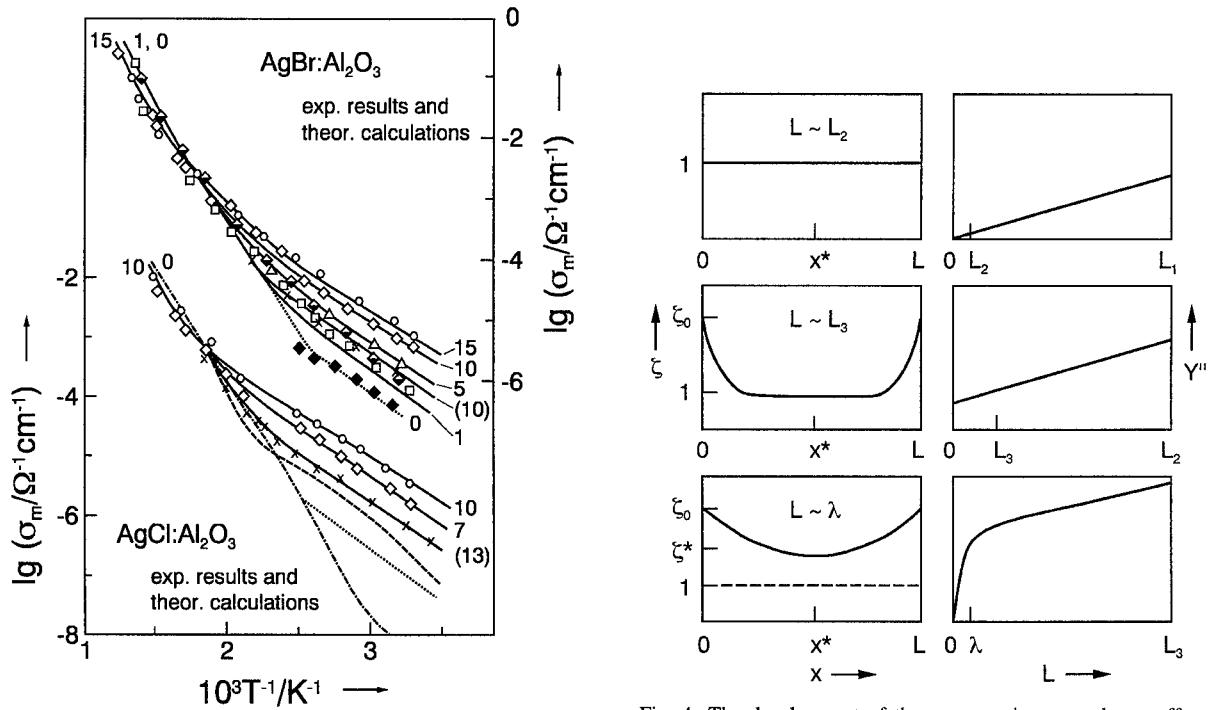
Fig. 3. The effect of 'heterogeneous doping' of AgCl and AgBr can be quantitatively interpreted by space charge effects [25].

Fig. 4. The development of the mesoscopic space charge effect. L.h.s.: concentration profiles ($\zeta \equiv c/c_\infty$). R.h.s.: thickness dependence of the parallel excess conductance.
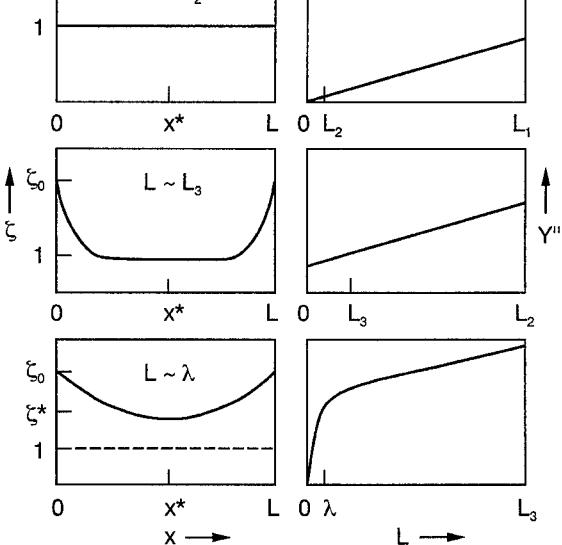
ice-like [41]. This point will be taken up again in Section 4.3. (Fig. 4).

4. Size effects on point-defect thermodynamics

4.1. 'Trivial' size effects

If the size of the crystal is reduced so is the distance between neighbouring interfaces, overall properties, e.g. the overall transport properties can significantly change just due to the increased interface to volume ratio, i.e. the local properties being invariant. Thus transport along the core regions may

dominate in nanocrystalline samples although it may be completely insignificant in microcrystalline samples. The same is true for space charge transport. Nonetheless these 'trivial' effects can be striking [37]. One example is the depression of the melting point of nanosized crystals. This example is taken up again in Section 4.2. But let us now consider the situation that also the local properties are size-dependent.

4.2. Mesoscopic space charge effect

Again, we first adopt the abrupt structural model. Fig. 5 highlights the occurrence of a mesoscopic
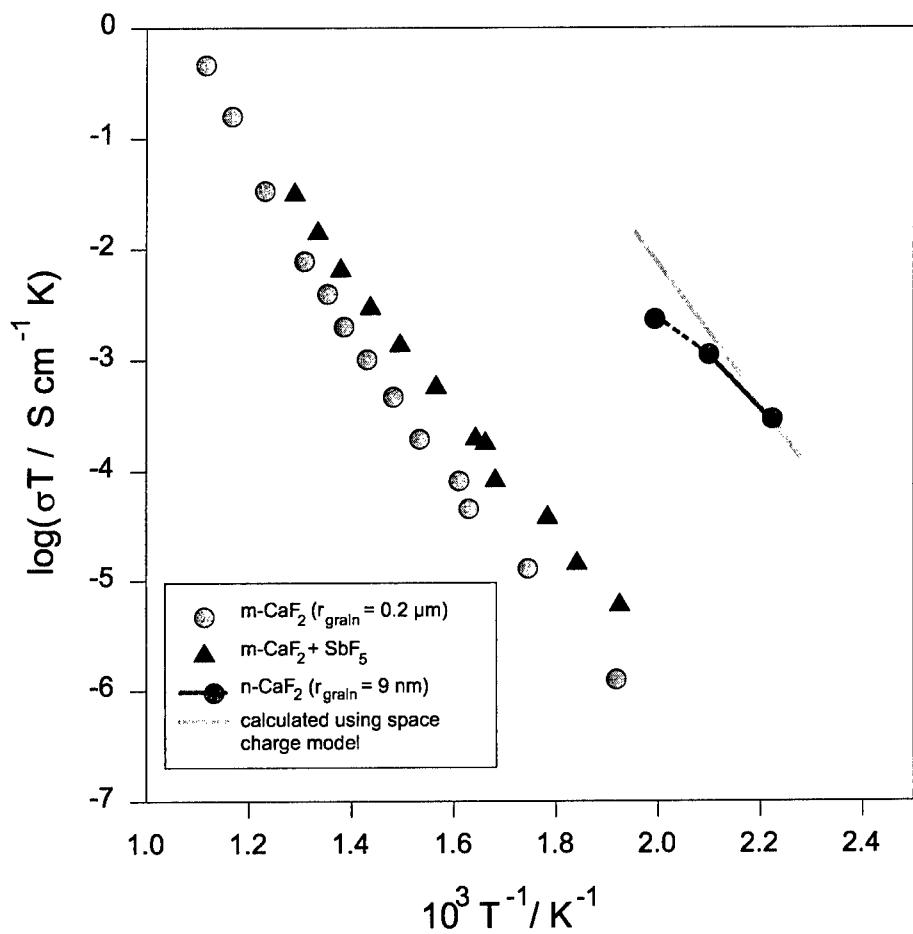
Fig. 5. Conductivity (without blocking grain-to-grain contacts) for nanocrystalline (n-) CaF_2 compared to coarse-grained (m-) CaF_2. The deflection of the data points at high T (n-CaF_2) indicates grain coarsening. Also shown are the conductivity data obtained by exposure of m-CaF_2 to the Lewis-acid SbF_5 (cf. also Fig. 2) [45,46].

effect if the sample thickness is no longer large compared with the Debye-length [42]. Then the space charge regions interfere, the sample is charged throughout, and in terms of conductivity an additional enhancement may occur for enrichment layers expressed by the nanosize factor (n.s.f.) [43,44] [$c_0 \equiv c(x = 0)$] (derived for a film!)

$$\text{n.s.f.} = \frac{4\lambda}{L}\left(\frac{c_0 - c^*}{c_0}\right)^{\frac{1}{2}} \qquad (14)$$

where c^* is the concentration in the center of the symmetrical film and related to L and c_0 via:

$$\frac{L}{2\lambda} = 2\sqrt{c_\infty / c^*}\left[\; \mathscr{E}\left(\frac{c_\infty}{c^*}, \frac{\pi}{2}\right) \right.$$
$$\left. - \mathscr{E}\left(\frac{c_\infty}{c^*}, \arcsin\sqrt{\frac{c^*}{c_0}}\right) \right] \qquad (15)$$

$\mathscr{E}$ denoting elliptical integrals of the first kind, c_∞ being the bulk value. Even though predicted quantitatively more than a decade ago [43,44] clear experimental evidence for this is still lacking. The thickness-dependent conductance of thin LiI-films on sapphire could be nicely fitted by Eq. (14) [43,44], however it is probable that lateral inhomogeneities (island formation) obscure the picture. This is supported by a large apparent Debye-length obtained when a homogeneous situation is assumed [42,26].

Fig. 5 shows the high conductivity of nanocrystalline CaF_2 [45,46]. The conductivity can be explained

by semi-infinite space charges. Owing to the high impurity content, the Debye-length can be assessed to be lower than the grain size of ~10 nm. In Ref. [47] the changed defect chemistry of nanocrystalline CeO_2 was explained by core effects. Also in this case, the sample thickness was still large compared to the Debye-length. Yet, a mesoscopic situation is certainly met in swollen Nafion or PEEK ion exchange membranes Fig. 6. There an organic backbone [per-fluorinated branched hydrocarbon network (Nafion)] or bundles of aromatic polyether ketones (PEEK) are separated by tiny water channels [48]. These organic backbones bear sulfonic acid groups. While the proton can be dissociated away, the anion is strongly bonded to the polymer. Since the thickness of the water channels is of the order of 1 nm and much lower than the Debye-length of water, these channels form mesoscopic space charge layers in which only very small gradients of the proton concentration exist. A systematic examination of the proton conductivity as the function of the separation thickness is necessary [49].

A further example is the already discussed conductivity enhancement in $AgI:Al_2O_3$ nanocomposites. As already outlined, the conductivities point towards space charge effects. However, a semi-infinite space charge model predicts too low an effect. Finite (mesoscopic) effects would require a lower grain size than estimated from the geometrical parameters. However, a recent structural analysis

| ◑ H_2O | + H_3O^+ | – SO_3^- | ■ polymer backbone |
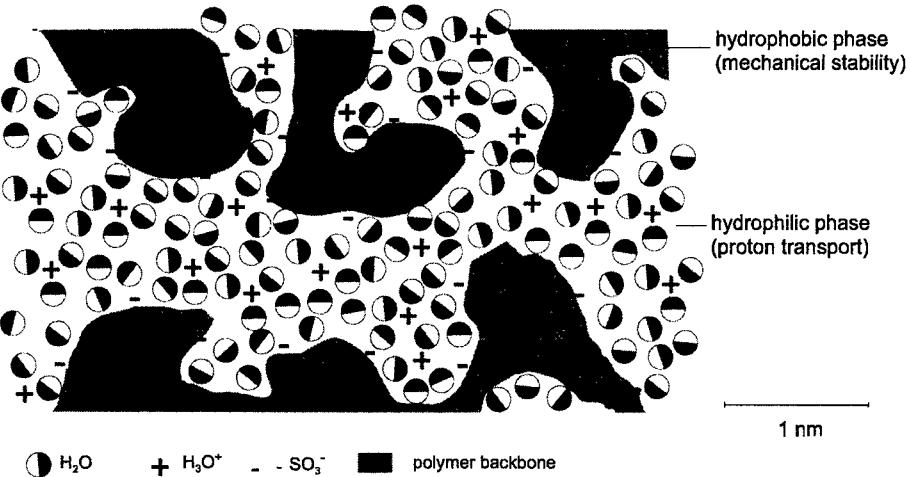
Fig. 6. Mesoscopic arrangement of acidified water channels in the PEEK polymers [48].

indicates the formation of a stacking fault structure formed at the interfaces (Fig. 7) [34]. This stacking fault sequence can also be conceived as a hetero-structure in which β- and γ-layers alternate, the layer distance being of atomistic dimensions. If we can suppose an interfacial effect at the β/γ-boundary for which we have indications, a far-reaching ionic disorder is to be expected and the observed conductivity behaviour can be at least half-quantitatively explained. In this respect, more detailed investigations on such super-lattices are required as is the case in quantum well research.

Beyond electrical properties, such questions are important for stability considerations, as well as for kinetic (and in particular catalytic) properties. We

γ-like   **β-like**
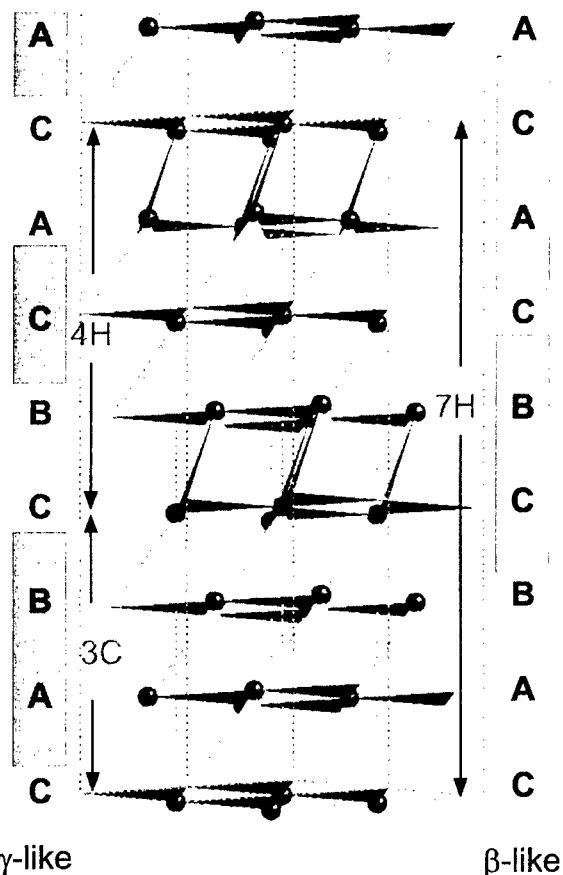
Fig. 7. Stacking fault (7H phase) forming at the Al_2O_3/AgI boundary, can be conceived as a β/γ/β/γ... sequence of (sub-) nanometre size leading to a pronounced disorder in the cation sublattice.

may mention (i) the fact, important for Li-batteries, that Li insertion into nanocrystalline hosts may not necessarily imply a homogeneous distribution of Li^+ and e^-, and (ii) the fact that drift effects in Taguchi gas sensors should be minimal, if $L \sim \lambda$, as the separation of the bulk and surface conductivity effects become almost irrelevant, and finally (iii) that pronounced size effects are expected for extent [47] and rate [50] of stoichiometric changes.

4.3. Mesoscopic structural effects

Now we are interested in potential size-dependencies of $\mu°$, i.e. bending of (free) energy levels (apart from electrical field effects). For electronic levels, this can occur without structural effects just due to the extension of the electron's wave-function. The simple electron-in-the-box model indicates that the energy levels and hence also the energy differences depend on L and thus approximately

$$\Delta\mu° \propto L^{-2}. \tag{16}$$

A clear example is illustrated by the colour changes exhibited by colloids as a function of size [51]. This dependence predicts a steep decay of this kind of level bending. Nano-electronics being concerned with nanoheterostructures, quantum wells, wires and dots relies on such confinement phenomena [4]. Similarly we expect confinement effects for protons but only under conditions where tunnelling is of relevance. In usual cases and in particular for larger ions, this is not the case. An extremely interesting topic is the exploration of nanosize effects in mixed conductors. In the case of typical ion conductors, a L-dependence of $\mu°$ implies structural changes. Then we must face the more complicated situation characterised by

Real structure = Inhomogeneous perfect structure

            + (inhomogeneous) defect structure

$$\tag{17}$$

Experiments with NaCl clusters (Fig. 8) [6,7] show that the rock-salt structure is obtained already for small cluster sizes (> 10 molecular units). Minor variations in the bond lengths are then obviously not leading to a significant energetic effect: If we consider the energy and decompose the small crys-
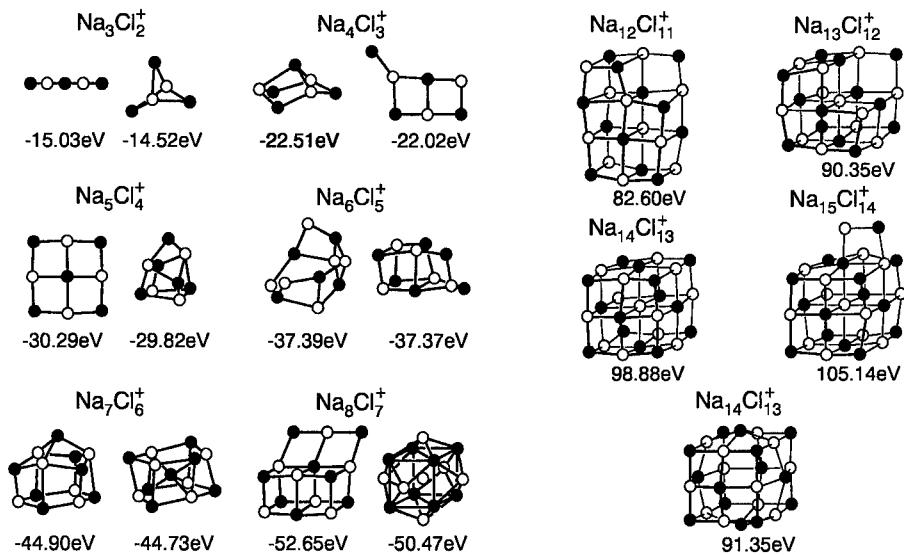
Fig. 8. Stable $(NaCl)_{n-1}$ Na^+-cluster according to Martin [6,7].

tals into 'bulk' and an outer shell of surface particles ('core') it turns out that the energies of the so-decomposed ground structures are quite invariant. More precisely, if surface and bulk energies are superimposed as $\alpha(L)N^{2/3} + \beta(L)N$, α and β are quite insensitive with thickness as the plot of $E/N^{2/3}$ vs. $N^{1/3}$ shows [52]. The situation seems to be similar in noble metals: The melting temperature changes of nanocrystalline Au particles are quite dramatic [53]. If the size of Au crystals is reduced to 20 Å, the melting point drops by 600 K. Nevertheless the effect can be understood by using only physical constants of massive gold [53], i.e. by trivial effects as denoted in Section 4.1. Note that for cubic clusters of 1000 atoms only half of the atoms are not sitting in surfaces. At smaller clusters also edge effects and corner effects become important. For a Wulff-crystal, the chemical potential correction $(\Delta\mu_{MX})$ compared to very large crystals is determined by $W \cdot V_m$, V_m being the molar volume and W the ratio of surface tension and distance between surface and centre which is the same for each plane. According to e.m.f. measurements [54], nanocrystalline copper shows an increase in the chemical potential which can be understood in this way.

Even though these findings cannot be generalised, it certainly will be, in many cases, a good approximation to state that such structural L-dependencies in

μ° are restricted to extremely small sizes ℓ. Generally speaking, we expect a mesoscopic effect in the carrier concentration (i.e. in the mass action constants K) and in the conductivities (i.e. in both K and u) if $L \lesssim \ell$.

In cases in which the Debye-length is significant, we will then have to face two mesoscopic regimes as indicated in Fig. 9: an electrical one for $\lambda \gtrsim L \gg \ell$ and a structural one for $\ell \gtrsim L$. If ℓ is not small compared to λ, a complicated mixed behaviour occurs.
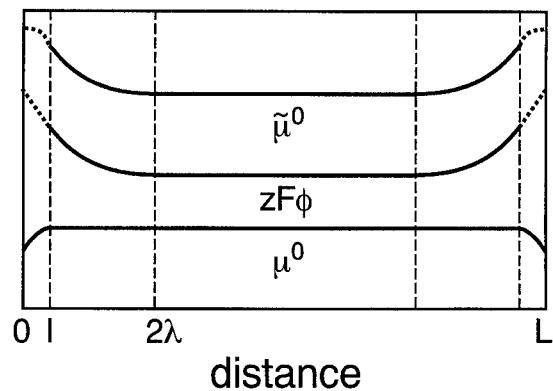
Fig. 9. If, at thicknesses smaller than ℓ, the structure changes, there is — in addition to space charge effects characterised by λ — a second size effect to be expected.

As outlined above, even with respect to the pure electrical effect not very much reliable data has been gathered. For the investigation of structural phenomena, this is even more true. Beyond that, conceptional problems still have to be solved as the question of the tensor character of the chemical potential if L becomes small. In addition, effects such as line and edge tension or triple junction properties may become highly relevant in nanosized samples. It is also worth mentioning that under those conditions the equilibrium crystal structure deviates from the Wulff-plot as it is also manifested in the individual equilibrium structure of small clusters. In short: even though a few conceptual points can be stated, the field of nano-ionics is largely terra incognita.

Acknowledgements

References

[1] B. Sakmann, E. Neher (Eds.), Single-channel Recording, Plenum Press, New York, 1995.

[2] R.J. Haug, K. von Klitzing, FED J. 6 (Suppl. 12) (1995) 4.

[3] K. von Klitzing, FED J. 4 (Suppl. 2) (1994) 2.

[4] K. von Klitzing, in: Max-Planck-Jahrbuch 1996, Verlag Vandenhoeck and Ruprecht, Göttingen, 1996, p. 111.

[5] A. Simon, Structure and Bonding 36 (1979) 81.

[6] T.P. Martin, Festkörperprobleme (Advances in Solid State Physics), Vieweg, Braunschweig XXIV (1984) 1.

[7] T.P. Martin, Phys. Reps. 95 (1983) 167.

[8] Nanostructured materials for energy applications, Y.-M. Chiang (Ed.), J. Electroceram. 1 (3) (1997).

[9] H.L. Tuller, Loc. Cit. (5) 211.

[10] J. Schoonman, Proceedings of the SSI-12-Conference, Thessaloniki, 1999, Solid State Ionics (2000) in press.

[11] C. Wagner, W. Schottky, Z. Physik. Chemie B11 (1930) 163.

[12] C. Wagner, Z. Physik. Chemie B32 (1936) 447.

[13] F.A. Kröger, Chemistry of Imperfect Crystals, North Holland, Amsterdam, 1964.

[14] G. Brouwer, Philips Res. Rep. 9 (1954) 366.

[15] J. Maier, Angew. Chem. Int. Ed. Engl. 32 (1993) 313.

[16] J. Maier, Angew. Chem. Int. Ed. Engl. 32 (1993) 528.

[17] N. Bjerrum, Kgl. Danske Videnskab. Selskab. Mat. Fys. Medd. 7 (1926) 3.

[18] A.B. Lidiard, in: S. Flügge (Ed.), Handbuch der Physik, Vol. 20, Springer, Berlin, 1957, p. 246.

[19] P. Debye, E. Hückel, Physik. Z. 24 (1923) 185.

[20] N. Hainovsky, J. Maier, Phys. Rev. B 51 (1995) 15789.

[21] F. Zimmer, P. Ballone, J. Maier, M. Parrinello, Ber. Bunsenges. Phys. Chem. 101 (1997) 1333.

[22] J. Jamnik, J. Maier, S. Pejovnik, Solid State Ionics 75 (1995) 51.

[23] A.P. Sutton, R.W. Balluffi, Interfaces in Crystalline Materials, Clarendon Press, Oxford, 1995.

[24] D. Wolf, in: D. Wolf, S. Yip (Eds.), Materials Interfaces. Atomistic-level Structure and Properties, Chapman and Hall, London, 1992, p. 1.

[25] J. Maier, J. Electrochem. Soc. 134 (1987) 1524.

[26] J. Maier, Prog. Solid State Chem. 23 (1995) 171.

[27] Y. Saito, J. Maier, J. Electrochem. Soc. 142 (1995) 3078.

[28] J. Maier, in: F.W. Poulsen, N. Bonanos, S. Linderoth, M. Mogensen, B. Zachau-Christiansen (Eds.), High Temperature Electrochemistry: Ceramics and Metals, Risø National Laboratory, Roskilde, Denmark, 1996, p. 67.

[29] J. Maier, Ber. Bunsenges. Phys. Chem. 93 (1989) 1468.

[30] J. Maier, Ber. Bunsenges. Phys. Chem. 93 (1989) 1474.

[31] R. Lipowsky, in: Phasenübergänge an Oberflächen (IFF Ferienkurs), FZ Jülich GmbH, Germany, 1993, p. 9.1.

[32] R. Lipowsky, Springer Tracts Mod. Phys. Vol. 127, in preparation.

[33] K. Shahi, J.B. Wagner, Appl. Phys. Lett. 37 (1980) 757.

[34] J.-S. Lee, St. Adams, J. Maier, Solid State Ionics, in press.

[35] N.F. Uvarov, E.F. Hairetdinov, A.I. Rykov, Yu.T. Pavlyukhin, Solid State Ionics 96 (1997) 233.

[36] J. Maier, J. Eur. Ceram. Soc. (2000) in press.

[37] J. Maier, Electrochem. (2000) in press.

[38] C.R.A. Catlow, R. James, W.C. Mackrodt, R.F. Stewart, Phys. Rev. B 25 (1982) 1006.

[39] C.R.A. Catlow, W.C. Mackrodt (Eds.), Computer Simulation of Solids, Lecture Notes in Physics, Vol. 166, Springer, Berlin, 1982.

[40] M. Elbaum, S.G. Lipson, J.G. Dash, J. Crystal Growth 129 (1993) 491.

[41] M. Vossen, F. Forstmann, A. Krämer, Solid State Ionics 94 (1997) 1.

[42] J. Maier, Solid State Ionics 23 (1987) 59.

[43] J. Maier, Solid State Ionics 23 (1987) 59.

[44] J. Maier, S. Prill, B. Reichert, Solid State Ionics 28–30 (1988) 1465.

[45] W. Puin, P. Heitjans, W. Dickenscheid, H. Gleiter, Defects in Insulating Materials, in: O. Kanert, J.-M. Spaeth (Eds.), World Scientific, Singapore, 1993, p. 137.

[46] W. Puin, S. Rodewald, R. Ramlau, P. Heitjans, J. Maier, Solid State Ionics 131 (2000) 159–164.

[47] Y.-M. Chiang, E.B. Lavik, I. Kosacki, H.L. Tuller, J.Y. Ying, J. Electroceram. 1 (1997) 7.

[48] K.D. Kreuer, in: B.V.R. Chowdari, K. Lal, S.A. Agnihotry, N. Khare, S.S. Sekhon, P.C. Srivastava, S. Chandra (Eds.), Solid State Ionics: Science and Technology, World Scientific Publishing Co, Singapore, 1998, p. 263.

[49] M. Ise, PhD Thesis, University of Stuttgart, 2000.

[50] J. Jamnik, J. Maier, J. Electrochem. Soc. 145 (1998) 1762.

[51] A. Henglein, Ber. Bunsenges. Phys. Chem. 101 (1997) 1562.

[52] H.G. Fritsche, Phys. Stat. Sol. (b) 154 (1989) 603.

[53] Ph. Buffat, J.-P. Borel, Phys. Rev. A 13 (1976) 2287.

[54] Ch.P. Gräf, U. Heim, G. Schwitzgebel, Solid State Ionics 131 (2000) 165–174.

Structure formation in diffusional growth and dewetting

E. Brener[1], H. Müller-Krumbhaar*, D. Temkin, T. Abel

Institut für Festkörperforschung, Forschungszentrum Jülich, D-52425 Jülich, Germany

Abstract

The morphology diagram of possible structures in two-dimensional diffusional growth is given in the parameter space of undercooling Δ versus anisotropy of surface tension ϵ. The building block of the dendritic structure is a dendrite with a parabolic tip, and the basic element of the seaweed structure is a doublon. The transition between these structures shows a jump in the growth velocity. We show the analogy of diffusional growth with dewetting patterns of a fluid film on a substrate. We also describe the structures and velocities of fractal dendrites and doublons destroyed by noise. The extension of these results to three-dimensional growth is briefly discussed. © 2000 Elsevier Science B.V. All rights reserved.

1. Introduction

During the last few years, our understanding of pattern formation in various non-linear dissipative systems has made remarkable progress. Building on these foundations, it has now become possible to develop a description of a large class of patterns that are found in diffusional growth. This leads to the construction of a *morphology diagram* and to predictions concerning the *transitions* between the different structures [1,2].

To introduce the topic, let us take a look at a few interesting patterns appearing in nature and experiments. Fig. 1 displays one of the most popular examples which has become a paradigm of the field: the snowflake. It also happens to be the first case of

Fig. 1. Drawing of a snowflake, adapted from a photograph by Kobayashi and Kuroda [3].

---

*Corresponding author. Tel.: +49-2461-613-428; fax: +49-2461-612-620.

E-mail address: h.mueller-krumbhaar@fz-juelich.de (H. Müller-Krumbhaar)

[1] On leave from ISSP RAN, Chernogolovka, 142432, Russia.

spontaneous pattern formation in nature that has been treated scientifically (rather than as a theological topic) in a publication. In his article on 'The Six-Cornered Snowflake' [4], Kepler speculated that the six-fold symmetry of snowflakes has to do with something we would call the crystal structure today. He also arrived at the conclusion that a detailed understanding of snowflakes was beyond his reach. Just how judicious this modest statement was, may be gathered from the fact that even 10 years ago, more than 350 years after Kepler, the basic mechanism by which the characteristic length scales of snowflake patterns arise was not known.

Snowflakes are ice crystals growing from a critical nucleus in an environment of supercooled vapor. The condensation process clearly is a first-order phase transition. Contrary to second-order transitions, first-order ones give rise to a sharp interface between the two phases. It is the dynamics of this interface that are of interest here.

Snowflakes are flat objects of approximate but not exact hexagonal symmetry. Their six main arms have a characteristic structure: they emit sidebranches at crystallographic angles. When these structures were given names, classical education was still prevailing, so they were called dendrites, after the greek 'τό δένδρον', meaning 'the tree'.

No two snowflakes are alike. Therefore, their shape must be extremely sensitive to the environmental changes brought about by their turbulent motion within the cloud. On the other hand, the six arms are very similar to each other. Hence, on the length scale of the size of a snowflake (1 cm), its environment must be spatially *homogeneous*.

The question then arises why such a *complex morphology* evolves in a uniform environment — why not simply spheres? Or, if the crystalline anisotropy plays a role, why not just hexagonal plates (according to the crystal system of ice)?

Another question that we may naturally ask is: how does the snowflake *select* its typical length scales, e.g. the tip radius of its main arms, the width and spacing of the sidebranches?

The growth dynamics of true snowflakes are complicated by several circumstances — there is a large density difference between the solid and the vapor; besides the vapor there is a second agent for heat transport, namely air; furthermore, the temporal fluctuations of the environment of a flake are strong.

Clearly, it will be much easier to understand the essential mechanisms by analysing experiments which are simple to prepare and still produce dendrites. Some most careful and beautiful experiments of this kind have been done in the group of Glicksman [5–8]. They consist of chemically pure succinonitrile $[C_2H_4(CN)_2]$, which is an important model substance because, being transparent, it can be easily observed during solidification, while its solidification properties are similar to those of (technologically important) metals. The solid phase grows into an undercooled melt. There are no facets on the crystal, its surface is rough. This means that the attachment kinetics of molecules at the interface are very fast — the free energy for the formation of a step on the interface is zero, there is no nucleation barrier. Thus kinetics are not a limiting factor in the growth process. Growth is controlled by how fast latent heat produced in the solidification process can be transported away via diffusion. (In the case of the snowflake, this is not true for the third dimension; growth in that direction is faceted, keeping the flake essentially two-dimensional.)

The main result of these experiments to be kept in mind is that, given the undercooling, the dendrite has both a *uniquely selected tip radius and constant velocity*.

Completely different structures are commonly formed by minerals crystallizing from viscous magmas or by certain polymers solidifying from the melt [9], so-called spherulites. Contrary to dendrites, spherulites are polycrystalline. They have approximately radial symmetry and their substructures are not oriented along crystallographic directions.

Their radius grows proportional with time, which means they have a stationary growth phase. Again, one would like to be able to make predictions about selected length scales.

It was proposed by Goldenfeld [9] that spherulites are three-dimensional examples for a growth structure which was then called 'dense branching morphology' and will be described shortly. Experimentally, densely branching patterns were first obtained in a non-crystalline system; this was the viscous fingering experiment in a circular Hele–Shaw cell [10]. An inviscid fluid is injected into a viscous one, displacing it and forming branchy structures in the process. It is still controversial [11,12] whether in such a system, governed by the Laplace instead of

the diffusion equation, the dense branching morphology can persist at large length scales.

There are well-known growth models, most notably diffusion-limited aggregation (DLA), that lead to the formation of *fractal* patterns [13].

Since DLA is a Laplacian system, it is natural to ask whether fractal structures are to be expected in diffusional growth, too.

An obvious classification of growth structures would then be to distinguish between *compact* and *fractal* patterns [1,2]. By compact growth we mean growth at a constant (average) density, irrespective of the value of this density. As we shall see later, fractal patterns in crystal growth are fractal only up to a certain size and compact beyond.

What we are aiming at is to formulate a theory that relates the diverse discussed patterns in some kind of *kinetic phase diagram*. The 'kinetic' used here reminds us that we are not dealing with phase transitions (which would imply thermodynamic equilibrium), but dynamic states manifesting themselves in typical growth patterns. In the literature, the term *morphology diagram* is widely used [14].

On the one hand, such a diagram indicates which patterns are selected for which system parameters. Its existence signifies, in particular, that there is a certain degree of independence of the observed morphologies of initial conditions. On the other hand, given the existence of such a diagram, one may try to exploit the analogy with a further phase diagram and ask questions about the nature of *transitions* between the different morphologies.

2. Formulation of the problem

We are interested in a non-equilibrium situation — growth of a stable phase from a metastable one. To be specific, we consider the two-dimensional growth of a pure substance from its undercooled melt, where the growth is controlled by the diffusion of the latent heat of freezing. It obeys the diffusion equation and appropriate boundary conditions at the moving (not known in advance) interface

$$\frac{\partial U}{\partial t} = D\nabla^2 U \tag{1}$$

$$v_n = D\vec{n} \cdot (\nabla U_S|_{\text{int}} - \nabla U_L|_{\text{int}}) \tag{2}$$

$$U|_{\text{int}} = \Delta - d(\Theta)K \tag{3}$$

The indices 'L' and 'S' refer to the liquid and solid, respectively. The specific heat, c_p, and the thermal diffusion constant D are considered to be the same in both phases, L is the latent heat; $U = (T - T_\infty)c_p/L$ is the appropriately rescaled temperature field measured from the imposed temperature T_∞ of the undercooled melt far away from the interface; in terms of these parameters,

$$\Delta = (T_M - T_\infty) c_p/L \tag{4}$$

is the dimensionless undercooling of the melt and T_M is the melting temperature.

The physics underlying Eqs. (1)–(3) is quite simple. A solidifying front releases latent heat which diffuses away as expressed by (1); requiring heat conservation at the interface gives (2) ($\vec{n}$ is the normal to the interface). Eq. (3) is the local equilibrium condition at the interface which takes into account the Gibbs–Thomson correction; K is the two-dimensional curvature and $d(\Theta)$ is the so-called anisotropic capillary length with an assumed fourfold symmetry,

$$d(\Theta) = d_0(1 - \epsilon \cos 4\Theta) \tag{5}$$

Here $d_0 = \gamma T_M c_p/L^2$ is a capillary length proportional to the isotropic part of the surface energy γ; Θ is the angle between the normal $\vec{n}$ to the interface and some fixed crystallographic direction, at which $d(\Theta)$ is minimal; ϵ is the strength of the anisotropy.

In Eq. (3) we neglect the kinetic effects, that is the dependence of the interface temperature on the growth velocity v_n which holds at the sufficiently small undercoolings and velocities.

Our main interest here is concerned with patterns which can grow at constant speed even at low undercoolings $\Delta < 1$, because if they exist they will dominate the systems behavior. A two-phase structure then must exist behind the growth front filling the space uniformly on sufficiently large scales. The fraction η of solid inside this two-phase region should be equal to Δ due to global conservation,

$$\eta = \Delta \tag{6}$$

One may define an envelope over the front of this complex two-phase structure, calling this suitably averaged envelope the *average front* in contrast to the local interface separating the solid from the

liquid. This average front can be considered as the real growth front in the sense that a two-phase mixture, solid plus liquid, grows into a one-phase region originally consisting of liquid only. These two-phase structures are developed from initially smooth interfaces by the well-known Mullins–Sekerka instability [15].

Eqs. (1)–(5) contain two-dimensional parameters, d_0 and D, and two dimensionless parameters, Δ and ϵ. It means that any characteristic length scale, ℓ, and growth velocity, v, of the possible structures can be presented in the form

$$\ell = d_0 f(\Delta, \epsilon), v = \frac{D}{d_0} \varphi(\Delta, \epsilon) \qquad (7)$$

Our aim is to predict, for given undercooling Δ and anisotropy ϵ, the type of the two-phase structure, and its characteristic length scales and velocity, that is to calculate the functions f and φ in the relation (7). As it turns out these functions have scaling forms for small Δ and ϵ, thus showing power law dependencies on Δ and ϵ.

We construct the kinetic phase diagram in the plane (Δ, ϵ) (Fig. 2), which represents the regions of existence of different structures and the lines of transitions between the structures [1,2]. We discrimi-

nate between *compact* structures (C) and *fractal* structures (F). A complementary classification deals with the existence of orientational order. A structure with pronounced orientational order will be called *dendritic* (D), and without apparent orientational order it will be called *seaweed* (S).

It turns out that noise which always exists in the system (for example the thermodynamic noise) appears to play a crucial role in the formation of fractal structures but is not so important for compact patterns.

3. Compact dendrites (CD)

Dendrites can grow at arbitrary small undercooling Δ, but usually a non-zero value of the anisotropy ϵ is required. The growth pattern evolving from a nucleus acquires a star-shaped envelope surrounding a well-defined backbone. The distances between the corners of the envelope increase with time. For small undercooling we can use the scaling relation for the motion of the corners as for free dendrites [16–19] with tip radius ρ_t and velocity v. These two relations come from the Ivantsov formula [20]

$$P \equiv \frac{v \rho_t}{2D} \sim \Delta^2 \qquad (8)$$

and from the selection condition for the stability parameter σ,

$$\frac{1}{\sqrt{\sigma}} \equiv \frac{\rho_t}{\sqrt{d_0 D / v}} \sim \epsilon^{-7/8} \qquad (9)$$

It is quite remarkable that Eq. (8) was obtained in 1947 but it took about 40 years to derive the very non-trivial relation (9). One can find the details in [16–19]. From Eqs. (8) and (9) follow the dependencies of ρ_t and v on the parameters Δ and ϵ:

$$\rho_t \sim d_0 \epsilon^{-7/4} \Delta^{-2}, v \sim \frac{D}{d_0} \epsilon^{7/4} \Delta^4 \qquad (10)$$

Eq. (10) really describes a needle-crystal which, without noise, has no sidebranches. The corresponding star structure then cannot fill the space with constant density and the amount of material solidified in parabolic form increases with time only according to $t^{3/2}$ rather than t^2 for a truly compact object in two dimensions.
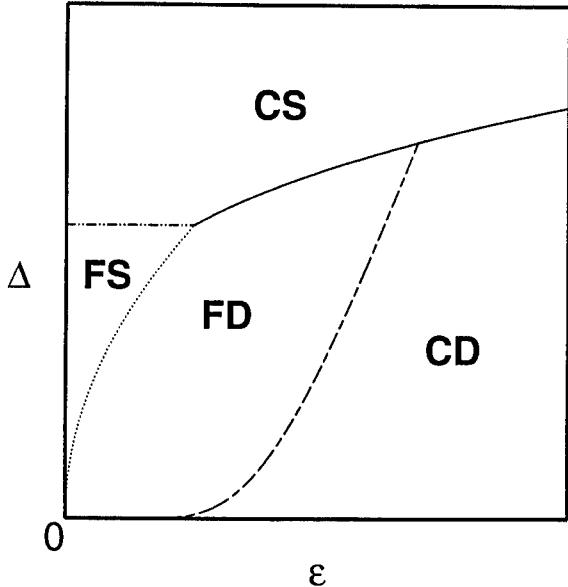
Fig. 2. Kinetic phase diagram.

A small amount of noise, however, cures this problem. The tip of the dendrite is still stable against small noise but has a 'convective' instability which produces sidebranches. Those branches continue to grow until they become independent primary branches a distance $\ell = D/v$ away from the corners of the star. The global shape then consists of an envelope of diamond type over the dendrite tips which appear a distance D/v apart from each other. The velocity scales like Eq. (10). The relative space filling by primary dendrites and sidebranches of course must be equal to Δ. The two basic length scales in this pattern accordingly are the diffusion length D/v and the tip radius ρ_t of a typical dendrite.

For small undercooling Δ those two length scales are well separated, $\rho_t \ll D/v$. While the dendritic structure becomes compact only at length scales larger than D/v, it shows fractal behavior at the intermediate length scale ℓ, $\rho_t < \ell < D/v$, with fractal dimension $D_f = 1.5$ [24]. In this fractal object the sidebranches interact due to the competition in the common diffusion field. Some of the sidebranches die and some continue to grow in the direction prescribed by the anisotropy. This competition leads to coarsening of the structure in such a way that the distance between the surviving sidebranches is adjusted to be of the same order of magnitude as the length of the sidebranches and is proportional to the distance from the dendritic tip. At the same time, the thickness of the surviving sidebranches is proportional to the square root of the product of ρ_t and the distance from the tip. On length scales larger than D/v the dendritic structure appears to be compact with mean density $\eta = \Delta$.

4. Compact seaweed (CS)

CD structures formally exist at arbitrary small anisotropy ϵ but their velocity goes to zero as $\epsilon \to 0$. It was recently discovered that there is another structure, compact seaweed (CS), which is favorable for smaller ϵ and larger Δ. The velocity of the structure remains finite at $\epsilon = 0$.

The compact-seaweed morphology [1,2] was originally introduced on the basis of experimental observations under the name dense branching morphology [25]. At that time, however, its introduction

as a morphological 'phase' distinct from the well-known dendritic morphologies was rather speculative. Computer simulations also were inconclusive at that time.

The first indication for the existence of such a distinct phase came (to our knowledge) from arguments [1,2] based on a theoretical study of crystal growth in a channel [26]. This analysis of channel growth gave, among other things, the following results. A finger type pattern symmetrically in the center of the channel could grow at a constant growth rate for dimensionless supercoolings $\Delta > 0.5$. The finger looks similar to the Saffmann–Taylor finger of viscous flow, but belongs to a different branch of the mathematical solution. The growth rate of the crystal increases with increasing driving force Δ, as expected. A specifically remarkable result of this theory [26] is that the driving force sets a length scale and thereby also a velocity: For a given driving force $0.5 < \Delta < 1$ there exists a characteristic channel width below which such a steadily growing finger is no longer possible.

However, it has been discovered recently that the spectrum of solutions for growth in a channel is much richer than had previously been assumed. Parity-broken solutions were found [27] and studied numerically in detail [28–30]. A similar solution exists also in an infinite space which was called 'doublon' for obvious reasons [28,29]. It consists of two fingers with a liquid channel along the axis of the symmetry between them. It has a parabolic envelope with radius ρ_t and a liquid channel of thickness h. The Peclet number, $P = v\rho_t/2D$ depends on Δ according to the Ivantsov relation (8). The analytical solution of the selection problem for doublons [31] shows that this solution for isotropic systems ($\epsilon = 0$) exists even at arbitrary small undercooling Δ and obeys the following selection conditions:

$$h \sim \rho_t, \frac{1}{\sqrt{\sigma}} \equiv \frac{\rho_t}{\sqrt{d_0 D/v}} \sim P^{-5/4} \qquad (11)$$

Eqs. (8) and (11) give

$$\rho_t \sim h \sim d_0 \Delta^{-7}, \quad v \sim \frac{D}{d_0} \Delta^9 \qquad (12)$$

If one includes finite anisotropy ϵ, doublon solutions exist only above the solid line on Fig. 2, for which

$$\Delta \sim \epsilon^{1/4} \tag{13}$$

For ϵ smaller than that given by (13) the doublons obey the same scaling law as given by Eq. (12) [31].

It should be noted that doublons in the range of their existence (13), grow faster than dendrites for the same parameters Δ and ϵ. This statement is confirmed by numerical calculations [28,29].

The numerical calculations also show that the double-fingering structure is stable against competition between the two fingers which belong to the doublon. It means that the axis of symmetry and the direction of growth are stable. Of course these directions are arbitrary in isotropic systems. It is not completely clear at the moment if the stability of the free doublon pair follows precisely the scaling law Eq. (13). In any case this line represents a lower bound on Δ for a given ϵ.

We assume that the doublons seem to represent a key point in the growth of compact-seaweed morphology (Fig. 3). The formation of a full CS-structure evolving from a growing nucleus is possible only due to noise, which triggers sidebranches, as in

Fig. 3. Seaweed structure.

the CD-structure. The resulting two-phase structure has an almost isotropic circular envelope which moves with approximately the same velocity [Eq. (12)] as a free doublon. The structure is fractal with $D_f = 1.5$ in the intermediate length scale between ρ_t and D/v, and it becomes compact with mean density $\eta = \Delta$ for the length scale larger than D/v. The region above the solid line, $\Delta \sim \epsilon^{1/4}$ (Fig. 2), corresponds to CS-structure where doublons exist and grow faster than dendrites. This line represents the discontinuous transitions between CD and CS-structures with a jump of velocities.

5. Surface dewetting as a diffusional growth process

As an application of this theory the effective equations of motion for a drying thin film wetting a substrate are derived. These equations are equivalent to the one-sided model of diffusional growth with an effective diffusion coefficient which depends on the viscosity and on the thermodynamic properties of the thin film.

According to the description given in [33], and also by Sharma [34,35] and de Gennes [36], there is a possibility for the almost dry part of the solid substrate to be in equilibrium with the wet part which is in fact a thin (but macroscopic) film of a liquid. Both parts (dry and wet) on the solid substrate are separated by an interface, which can be described by a height variable $h(x)$ with x being the coordinate across the interface from the dry to the wet part. Towards the dry part, the height variable goes to a very small value h_-, towards the wet part the film thickness goes to an equilibrium value $h_\infty(p)$ for given pressure p in coexistence with the vapor phase. At a specific pressure p_0 the liquid film can be also in equilibrium with the (almost) dry surface, the corresponding thickness of this wet film then is defined as $h_0 = h_\infty(p_0)$. For lower vapor pressure, the equilibrium film thickness $h_\infty(p)$ would decrease to a value smaller than h_0, but it would be metastable only and the the stable dry area would expand at the cost of the wet area. This is the dewetting phenomenon under consideration. Patterns similar to Fig. 3 have been recently observed experimentally [37].

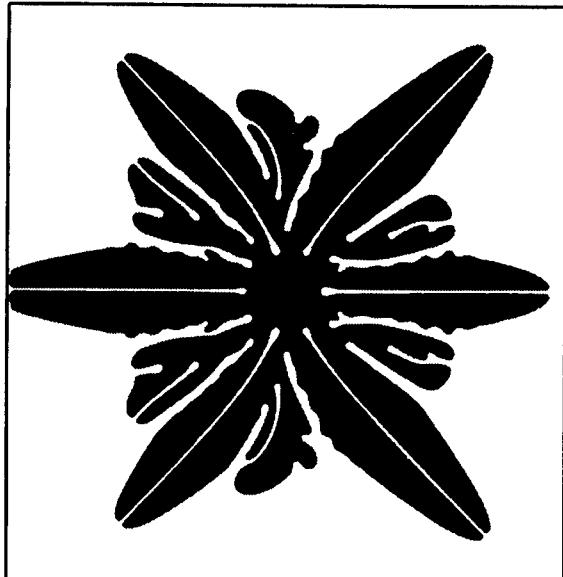We assume a surface-tension γ exists between the

liquid and the vapor. The free energy of the film then can be written as

$$G = \int \{g(h(x, y)) + \frac{\gamma}{2} |\nabla h|^2\} \, dx \, dy \tag{14}$$

In equilibrium a double-tangent construction to $g(h)$ gives two solutions of h_- for the dry part and of $h_0(p)$ for the wet part of the surface. This leads to the evolution equation [34,35,37] for the film variable $h(x,y;t)$:

$$\frac{\partial h}{\partial t} = \nabla \cdot \frac{h^3}{3\eta} \nabla \left[\frac{dg(h)}{dh} - \gamma \nabla^2 h \right]$$
$$- \alpha \left[\frac{dg(h)}{dh} - \gamma \nabla^2 h - \mu(p) \right] \tag{15}$$

Note that a relaxational term proportional to α has been added. This term alone guarantees that a homogeneous liquid film will relax to its equilibrium value by evaporation or condensation. $\mu(p)$ is the chemical potential of the vapor. For $h = h_\infty(p)$ this term vanishes.

The first part of Eq. (15), proportional to the inverse viscosity η^{-1} of the liquid film, describes a creeping motion of a thin film flow on the surface. In the (almost) dry area the contributions of both terms to the total flow and evaporation of material can be basically neglected, because of the small value of h_-, typically less than one monolayer of adsorbed fluid. Inside the wet area we can to the lowest order linearize $h = h_\infty [1 + u(x, y)]$, where u is now a small deviation from the asymptotic equilibrium value for $h_\infty(p)$ in the liquid. Since $\nabla h_\infty(p) \equiv 0$ the only surviving terms are linear in u and its spatial derivatives ∇u and Δu. Therefore, inside the wet area, the evolution equation for the variable part u of the height variable h becomes

$$\frac{\partial u}{\partial t} = D_{\text{eff}} \Delta u - \lambda_{\text{eff}} u \tag{16}$$

We have dropped here the terms $\sim \gamma \Delta^2 u$ since the effective diffusion constant $D_{\text{eff}} = (h_0^3/3\eta)\{d^2g/dh^2\} + \alpha\gamma$ is positive and dominates the long-wavelength behaviour over the fourth-order term. The relaxation coefficient is $\lambda_{\text{eff}} = \alpha\{d^2g/dh^2\}$. Derivatives are taken around the equilibrium value $h = h_0$. Note that (16) now is precisely the equation of

motion studied in [41], generalizing our basic model (Eq. (1)).

Of course, this approximation holds only inside the wet region, not directly at the dry–wet interface. This interface region gives rise to a profile $h(x)$ similar to a tanh function. The development of the tanh profile from the dry to the wet part occurs over a distance that is short compared to the typical patterns being observed in the dewetting process. We can therefore replace this profile by a sharp interface between the dry and the wet part, but must add the corresponding boundary conditions to the equation of motion (16) for the wet side. Obviously, the boundary conditions consist of a conservation law Eq. (2) which guarantees that a displacement of the dry–wet interface must locally conserve the fluid. Under dewetting conditions this leads to a swelling of fluid $u > 0$ at the interface. The second condition clearly comes from the surface tension γ which tends to keep the dry–wet interface straight. This is then just the usual Gibbs–Thomson condition for an interface, as described in Eqs. (3) and (4) above, with the capillary length being approximately $d_0 \approx \gamma / (\{d^2g(h)/dh^2\}\ell)$ where ℓ is the thickness of the dry–wet interface, and the dimensionless driving force is $\Delta = (h_0 - h_\infty)/h_0$. In summary, we have for this viscous fluid-flow problem of surface dewetting exactly the same equations as for the diffusional growth of an isotropic solid.

6. Fractal structures

For the compact structures described above noise is important only as the trigger of sidebranches. It has been assumed that the tips (of dendrites or doublons) remain undestroyed. However, the strength of noise may be large enough not only to trigger the sidebranches but also to destroy the tips. In order to estimate the parameters for which it happens let us look at the theory of sidebranch formation more carefully. According to the result of Langer [32] the root mean square amplitude, $\langle \zeta^2 \rangle^{1/2}$ of the sidebranches on the underlying parabolic interface generated by thermal fluctuations depends on the distance from the tip z according to

$$\frac{\langle \zeta^2 \rangle^{1/2}}{\rho_t} \sim \Gamma \exp\left[\frac{2^{7/4}}{3\sqrt{3}\sigma} \left(\frac{z}{\rho_t}\right)^{1/4} \right] \tag{17}$$

Here the stability parameter σ is given by Eqs. (9) and (11) for dendrites and doublons, respectively; Γ is the relative noise strength ($\Gamma \ll 1$)

$$\Gamma = (T/T_0)\left(\frac{2Dd_0^3}{v\rho_t^4}\right)^{1/2}, \quad T_0 = \left(\frac{L^2 d_0^3}{k_B c_p}\right)^{1/2} \tag{18}$$

where k_B is the Boltzmann constant. The tip becomes destroyed if the amplitude of the sidebranches is of the order of ρ_t at the distance $z \sim \rho_t$ down the shaft. Thus we obtain from Eq. (14) the following condition

$$\frac{1}{\sqrt{\sigma^*}} \sim |\ln \Gamma| \tag{19}$$

The tips of the structures will be destroyed if the stability parameter σ becomes smaller than the critical value σ^* given by Eq. (16). Using the value $\sigma \sim \epsilon^{7/4}$ [Eq. (9)], one obtains from Eq. (16) a line of smooth transition from CD to FD-structures in Fig. 2:

$$\epsilon^* \sim |\ln \Gamma|^{-8/7} \tag{20}$$

The analogous line which separates CS and FS-structures in Fig. 2 can be obtained using Eqs. (8), (11) and (16):

$$\Delta^* \sim |\ln \Gamma|^{-2/5} \tag{21}$$

Eq. (16) has the following physical meaning. Let us rewrite this relation, using the definition of $\sigma = d_0 D/ (v\rho_t^2)$ [Eq. (9)], which gives the following condition for a stable tip radius:

$$\rho_t \lesssim \rho_{MS}|\ln \Gamma| \tag{22}$$

where $\rho_{MS} \sim \sqrt{d_0 D/v}$ is the Mullins–Sekerka length describing the instability of a planar interface. One can think of the right-hand side of (19) as the characteristic length scale, a_Γ, of the instability due to noise

$$a_\Gamma = \rho_{MS}|\ln \Gamma| \sim \sqrt{d_0 D/v}|\ln \Gamma| \tag{23}$$

The tip is stable if $\rho_t < a_\Gamma$ and it becomes destroyed if $\rho_t > a_\Gamma$. The same small-size cutoff a_Γ depending on noise Γ was introduced in our previous paper [1,2] based on the consideration of the self-similar development of perturbations induced by the Mul-

lins–Sekerka instability. At that time, however, the existence of doublons was not known.

A new approach, therefore, is required for the description of the fractal patterns with the destroyed tips. Such destroyed fractal structures have been already investigated in the framework of Saffmann–Taylor viscous fingering and diffusion-limited aggregation [21–23]. The important result of these investigations is that there exists an effective envelope obtained by averaging over the structures, which has precisely the same shape as an ideal stable solution — the shape of the Saffmann–Taylor finger in isotropic systems and parabolic shape in anisotropic systems. The density inside this effective envelope is $\tilde{\eta} < 1$. The envelope has a characteristic tip radius $\tilde{\rho}_t$. Because the underlying structure is fractal with fractal dimension $D_f \approx 1.71$ in the intermediate length scale between small-length cutoff a_Γ and $\tilde{\rho}_t$, the density $\tilde{\eta}$ inside the envelope can be obtained from the definition of the fractal dimension (apart from a constant prefactor)

$$\tilde{\rho}_t^{D_f} \sim \int_{a_\Gamma}^{\tilde{\rho}_t} dr\, r\tilde{\eta}(r)$$

which gives more explicitly

$$\tilde{\eta}(\tilde{\rho}_t) \sim \left(\frac{a_\Gamma}{\tilde{\rho}_t}\right)^{2-D_f} \tag{24}$$

Following these results, we will now try to define an averaged or coarse-grained structure over such a noisy fractal pattern and to formulate an equation of motion for this coarse-grained structure using scaling arguments. More explicitly we try to estimate the characteristic length scale of the structure and its growth velocity by considering the steady-state motion of an effective parabolic envelope which replaces the destroyed dendrite or doublon. The density of the solid phase inside the envelope with tip radius $\tilde{\rho}_t$ is given by Eq. (21), where the small size cutoff a_Γ is defined by Eq. (20)

$$\tilde{\eta}(\tilde{\rho}_t) \sim \left(\frac{\sqrt{d_0 D/v}|\ln \Gamma|}{\tilde{\rho}_t}\right)^{2-D_f} \tag{25}$$

The temperature inside the envelope is assumed to be close to the melting temperature. Because the density $\tilde{\eta}$ inside the envelope is smaller than 1, we have to

replace the latent heat L by $\tilde{\eta}L$. It changes Δ in Eq. (4) to $(\Delta/\tilde{\eta})$ and modifies the Ivantsov relation to

$$P \equiv \frac{v\tilde{\rho}_t}{2D} \sim \left(\frac{\Delta}{\tilde{\eta}}\right)^2 \qquad (26)$$

The crucial point of the analysis is a modification of the selection conditions (9) and (11). The experimental and numerical results [21–23] (the existence of a selected envelope) support the idea that those selection conditions do exist. Unfortunately, we do not know any results which allow us to write down these modifications explicitly. But, using scaling arguments, we can write the selection conditions in the following scaling form with scaling exponent β which for the moment is undetermined but will be specified later. For dendrites we can write

$$\frac{1}{\sqrt{\sigma}} \equiv \frac{\tilde{\rho}_t}{\sqrt{d_0 D/v}} \sim \epsilon^{-7/8} \, \tilde{\eta}^{-\beta} \qquad (27)$$

and for doublons

$$\frac{1}{\sqrt{\sigma}} \equiv \frac{\tilde{\rho}_t}{\sqrt{d_0 D/v}} \sim P^{-5/4} \, \tilde{\eta}^{-\beta} \qquad (28)$$

These relations (24) and (25) transform into Eqs. (9) and (11), respectively, for $\tilde{\eta} \sim 1$.

The selection relations (24) and (25) may be interpreted as the conditions of selection due to an effective surface tension. We have chosen the same β in both Eqs. (24) and (25) because in some sense the factor $\tilde{\eta}^{-\beta}$ can be seen as a renormalization factor for the capillary length $d_0 \rightarrow d_0/\tilde{\eta}^{2\beta}$. To make an estimate of possible values of β it is natural to assume that a coarse-grained surface energy should decrease with decreasing $\tilde{\eta}$, giving $\beta < 1/2$ as a reasonable restriction. We have shown [1,2] that the scaling exponent β can be expressed in terms of bulk D_f and surface D_s fractal dimensions:

$$\beta = \frac{1}{2}\left(1 - \frac{D_s - 1}{2 - D_f}\right) \qquad (29)$$

All the characteristics of fractal structures depend on the noise strength Γ. We can estimate Γ in the fractal region using Eq. (15) and replacing ρ_t by the noise-induced length scale a_Γ from Eq. (20). It gives

$$\Gamma |\ln \Gamma|^2 \sim \left(\frac{T}{T_0}\right)\left(\frac{vd_0}{D}\right)^{1/2} \qquad (30)$$

The noise strength $\Gamma \ll 1$ because the capillary length d_0 is much smaller the diffusion length D/v.

7. Conclusion

We have discussed the structure formation in diffusion-controlled growth. The given description refers to solidification of a pure undercooled melt but it also can be applied to growth of a pure solid from solution or isothermal solidification of a binary melt. More generally one may speak of systems with a conserved quantity growing by diffusion. The main control parameters of the process are dimensional undercooling Δ and the strength of the surface tension anisotropy ϵ. It turns out that the noise is also very important for the structure formation and we characterize it by the dimensionless quantity Γ.

The resulting morphology diagram (Fig. 2) with axes Δ vs. ϵ classifies different kinds of structures and transitions between them.

The dendritic structure has pronounced orientational order and it is favorable for small Δ and relatively large ϵ. The seaweed structure does not require anisotropy and is favored for larger Δ and smaller ϵ. The transition between these two structures takes place around the solid line on Fig. 2 [Eq. (13)] which is continued by the dotted line into the fractal region. This transition is discontinuous with a jump of velocities since the doublons move faster than the dendrites as soon as they exist. The main element of the dendritic structure is a dendrite with a parabolic tip, and the main element of the seaweed structure is a doublon (Fig. 3). For compact dendritic and compact seaweed structures the tips of dendrites and doublons are stable against the noise which is relatively small in these regions. The noise triggers sidebranches which fill the space and make the structures compact so that the mean density of the solid phase is $\eta = \Delta$ on the length scale larger than D/v. In the intermediate region of lengths between the tip radius ρ_t and diffusion length D/v the structure can be described as a fractal but with a trivial fractal dimension $D_f = 3/2$ which comes from the parabolic shape of the dendrite.

The region of fractal dendritic and fractal seaweed structures near the origin of the morphology diagram is characterized by noise being sufficiently large to

destroy even the tips of dendrites and doublons. It means that the noise-induced length scale a_l [Eq. (20)] is smaller than $\tilde{\rho}_t$. In the range between a_l and $\tilde{\rho}_t$ the structures are fractal with a non-trivial fractal dimension D_f ($D_f \approx 1.71$). This is the reason why we called these structures 'fractal'. Furthermore, these patterns are also fractal in the range between $\tilde{\rho}_t$ and D/v but again with the trivial fractal dimension $D_f = 3/2$. Finally they become compact on length scales larger than the diffusion length D/v just as compact dendritic and compact seaweed structures. Note that if one performed a measurement of the fractal dimension on length scales around the cross-over length $\tilde{\rho}_t$ one would observe an interpolation between our two different values of D_f, the precise result depending on the interval chosen for the measurement. Since both the dendritic and the seaweed patterns maintain their basic identities inside the noisy region the transitions from the compact to the fractal regions represent rather smooth changes in length scales.

We have described the structures and growth velocities of the destroyed fractal dendrites and doublons by introducing renormalized quantities for capillary length and density. We have quantitatively introduced an effective parabolic envelope following the results of [22–24]. The most non-trivial part of our analysis is a modification of the selection conditions [Eqs. (24) and (25)]. At this point we have used scaling arguments which leave us only with one undetermined scaling exponent β. This exponent subsequently is determined by the fractal dimensions D_s for the surface and D_f for the bulk of the growing pattern. The closed set of equations for the growth rate and the tip radius are Eqs. (22)–(24) for fractal dendritic growth, and Eqs. (22), (23) and (25) for fractal doublon growth. The two-dimensional theory together with a small modification [41] in addition explains the patterns observed on a solid surface which was covered by a thin wetting layer of fluid. When a dry spot nucleates in this layer dewetting occurs through the propagation of the essentially one-dimensional separation line between the wet and the dry parts of the surface. Doublon structures then can be clearly observed.

The scaling arguments given here for two-dimensional growth patterns formally can be extended in a straightforward fashion to three dimensions. For

dendritic structures this seems to be perfectly permissible since the basic growth laws are rather similar in two and three dimensions [38,39]:

$$\rho_t \sim d_0 \, \epsilon^{-7/4} \, |\ln \Delta|/\Delta, \, v \sim \frac{D}{d_0} \, \epsilon^{7/4} \, (\Delta/\ln \Delta)^2 \qquad (31)$$

(compare to Eq. (10) for 2-D). There is, however, the crucial difference between the 3-D and the 2-D case. In the later, small anisotropy implies that the shape of the selected needle crystal is close to the Ivantsov parabola everywhere; in the former, strong deviations from the Ivantsov paraboloid appear for any anisotropy. This shape, in units of the tip radius of curvature, depends mostly on the crystalline symmetry and it is almost independent of the material and growth parameters. The shape of the 3-D dendrite, which has been described analytically [39], together with sidebranching activity [24] is presented in Fig. 4. For the seaweed patterns much less is known since our preliminary results are mostly numerical ones [40] (Fig. 5). The crucial point here is that this self-organized triplet structure is not imposed by the symmetry of the calculation box and it consists of three cooperating symmetry-broken fingertips. A hexagonal or triplet structure should be expected to occur under free growth conditions from the basic symmetry considerations, since these growth problems do not have reflection symmetry about some
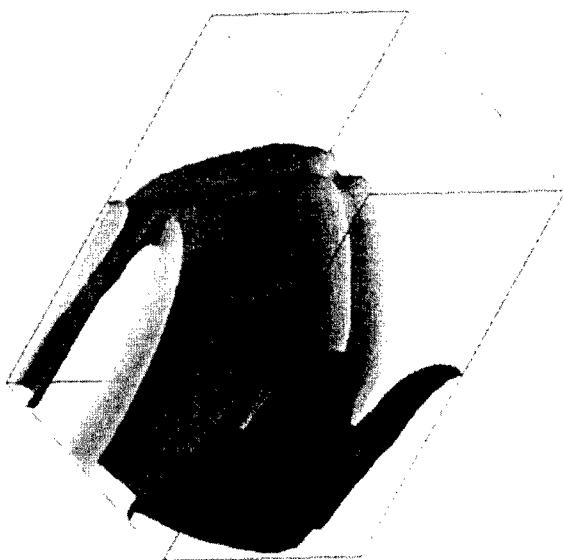

Fig. 4. 3-D dendrite.

Fig. 5. 3-D triplon.

average interface position. The resulting multiplets consisting of symmetry-broken cooperating fingers of the growing phase finally seem to be the basic building blocks for the compact seaweed morphology, in particular the triplet structure appears to be characteristic for free growth. We expect these triplons even to appear in systems with convection driven by surface tension, provided the growth rate is faster than the convection rate defined as the ratio of surface tension divided by viscosity. At present, however, there is still a need for detailed experiments in this region of low crystalline anisotropy but rather high driving force.

References

[1] E. Brener, H. Müller-Krumbhaar, D. Temkin, Europhys. Lett. 17 (1992) 535.

[2] E. Brener, H. Müller-Krumbhaar, D. Temkin, Phys. Rev. E 54 (1996) 2714.

[3] T. Kobayashi, T. Kuroda, in: I. Sunagawa (Ed.), Morphology of Crystals, Vol. Part B, Terra Scientific Publishing, Tokyo, 1987, p. 645.

[4] J. Kepler, The Six-Cornered Snowflake, Clarendon Press, Oxford, 1966 (translated by C. Hardie); originally published as Seu de Nive Sexangula, Godfrey, Tampach, Frankfurt am Main, 1611.

[5] M.E. Glicksman, R.J. Shaefer, J.D. Ayers, Metall. Trans. A 7 (1976) 1747.

[6] S.C. Huang, M.E. Glicksman, Acta Metall. 29 (1981) 701.

[7] S.C. Huang, M.E. Glicksman, Acta Metall. 29 (1981) 717.

[8] M.E. Glicksman, Mater. Sci. Eng. 65 (1984) 45.

[9] N. Goldenfeld, J. Cryst. Growth 84 (1987) 601.

[10] E. Ben-Jacob, G. Deutscher, P. Garik, N.D. Goldenfeld, Y. Lereah, Phys. Rev. Lett. 57 (1986) 1903.

[11] S.N. Rauseo, P.D. Barnes, J.V. Maher, Phys. Rev. A 35 (1987) 1245.

[12] Y. Couder, in: H.E. Stanley, N. Ostrowsky (Eds.), Random Fluctuations and Pattern Growth: Experiments and Models, Kluwer Academic Publishers, Dordrecht, 1988, p. 75.

[13] P. Ossadnik, Phys. Rev. A45 (1992) 1058.

[14] E. Ben-Jacob, P. Garik, Physica D 38 (1989) 16.

[15] W. Mullins, R. Sekerka, J. Appl. Phys. 34 (1963) 323.

[16] J.S. Langer, in: J. Souletie, J. Vannimenus, R. Stora (Eds.), Chance and Matter, Elsevier, Amsterdam, 1987.

[17] D.A. Kessler, J. Koplik, H. Levine, Adv. Phys. 37 (1988) 255.

[18] E.A. Brener, V.I. Mel'nikov, Adv. Phys. 40 (1991) 53.

[19] Y. Pomeau, M. Ben Amar, in: C. Goldréche (Ed.), Solids Far from Equilibrium, Cambridge University Press, Cambridge, 1992.

[20] G.P. Ivantsov, Dokl. Acad. Nauk. SSSR 58 (1947) 567.

[21] A. Arneodo, Y. Couder, G. Grasseau, V. Hakim, M. Rabaud, Phys. Rev. Lett. 63 (1989) 984.

[22] Y. Couder, F. Argoul, A. Arneodo, J. Maurer, M. Rabaud, Phys. Rev. A 42 (1990) 3499.

[23] A. Arneodo, F. Argoul, Y. Couder, M. Rabaud, Phys. Rev. Lett. 66 (1991) 2332.

[24] E. Brener, D. Temkin, Phys. Rev. E 51 (1995) 351.

[25] E. Ben-Jacob, G. Deutscher, P. Garik, N. Goldenfeld, Y. Lereah, Phys. Rev. Lett. 57 (1986) 1903.

[26] E. Brener, M. Geilikman, D. Temkin, Sov. Phys. JETP 67 (1988) 1002.

[27] E. Brener, H. Müller-Krumbhaar, Y. Saito, D. Temkin, Phys. Rev. E 47 (1993) 1151.

[28] T. Ihle, H. Müller-Krumbhaar, Phys. Rev. Lett. 70 (1993) 3083.

[29] T. Ihle, H. Müller-Krumbhaar, Phys. Rev. E 49 (1994) 2972.

[30] R. Kupfermann, D. Kessler, E. Ben-Jacob, Physica A 213 (1995) 451.

[31] M. Ben Amar, E. Brener, Phys. Rev. Lett. 75 (1995) 561.

[32] J.S. Langer, Phys. Rev. A 36 (1987) 3350.

[33] L. Landau, E. Lifshitz, Statistical Physics, Akademie-Verlag, Berlin, 1970.

[34] A. Sharma, A.T. Jameel, JCIS 161 (1993) 190.

[35] A. Sharma, A.T. Jameel, JCIS 164 (1994) 416.

[36] P.G. de Gennes, Rev. Mod. Phys. 57 (1995) 827.

[37] N. Samid-Merzel, S.G. Lipson, D.S. Thannhauser, Physica A, in press.

[38] M. Ben Amar, E. Brener, Phys. Rev. Lett. 71 (1993) 589.

[39] E. Brener, Phys. Rev. Lett. 71 (1993) 3653.

[40] E. Brener, H. Müller-Krumbhaar, D. Temkin, T. Abel, Physica A 249 (1988) 73.

[41] T. Ihle, H. Müller-Krumbhaar, J. Phys. I France 6 (1996) 949.

Exit wave reconstructions of surfaces and interfaces using through focus series of HREM images

H.W. Zandbergen[a],[*], D. van Dyck[b]

[a]National Centre for HREM, Laboratory of Materials Science, Delft University of Technology, Rotterdamseweg 137, 2628 AL Delft, The Netherlands

[b]EMAT, University of Antwerp (RUCA), Groenenborgerlaan 171, B2020 Antwerp, Belgium

Abstract

The through focus exit wave reconstruction technique uses a series of high resolution electron microscopy (HREM) images to reconstruct the complex electron wavefunction at the exit plane of the specimen. The main advantage of this technique compared to conventional HREM is better interpretable images due to the deblurring of the information. This is in particular valid for surfaces and interfaces, as is shown by examples of exit waves of a (001) surface of NiO, a single slab of $(Mo,Co)S_2$ on γ-Al_2O_3 and the sapphire/CeO_2 interface. © 2000 Elsevier Science B.V. All rights reserved.

Keywords: High resolution electron microscopy; Surfaces; Interfaces; Exit wave reconstructions

1. Introduction

Knowledge of the atomic arrangements of surfaces and interfaces is of vital importance for the understanding of the properties. With the increasing need of the accurate determination of the atomic arrangements at non-periodic structures in materials design and control of microstructures and nanostructures, techniques that allow quantitative structural information at the sub-angstrom level will be indispensable. Compared to other techniques used to obtain structural information of materials, high resolution electron microscopy (HREM) has the great advantage that it yields local information about the atomic arrangements, projected along the direction of electron incidence at a resolution comparable to the interatomic distances. By combining the information obtained from different projections one can in principle obtain three-dimensional structural information.

Several groups [1–5] have used HREM to determine the atomic arrangements at selected grain boundaries with a high precision. Yan et al. [6] have shown that it is even possible to determine the composition of individual atom columns, using electron energy loss spectroscopy. Still the fraction of grain boundaries that can be studied by conventional HREM is limited. Recent developments in the processing of HREM images make it possible to reconstruct the electron wavefunction at the exit of

---

*Corresponding author. Tel.: +31-15-278-2266; fax: +31-15-278-6730.

E-mail address: h.w.zandbergen@tnw.tudelft.nl (H.W. Zandbergen)

the object. At present two methods are used in a routinely manner for exit waves reconstructions: through-focus electron holography and off-axis electron holography [7–9]. A major advantage of the reconstructed exit wave is that it allows a more straightforward quantitative interpretation than HREM images, in particular for non-period features like grain boundaries.

The recent papers in this journal, for which HREM was applied as a major experimental tool, can roughly be divided into three groups. The first group concerns the investigation of substitutions and the presence of extra atoms and vacancies [10–12], whereby one is mainly interested in the (super)structure. In the case only small crystals are available and one is interested in the average structure, the best tool is quantitative electron diffraction [13,14]. The second group is the study of the morphology and the microstructure [15–17]. The third and most important group is the investigation of grain boundaries (atomic structure, presence of second phases, local composition) [17,18]. In the present paper we will concentrate on the last group, HREM on grain boundaries and surfaces, because in this field the use of exit wave reconstruction has the most advantages.

In the HREM investigation of grain boundaries three aspects are very important restrictions: the shape and orientation of the grain boundary, the crystal lattices of the adjacent crystals and the resolution of the electron microscope.

The shape and orientation of the grain boundary is important, because HREM provides in first approximation projections of the structure, such that only lateral information and no depth information is available. This implies that the information of a grain boundary that is not parallel to the electron beam will be smeared out. Concerning the determination of rough shapes, a lot of development has been done in the last few years on the determination of the shape of biological particles by means of electron tomography [19,20]. The present state of the art is that a 3D resolution of about 1 nm can be obtained. For this a tilt series from $-70°$ to $+70°$ with increments of $2°$ are typically used. The 3D reconstruction of these biological specimens is based on contrast changes due to the overlap of scattering material in projection. In the study of inorganic solid state materials a 1-nm resolution is insufficient and also

more difficult to obtain. The 1-nm resolution is insufficient because one will be interested in the atomic arrangements at the grain boundary (e.g. even an amorphous grain boundary layer of 0.5 nm can strongly influence the properties). The 3D reconstruction of grain boundaries is more difficult when these materials consist of (small) crystals. Crystallinity results in extra contrast, which depends very strongly on the orientation. In orientations where the crystal is in a low-index[1] orientation, it scatters the electrons much stronger than in a high-index orientation. This cancels the one-to-one correspondence between contrast and the projected average scattering potential.

A crystalline specimen allows one to obtain a structure image. In this case one has to orient the crystal such that the projection of the structure along the electron beam results in image features that can be resolved given the resolution of the electron microscope. This implies that the imaging can only be done with the electron beam along a small selection of crystal directions. Obviously, the better the resolution of the electron microscope the more directions can be used.

If the crystal is perfectly aligned, the atoms can be considered as aligned in columns. In this case a column scattering potential [21], as schematically shown in Fig. 1, can replace the scattering potential of the atoms. The column scattering potential depends on the weight of the atoms and their distance along the column. If the crystal is tilted such that the column is not exactly along the electron beam (mistilt less than $1°$) this column approach is still valid [22].

Summing up the requirements for obtaining HREM images of grain boundaries that can be interpreted in a straightforward way: (i) the grain boundary is straight, (ii) the grain boundary is parallel to the electron beam, (iii) one of the grains and preferable both are in such an orientation, that lattice imaging is possible. Obviously most of these requirements become the more stringent the thicker the specimen. On the other side, a too thin specimen might not reflect the initial structure of the grain boundary due to changes induced by the thinning of

---

[1] A low index orientation is an orientation [hkl] that has a low sum $h + k + l$.
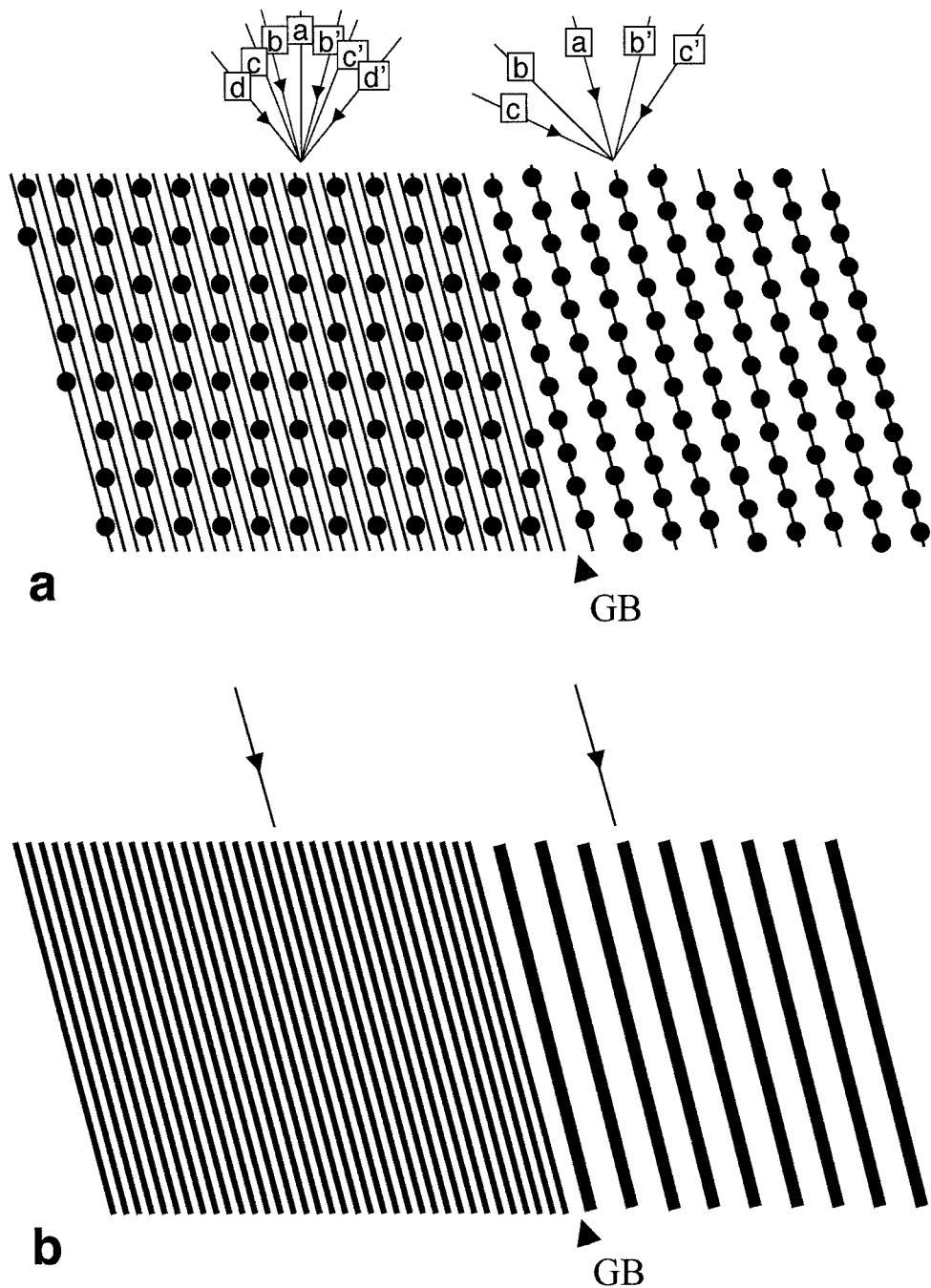
Fig. 1. (a) Schematic representation of an atomic arrangement around a grain boundary. It is supposed that lattice imaging is only possible along the directions a, b, c and d. The crystallographic arrangement of the grains is such that the direction b in the left grain is parallel to the direction a of the right grain, and the grain boundary is parallel to the a direction of the grain on the right. Because of that favourable orientation relation structure images of both grains are obtainable and the image of the grain boundary is as sharp as possible. For this orientation columns can replace the rows of atoms, each with its own scattering potential depending of the weight of its atoms and their spacing. The further the orientation deviates from the directions a, b, c and d, the poorer the contrast of the HREM images, which trend is faster for thicker specimens. Thus a very thin specimen will still allow an appreciable misorientation (several degrees).

the specimen or lattice relaxations due to the very limited thickness of the specimen. The interaction between electrons and matter is very large (about 10^4 times larger than for X-rays), such that very small specimen thicknesses can be investigated. The specimen thickness required for a good image contrast ranges from 1 to 10 nm depending on the scattering potential. This implies that the requirements that the electron beam is parallel to the grain boundary and parallel to atom columns are not very stringent. Obviously, the better the resolution of the microscope, the more directions one can get structural images from. In particular for the study of grain boundaries this increase in suitable directions is important.[2]

Compared to the imaging of the atomic arrangement at a grain boundary, the imaging of the atomic arrangement of a surface is much easier. In the first place the requirement that the second grain is also in an orientation allowing structure imaging does not have to be fulfilled. Secondly no information from the second grain, due to delocalisation of information, is complicating the interpretation of the image of the surface. In most cases the crystallographic planes occurring at grain boundaries are also the most stable surface planes, because such surfaces and interfaces tend will have a relatively low energy. Thus a surface can serve very well as a model material to investigate the atomic arrangements.

In this paper we want to illustrate the use of through-focus exit wave reconstructions, in particular on grain boundaries. To illustrate the differences in delocalisation of information between reconstructed exit waves and HREM images, we show some

simple examples rather than giving examples of quantitative comparisons. Surfaces are used to illustrate the problems arising with the imaging of grain boundaries, because they can serve as simplifications of grain boundaries. After a short introduction to the resolution of the electron microscope and the delocalisation of information due to the imperfection of the microscope, three examples of reconstructed exit waves are discussed.

1.1. The resolution of the electron microscope

Concerning the resolution of a HREM, one has to distinguish between point resolution (or structural resolution) as the finest detail that can be interpreted directly in terms of the structure, and the information limit which is the finest detail that can be resolved by the instrument, irrespective of a possible interpretation. The electron microscope in the phase contrast mode at optimum focus (Scherzer focus) directly reveals the projected potential, i.e. the structure, of the object, provided the object is very thin and the atom columns are sufficiently separated. All spatial frequencies g with a nearly constant phase shift are transferred from object to image (see Fig. 2). Hence the point resolution, ρ_S, can be obtained from the first zero of the transfer function. The information
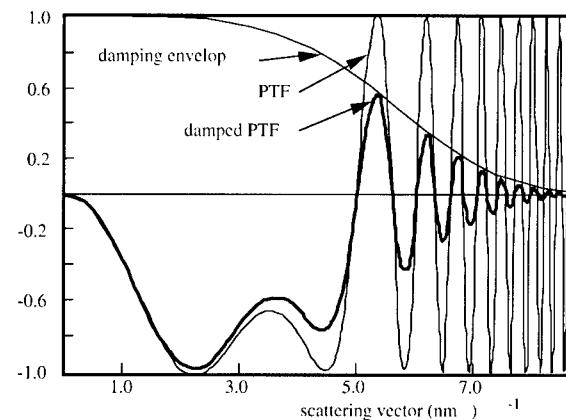
Fig. 2. Transfer function (imaginary part, and thus for the phase) for 300 kV with a C_s of 1.3 mm and a defocus of -63 nm (which is close to Scherzer focus). The damping corresponds to a defocus spread of 6 nm and a divergence of 0.1 mrad. The point resolution $= 0.2$ nm and the information is 0.14 nm assuming that the contrast should be at least 10%.

---

[2]Assuming that a HREM allows a double tilt of $\pm 30°$, one out of three grain boundary can be aligned along the electron beam. Assume next that by rotation of the specimen about the interface normal with a range of 40°, one orientation can be reached allowing structure imaging for the first or the second adjacent grain. Then the chance of being able to have a grain boundary being parallel to the electron beam with the first grain only (the situation for a surface) is still one out of three. Assuming random orientation of the grains and that the maximum misorientation is 2°, the chance that an orientation can be found in which both grains are in a both grains in an orientation allowing structure imaging is 1 over 30. A doubling of the number of orientations allowing structure imaging increases this chance to 2 over 15.

beyond ρ_S is redistributed over a larger image area (delocalisation of information). In particular the high frequency information can be delocalised over several nanometers even for a good electron microscope and optimal imaging conditions. The information limit corresponds to the maximal diffracted beam angle that is still transmitted with appreciable signal-to-noise ratio. Since the information limit is mostly better than the point resolution, a promising way of increasing the resolution is by restoring the information that is present between ρ_S and ρ_I and which obviously has the wrong phase. This information has to be unscrambled for which purpose exit wave reconstruction has been developed. In that case ρ_I will determine the final resolution.

Recently two exit wave reconstruction methods to unscramble the delocalised information have been developed: through-focus electron holography and off-axis electron holography [7]. The exit wave reconstruction (unscrambling of the information) is done in two steps. First, the wavefunction in the image plane is reconstructed. Since by recording the image only the amplitude information is collected, one has to use a method to determine also the missing phase information. The phase in HREM images can be determined by holographic methods of which two approaches exist: off-axis holography [8] and focus variation [9]. For both techniques one needs a very high-resolution camera (CCD), a powerful image processor, and a field emission source to provide the necessary spatial coherence. In off-axis holography [8], the beam is split by an electrostatic biprism into a reference beam and a beam that traverses the object. Interference of both beams in the image plane then yields fringes, the positions of which yield the phase information. In the focus variation method, the focus is used as a controllable parameter so as to yield a through focus series from which both amplitude and phase information can be extracted [23–27]. Images are captured at very close focus values so as to collect all information in a three-dimensional space, composed of the intensities of the image $R(x,y)$ and the defocus. Schiske [23], Kirkland [24] and Saxton [25] have already suggested such methods. An alternative to the use of exit wave reconstructions is to improve the point resolution of the electron microscope. A 0.1-nm point resolution is already obtainable with

high-voltage high-resolution electron microscopes [28,29]. Such microscopes have as disadvantage their price and an increased chance of irradiation damage.

In the exit waver reconstruction, after determining the image wave one has to reconstruct the exit wave of the object. For this the microscope parameters have to be known very precisely. This forces the microscopist to perform the experiments with care and to decide beforehand which information he wants to achieve, such that the experiments are optimised to obtain this information. In the case one aims at the highest resolution, the best focus range is around Lichte focus (about three times Scherzer focus) for which the damping of the high frequency information is smallest.

Coene et al. [9] have developed a procedure to refine the exit wave by iteration comparing the simulated images for the whole through focus series. The best-matching criterion for this purpose is the maximum-likelihood criterion. In this way all information, both linear and non-linear, that is present in the images is fully exploited, so that the highest precision is achieved.

2. Experimental

Electron transparent areas of the various specimens were obtained by crushing (NiO and $(Mo,Co)S_2$ on γ-Al_2O_3) or by ion milling (sapphire/CeO_2 interface). The crushing was done under ethanol, after which a suspension was dripped onto a Cu grid with a carbon-coated holey film. The ion milling was done with the thin film side facing away from the ion gun with a final ion-polishing step using an acceleration voltage of 3 kV, a gun current of 0.3 mA, and an angle of 8°. Electron microscopy was performed with a Philips CM30ST electron microscope with a field emission gun operated at 300 kV and a Link EDX element analysis system. The information limit of this microscope is 0.14 nm. The high-resolution images were recorded with a 1024×1024 pixel Photometrix CCD camera with a dynamic range of 12 bits. For the through focus exit wave reconstructions (TF-EWR), a series of 15–20 HREM images was recorded with focus increments of 5.2 nm.

The choice of representation of the exit wave is to

a large extent arbitrary. One can either display a positive phase shift deviating from $2n\pi$ of the phase of an area having no atoms (e.g. vacuum) as black or white. Similarly a decrease in the amplitude can be displayed in two ways. In this paper the amplitude decrease and the positive phase shift in thin areas are displayed by a darkening. Thus for small thicknesses the heavy scattering atoms appear as dark dots in the amplitude as well as in the phase image, allowing easy comparison of these two images.

In order to determine the structure of a surface or interface by transmission electron microscopy one has to view parallel to the surface (profile imaging) or the interface as is shown in Fig. 3. Additional requirements are that one has to look in a direction along which the atoms are aligned in columns that are sufficiently separated and the specimen has to be very thin e.g. 20 nm or less.

2.1. Example 1: image calculations of a [100] surface of NiO imaged in profile

The complexity in the structure determination from conventional HREM images as compared to exit waves is demonstrated in Fig. 4. This figure shows calculated exit waves and calculated conventional HREM images for a range of defocus values of the (001) surface of NiO viewed along the [110] direction for two thicknesses, e.g. 1 and 5 nm. In the model used for this calculation all atoms have a Debye–Waller factor of 125 pm^2 except for the Ni atoms at the (001) surface, which have a Debye Waller factor of 375 pm^2. This Ni atom can be clearly distinguished in the amplitude of the exit wave, since it is much less dark. In the HREM images this different Ni atom is, however, not observable. In fact, these images would be almost the
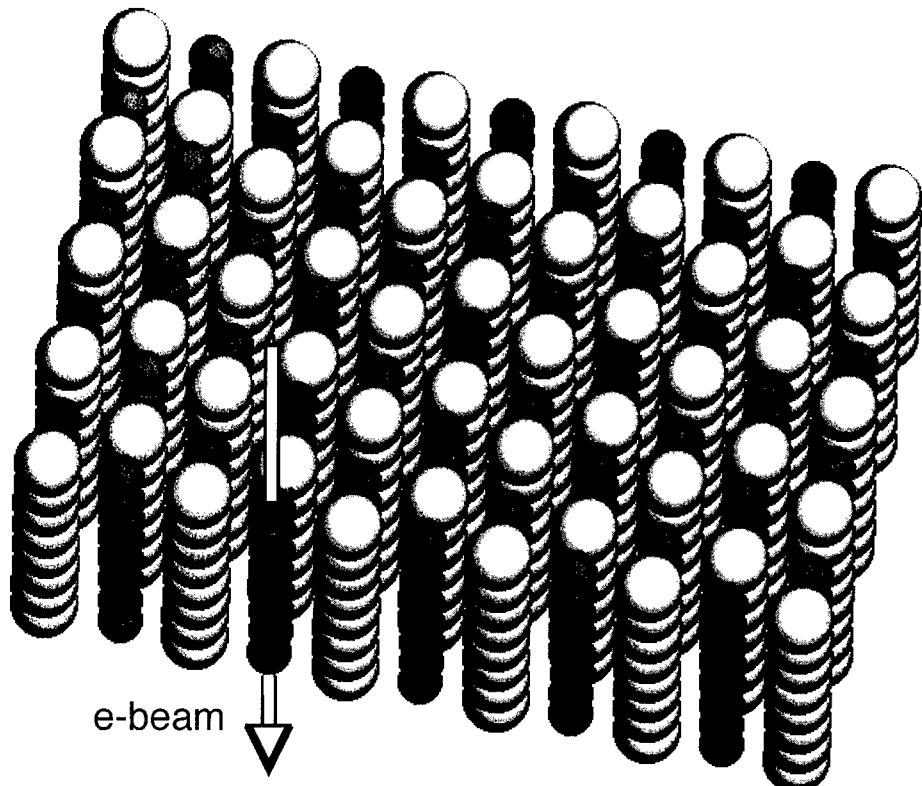

e-beam

Fig. 3. Schematic representation of profile imaging. The arrow indicates the direction of the electron beam.
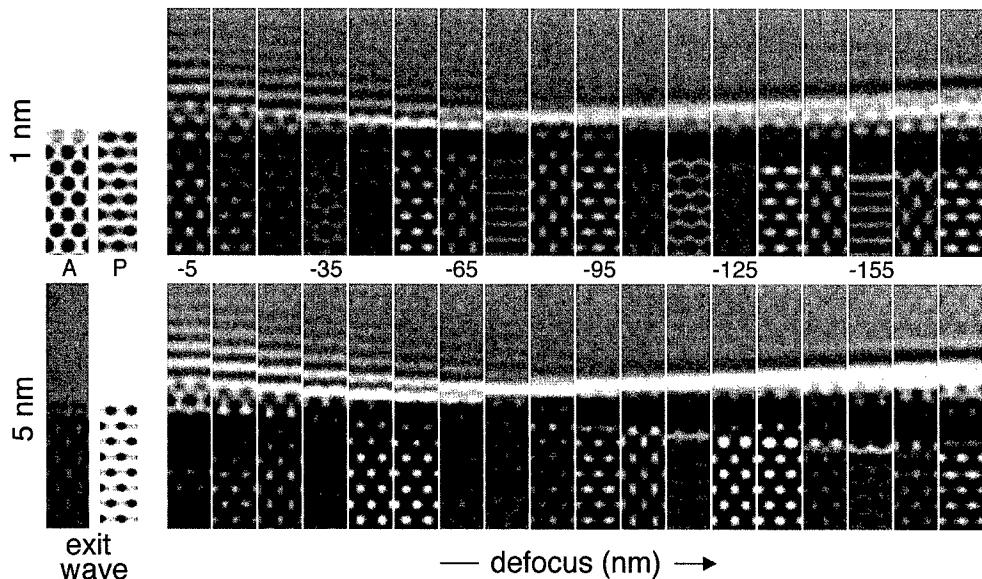
Fig. 4. Calculated images for a (001) NiO surface in profile imaging, using $C_s = 1.3$ mm, a defocus spread of 6 nm, a divergence of 0.1 mrad and a mechanical vibration of 0.05 nm.

same, if this Ni would have also a Debye–Waller factor of 125 pm^2.

One can see that in the HREM images the information of the surface is delocalised. The extend of this delocalisation depends on the defocus. The information of the 'single crystalline' part is of course also delocalised, but this is not visible due to the periodicity of this area. In this figure the smallest delocalisation seems to occur at a defocus of about −70 nm. However, this minimum delocalisation depends on the scattering angle, the wavelength and the spherical aberration of the objective lens. For a spherical aberration of 1.35 mm and a defocus of about −70 nm, a minimum delocalisation is obtained for a reflection g of about 5 nm^{-1}. But for a reflection of 10 nm^{-1} the delocalisation is still very large at a defocus of −70 nm and the minimum delocalisation occurs at a defocus of about −270 nm. No defocus can be chosen to have the minimum delocalisation for all diffracted beams.

In contrast to the HREM images, in which the information is delocalised, the exit wave shows a sharp edge of the specimen and the difference in Debye Waller factor is also clearly seen. Obviously

the exit wave leads to a much more accurate description of the atom positions at and near the surface. Note that the effect of a larger Debye Waller factor is in first approximation quite similar to a smaller scattering potential. In the phase image one can see that the dot corresponding to the Ni atom with the Debye Waller factor of 3 shows a larger extension. Thus, only in combination with the size of the dots a larger Debye Waller factor can be distinguished from a partial occupancy.

2.2. Example 2: reconstructed exit wave of a [100] surface of NiO imaged in profile

Fig. 5 shows a reconstructed exit wave of the (001) surface of NiO in profile and one of the HREM images of the through focus series used for this reconstruction. The black dots in the exit wave correspond with Ni columns in the viewing direction. The Ni atoms are imaged as black dots in the amplitude, whereas the black dots in the phase image correspond to the Ni positions in the thin part of the crystal and to O positions in the thicker part. The black dots of the Ni columns in the amplitude at the

Fig. 5. Profile images of the (001) surface of NiO. (a) Shows an experimental image taken at −100 nm; (b) and (c) shows the amplitude and phase of the exit wave, calculated from a through focus series of 15 images, of which the image (a) is the first image. The dark dots correspond with Ni columns in the viewing direction. The Ni atoms are imaged as dark dots in the amplitude, whereas in the phase image the dark dots correspond to the Ni positions in the thin part of the crystal and to O positions in the thicker part. The bl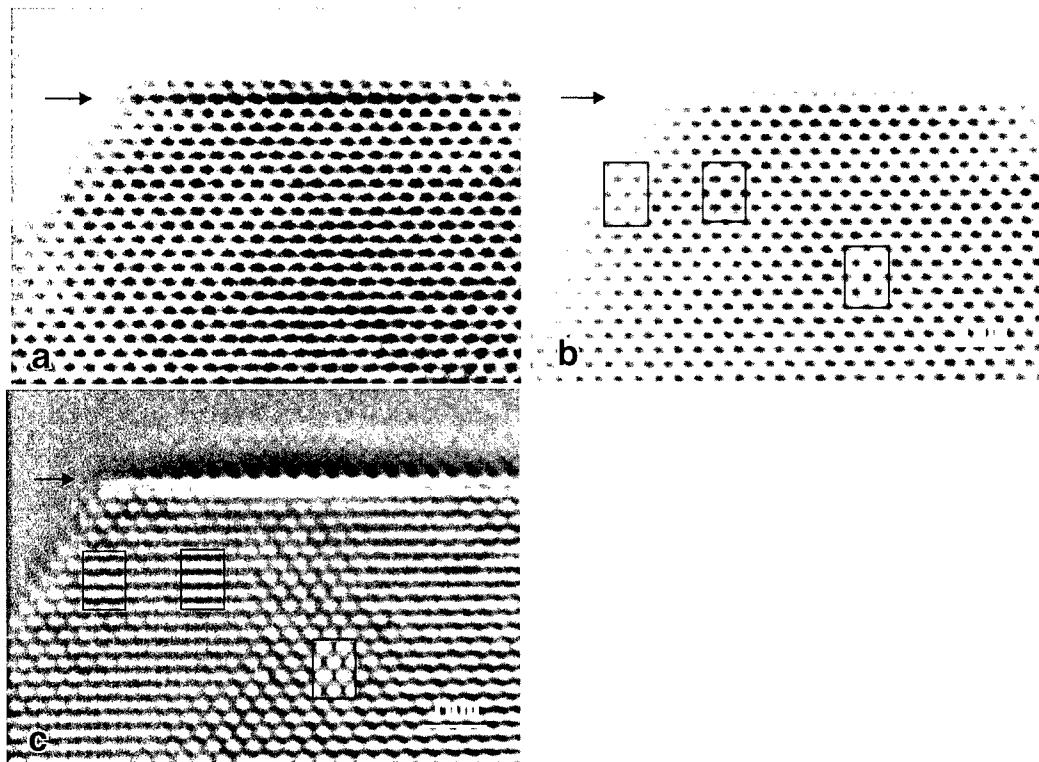ack dots of the Ni columns in the amplitude at the surface are less dark, probably due to a larger Debye–Waller factor. The arrows point to the same line position, from which is clear that in (a) one row of black dots is actually located above the surface.

surface are less black, which is probably due to the larger Debye Waller factor, which is normally larger for atoms at the surface. The experimental image does not show this feature of less contrast at the surface because of delocalisation and because it contains information from both the amplitude and the phase of the exit wave (the phase is less sensitive to differences in Debye Waller factors). Furthermore, the experimental image shows one extra row of black dots, situated outside the crystal, which is obviously due to the delocalisation discussed in Example 1.

In case one is only interested in the atomic positions in a single crystalline area, and the crystal is well aligned, a small deviation from the absolute focus will in most cases not lead to a change in the positions of the black or white dots. Thus the atom positions can still be determined quite accurately.

However, in the case of a defect, grain boundary or crystal surface (in profile view), a slight deviation in focus can lead to substantial shifts in the positions of the black dots, as is evident in Fig. 5, which shows the effect of +10, +5, 0, −5 and −10 nm focus shift from the absolute focus for a reconstructed exit wave of a (100) surface of NiO. The focus shifts of +10 and −10 nm result in shifts of the black dots of −0.02 and +0.02 nm away from the bulk respectively.

2.3. Example 3: MoS_2 slabs on γ-Al_2O_3

MoS_2 to which cobalt sulfide or nickel sulfide has been added on an atomic scale (CoMoS and NiMoS catalysts, respectively) is employed on a large scale as catalyst in the hydrotreating of oil. In order to

have a large surface area and to prevent rapid sintering to larger particles, frequently γ-Al_2O_3 consisting of small particles is used as support for the CoMoS and NiMoS catalytic phase. MoS_2 is present as slabs, as shown in Fig. 7. The most active phase is believed [30] to be the one for which the edges of the MoS_2 slabs are decorated with Co or Ni (see Fig. 7).

Fig. 8 shows the phase and amplitude of a reconstructed exit wave and one of the HREM images, which was used for the reconstruction. A string of dark dots can be seen in the amplitude image, which are the strongly scattering atoms, e.g. Mo and Co. The last dark dot of the string is much less dark than the others ones, indicating that in this column much less scattering potential is present. This could be due to a large fraction of Co in this column. However, if the slab has a rather pancake-like shape (see Fig. 7b), the projection of the edges will also result in less scattering potential. Finally, the atoms at the edges could have a larger Debye Waller factor. The sulphur atoms are more visible in the phase of the exit wave. The black dots of the sulphur atoms form with the Mo atoms V shapes, which are typical for the MoS_2 structure along this projection. Note that along the electron beam direction the CoMoS slab will probably also have a

curved shape. Only that part of the curved columns of atoms, which is more or less parallel to the electron beam, has resulted in significant contrast.

2.4. Example 4: correction for the delocalisation at an interface

Single crystalline Al_2O_3 (sapphire) is considered as a very suitable substrate material for microwave applications due to its low dielectric losses, availability of large crystals and relatively low cost. Unfortunately, the high reactivity of sapphire with high temperature superconductor materials prevents direct epitaxial growth of thin films. The problem can be solved by the deposition of an intermediate buffer layer. Cubic CeO_2 demonstrates a low reactivity and the ability to epitaxy with R–Al_2O_3 ($1\bar{1}02$) and the YBCO phase. Because of this, it is considered to be a good buffer layer material [31,32]. However, the critical properties of the superconducting layer are strongly dependent on the single crystalline quality and the smoothness of the buffer layer: a smooth surface and a low density of mismatch dislocations in the buffer layer, facilitate the epitaxy of the HTSC layer with high crystallinity and consequently high T_c and J_c characteristics [33]. In this respect, the accommodation of the lattice mismatches at the
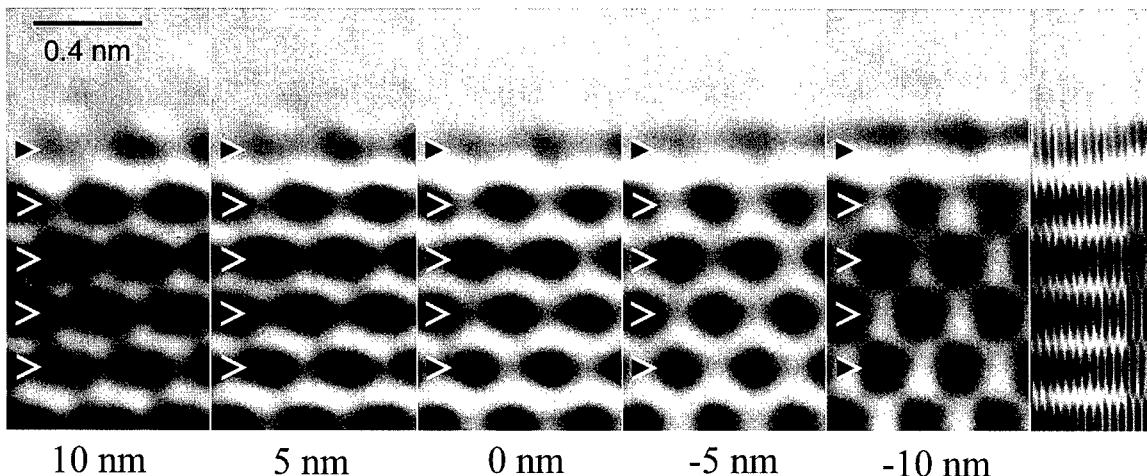
Fig. 6. Experimental exit wave (amplitude) of the (001) surface of NiO in profile view at various focus values. The dark dots correspond with Ni columns in the viewing direction. The applied focus propagations are given below the images. The image on the far right represents the same series of images but compressed in horizontal direction, which is about the same as looking at a glancing angle in horizontal direction. The position of the row of dots at the surface is shifted away from the bulk when a negative focus propagator is applied.
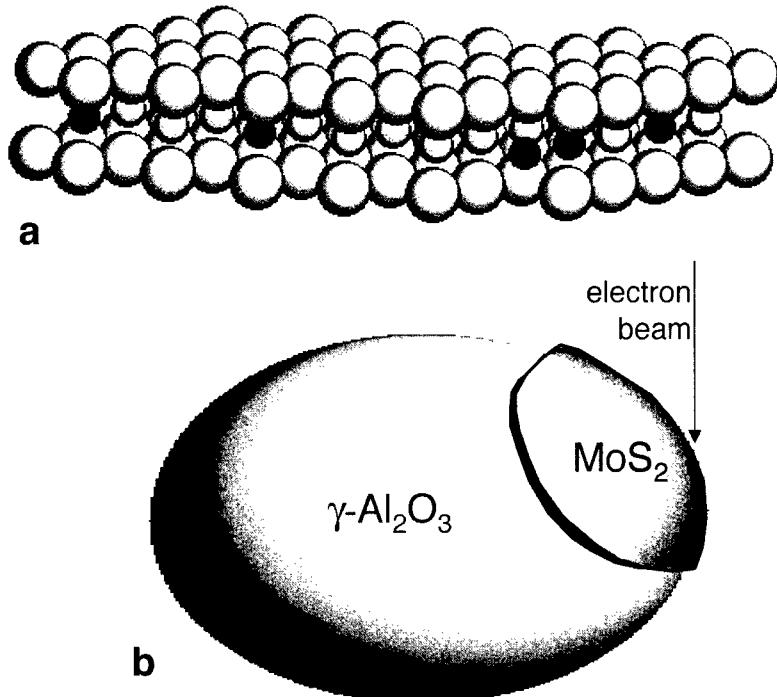
Fig. 7. Schematic representation of the morphology of MoS_2 particles and their location on the γ-Al_2O_3 substrate. The position of the Co atoms at the edges is illustrated in (a). The dark small atoms are Co atoms, and the large and small bright atoms are S and Mo, respectively. The covering of the γ-Al_2O_3 particle by the MoS_2 particle like a blanket is illustrated in (b).
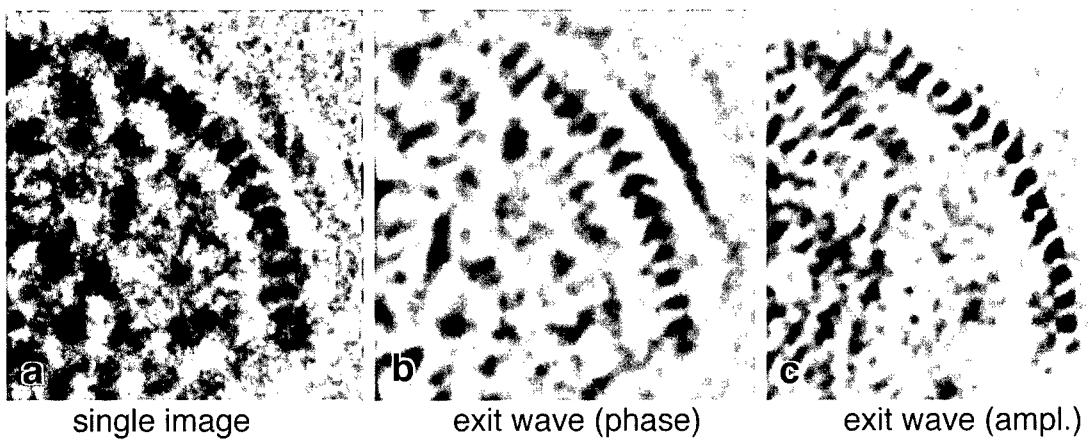
Fig. 8. HREM image and exit wave of a MoS_2 particle on γ-Al_2O_3. (a) Shows one of the HREM images of the through focus series. (b) and (c) Show the amplitude and phase of the reconstructed exit wave.

$YBCO/CeO_2$ and CeO_2/R–Al_2O_3 interfaces are important for the optimisation of the manufacturing of devices.

Fig. 9 shows images of a sapphire/CeO_2 interface. Fig. 9 show a typical HREM image and a reconstructed exit wave, respectively. Note that, whereas
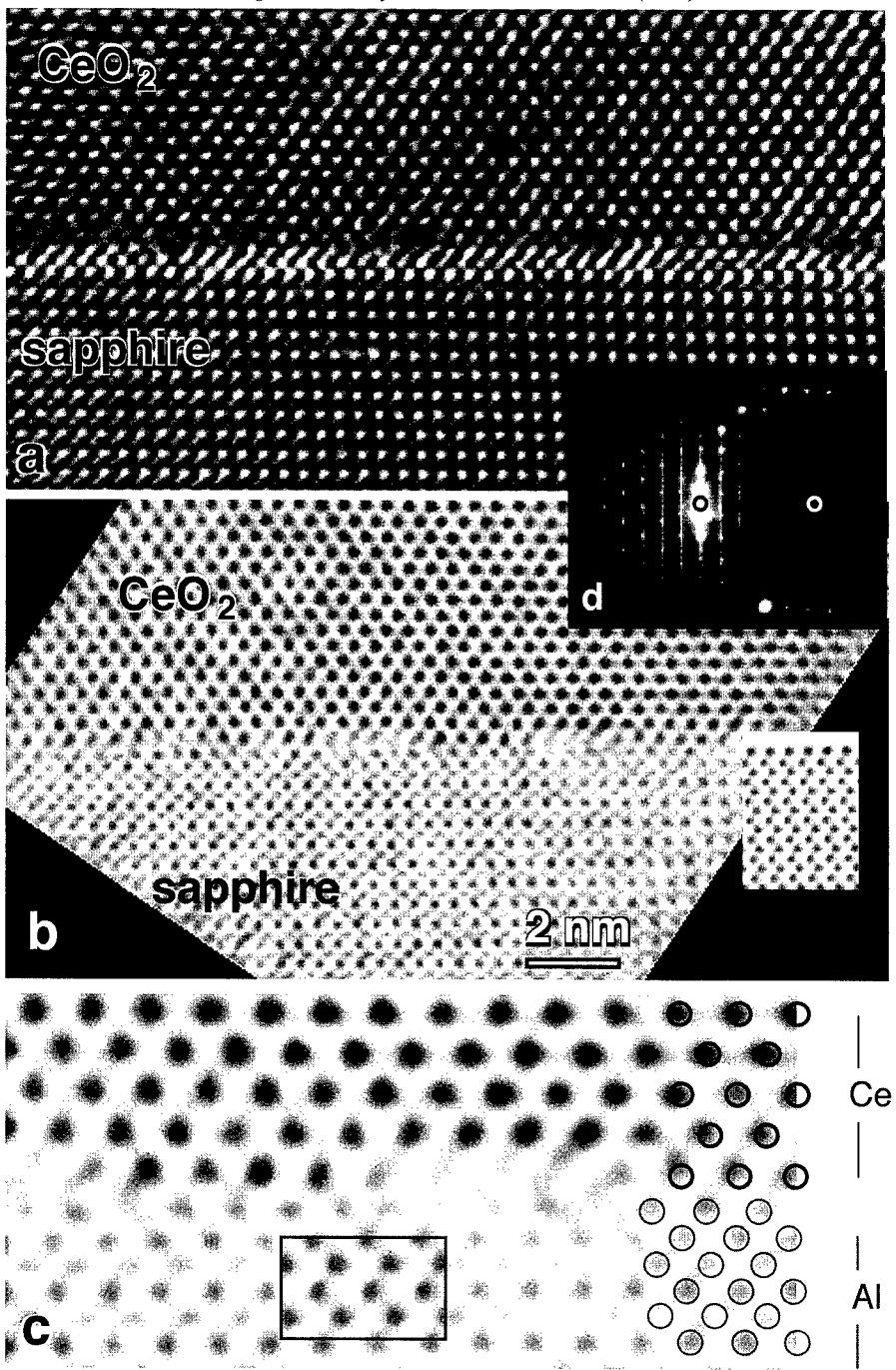
Fig. 9. HREM and exit wave images of the CeO$_2$/sapphire interface. (a) Shows a HREM image. (b) Shows the amplitude of the reconstructed exit wave. Whereas the exit wave shows a very sharp interface, in the HREM image the interface is fuzzy due to the delocalisation of information. (c) Shows an enlargement of a section of the exit wave. Open circles represent the bulk positions of Ce atoms. The Ce atoms neighbouring the interface are shifted towards the bulk of the CeO$_2$ layer. (d) Shows a diffraction pattern of an area containing substrate, CeO$_2$, and YBCO. From this it can be concluded that the sapphire is tilted over 1.7° about the interface normal. Due to the tilt the black dots in the sapphire will not correspond to the Al positions. Insets in (b) and (c) are calculated exit waves using a specimen thickness of 8 nm, a tilt of 1.7° as (d), an isotropic specimen vibration of 0.05 nm, no objective aperture and a defocus spread of 6 nm.

the exit waves reveals a very sharp interface, in the HREM image the interface is fuzzy. This is due to the delocalisation of information occurring in the imaging process. Obviously the exit wave gives much more precise information about the atomic positions at the interface.

The misfit between the sapphire and the CeO_2 lattices, being 5.4% in [$10\bar{1}1$] and 12% in [$1\bar{2}10$] directions, is mainly accommodated in the very first atomic layers of CeO_2, as can be seen in Fig. 9. This figure shows a reconstructed exit wave of the sapphire/CeO_2 interface. At regular intervals one can observe a different contrast in the CeO_2 layer next to the interface. The average spacing between these areas is 4 nm, which agrees well with the dislocation spacing which one expects from lattice parameters mismatch for the (001) lattice spacing of CeO_2 (0.541 nm) and the ($1\bar{1}02$) lattice spacing of sapphire (0.4759 nm). One expects a dislocation spacing of 3.95 nm. The mismatch observable in the image plane should also be present along the viewing direction since in this direction a mismatch also occurs.

An enlargement of the exit wave of the interface is shown in Fig. 9c. The positions of the Ce atoms and the Al atoms, corresponding to their positions in the bulk are given as open circles. The black dots corresponding to the Ce atoms neighbouring the interface are more elongated along the interface normal that the corresponding black dots in the bulk and they are a little bit shifted away from the interface. The elongation might be due to small variations in the positions along the viewing direction. The shift away from the interface suggests an interface relaxation in which the Ce atoms are drawn into the CeO_2 lattice. The black dots at the Ce positions of the first atomic plane of the buffer are absent at the locations of the misfit dislocations. In the phase image of this exit wave, however, one can still observe dots at these sites, which indicates that the atom columns on these sites are less ordered in the viewing direction. This is quite logical given the two-dimensional dislocation network.

The exit wave of the sapphire in Fig. 9c shows two types of dark dots. However, calculated exit waves for sapphire show that these two types of dots are both Al and should have the same intensity, whereby the Al atoms are not in the centre of the

four surrounding Al atoms as is shown in the insets in Fig. 9b and c. In the experimental exit wave the weak dark dots seems to be almost in the centre. This discrepancy can be explained only partly by the rather large misorientation of the sapphire. Image calculations show that for such a tilt the intensities of the two types of dots can be slightly different, but less than in the experimental exit wave. Also the centering of the black dots in the centre of the four surrounding black dots as observed in the experimental image can only be obtained by a shift of the Al position along the c-axis (e.g. z(Al) is 0.372 instead of 0.352). It should be noted that due to the tilt the position of the dark dots in the exit wave would be different from the actual atomic positions. One also has to take into account that when the actual columns of Al atoms are tilted over 1.7°, the projection of the top of the column is shifted over 0.15 nm from the projection of the bottom of the column for an 8 nm thick specimen. Thus although the dark dots corresponding to the Al atoms neighbouring the interface are shifted towards the interface, they might not correspond to the actual position of the Al atoms.

3. Discussion

The electron–matter interaction is sufficiently well understood to allow a calculation of HREM images. Such calculations are frequently used to verify a postulated structural model. In the image simulation algorithm three stages can be distinguished. First, the electron scatters dynamically in the crystal. This interaction can be simulated using the multislice methods. As an input to the multislice program one has to specify all the object parameters such as unit cell, position and type of cell atoms, Debye–Waller factors, object orientation and thickness, and the wavelength of the electrons. The result of this calculation yields the wavefunction at the exit face of the crystal. In a second step, the formation of the image in the electron microscope is simulated where all the instrumental parameters have to be specified. Finally, the electron intensity in the image plane is calculated by squaring the wavefunction. Several commercial software packages [34–37] exist for high-resolution image simulations. For calculations of conventional HREM images one has to do all

three steps. For a calculation to compare with the reconstructed exit wave only the first step with a subsequent band filtering to account for the information limit are required.

Several groups have done excellent quantitative characterisations using HREM images (grain boundaries [1–5], interfaces [38–40] and single-crystalline areas [41]). However, a large majority of the present use of image simulation is that the image comparison is done visually and not quantitatively or in a recursive refinement. Since a large number of parameters can be adjusted, visual comparison is not very reliable. Obviously, a development towards standard use of quantitative comparison is required. A major step in this development is the exit wave reconstruction technique, because that gives more precise data and also forces the electron microscopist to calibrate the microscope and to work according to clear procedures. This is needed because the exit wave can only be correctly interpreted if this is done at the exact focus and with a proper correction of all the lens aberrations, because otherwise phase and amplitude information are mixed. A robust method for determining the exact focus is to exploit the entropy of the exit wave as a function of focus [42,43]. An efficient correction for all microscope parameters is possible with the fingerprint method reported by Thust et al. [44]. The local misorientation can be measured directly by using nanodiffraction. But the change in doses (electrons per unit area) and total electron flux upon switching from nanodiffraction mode to HREM mode can lead to small but very significant changes in the orientation. The determination of the orientation from the exit wave is in principle possible as is illustrated by Bokel et al. [45,46]. They showed that the local misorientation on a unit cell scale could be determined from 'single crystalline' areas in the exit wave, provided this structure is known.

If one wants to determine the structure of an object without modelling a major final step remains: the retrieval of the projected structure of the object from the wavefunction at the exit face. This is certainly not a straightforward process. It is most simple if the object is thin enough to act as a phase object (typically less than 2–4 nm for the compounds discussed in this paper): in that case the phase is proportional to the electrostatic potential of the structure, projected along the beam direction. However, even in this case it will be very hard or impossible to determine the exact atomic weight of a given dark dot in the exit wave, because its contrast will not only depend on the atoms in the projected column but also on their Debye–Waller factor as is shown in Fig. 2. If the object is thicker, the problem is even more complicated.

However, if the distance between the columns is not too small, a correspondence between the wavefunction at the exit face and the column structure of the crystal is maintained. Within the columns, the electrons oscillate as a function of depth without leaving the column. Hence, the classical picture of electrons traversing the crystal as plane-like waves in the direction of the Bragg beams, which historically stems from X-ray diffraction, is in fact misleading. It is important to note that channelling is not a property of a crystal, but occurs even in an isolated column and is not much affected by the neighbouring columns, provided the columns do not overlap. Hence, the one-to-one relationship is still present in case of defects such as surfaces, interfaces or dislocations provided they are oriented with the atom columns parallel to the incident beam. One can explicitly specify the thickness dependency of the wavefunction at the exit face of a column. In that case the structure can be considered as individual columns of which the scattering and thus the contrast changes with specimen thickness. This leads to a situation that the positions of the black dots in the exit wave do not change their position but do change their relative intensities with thickness. Thus, if the thickness of a specimen is unknown, one is unable to indicate the scattering of a given projected column but the position of this column can be determined quite accurately. In this way the exit wave still retains a strong correspondence with the projected structure, whereby the positions are still (almost) the same but the contrast (in phase or amplitude) cannot be used to determine the scattering potential in the projected structure unless the thickness is accurately known. We used this to determine the structure of $Ce_5Cu_{12}P_9$ [13]; from the exit wave we were able to determine the positions of the columns. This model was the basis of a structure refinement using electron diffraction data for several thicknesses, whereby first the position of the columns was refined assuming all

columns to be equal Cu columns. Next the occupancies were refined, allowing one to decide which atom columns contained, Ce, Cu or P. The final refinement gave very accurate atomic positions.

In conclusion, exit wave reconstruction has now been matured into an important step towards quantitative structure determination of crystalline objects. By extending in this way the resolution limit of the microscope up to the information limit, which is beyond the size of an individual atom, it has become possible to resolve atomic structures without much a priori knowledge. Further development is needed in particular in the interpretation of exit waves from misoriented areas.

Acknowledgements

References

[1] K.L. Merkle (Ed.), Interface Science, Vol. 2, Kluwer, Boston, 1995, pp. 311–345.

[2] G. Möbus, R. Schweinfest, T. Gemming, T. Wagner, M. Rühle, J. Microsc. 190 (1998) 109–130.

[3] W.E. King, G.H. Cambell, S.M. Foiles, D. Cohen, K.M. Hanson, J. Microsc. 190 (1998) 131–143.

[4] O. Kienzle, F. Ernst, G. Möbus, J. Microsc. 190 (1998) 144–158.

[5] G. Möbus, M. Rühle, Ultramicroscopy 56 (1994) 54.

[6] Y. Yan, M.F. Chisholm, G. Duscher, A. Matti, S.J. Pennycook, S.T. Pantelides, Phys. Rev. Lett. 81 (1998) 3675–3678.

[7] D. Van Dyck, H. Lichte, K.D. van der Mast, Ultramicroscopy 64 (1996) 1.

[8] H. Lichte, Ultramicroscopy 47 (1992) 223.

[9] W. Coene, G. Janssen, M. Op De Beeck, D. Van Dyck, Phys. Rev. Lett. 69 (1992) 3743.

[10] P. Peres, F. Weill, C. Delmas, Solid State Ionics 116 (1999) 19–27.

[11] M.R. Palacín, F. Krumeich, P. Gómez-Romero, Solid State Ionics 101–103 (1997) 1079–1085.

[12] K. Kinoshita, J. Bonevich, X. Song, T.D. Tran, Solid State Ionics 86–88 (1996) 1343–1350.

[13] H.W. Zandbergen, J. Jansen, J. Microsc. 190 (1998) 222.

[14] J. Jansen, D. Tang, H.W. Zandbergen, H. Schenk, Acta Crystallogr. A 54 (1998) 91.

[15] S. Nicolopoulos, M. Vallet-Regí, J.M. González-Calbert, Solid State Ionics 101–103 (1997) 175–182.

[16] T. He, C.L. Jia, P. Ehrhart, P. Meuffels, Solid State Ionics 89 (1996) 9–12.

[17] M. Zimnol, A. Graff, H. Sieber, S. Senz, S. Schmidt, R. Mattheis, D. Hesse, Solid State Ionics 101–103 (1997) 667–672.

[18] D. Hesse, Solid State Ionics 95 (1997) 1–15.

[19] J. Walz et al., J. Struct. Biol. 120 (1997) 387–395.

[20] T.S. Bakker, R.H. Cheng, J. Struct. Biol. 116 (1996) 120.

[21] D. Van Dyck, M. op De Beeck, Ultramicroscopy 64 (1996) 99.

[22] D. van Dyck, R.M.J. Bokel, H.W. Zandbergen, Microsc. Microanal. 4 (1998) 428–434.

[23] P. Schiske, in: P. Hawkes (Ed.), Image Processing of Computer-Aided Design in Electron Optics, 1973.

[24] E.J. Kirkland, Improved high resolution image processing of bright field electron micrographs. I. Theory, Ultramicroscopy 15 (1984) 151–172.

[25] W.O. Saxton, Focal series restoration in HREM, in: Proc. XIth Int. Congress on Electron Microscopy, Kyoto, 1986, p. 1, Post deadline contributions.

[26] D. Van Dyck, M. Op de Beeck, in: Proc. XIIth Int. Congress for Electron Microscopy, Seattle. San Francisco Press, San Francisco, 1990, pp. 26–27.

[27] M. Op de Beeck, D. Van Dyck, W. Coene, in: A. Tonomura et al. (Eds.), Electron Holography, North Holland-Elsevier, Amsterdam, 1995, pp. 307–316, ISBN 0-444-82051-5.

[28] F. Phillipp, Mater. Trans. J. Inst. Metall. 39 (1998) 888–902.

[29] K. Mitsuiski, M. Kawasaki, M. Takegushi, M. Furuya, Phys. Rev. Lett. 82 (1999) 3082–3084.

[30] H. Topsoe, B.S. Clausen, E.E. Massoth, in: J.R. Andersson, M. Boudart (Eds.), Catalysis, Science and Technology, Vol. 11, Springer, Berlin, 1996.

[31] F. Wang, R. Woerdenweber, Thin Solid Films 227 (1993) 200.

[32] H.W. Zandbergen, I.E. Graboy, V.L. Svetchnikov, A. Kaul, Physica C (1998) submitted.

[33] I.E. Graboy, N.V. Markov, V.V. Maleev, A.R. Kaul, S.N. Polyakov, V.L. Svetchnikov, H.W. Zandbergen, K.H. Dahmen, J. Alloys Compd. 251 (1997) 318.

[34] P.A. Stadelman, Ultramicroscopy 21 (1987) 131–146.

[35] R. Kilaas, R. Gronsky, Ultramicroscopy 11 (1982) 289–298.

[36] D. Van Dyck, W. Coene, Ultramicroscopy 15 (1984) 29.

[37] D. Van Dyck, W. Coene, Ultramicroscopy 15 (1984) 41.

[38] P. Schwander, W.R. Rau, A. Ourmazd, J. Microsc. 190 (1998) 171–183.

[39] R. Hillebrand, J. Microsc. 190 (1998) 61–72.

[40] V. Radmilovic, S. Ratkovic, U. Dahmen, Microsc. Microanal. 3 (Suppl. 2) (1998) 665–666.

[41] T. Gemming, G. Möbus, M. Exner, F. Ernst, M. Rühle, J. Microsc. 190 (1998) 89–98.

[42] D. Tang, H.W. Zandbergen, J. Jansen, M. Op de Beeck, D. van Dyck, Ultramicroscopy 64 (1996) 265–276.

[43] D. Van Dyck, M. Op de Beeck, D. Tang, J. Jansen, H.W. Zandbergen, in: IEEE Int. Conf. on Image Processing, Los Alamitos, 1996, pp. 737–770.

[44] A. Thust, M.F.H. Overwijk, W.M.J. Coene, M. Lentzen, Ultramicroscopy 64 (1996) 249.

[45] R.M.J. Bokel, J. Jansen, H.W. Zandbergen, Ultramicroscopy 2000 (submitted).

[46] R.M.J. Bokel, J. Jansen, H.W. Zandbergen, D. Van Dyck, in: Proc. 14th Int. Congress on Electron Microscopy, Cancun, Mexico, Vol. II, 1998, p. 407.

Nanoscale variation in electric potential at oxide bicrystal and polycrystal interfaces

Bryan D. Huey, Dawn A. Bonnell*

The University of Pennsylvania, Department of Materials Science, Philadelphia, PA 19104, USA

Abstract

Scanning surface potential microscopy (SSPM), has been used to measure spatial variations in grain boundary properties in $SrTiO_3$ and ZnO. Experimental measurements of a Fe-doped $SrTiO_3$ $\Sigma 3$ bicrystal are compared to finite element calculations to quantify the effects of tip geometry and sample-tip separation. Experimental and numerical treatments include realistic tip interactions and lateral inhomogeneity in sample properties. A procedure for extracting actual interface potentials from separation dependence is proposed. Both the sign and magnitude of the grain boundary potential barrier measured with SSPM agree with macroscopic measurements. For experimentally available tips, the effect of tip geometry was found not to contribute to uncertainty. In application to polycrystalline materials, the voltage dependence of individual interface properties has been determined in micropatterned, ZnO-based, polycrystalline varistor devices. © 2000 Elsevier Science B.V. All rights reserved.

1. Introduction

To support continued miniaturization and hybridization of oxide electronic devices, a fundamental understanding of interfacial effects at the nanometer scale is necessary. It is at this spatial scale that potential barriers exist due to charge trapped at interfaces, facilitated by segregation of dopants and impurities [1] as well as the presence of thin amorphous layers [2,3]. Such scales are experimentally difficult to access, and relevant property measurements at oxide interfaces have only been

*Corresponding author. Tel.: +1-215-898-6231; fax: +1-215-573-2128.

E-mail address: bonell@soll.lrsm.upenn.edu (D.A. Bonnell)

achieved using either transmission electron microscopy (TEM) or probe-based measurements. For example, scanning tunneling microscopy (STM) has been used to detect variations in conductivity at polycrystalline ZnO grain boundaries [4], and to measure Schottky barrier formation at the interfaces between TiO_2 and metal clusters [5]. Electrostatic force detection based on atomic force microscopy (AFM) at in situ biased Nb-doped TiO_2 polycrystals observed the voltage dependence of grain boundary potential barriers [6]. Potential variations were quantified using scanning surface potential microscopy (SSPM), in an investigation of ZnO varistor materials also with in situ applied biases [7]. This technique was applied by Nabhan et al. [8] to directly observe potential barriers in acceptor p-type poly-

crystalline silicon. Vandervorst et al. [9] applied a scanning probe tip as a contact voltage probe to detect potential variations in CMOS transistors. For the particular case of $SrTiO_3$ bicrystal interfaces Maier et al. [10,11] have investigated tilt and twist acceptor-doped $SrTiO_3$ bicrystal interfaces at temperatures above 500°C using macroscopic impedance measurements and in situ electrocoloration. Dravid et al. [12] employed holographic phase contrast in TEM to estimate the charge and potential barrier associated with bicrystal grain boundaries, and to observe the disappearance of the barrier with the application of large external biases [13]. However, difficulties in interpretation and sample preparation for in situ TEM studies suggest that probe-based techniques may be better suited for the investigation of samples of interest to the device fabrication community.

Since the scanning techniques of surface potential measurement are new and in situ measurements have only been accomplished recently, careful consideration of tip–sample interactions and resolution limits based on model experiments is required. This paper first compares surface potential measurements of bicrystal interfaces by SSPM with numerical calculations. The spatial variation of the interface potential barrier of well characterized $SrTiO_3$ bicrystals provides the model system. Finally, individual grain boundaries of polycrystalline ZnO-based commercial varistors were investigated under in situ applied fields, allowing determination of the voltage dependence of grain boundary electronic properties and demonstrating the general application of the approach.

2. Experimental details

A bicrystal presents an ideal geometry with which to investigate interactions between a tip and a true sample surface. A 70.6° pure tilt $\Sigma 3$ grain boundary along the {111} plane in acceptor-doped $SrTiO_3$ (4.8×10^{18} Fe atoms/cm^3) was fabricated using the Verneuil method [14]. Macroscopic conductivity and capacitance measurements at elevated temperatures (500–1000°C) yielded average values for the grain boundary potential barrier and depletion width of 300 mV and 400 nm, respectively (the activated

carrier concentration is 2.6×10^{17} charges/cm^3) [15]. The ideal atomic structure of the grain boundary core was measured with high resolution transmission electron microscopy for similar samples (1.3×10^{19} Fe atoms/cm^3 $\Sigma 3$ {111} bicrystals); the interface was found to consist of Sr and O atoms at the boundary plane with perfect mirror symmetry [16]. The bicrystal used herein was polished with diamond impregnated films down to 0.05 μm grit size. To apply local lateral electrostatic fields to the interface, a grid of 400 nm thick, 100 μm diameter Al contacts separated by 350 μm gaps was electron beam evaporated through a shadow mask onto the surface of the bicrystal.

Individual grain boundaries in commercial ZnO-based polycrystalline varistors [17] were isolated using microlithography. Contacts were deposited on these samples using standard lift-off metallization described in detail elsewhere [7]. The measurement is considered in situ because micropatterning allows external lateral biases to be applied at individual grain boundaries during SSPM. Biases were applied with a function generator (Wavetek model 20), and current was monitored with a multimeter (Keithly model 175) connected in series with the sample.

The configuration of local electrostatic potential variation near an interface is described as follows. A two dimensional defect such as a grain boundary can trap charge, and in an oxide the consequence to local field variation extends over a large range due to the magnitude of the dielectric constants. Using traditional semiconductor models, a grain boundary interface charge can be treated as a delta function, with an oppositely charged depletion region extending into the adjacent grains so that charge is conserved. Fig. 1(a), left, depicts a negative grain boundary charge (infinitesimally thin) as well as a positive depletion region (in extinction and using the abrupt junction approximation). Solving Poisson's equation for this charge density distribution yields the equilibrium energy band diagram indicated in Fig. 1(b), left, for a n-type semiconductor. In the event that a positive bias (V) is applied to the right grain while the left grain is grounded, the depletion region lengthens or shortens for the 'reverse' and 'forward' biased grains, respectively. The interface charge can also increase, if empty interface states above the Fermi level are available. The charge distribution for
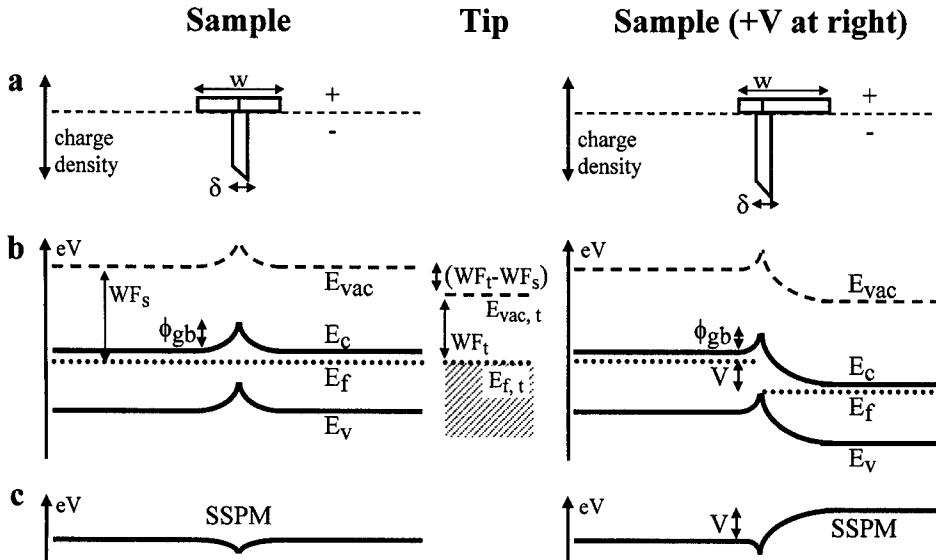
Fig. 1. The relationship between (a) charge density, (b) energy band diagram, and (c) measured surface potential for a grounded npn junction or polycrystalline grain boundary in thermal equilibrium with the SSPM tip (center). The left and right sides, respectively, depict the model without and with an external bias (V) applied to the right side. Parameters include: w=depletion width; δ=thickness of p region ($\rightarrow 0$); ϕ_{gb}=potential barrier height; WF_s and WF_t=work function of sample and tip, respectively; and E_{vac}, E_c, E_f, and E_v=vacuum level, conduction band, Fermi level, and valence bands.

this biased case is shown at the far right of Fig. 1(a), while the right of Fig. 1(b) indicates the modified band diagram for an external applied bias. The potential barrier broadens, becomes asymmetric, and decreases in magnitude.

To measure the voltage dependence of potential barriers, SSPM was employed. SSPM is based on the century old concept of a Kelvin probe [18] or null force probe [19–22]. Sensitivity to the surface potential of a sample is achieved by nulling the capacitive force acting on a biased Permalloy coated AFM tip oscillating above a surface. Using standard intermittent contact AFM, the grounded tip first acquires a trace of the surface topography in the vicinity of a grain boundary intersecting a surface. The tip then retraces the topographic profile, separated from the surface 50–100 nm, thereby maintaining a constant tip-sample separation. During the second scan, a variable DC bias (V_{Null}) is applied to the tip (V_{Tip}) as well as a fixed frequency AC bias ($V_{AC} \cdot \sin(\omega t)$). This leads to a potential difference (ΔV) between tip and an arbitrarily biased sample (V_{Sample}) that includes DC and AC components,

where the work functions of tip and sample (WF) are considered:

$$\Delta V = V_{Tip} - V_{Sample}$$

$$= (V_{Null} - V_{Sample} - (WF_{Tip} - WF_{Sample}))$$

$$+ V_{AC}\sin(\omega t) = V_{DC} + V_{AC}\sin(\omega t)$$

The capacitive force exerted on the tip above the surface is then proportional to the square of ΔV, resulting in three distinct force components (DC, ω, and 2ω), where z is the separation between tip and specimen and C_{Eff} is the total effective capacitance including the tip apex, tip edges, and cantilever surface:

$$F = \frac{1}{2} \cdot \frac{\partial C_{Eff}}{\partial z}$$

$$\cdot \left[\left(V_{DC}^2 + \frac{1}{2} V_{AC}^2 \right) - \frac{1}{2} V_{AC}^2 \cos(2\omega t) \right.$$

$$\left. + 2 V_{DC} V_{AC}\sin(\omega t) \right]$$

The force component acting on the tip (and causing

it to oscillate) at ω will be eliminated (null) when the adjustable tip bias and the sample surface potential are equal ($V_{DC} = 0$), offset by the differences in work function:

$$V_{Null} = V_{Sample} + (WF_{Tip} - WF_{Sample})$$

In this manner, the surface potential at any position of the surface is determined by recording the adjustable tip bias (V_{Null}) that nulls the tip oscillation at ω. Fig. 1(c) depicts the anticipated SSPM profiles for the grounded and biased cases of the grain boundary with negative interface charge considered in Fig. 1(a) and (b). As can be seen, SSPM yields the surface potential, which is the mirror image of the energy band diagram, offset by the tip–sample work function difference. It is important to note that the tip and sample apparent work functions can be affected by surface adsorption. However, assuming that this effect is constant with lateral position, the measured surface potential is offset by a constant and spatial variations are valid.

This simplified description of SSPM does not take into account capacitive interactions between the biased tip and a *heterogeneous* surface potential in the sample. Fig. 2 depicts this case, including six distinct regions of differing surface potential. Following Henning et al. [5], the equation that describes the force acting on the tip at ω for n distinct surface regions is thus revised (where $C_{Eff,i}$, $V_{S,i}$, and $WF_{S,i}$ represent the ith components of capacitance, surface

Fig. 2. Schematic diagram of how a heterogeneous potential distribution on a sample surface contributes to the capacitance measured by a tip. Regions directly below the tip affect a smaller tip area than do surrounding regions, resulting in a non-linear interaction.

potential, and work function for the surface region 'i,' respectively, and $V_{Null,Het}$ is the measured surface potential by the SSPM tip) [23]

$$F_{Tip,\omega} = \frac{\partial C_{Eff}}{\partial z} V_{DC} V_{AC} = V_{AC} \sum_{i=1}^{n} \frac{\partial C_{Eff,i}}{\partial z} V_{DC,i}$$

$$= V_{AC} \sum_{i=1}^{n} \frac{\partial C_{Eff,i}}{\partial z} [V_{Null,Het} - V_{S,i} - (WF_{Tip}$$

$$- WF_{S,i})]$$

Solving for $F = 0$, the analytical solution for the SSPM measured surface potential of a heterogeneous sample ($V_{Null,Het}$) is:

$$V_{Null,Het} = \frac{\sum_{i=1}^{n} \frac{\partial C_{Eff,i}}{\partial z} [V_{S,i} + (WF_{Tip} - WF_{S,i})]}{\sum_{i=1}^{n} \frac{\partial C_{Eff,i}}{\partial z}}$$

These relations are used in the comparison of experimental results and numerical calculations.

3. Results and discussion

The topographic structure of the $\Sigma 3$ SrTiO$_3$ grain boundary is shown in Fig. 3(a), where only polishing damage is visible. Fig. 3(b) reveals a variation in the surface potential measured with a tip height of 80 nm that takes the form of a ridge of raised surface potential. The contrast variation is more visible in Fig. 3(c). The average height of this feature is 25 mV (95% confidence is ±9 mV), and the depletion width is 2770±40 nm. It is noteworthy that the grain boundary is not visible in the topography; the position was confirmed ex situ by electron backscattering (EBSP) in a scanning electron microscope (SEM) [24]. Note that the feature clearly varies with position, ranging from 11 to 39 mV in height and 2.150–3.520 μm in width (in excess of the experimental energy noise of 5 mV). Furthermore, the 'apparent' interface potential and depletion width depend on the height at which the image was obtained. Table 1 summarizes 'apparent' properties at several heights.

The presence of increased surface potential at the grain boundary position can only result from a depression in the corresponding band diagram, the
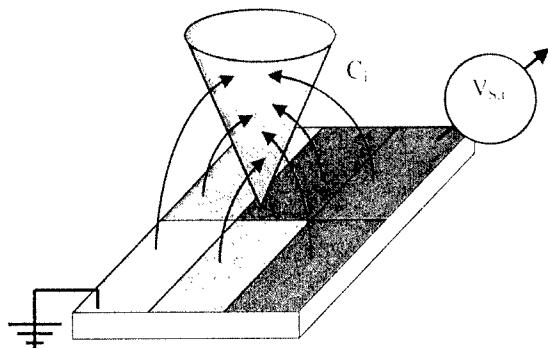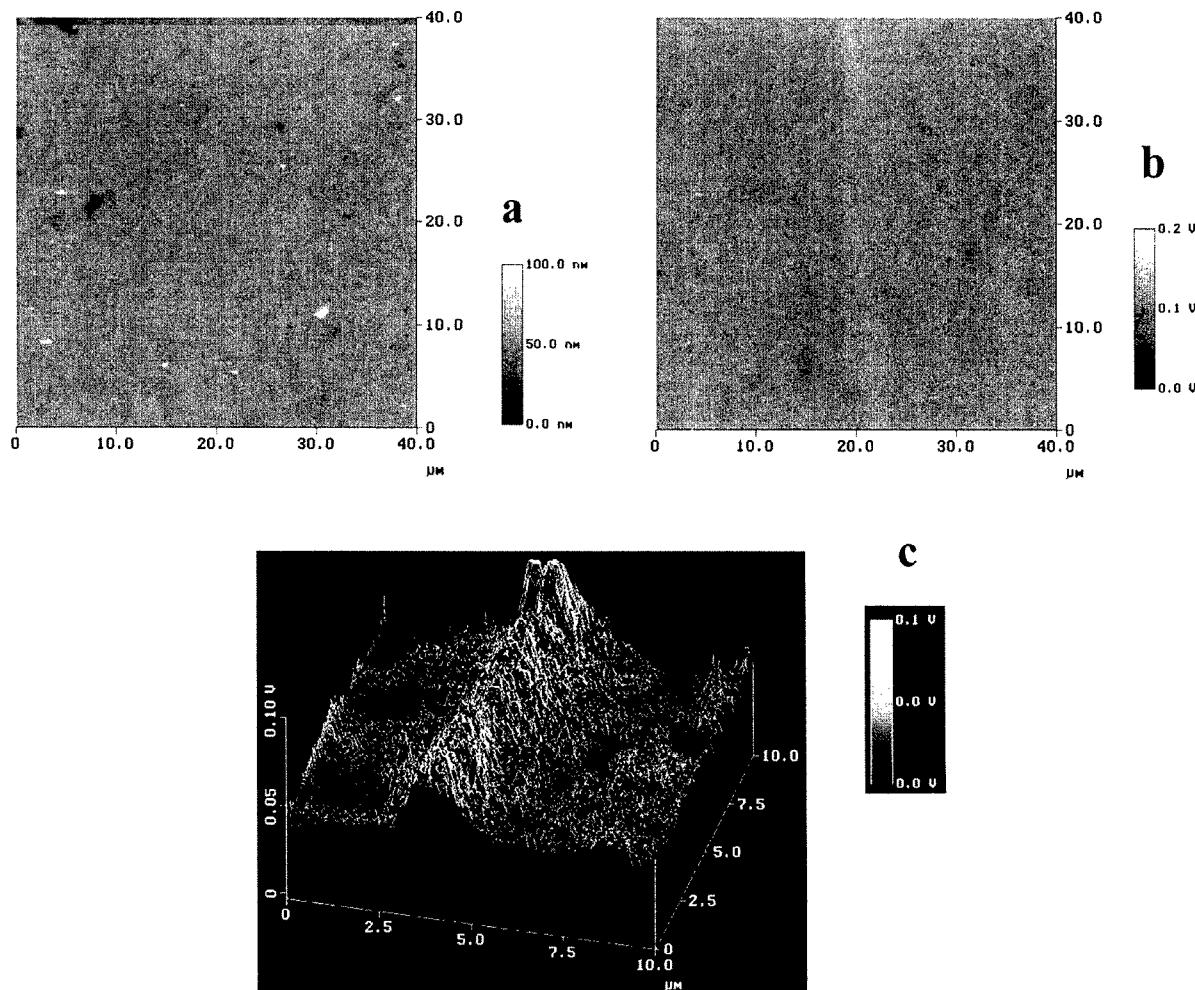
Fig. 3. Topographic structure (a) and surface potential in plan view (b) and 3-D rendering (c) of a SrTiO$_3$ Σ3 grain boundary.

Table 1
Dependence of apparent properties on tip height

Apparent property	$z = 60$ nm	$z = 80$ nm	$z = 100$ nm
Interface potential (mV)	46±5	25±9	17±2
Depletion width (nm)	1770±170	2770±40	3240±30

inverse of Fig. 1(c), as expected for an acceptor-doped material. A potential trough indicative of positive interface charge impedes current flow, because positive charge carriers dominate conduction for the bicrystal in contrast to the n-type varistors. The 'apparent' interface potential is of the same sign but is approximately one order of magnitude lower

than the macroscopically derived potential barrier properties [10]. This discrepancy may be due to interactions between the surface and the entire tip, mediation of the SSPM results by the presence of surface charge, or attenuation of electrostatic fields away from the surface complicated by the heterogeneous potential distribution at the grain boundary. In an effort to quantify these effects, two-dimensional finite element calculations [25] discretely solving Poisson's equation for the experimental tip/sample geometry are compared.

Fig. 4(a) and (b) depict the model used in the simulation, including a tip with a 50 nm radius of curvature, a tip length of 12.5 μm, a tip half angle of
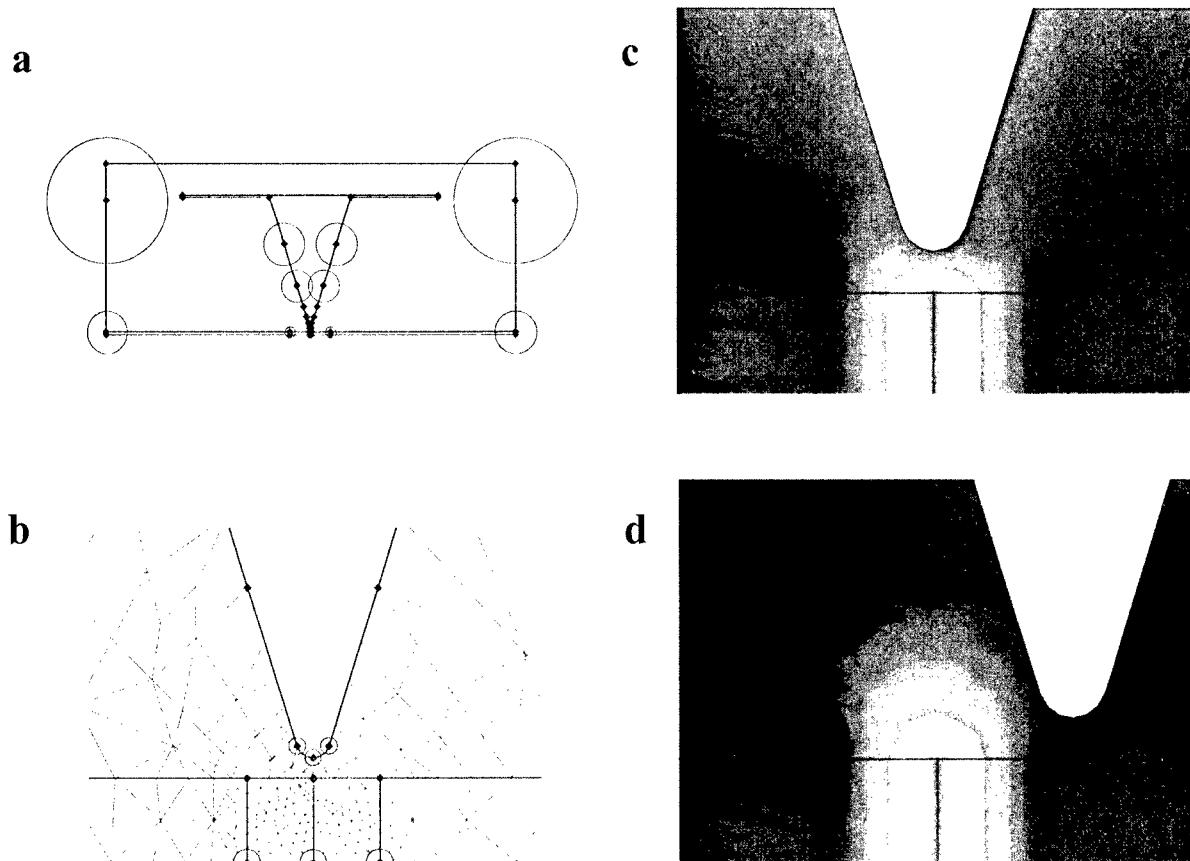
Fig. 4. Two dimensional finite element calculations of a charged grain boundary intersecting a surface. The model includes tip (length = 12.5 μm, half angle = 17.5°) and cantilever width = 25 μm. (a) The details in the tip region (b) show the interface which has a charge of $+1 \times 10^{13}$ e/cm^2, and adjacent depletion regions with -2.6×10^{17} e/cm^3. Solutions for the electric potential with the tip over the interface (c) and displaced laterally (d) are compared.

17.5°, a cantilever width of 25 μm, a tip–sample separation of 60 nm, and a grain boundary with the macroscopic potential barrier oriented perpendicular to the surface. Boundary conditions include a positive interface charge of $+1.0 \times 10^{13}$ charges/cm^2 for the centered grain boundary, a potential barrier of 300 mV, and symmetric, negatively charged depletion regions extending 200 nm into each of the adjacent grains with an ionized acceptor concentration of -2.6×10^{17} charges/cm^3. The number of nodes at which Poisson's equation is discretely solved is 485, where at least 25 nodes are always present between the tip apex and the sample (the simulation mesh is indicated in Fig. 4(b), a close-up of Fig. 4(a)). Fig. 4(c) shows the simulation in the vicinity of the tip

lifted directly above the grain boundary, in which the contrast represents the potential distribution ranging between 0 and 300 mV (darkest to lightest). A parabolic potential barrier exists at the interface as anticipated. The tip experiences a net null force in the simulation following the procedure of Jacobs et al. [26]. By repeating calculations with the tip at successively larger lateral displacements from the grain boundary, as exemplified in Fig. 4(d), a potential barrier profile simulating the SSPM experiment is obtained. Fig. 5 depicts the calculations for the experimental tip geometry, as well as a SSPM measured surface potential profile extracted from a potential image acquired 60 nm above the surface. Note that the calculated potential maximum agrees
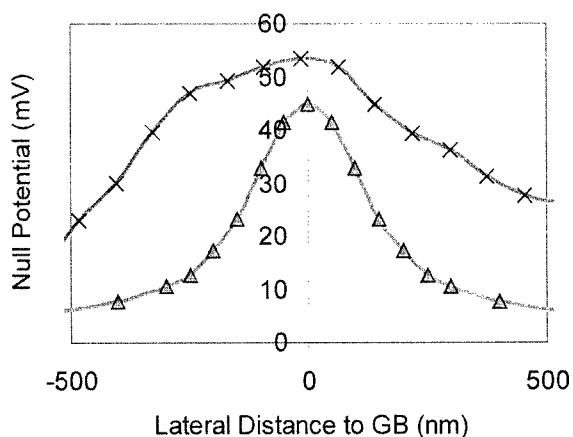
Fig. 5. Comparison of experimental (cross hatches) and calculated (triangles) potential profiles at 60 nm above the surface. The average experimentally measured potential maximum was 46±5 mV.

with the average measured value, 46 mV, although the particular profile compared in the figure is in the upper range of the experimental distribution.

Of course electric fields decay with distance from the surface so the measured valued depends on the height at which it was obtained. To extract the actual value at the surface, the distance dependence of results from the numerical calculations is parameterized, thus accounting for the inhomogeneous surface potential and realistic tip dimensions. The ideal relation, i.e. that from the calculations, can be described as:

$$\Phi_z = \Phi_0 \exp[Bz^C]$$

where Φ_z is the potential measured at some height z, Φ_0 is the potential at the interface, B and C are constants that characterize the complex sample–tip interaction, equal -0.47 ± 0.01 and 0.345 ± 0.005, respectively. Using this functional form to determine the interface potential from the measurements yields 260 ± 10 mV, in good agreement with macroscopic measurements.

The 'apparent' depletion depth measured with SSPM is larger than expected from macroscopic transport measurements. Tip geometry is an obvious and well known factor in spatial resolution degradation in scanning probe microscopies. To quantify

this effect, numerical calculations with models similar to that in Fig. 4 were done for the most 'ideal' shapes available as conducting tips [27]. These calculations showed a negligible dependence of the potential barrier height on tip geometry at heights in the range of 60–100 nm; differences of 10–20% in apparent feature width might be determined for tips with radii of curvature between 25 nm up to an upper limit of 200 nm. A procedure for extracting the actual value from the measurements has not yet been developed.

The remaining differences between properties determined from macroscopic transport studies and local probe measurements may be related to sample conditions. It is known that oxide surfaces adsorb atmospheric molecules that alter the surface charge [28]. The presence of surface charge might dampen or heighten lateral potential variations. Preliminary simulations accounting for surface charge and associated surface band bending suggest this effect is negligible. It is also possible that the interface intersects the surface at an angle that deviates from 90°. Relative misorientation determined by EBS is less than ±5° and would not account for significant variations in depletion width. Finally, the bicrystal grain boundary may not be as perfect macroscopically as suggested by TEM. Amorphous interfacial films, facets, and pores are likely to exist along the boundary. This possibility is supported by recent near field optical studies on similar bicrystals and thin films [29].

With this insight, polycrystalline materials can be quantified from several perspectives. Fig. 6(a) and (b) compare the topography and surface potential of the ZnO varistor when leads just to the left and right of the imaged region are grounded. Again, a grain boundary is not apparent in the topographic structure. Two regions of depressed surface potential exist in Fig. 6(b) (≈ 70 mV), resulting from the presence of second phases with a larger apparent work function than that of the surrounding grains (including the mediation of the sample work function by surface adsorbates). These regions have been confirmed to be Bi and Ti rich second phases by energy dispersive spectroscopy in SEM [7]. Fig. 6(c) and (d) depict the surface potential distribution when a bias of ±1 V is externally applied to the left contact, respectively, causing current flow through the var-
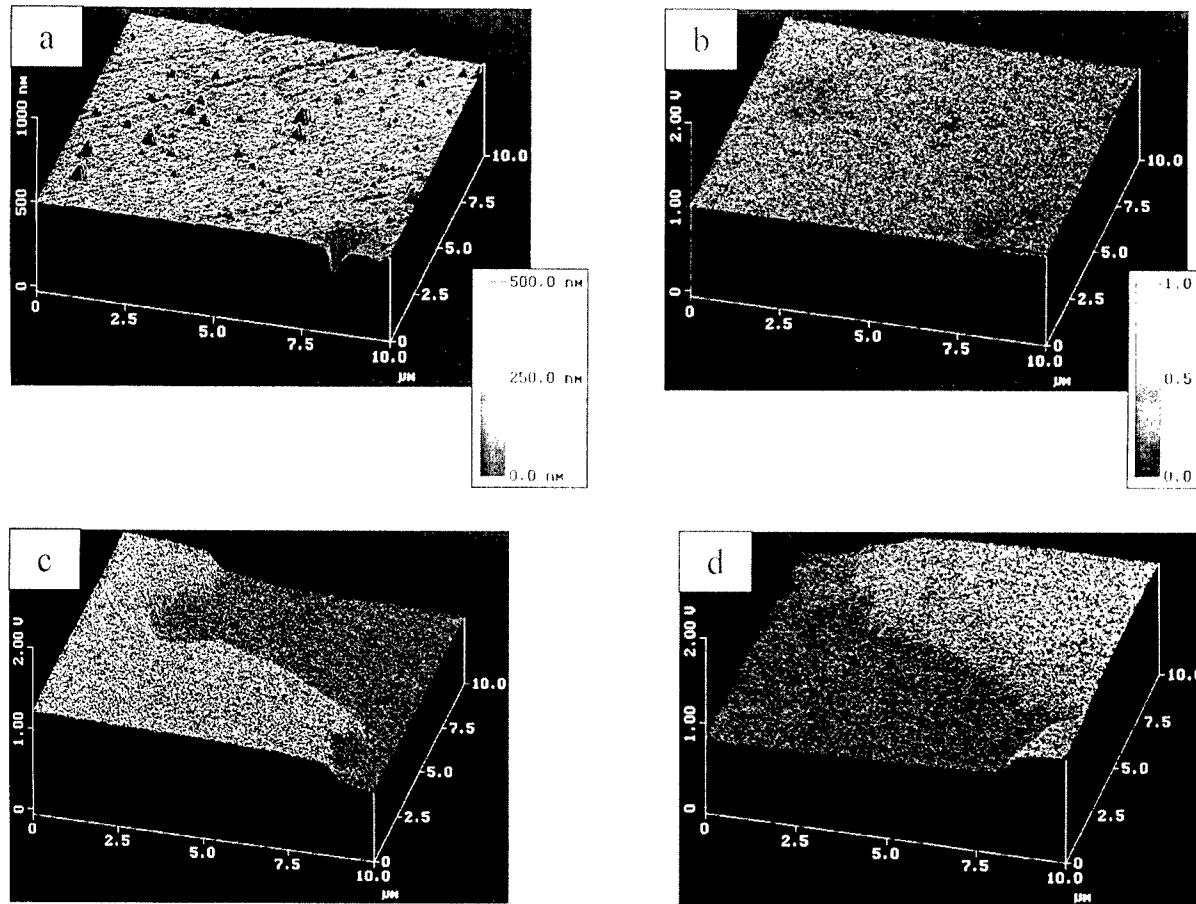
Fig. 6. Topographic structure (a) and surface potential of unbiased region of a polycrystalline ZnO surface. Surface potential variation at a grain boundary with laterally applied (c) forward and (d) reverse bias (± 1.00 V applied approximately 30 μm to the left and right).

istor during this in situ SSPM experiment. The sharp, irregular contrast step in the center of these surface potential images represents a highly resistive feature, resulting from the presence of a potential barrier containing grain boundary. The height of the potential step is approximately 190 mV, although it varies as a function of position (220–160 mV from top to bottom of the 10 μm grain boundary). The potential step also inverts when the polarity of the external bias is reversed, as expected, except at the 2nd phases where the electrically active interface switches from one side to the other of the impurity region. Reanalyzing Fig. 6(b), an average step of 7

mV exists along the entire grain boundary correlating to the difference in relative effective work functions of the adjacent grains.

Extracting surface potential profiles at a given position for a series of external biases, and knowing the current flowing through the device during the in situ SSPM measurements, the voltage dependence of the potential barrier can be determined. Current is assumed to flow by thermionic emission over the potential barrier (E_F refers to the Fermi energy with respect to the conduction band minimum; k is Boltzman's constant; T is room temperature; I/Area is the measured current density flowing through the

leads during the in situ experiment (the cross sectional area is taken from the microfabricated contact dimensions); and V_{app} is the bias dropping at the grain boundary measured directly from SSPM profiles):

$$\phi_{gb}(V) = -E_F - kT$$
$$\cdot \ln\left[\frac{1}{AT^2} \cdot \frac{I/\text{Area}}{1 - \exp\left(-\dfrac{V_{app}}{kT}\right)}\right]$$

Fig. 7 presents the voltage dependence of the individual potential barrier from Fig. 6 and compares results from the local and macroscopic measurements. The two curves for the local properties represent upper and lower bounds for the actual potential barrier directly beneath the tip. Specifically, the lower bound is obtained by assuming all measured current flows through (over) the potential barrier directly beneath the tip. The upper bound is determined assuming that a purely resistive current path exists somewhere between the contacts in parallel with the studied potential barrier. This constant shunting resistor is defined by the resistance between the leads at zero applied bias. For either limiting case, the local properties of the single

boundary differ substantially from the macroscopic, average response.

4. Conclusion

A correlation of scanning probe-based measurements of surface potential and actual local properties has been made for the case of a charged interface intersecting a surface. The potential barrier of an acceptor-doped, $SrTiO_3$ $\Sigma 3$ bicrystal grain boundary is found to correspond to a positively charged interface and a negative depletion charge. There is an intrinsic experimental problem with measurement at the surface so the actual properties must be extracted from measurements above the surface. Analytical solutions of simple geometries would not provide the correct relation between the experiment and properties because the tip–sample interactions are complex due to tip geometry and sample inhomogeneity. This model system allowed characterization of realistic tip–sample interactions and lateral sample inhomogeneity by two dimensional finite element analysis. A relation that was determined numerically was applied to experimental measurements to extract actual local properties. Extending SSPM to study grain boundaries of micropatterned polycrystalline ZnO varistors, the voltage dependence of individual interfaces has been measured in situ. There is a significant difference between the macroscopically derived barrier response and the voltage dependence of the individual grain boundary.
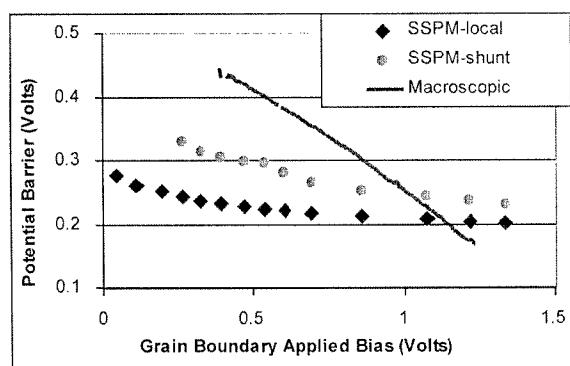
Fig. 7. SSPM derived local voltage dependence of individual grain boundary potential barrier in Fig. 6 compared to the macroscopic properties that average over hundreds of grain boundaries. The two curves for the local data represent the upper and lower limits due to assumptions regarding the current path.

References

[1] T.K. Gupta, Microstructural engineering through donor and acceptor doping in the grain and grain-boundary of a polycrystalline semiconducting ceramic, J. Mater. Res. 7 (12) (1992) 3280.

[2] E. Olsson, G.L. Dunlop, R. Osterlund, Development of interfacial microstructure during cooling of a ZnO varistor material, J. Appl. Phys. 66 (v. 15) (1989) 5072–5077.

[3] H.F. Wang, Y.M. Chiang, Thermodynamic stability of intergranular amorphous films in bismuth-doped zinc oxide, J. Am. Ceram. Soc. 81 (1) (1998) 89.

[4] D. Bonnell, I. Solomon, Measurement of space charge adjacent to oxide grain boundaries by tunneling spectroscopy, Ultramicroscopy 42–44 (1992) 788–792.

[5] D.L. Carroll, M. Wagner, M. Ruhle, D.A. Bonnell, Schottky barrier formation at nanoscale metal-oxide interfaces, Phys. Rev. B 55 (15) (1997) 9792–9799.

[6] D.A. Bonnell, B.D. Huey, D.L. Carroll, In situ measurement of electric fields at individual grain boundaries in TiO_2, Solid State Ionics (1995).

[7] B.D. Huey, D. Lisjak, D.A. Bonnell, Nanometer scale variations in interface potential by scanning probe microscopy, J. Am. Ceram. Soc. (1999) accepted.

[8] W. Nabhan, B. Equer, A. Broniatowski, G. DeRosny, A high-resolution scanning Kelvin probe microscope for contact potential measurements on the 100 nm scale, Rev. Sci. Instr. 68 (8) (1997) 3108.

[9] T. Trenkler, P. De Wolf, W. Vandervorst, Nanopotentiometry: local potential measurements in complementary metal-oxide-semiconductor transistors using atomic force microscopy, J. Vac. Sci. Technol. V 16 (1) (1998) 367–371.

[10] I. Denk, J. Claus, J. Maier, Electrochemical investigations of $SrTiO_3$ boundaries, J. Electrochem. Soc. 144 (10) (1997) 3526–3536.

[11] I. Denk, F. Noll, J. Maier, In situ profiles of oxygen diffusion in $SrTiO_3$: Bulk behavior and boundary effects, J. Am. Ceram. Soc. 80 (2) (1997) 279–285.

[12] V. Ravikumar, R.P. Rodrigues, V.P. Dravid, An investigation of acceptor-doped grain boundaries in $SrTiO_3$, J. Phys. D: Appl. Phys. 29 (1996) 1799–1806.

[13] K.D. Johnson, V. Dravid, Grain boundary barrier breakdown in niobium donor-doped strontium titanate using in situ electron holography, Appl. Phys. Lett. 74 (4) (1999) 621–623.

[14] Frank & Schulte Gmbh, Essen, Germany.

[15] M. Leonhardt, Personal Communication, 1998.

[16] O. Kienzle, F. Ernst, Effect of shear stress on the atomistic structure of a grain boundary in strontium titanate, J. Am. Ceram. Soc. 80 (7) (1997) 1639–1644.

[17] Harris Semiconductor, type V24RA22.

[18] J. Janata, 100th anniversary of the Kelvin probe. AVSNewsletter, 1997(May/June): p. 4–5.

[19] M. Nonnenmacher, M.P. O'Boyle, H.K. Wickramasinghe, Kelvin probe force microscopy, Appl. Phys. Lett. 58 (25) (1991) 2921–2923.

[20] M. Nonnenmacher, M. Oboyle, H.K. Wickramasinghe, Surface investigations with a Kelvin probe force microscope, Ultramicroscopy 42 (1992) 268.

[21] H.O. Jacobs, H.F. Knapp, S. Muller, A. Stemmer, Surface potential mapping: a qualitative material contrast in SPM, Ultramicroscopy 69 (1997) 39–49.

[22] J.M.R. Weaver, D.W. Abraham, High resolution AFM potentiometry, J. Vac. Sci. Technol. B 9 (3) (1991) 1559–1561.

[23] A.K. Henning, T. Hochwitz, Scanning probe microscopy for 2-D semiconductor dopant profiling and device failure analysis, Mater. Sci. Eng. B – Solid State M 42 (1–3) (1996) 88.

[24] EBSP patterns collected in JEOL 6400 SEM using a Merlin LTC216-F40E low light camera, a custom Camera Designs Ltd. CCU-1852C camera control unit, and a Hamamatsu Argus 10 image processor.

[25] QuickField v. 4.1, Tera Analysis.

[26] H.O. Jacobs, P. Leuchtmann, O.J. Homan, A. Stemmer, Resolution and contrast in Kelvin probe force microscopy, J. Appl. Phys. D 84 (3) (1998) 1168–1173.

[27] G.D. Skidmore, E.D. Dahlberg, Improved spatial resolution in magnetic force microscopy, Appl. Phys. Lett. 71 (22) (1997) 3293–3295.

[28] D.A. Bonnell, Atomic structure of transition metal oxide surfaces from scanning tunneling microscopy, Progr. Surf. Sci. 57 (1998) 187–252.

[29] B.D. Huey, D.A. Bonnell, to be published.

[30] J.W.P. Hsu, E.B. McDaniel, R.A. Rao, C.B. Eom, Mater. Res. Soc. 474 (1997) 91–98.

Self-assembling nanostructures and atomic layer precise etching in molecular beam epitaxy

K. Eberl*, M.K. Zundel, H. Schuler

Max-Planck-Institut für Festkörperforschung, Heisenbergstrasse 1, 70569 Stuttgart, Germany

Abstract

We report on the preparation of 10 nm lateral size semiconductor structures based on island formation in strained layer growth in molecular beam epitaxy. Red light emitting InP quantum dot injection lasers are presented. They contain densely stacked layers of self-assembled InP quantum dots embedded in a $Ga_{0.51}In_{0.49}P$ wave guide layer. In the second part of this contribution we report on a new atomic layer precise etching technique in MBE, which allows improved interface control for the preparation of semiconductor nanostructures. The etching process involves $AsBr_3$ exposure of a GaAs or AlGaAs surface. Switching between atomic layer precise growth and etching is possible within a few seconds. © 2000 Elsevier Science B.V. All rights reserved.

Keywords: Molecular beam epitaxy; P-compounds; Self assembling quantum dots; Laser diodes; In-situ etching; Surface patterning; V-groove; MBE regrowth

PACS: 81.15.Hi; 78.66.Fd; 85.30.Vw; 42.55.Px

1. Introduction

Molecular beam epitaxy (MBE) allows atomic layer precise layer thickness control in semiconductor thin film deposition. Thin epitaxial layers are prepared by MBE for fast transistors and laser diodes in industrial production systems. The synthesis of lateral nanostructures is more difficult and generally involves lithography and etching in semiconductor technology which faces problems like limited res-

olution and defect introduction at the sidewalls due to reactive ion etching.

Extremely small 10 nm size quantum dots (QD) turned just recently out to be relatively easy to prepare by applying Stranski–Krastanow growth mode in strained layer heteroepitaxy [1]. Interesting applications for self-assembled QD in different material systems are light-emitting diodes and semiconductor laser diodes. Optoelectronic devices with QD on Si substrate are interesting due to the strong lateral localization of carriers in the active medium and the resulting reduced sensitivity to non-radiative recombination in threading dislocations, which are generally formed by growth of strain relaxed GaAs on Si substrate. Gerárd et al. reported about self

---

*Corresponding author. Tel.: + 49-711-689-1312; fax: + 49-711-689-1010.

E-mail address: eberl@servix.mpi-stuttgart.mpg.de (K. Eberl)

assembled InAs dots in thick GaAs layers grown on Si which show improved photoluminescence (PL) as compared to layers with quantum wells [2]. For semiconductor lasers containing QD a lower threshold current density, a higher characteristic temperature, and an increased gain and differential gain in comparison with quantum well lasers were theoretically predicted [3,4] due to the discrete energy levels in zero-dimensional systems. For InAs [5] and $In_xGa_{1-x}As$ [6,7] dots in GaAs, and $In_xAl_{1-x}As$ in $Al_yGa_{1-y}As$ [8], injection lasers have been successfully demonstrated and show some of the characteristic properties which have been predicted.

Another currently more and more intensively investigated field is in-situ surface treatment. In the second part of this contribution we report about atomic layer precise etching in MBE with $AsBr_3$ as the etching species. Selective etching of SiO_2 masked GaAs (100) substrates allows in-situ preparation of extremely sharp V-grooves with almost perfectly planar {110} side facets. This new technique may become important in future for the preparation of monolithically integrated devices which involve two epitaxial growth steps with extensive processing in between.

2. Self assembling InP quantum dots

$Ga_{0.52}In_{0.48}P$ is lattice matched to GaAs substrate and has a direct band gap at 1.95 eV at 4 K. The lattice mismatch between InP and $Ga_{0.52}In_{0.48}P$ is 3.7%. The deposition of InP on a $Ga_{0.52}In_{0.48}P$ layer results in island formation after exceeding 1.5 monolayers. The size of the InP islands is about 15 nm in diameter and 2–3 nm in height after deposition of three monolayers of InP. The density is about 5 × 10^{10} cm^2 as shown in the atomic force micrograph in Fig. 1 [12]. These InP islands form almost ideal quantum dots because of their extremely small size and because they can be fully embedded in the barrier material $Ga_{0.52}In_{0.48}P$ by MBE overgrowth. Vertical stacking of layers with InP islands results in a strong correlation of the islands due to strain fields. The InP islands in the second and third layer tend to nucleate preferentially right above the underlayer islands if the spacer layer is thinner than the extension of the strain field [1].

A cross-sectional transmission electron micrograph (TEM) of the QD laser structure is shown in Fig. 2. The growth and fabrication details are presented elsewhere [9]. The InP dots appear as dark
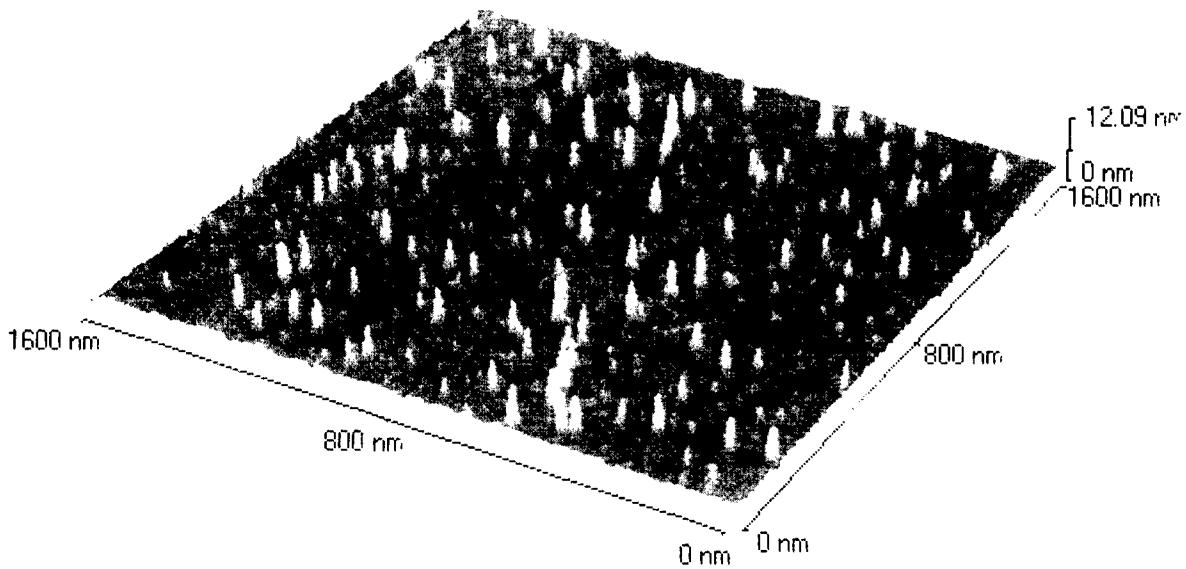

Fig. 1. Atomic force micrograph from the surface of three monolayers of InP deposited onto a GaInP buffer layer on GaAs substrate. The InP forms extremely small islands.
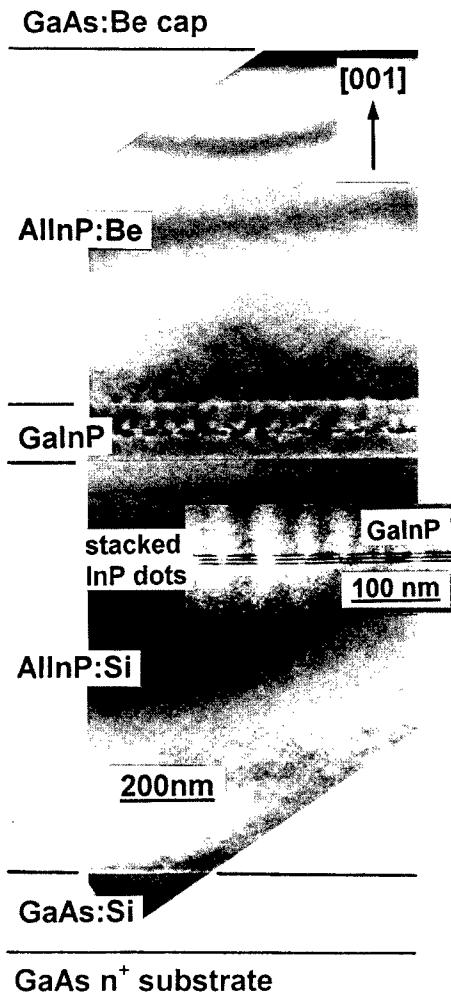
Fig. 2. Overview cross-sectional TEM micrograph of a InP quantum dot laser structure containing a 3-fold stack of InP dots embedded in the GaInP wave guide layer. The wave guide is surrounded by doped $Al_{0.53}In_{0.47}P$ cladding layers.

contrast. The 0.9 μm thick p- and n-type doped AlInP cladding layers are surrounding the $Ga_{0.52}In_{0.48}P$ wave guide layer which contains the 3-fold stack of InP dots [1,9]. Under pulsed operation we obtain the typical output power versus injection current density characteristic at 150 K which is shown in Fig. 3. Thereby the threshold current density is 265 A/cm². The inset shows the electroluminescence (EL) spectrum below threshold multiplied by 250. The energy position is at 1.741 eV

with a FWHM of 23 meV which is in good agreement with PL measurements at 150 K (not shown here). The spectrum above threshold demonstrates a typical narrowed laser line at 1.748 eV indicating ground state QD lasing, since excited states and wetting layer luminescence is observed at higher energies of 1.80 and 1.89 eV, respectively.

Fig. 4 presents the temperature dependence of the threshold current density of three QD laser diodes with different dot sizes. With increasing dot size from nominally deposited 2.8–3.2 ML InP we obtain decreasing threshold current densities, as expected for the stronger energetic confinement of larger dots in GaInP barriers. For the sample with 3.2 ML InP dots we found a temperature independent threshold below 120 K as predicted for quantum dot lasers [3]. Above 120 K an increase is found due to thermal activated carrier evaporation out of the dots into barrier states. To achieve lasing at higher temperatures the carrier confinement has to be increased on the one hand by larger dots and on the other hand by higher barriers. The dot size reaches a limit at 3.2 ML InP due to nucleation of dislocations in the case of a stack of three or more dot layers. Thus, the more promising way is to use higher barriers, e.g. the quarternary AlGaInP or alternatively quasi-quarternary short-period superlattices (qqSL). First results from InP quantum dots in AlGaInP are presented in Ref. [10]. PL measurements on samples containing a 3-fold InP dot stack and qqSL as barriers showed one order of magnitude improvement in PL intensity at room temperature with respect to test-samples with GaInP barriers [11].

3. Atomic layer precise etching in MBE

Recently, intensity oscillations in reflection high energy electron diffraction (RHEED) have been observed during in-situ etching of GaAs using iodine [13,14], $AsCl_3$ [15–18], $AsBr_3$ [19–21] and tris-dimethylaminoarsenic (TDMAAs) [22–27]. PCl_3 was used by Tsang et al. [28] and Gentner et al. [29] for the etching of InP in CBE. The in-situ etching under optimized conditions occurs via a layer-by-layer mechanism analogous to the reverse process of MBE growth and thus provides control on the atomic scale. The combination of in-situ etching and MBE-
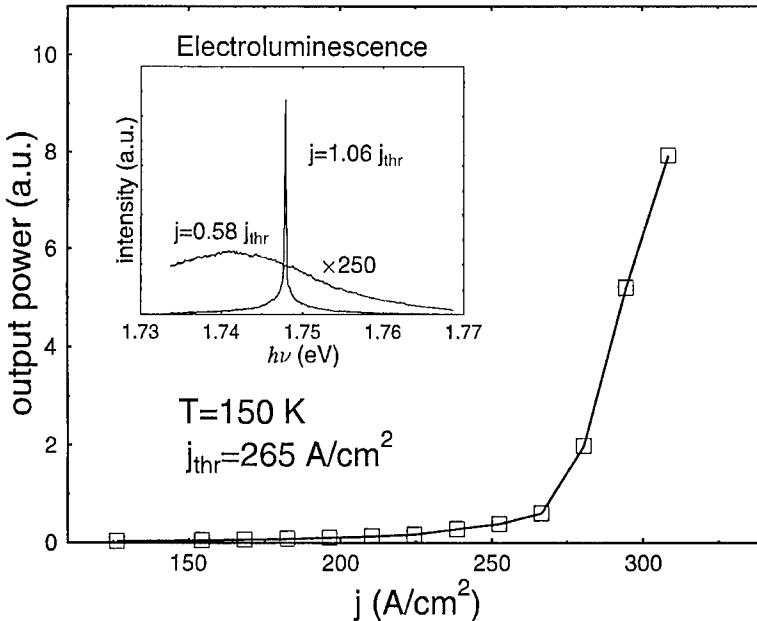
Fig. 3. Output power of the InP quantum dot laser diode versus injection current density under pulsed conditions at 150 K. The inset shows EL spectra below and above threshold current density $j_{thr} = 265$ A/cm^2 at 150 K.

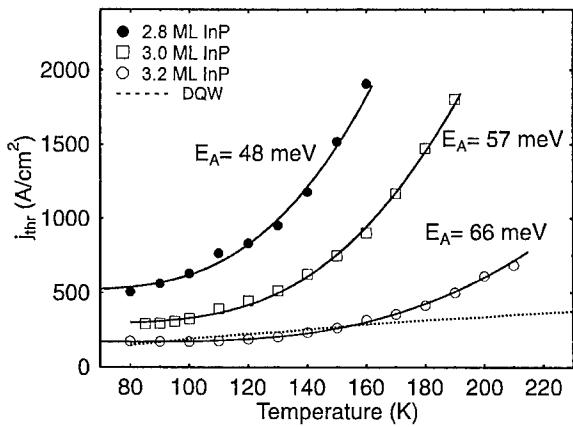Fig. 4. Threshold current density j_{thr} versus temperature T for dot laser samples A (2.8 ML InP dots), B (3.0 ML), and C (3.2 ML) and for a GaInP/AlGaInP double quantum well laser diode as.

growth within the same MBE chamber offers considerable potential for fabricating low dimensional structures and novel devices.

We use AsBr$_3$ for the etching within a solid source MBE growth chamber, because the Br has a lower electron affinity than F and Cl and therefore less chemical reactivity against MBE equipment. AsBr$_3$

provides also arsenic over-pressure which helps to stabilize the GaAs surface even without additional As flux from a separate As source. It is available in high purity (6 N) and requires no precracking and no carrier gas. AsBr$_3$ is less critical to handle, since the melting point ($T_m = 32.8°C$) is above room temperature and the source material is kept below the melting point during etching.

In the following we describe the etching process and report selective in-situ etching of SiO$_2$ masked GaAs (100) substrates and MBE regrowth. Optimum conditions for thick layer GaAs etching and etching rates for GaAs/AlGaAs heterostructures and substrate orientations as a function of substrate temperature have been reported earlier [20,30].

The experiments are carried out in a modified conventional solid source MBE system with a gas manifold for AsBr$_3$ (6 N) to be introduced without carrier gas. A schematic illustration of the system set-up and a detailed description of the etching conditions are provided in Ref. [20]. Fig. 5 illustrates the etching mechanism. AsBr$_3$ molecules impinge on the surface with a beam equivalent pressure of about 2×10^{-6} mbar for a typical GaAs etching rate of 0.1 nm/s. After surface migration of adsorbed AsBr$_x$
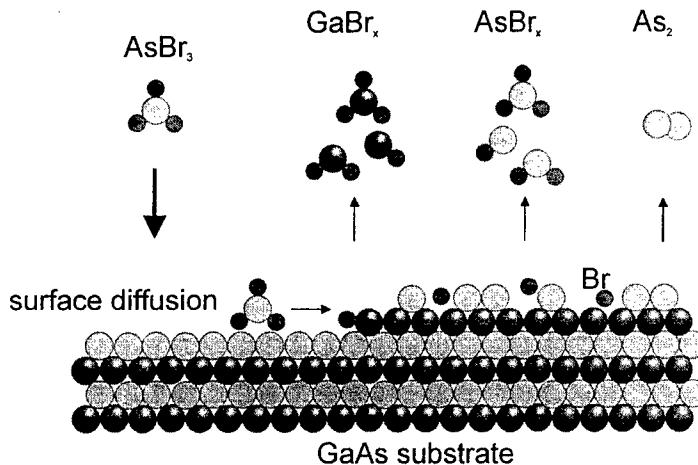
AsBr₃ etching mechanism

Fig. 5. Schematic illustration of the AsBr₃ etching mechanism of the GaAs surface.

and/or Br_x molecules $GaBr_x$ molecules are formed due to their higher binding energy compared to $AsBr_x$. The etching process is performed by $GaBr_x$ desorption from the GaAs surface. Some $AsBr_x$ molecules as well as excess As may also be desorbed. Zhang et al. [31] studied the reaction mechanism by modulated beam mass spectroscopy and found that GaBr is the main etching product. Their results indicate, that the etching rate limiting step is the formation or desorption of GaBr and not the decomposition of $AsBr_3$. Significant undercut of the SiO_2 mask in selective etching experiments discussed later in Fig. 7 indicate that surface migration of $AsBr_x$ and/or Br_x molecules is in the order of several 100 nm at temperatures above 600°C.

Fig. 6 shows RHEED intensity oscillations during GaAs growth and etching. Within the time range marked as 'AsBr₃ etching' AsBr₃ molecules are supplied in addition to the Ga and As₄ fluxes for GaAs growth. That means, growth and etching are performed at the same time such that the net growth rate is reduced from about 0.7 monolayers (ML)/s to about 0.47 ML/s as indicated in the power spectrum shown in the inset of Fig. 6. The well separated sharp peaks for growth and growth plus etching indicate fast switching and quite constant etching rate within a few seconds after the AsBr₃ flux is

Fig. 6. RHEED intensity oscillations during growth and etching of GaAs (100). The substrate temperature was $T_s = 600°C$. During the period where AsBr₃ molecules are supplied in addition to the Ga and As₄ flux the growth rate is reduced as shown by the extended periodicity. This is quantitatively depicted in the Fourier transform spectra in the inset. The well separated sharp peaks for growth and growth plus etching indicate fast switching and constant etching as soon as the AsBr₃ flux is initiated and terminated.

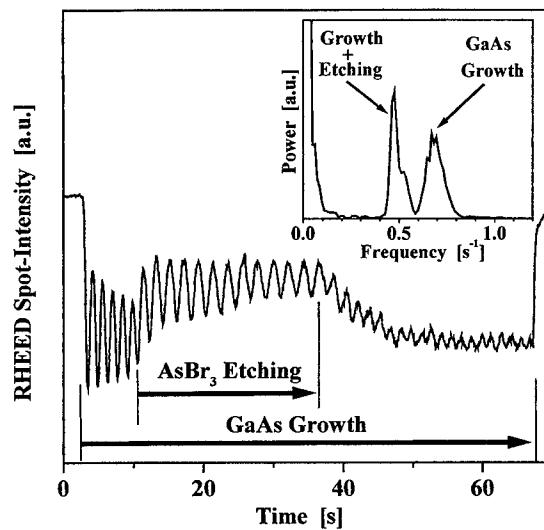initiated. The results in Fig. 6 together with earlier RHEED studies presented in Ref. [21] demonstrate the possibility of this technique to switch between growth and etching and vice versa within seconds. The continuous reduction of the period length after the region from growth plus etching to nominally pure growth in Fig. 6 indicates that it takes about 5–10 s before the etching is reduced down to detectable limits. It turns out that it takes a few seconds to pump away all the $AsBr_3$ which is left in the injector and the chamber to finally stop the etching process.

A possible application of this etching technique

combined with epitaxial growth is to use the pronounced anisotropy of the process for in-situ surface patterning. Gentner et al. demonstrated the successful preparation of buried layer laser diodes applying PCl_3 etching and epitaxial regrowth [29]. The combination of planar facet etching and regrowth in a clean environment may also allow to realize quantum wires with improved width fluctuations by regrowth into sharp V-grooves. Fig. 7 shows a schematic illustration and scanning electron microscopy (SEM) images of selective etching of SiO_2 stripe masked GaAs (100) substrates. The stripes are oriented in the [010] direction. At low temperatures
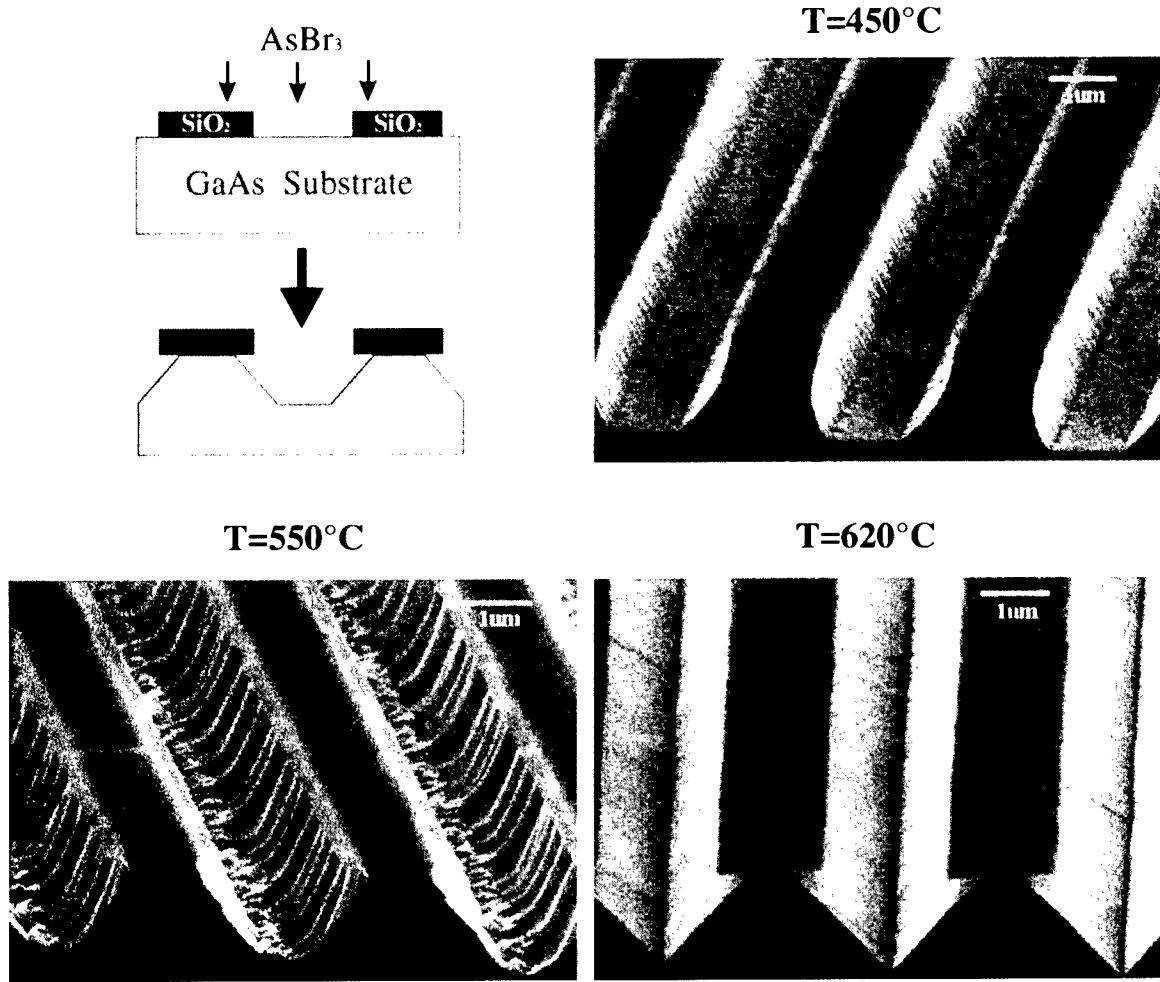

Fig. 7. Schematic illustration and SEM images of selective etching of SiO_2 stripe masked GaAs (100) substrate at different substrate temperatures. The stripes are oriented in the [010] direction. At $T_s = 620°C$ very flat {110} side facets with a sharp V-groove are produced.

of $T_s = 450°C$ there is hardly any under-etching of the SiO_2 mask and the sidewalls are {010} facets in the upper area. Towards the flat (100) bottom still relatively steep higher index facets appear. The etching depth is about 1 μm in all cases shown in Fig. 7. For $T_s = 550°C$ a clear undercut of the SiO_2 mask is observable and the shape of the groove develops already a rough V-like shape. At $T_s = 620°C$ very flat {110} 45° side facets and a sharp V-groove is achieved. The increased diffusion length of $AsBr_x$ and/or Br_x molecules causes enhanced under-etching of the mask. The GaAs edge underneath the SiO_2 mask is very sharp which is clearly seen after removing the SiO_2 mask. This is not the case for $T_s = 550°C$.

For higher substrate temperatures the {110} planes are obviously almost perfectly planarized during the etching process. The {110} planes etch slower than the other facets. This is also observed for SiO_2 mask orientation along the [01-1] direction where we observe very flat 90° facets which are again {110} planes [32].

4. Conclusions

It was demonstrated that island formation in strained layer heteroepitaxy allows the preparation of 10 nm size lateral structures without lithography in MBE. This concept is applied for quantum dot laser diodes. Lasing of a 3-fold InP dot stack within a GaInP/AlInP separate confinement heterostructure laser diode grown on GaAs substrate is observed up to $-30°C$. Significant improvement of the PL linewidth and intensity is expected after systematic optimization of growth conditions.

We demonstrated that atomic layer precise etching in solid source MBE with $AsBr_3$ is a useful technique for in-situ surface patterning. Selective etching of SiO_2 masked GaAs (100) substrates with the stripes aligned along the [100] direction provides very sharp V-grooves with almost perfectly planar {110} facets. MBE regrowth of in-situ prepared V-grooves allows the preparation of buried layers and/or completely embedded quantum wires.

The results demonstrate that the $AsBr_3$ etching is compatible with MBE growth. The switching between growth, etching and regrowth is possible within seconds. Three years experience with in-situ etching in our system did not cause any degeneracy of the sample quality. It is a clean process and does not introduce non-radiative recombination centers into the layers even when the etching step is introduced directly within the active layer of the sample.

References

[1] M.K. Zundel, P. Specht, N.Y. Jin-Phillipp, F. Phillipp, K. Eberl, Appl. Phys. Lett. 71 (1997) 2972, and references 1–15 therein.
[2] J.M. Gérard, O. Cabrol, B. Sermage, Appl. Phys. Lett. 68 (1996) 3123.
[3] Y. Arakawa, H. Sakaki, Appl. Phys. Lett. 40 (1982) 939.
[4] M. Asada, Y. Miyamoto, Y. Suematsu, IEEE J. Quantum Electron. 22 (1986) 1915.
[5] D. Bimberg, N. Ledentsov, M. Grundmann, N. Kirstaedter, O.G. Schmidt, M.H. Mao, V. Ustinov, A. Egorov, A. Zhukov, P. Kopev, Z. Alferov, S.S. Ruvimov, U. Gösele, J. Heydenreich, Jpn. J. Appl. Phys. 35 (1996) 1311.
[6] K. Kamath, P. Bhattacharya, T. Sosnowski, T. Norris, J. Phillips, Electron Lett. 32 (1996) 1374.
[7] H. Saito, K. Nishi, I. Ogura, S. Sugou, Y. Sugimoto, Appl. Phys. Lett. 69 (1996) 3140.
[8] S. Fafard, K. Hinzer, S. Raymond, M. Dion, J. McCaffrey, Y. Feng, S. Charbonneau, Science 274 (1996) 1350.
[9] M.K. Zundel, K. Eberl, N.Y. Jin-Phillipp, F. Phillipp, T. Riedl, E. Fehrenbacher, A. Hangleiter, Appl. Phys. Lett. 73, 28. Sept. (1998), to be published
[10] Y. Kaneko, K. Kishino, J. Appl. Phys. 76 (1994) 1809–1818.
[11] M.K. Zundel et al., in: Proc. ICPS 24th Jerusalem 1998, to be published.
[12] A. Kurtenbach, K. Eberl, T. Shitara, Appl. Phys. Lett. 66 (1995) 361.
[13] M. Micovic, C.D. Nordquist, D. Lubyshev, T.S. Mayer, D.L. Miller, R.W. Streater, A.J. SpringThorpe, J. Vac. Sci. Technol. B 16 (1998) 962.
[14] M. Micovic, D.L. Miller, F. Flack, R.W. Streater, A.J. Spring Thorpe, Appl. Phys. Lett. 69 (1996) 2680.

[15] H. Chiu, M.O. Williams, J.F. Ferguson, W.T. Tsang, R.M. Kapre, Appl. Phys. Lett. 65 (1993) 448.

[16] T. Tsang, R. Kapre, P.F. Sciortino Jr., Appl. Phys. Lett. 62 (1993) 2084.

[17] W.T. Tsang, in: K. Eberl et al. (Ed.), Low Dimensional Structures Prepared by Epitaxial Growth or Regrowth on Patterned Substrate, Vol. 298, Kluwer Academic Publishers, 1995, p. 357.

[18] J.M. Ortion, Y. Cordier, J.Ch. Garcia, C. Grattepain, J. Cryst. Growth 164 (1996) 97.

[19] K.P. Smilauer, B.A. Joyce, T. Kawamura, D.D. Vvedensky et al., Phys. Rev. Lett. 74 (1995) 3298.

[20] T. Kaneko, T. Saeger, K. Eberl, in: S.M. Prokes, R.C. Cammarata, K.L. Wang, A. Christou (Eds.), Surface/Interface and Stress Effects in Electronic Material Nanostructures, Vol. 405, Material Research Society, Pittsburgh, PA, USA, 1996, p. 67.

[21] K. Eberl, T. Kaneko, S. Maier, Electrochem. Soc. Proc. 97–21 (1997) 259.

[22] H. Asahi, X.F. Liu, K. Inoue, D. Marx, K. Asami, M. Miki, S. Gonda, J. Cryst. Growth 145 (1994) 668.

[23] T. Hayashi, H. Asahi, K. Yamamoto, K. Hidaka, S. Gonda, Jpn. J. Appl. Phys. 35 (1) (1996) 3814.

[24] C.W. Tu, N.Y. Li, Electrochem. Soc. Proc. 97–21 (1997) 10.

[25] N.Y. Li, C.W. Tu, Compound Semiconductor Electronics and Photonic, Mater. Res. Soc. Symp. Proc. 421 (1996) 15.

[26] N.Y. Li, Y.M. Hsin, W.G. Bi, P.M. Asbeck, C.W. Tu, Appl. Phys. Lett. 70 (1997) 2589.

[27] J. Sato, H. Asahi, T. Tashima, K. Hidaka, K. Yamamoto, K. Asami, S. Gonda, J. Cryst. Growth 188 (1998) 363.

[28] W.T. Tsang, T.H. Chiu, R.M. Kapre, Appl. Phys. Lett. 63 (1993) 3500.

[29] J.L. Gentner, P. Jarry, L. Goldstein, IEEE J Select. Top. Quantum Electronics 3 (1997) 845.

[30] M. Ritz, T. Kaneko, K. Eberl, Appl. Phys. Lett. 71 (1997) 695.

[31] J. Zhang, O.P. Naji, P. Steans, P. Tejedor, T. Kaneko, T.S. Jones, B.A. Joyce, J. Cryst. Growth 175/176 (1997) 1284.

[32] H. Schuler, M.O. Lipinski, K. Eberl, Semicond. Sci. Technol. 15 (2000) 169.

Nanoscale decoration of electrode surfaces with an STM

D.M. Kolb*, G.E. Engelmann, J.C. Ziegler

Department of Electrochemistry, University of Ulm, 89069 Ulm, Germany

Received 23 March 1999; received in revised form 25 May 1999; accepted 30 May 1999

Abstract

The tip of a scanning tunnelling microscope (STM) has been used to deposit nanometer-sized clusters of copper or silver on bare and thiol-covered gold electrode surfaces at predetermined positions. First, metal is deposited electrochemically onto the STM tip, then the clusters are formed by a jump-to-contact between the tip and the substrate during a short and very controlled approach of the tip towards the surface. When Ni is deposited onto the tip, the jump-to-contact occurs in the opposite direction leaving holes in the gold surface. The stability of the metal clusters against anodic dissolution is discussed. Finally, it is shown how the tip approach can be used to determine tunnel barriers at the metal–electrolyte interface. © 2000 Elsevier Science B.V. All rights reserved.

Keywords: Clusters; Electrochemical nanostructuring; SAM; STM; Tunnel barrier

1. Introduction

The past few years have witnessed the tremendous success of scanning tunnelling microscopy (STM) not only as a technique to image surfaces in real space and with atomic-scale resolution, but also as a tool for positioning single atoms and molecules on surfaces with an hitherto unprecedented precision. The tip–substrate interaction at close distances (say, of the order of an atomic diameter), which generally is a much feared problem in surface imaging as it may give rise to artefacts, has been successfully employed to manipulate single atoms or molecules with the tip. Impressive examples of this kind of nanostructuring have been given by several groups working under ultrahigh vacuum conditions (UHV) and mainly at low temperatures [1–5]; among them is Don Eigler's famous quantum corral, which consists of 48 Fe atoms arranged with the tip of an STM in a circle on a Cu(111) surface [6].

The nanostructuring of electrode surfaces, primarily of noble-metal or graphite surfaces in contact with an aqueous solution, started soon after the corresponding work in UHV, although the tip-generated entities were clearly larger than individual atoms. Structures from single atoms would not have been stable enough to survive in an electrochemical environment at room temperature. The most common approach to an electrochemical nanostructuring of surfaces was to create surface defects by the tip, which then acted as nucleation centers for the metal deposition at preselected positions [7–9]. This was

---

*Corresponding author. Tel.: + 49-731-502-5400; fax: + 49-731-502-5409.

E-mail address: dieter.kolb@chemie.uni-ulm.de (D.M. Kolb)

done by applying high-voltage pulses (1.5–6 V) for a short (μs) or ultrashort (ns) time between tip and sample that leads to the formation of holes in the surface by either mechanical contact or some sort of sputtering process. Metal deposition from solution was subsequently observed at the tip-induced defects. Quite recently, metal clusters were shown to be positioned at will on metal and semiconductor surfaces by a two-step process that involves metal deposition from solution onto the tip, followed by a burst-like dissolution and redeposition on the sample right underneath the tip [10,11]. Over the last several years our group has developed yet another technique, by which flat electrode surfaces can be decorated with small metal clusters via a tip-induced deposition that leaves the sample surfaces undamaged [12–16].

In the following, we will briefly reiterate the principles of our method and show some examples of Cu clusters on bare and thiol-covered Au(111), before results on a new system, namely Ag clusters on Au(111), are presented. Like in the case of Cu clusters, a surprisingly high stability of the small Ag clusters on gold against anodic dissolution is found. Finally it is shown what happens to a gold surface during the tip approach, if a metal with high cohesive energy like Ni has been deposited onto the tip.

2. Experimental

The experimental set-up for nanostructuring a gold surface with metal clusters has been described in previous publications [13–16]. For the sake of convenience, however, the most pertinent data are briefly repeated here. For nanodecoration and surface imaging a PicoSPM (Molecular Imaging, Tempe, USA) was used with separate control of tip and sample potential by a bipotentiostat. The tip approach, during which the transfer of metal from the tip to the substrate occurs, was enforced by applying a voltage pulse directly onto the z-piezo. Actually, tip approach as well as tip movement in x- and y-direction during nanostructuring was externally controlled by a microprocessor which makes the cluster formation and the surface decoration a fully automated process.

STM tips were made from a 0.25-mm diameter Pt/Ir (80:20) wire that was etched in a lamella of 3.4

M NaCN. The tips were coated either with Apiezon wax [17,18] or with an electrodeposition paint [19] to reduce the area in contact with the electrolyte down to about 10^{-7} cm^2. Consequently, Faradaic currents at the tip/electrolyte interface were typically below 50 pA and thus, sufficiently lower than our tunnel currents which were usually around 2 nA. All STM images were obtained in the constant-current mode. They are unfiltered, but corrected for any tilt of the sample surface.

The samples were either Au(111) films on glass or a massive Au(111) crystal. Both types of electrodes were flame-annealed at yellow heat in a H$_2$-flame [20,21] and cooled down to room temperature in a nitrogen atmosphere prior to each experiment. The ethanethiol-covered Au(111) surface was obtained by immersing the Au(111) film electrode overnight in a 1 mM ethanolic solution of ethanethiol where a so-called self-assembled monolayer (SAM) is spontaneously formed [22]. The reference electrodes were simply a Cu or a Pt wire for Cu deposition, Hg/Hg$_2$SO$_4$ for Ag deposition and a Pt wire for Ni deposition. The solutions were 0.05 M H$_2$SO$_4$ with 0.1 or 1 mM CuSO$_4$ and Ag$_2$SO$_4$ for Cu and Ag deposition, respectively, and 0.01 M H$_3$BO$_3$ + 0.2 mM HCl + 1 mM NiSO$_4$ (Watts bath) for Ni deposition, made of Merck suprapur chemicals except for CuSO$_4$, Ag$_2$SO$_4$ and NiSO$_4$, which were of p.a. quality. In the case of Cu and Ag deposition, potentials are quoted against the reversible Me/Me^{z+} potential in that solution, in the case of Ni, all potentials are quoted against SCE.

3. Results and discussion

3.1. Cu clusters on Au(111)

The proposed mechanism for the tip-induced cluster formation is sketched in Fig. 1, highlighting the two requirements that have to be fulfilled:

(i) First, metal has to be deposited onto the tip, which is achieved by simply choosing a tip potential negative of the corresponding bulk metal deposition potential.

(ii) Secondly, the metal-loaded tip has to approach the surface for a short period of time,
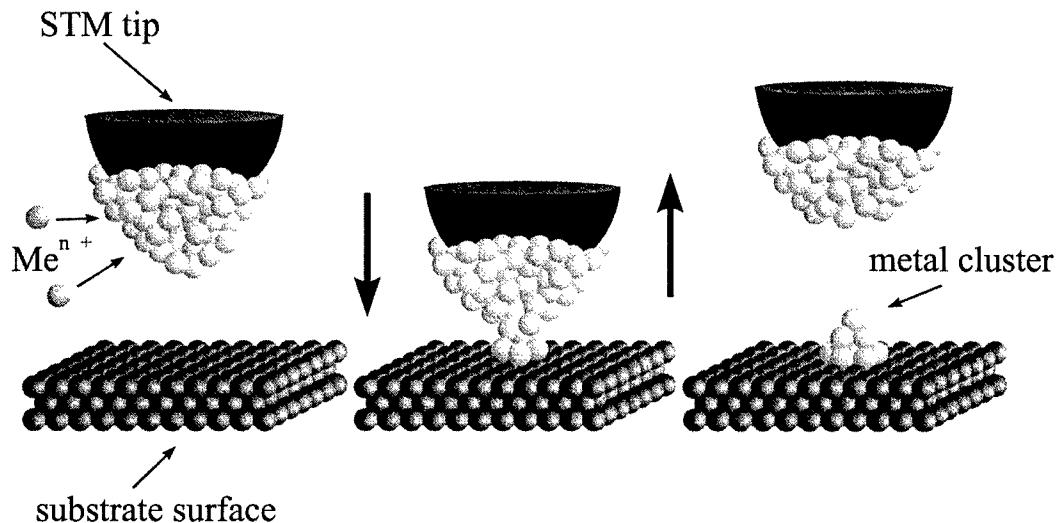
Fig. 1. Schematic diagram of the tip-induced cluster formation.

during which a so-called jump-to-contact [23,24] occurs.

The resulting connective neck breaks upon the subsequent retreat of the tip leaving a small metal cluster on the surface. We stress the point that the direction of the material transfer will depend on the cohesive energies of both sides, and for Ni and Au(111) it is opposite to the Cu case (see Section 3.4 and Ref. [24]). As has been shown before, the externally enforced tip approach allows the fast generation of Cu clusters with a remarkably uniform size distribution. In Fig. 2a an array of 225 Cu clusters is shown, all about 0.6 nm high, which was

197 x 197 nm²   197 x 197 nm²

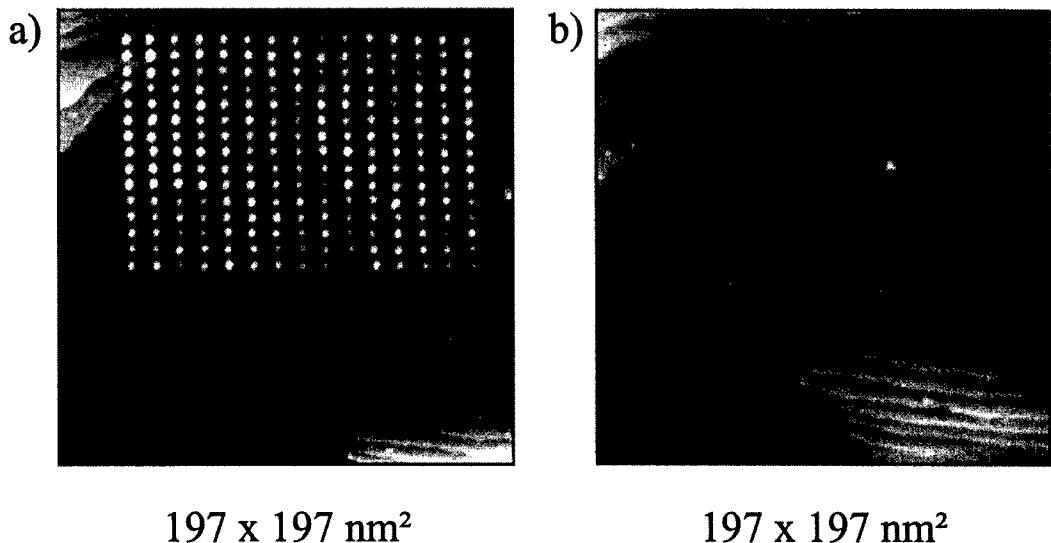Fig. 2. (a) STM image of an array of 225 Cu clusters on Au(111) in 0.05 M H_2SO_4 + 0.1 mM $CuSO_4$ generated by 225 voltage pulses to the z-piezo. The Cu clusters are placed on a Cu-monolayer-covered Au(111) surface due to underpotential deposition. E_{sample} = + 10 mV vs. Cu/Cu^{++}, E_{tip} = − 30 mV, I_t = 2 nA. (b) Same area, but after anodic dissolution of the Cu clusters at + 300 mV.

accomplished within 30 s. Besides the remarkably uniform cluster height, several points are noteworthy. The clusters were generated with 2-ms voltage pulses to the z-piezo with a repetition rate of 120 Hz. With a minimum pulse duration of 0.1 ms as determined in earlier experiments [25], a much higher cluster deposition rate, e.g. in the kHz range, seems feasible. Furthermore we note from Fig. 2a that monoatomic high steps of the substrate cause no problems for the preselected cluster patterning, suggesting that nanostructuring of slightly rough surfaces by our technique may still work. Despite the fabrication of many Cu clusters in quick succession (the largest array so far consisted of 10 000 Cu clusters [26]), there is no sign of depletion of Cu on the tip. The re-filling of the tip during the cluster fabrication by an on-going deposition reaction at the tip is surprisingly fast and — quite importantly — retains the high imaging quality of the tip. Hence, 'writing' and 'reading' are possible with the same tip. Anodic dissolution of the Cu clusters uncovers a perfectly flat Au(111) surface (Fig. 2b), a fact that supports our statement of an undamaged surface and that we are not dealing with tip-induced defects in the substrate. In other words, a tip-induced nanostructure can be completely erased. Finally, the stability of the Cu clusters against anodic dissolution is remarkable [11,14,27]. Studies have shown that the Cu nanoclusters are stable at + 10 mV vs. Cu/Cu^{++} for at least 1 h and considerable 'overpotentials' of + 100 mV and more are required to dissolve the tip-induced Cu clusters completely within minutes. Similar findings will be reported in Section 3.3 for Ag clusters on gold. The origin of this unusual electrochemical stability of the nanofabricated clusters has been explained on the basis of a quantum-size effect [27].

As mentioned before, all three spatial coordinates of the tip can be externally controlled by a microprocessor, which makes the nanodecoration of an electrode surface with metal clusters a fully-automated process, allowing even complex patterns to be made fast and reproducible. Fig. 3 shows a pattern made of about 400 Cu clusters on Au(111) with the clusters arranged in a rhombic fashion. The clusters are sitting on quite a stepped Au(111) surface, which is covered by a monolayer of Cu due to underpotential deposition (upd) at $E_{sample} = 10$ mV vs. Cu/

Cu^{2+}. Other, more complicated structures such as letters and words, have been shown in previous publications [16].

The Cu clusters presented so far were all formed directly by the jump-to-contact during tip approach. Their height can be varied within certain limits by the extent of the approach, typically within 0.3–1.2 nm (i.e. from one to about five Cu monolayers) [13–15]. In certain instances, however, somewhat larger clusters are desirable, e.g. when dealing with magnetic metals. In such a case, the tip-induced metal clusters can be used as nucleation centers to grow larger ones at predetermined positions by normal deposition from solution. In Fig. 4 a so-called $x - t$ scan is shown, where a single scan in the x-direction is repeatedly recorded (y = constant) and plotted as a function of time. Thus the development of a certain structural feature with time, like the growth of an individual cluster, can be monitored in great detail. The image in Fig. 4 shows the growth of a tip-generated Cu cluster after the potential was stepped from + 10 mV vs. Cu/Cu^{++} to − 280 mV vs. Cu/Cu^{++}. It can be clearly seen that the tip-generated cluster first grows mainly laterally, before several new layers nucleate on top of the cluster. Within the time span covered in Fig. 4, a total of eight Cu monolayers is seen to nucleate and grow on the tip-induced cluster, expanding the latter to a formidable size.

3.2. Cu clusters on thiol-covered Au(111)

An important question to be addressed in the near future is the influence of a chemical surface modification on the tip–substrate interaction in general and on the jump-to-contact behaviour in particular. Self-assembled monolayers (SAM) of alkanethiols on Au(111) are among the most popular systems for surface chemical modifications, because well-ordered and stable adlayers are conveniently achieved simply by dipping the sample for a prolonged period of time in an ethanolic solution of the thiol under consideration. Since our group has recently finished an extended investigation on the structure of ethanethiol on Au(111) [22], we used this system to test whether tip-generated Cu clusters can be placed on such surfaces. Fig. 5 demonstrates that this is indeed
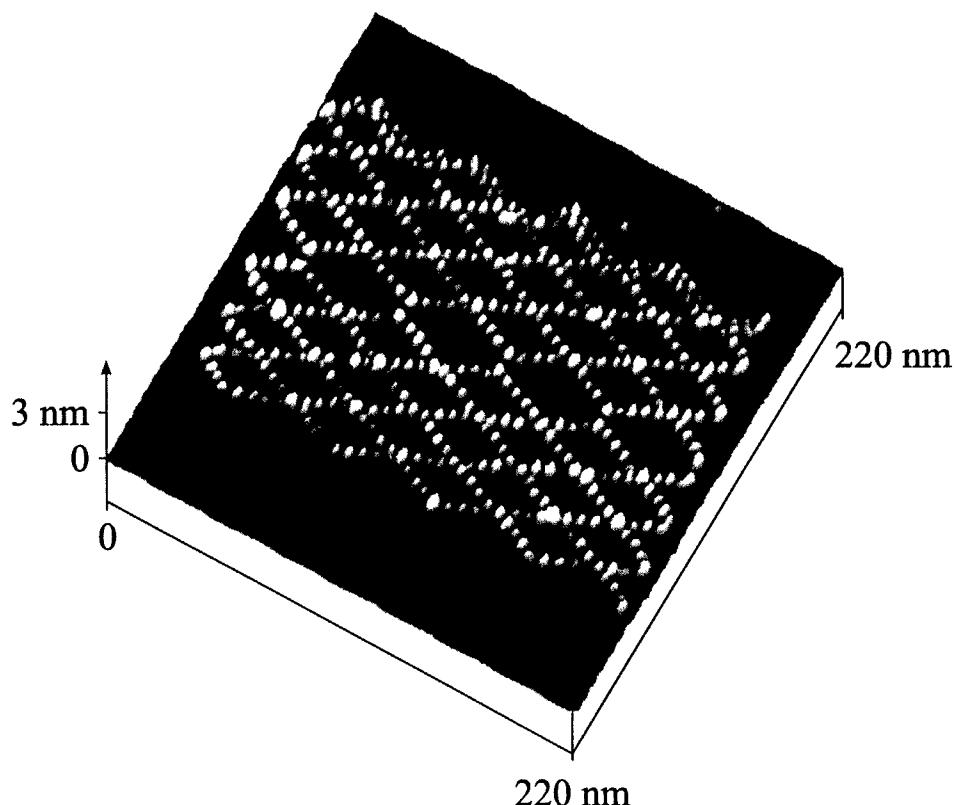
Fig. 3. STM image of about 400 Cu clusters on Au(111) in 0.05 M H_2SO_4 + 1 mM $CuSO_4$. E_{sample} = + 10 mV vs. Cu/Cu^{++}, E_{tip} = − 30 mV, I_t = 2 nA.

possible. A square array of 25 Cu clusters with heights between 0.7 and 1.1 nm was generated by 25 externally enforced tip approaches. It was recently shown in our group that at a potential of + 10 mV vs. Cu/Cu^{++} which is required to keep the Cu clusters on the surface for a longer period of time, the ethanethiol SAM is in a disordered state with small ethanethiol islands on top of it [22]. These islands are clearly seen in Fig. 5 as grey, 0.2 nm high blobs scattered all over the surface. Anodic dissolution of the Cu clusters left a Au(111) surface with an intact SAM. Because of the structural transition of the ordered SAM at about 200 mV vs. Cu/Cu^{++} into a disordered state, which prevails at potentials closer to the Cu/Cu^{++} Nernst potential, we are presently not able to characterize on a molecular level the SAM structure onto which the Cu clusters are placed. However, it is reasonable to assume that the

disordered state is less densely packed with ethanethiol molecules than the ordered state, the molecularly resolved STM images of which clearly reveal structures with a maximum coverage of about one-third monolayer. It thus appears that Cu atoms at the tip can still interact with a sufficiently large number of bare gold atoms to allow a jump-to-contact to occur.

We note in passing that very similar arrays of Cu clusters were also produced with octadecanethiol-covered Au(111) electrodes [28]. The fact that the alkane chain length apparently has no major influence on the cluster generation process seems understandable in view of the close proximity of tip and substrate: under the experimental conditions which we have chosen, the tip is ploughing through the alkane chains of the thiol monolayer rather than scanning above it.
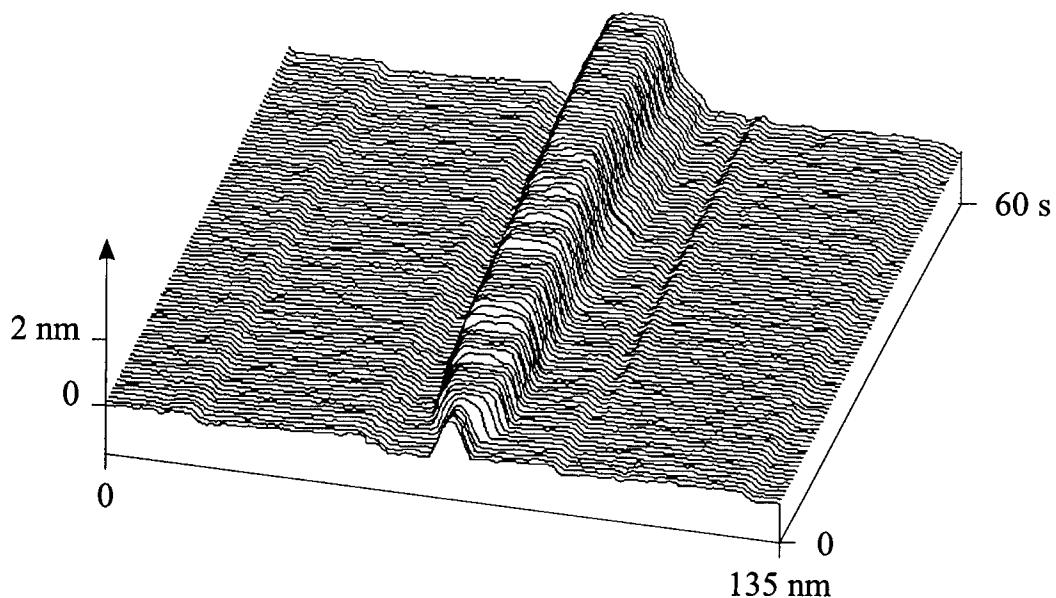
Fig. 4. STM image ($x - t$-scan) of a growing Cu cluster after stepping the potential from $+ 10$ mV to $- 280$ mV vs. Cu/Cu^{+} (at $t = 2.5$ s). $E_{tip} = - 30$ mV, $I_t = 2$ nA. Electrolyte: 0.05 M H$_2$SO$_4$ + 0.1 mM CuSO$_4$.

3.3. Ag clusters on Au(111)

Ag deposition on Au(111) starts at underpotentials like in the case of Cu [29,30]. Hence, the jump-to-contact occurs between bulk Ag on the tip and a Ag monolayer on Au(111), and the tip-generated Ag clusters are placed on the upd layer of Ag on Au(111). The successful decoration with Ag nano-clusters of a Au(111) electrode at $+ 0.1$ V vs. Ag/Ag^{+}, where the surface is covered by a mono-layer of Ag [30], is demonstrated in Fig. 6, which shows the STM image of a square array of 25 Ag clusters. A series of experiments has revealed that the reproducibility of the cluster generation process is by far not as good as for Cu on gold. This is particularly true for the cluster height which varies in Fig. 6 between 0.3 and 1.1 nm.

Like in the case of Cu on Au(111) [14,27], the Ag clusters are surprisingly stable against anodic disso-lution. Fig. 7 summarizes the results of a series of experiments, in which the heights of individual clusters were measured at certain time intervals for three different electrode potentials. We note that at a potential of $+ 50$ mV vs. Ag/Ag^{+} the clusters are stable over several minutes and even for 'overpoten-tials' as high as 200 mV, the Ag clusters do not

dissolve momentarily. The reason for this unusually high stability was explained in a recent publication [27].

3.4. The Ni/Au(111) system

In an attempt to decorate a gold surface with nanoclusters of a magnetic metal, Ni was deposited onto the Pt/Ir tip in a so-called Watts bath. The latter is a commonly used electrolyte for Ni plating. However, after various externally enforced ap-proaches of the Ni-coated STM tip only holes in the Au(111) surface were seen, but no Ni clusters (Fig. 8a). This observation is in full agreement with the theoretical predictions of Landman et al. [23,24], who performed calculations for the interaction be-tween a Ni tip and a Au surface, and found a jump-to-contact from the gold to the nickel. This is schematically shown in Fig. 8c, illustrating the hole formation in the gold surface due to gold atoms jumping to the tip.

The STM image in Fig. 8a reveals that the hole production is rather erratic and works only a few times, since the tip was approached 25 times towards the surface. This may be explained by the fact that with the first jump-to-contact the Ni tip is trans-

100 x 100 nm²
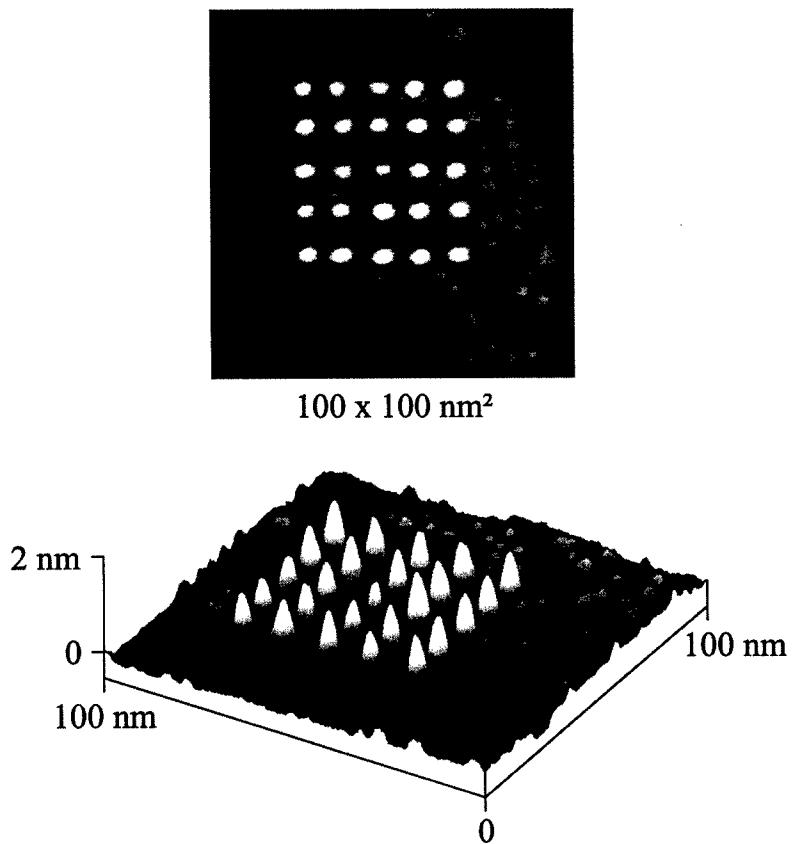
Fig. 5. STM image (top view and 3D-plot) of 25 Cu clusters placed on an ethanethiol-modified Au(111) surface in 0.05 M H_2SO_4 + 1 mM $CuSO_4$. E_{sample} = + 10 mV vs. Cu/Cu^{++}, E_{tip} = − 30 mV, I_t = 2 nA.
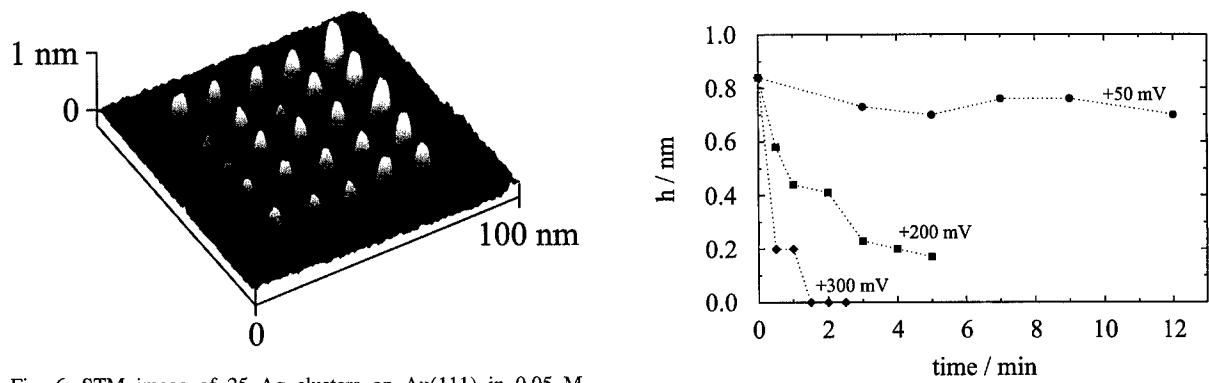
Fig. 6. STM image of 25 Ag clusters on Au(111) in 0.05 M H_2SO_4 + 0.1 mM Ag_2SO_4. E_{sample} = + 100 mV vs. Ag/Ag^+, E_{tip} = 0 mV, I_t = 2 nA.

Fig. 7. Variation of cluster height with time during the dissolution of Ag clusters on Au(111) at various electrode potentials.

Fig. 8. (a) STM image of a Au(111) electrode in 1 mM $NiSO_4$ + 10 mM H_3BO_3 + 0.2 mM HCl, showing the hole formation with a Ni-covered Pt–Ir tip. The five lines in the upper part of the image re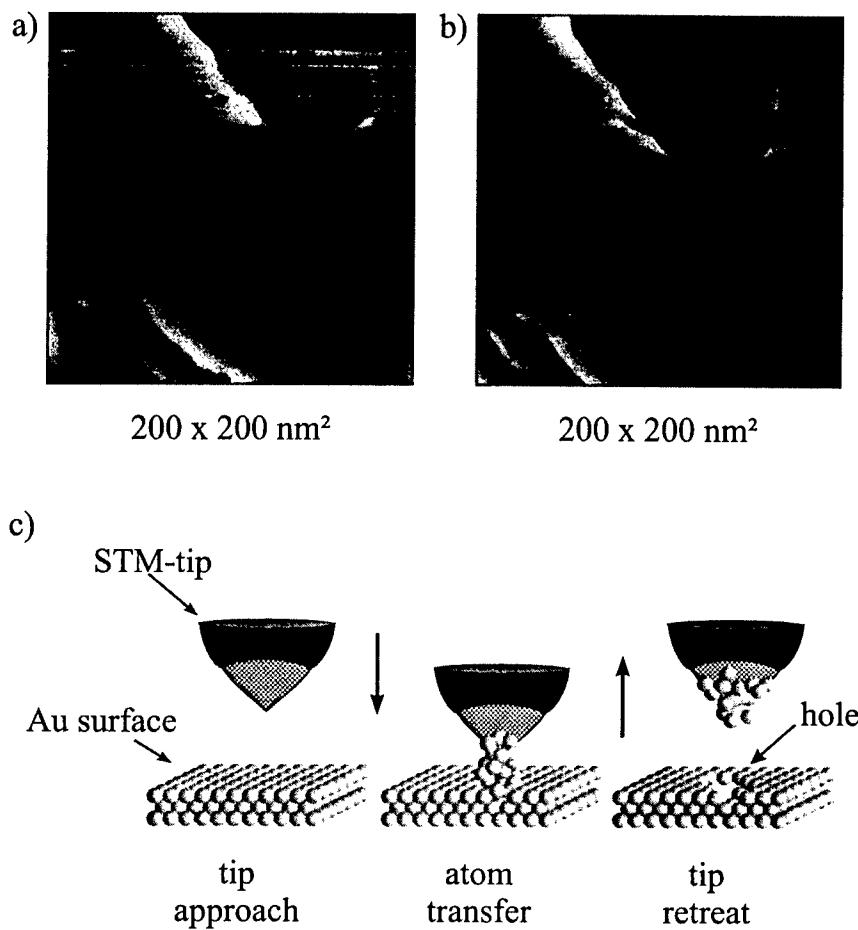flect the pulses on the z-piezo (five pulses per line). E_{sample} = − 320 mV vs. SCE, E_{tip} = − 470 mV, I_t = 2 nA. (b) Same area, imaged 1 min later. E_{sample} = − 320 mV vs. SCE, E_{tip} = − 470 mV, I_t = 2 nA. (c) Suggested mechanism of the hole formation in the Au(111) substrate during the approach of a Ni-covered STM tip.

formed into a gold-covered tip. The image in Fig. 8b was recorded 1 min after the hole production and after image (a) and it demonstrates the relatively high mobility of the advacancy islands on gold which causes these holes to migrate to step edges or to merge with each other. We may briefly mention here, that preliminary experiments with Co^{++} containing electrolytes led to a tip-induced Co cluster formation on Au(111), although the production was very irregular. This system is currently under investigation.

3.5. Determination of tunnel barriers

The externally enforced tip approach for cluster fabrication can also be employed to determine rather precisely tunnel barriers at the metal–electrolyte interface. This has been demonstrated for Cu and Au(111) [26], where a barrier height of Φ_T = 1.5 eV was found. In Fig. 9 the logarithmic dependence of the momentarily flowing tunnel current I_T as a function of the tip approach Δz is shown. The latter can be converted from mV to nm by the conversion
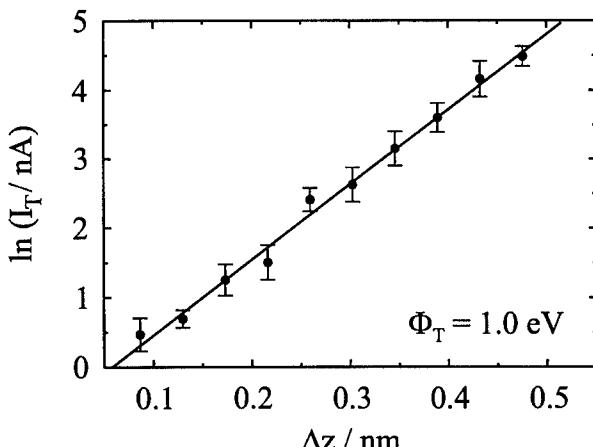
Fig. 9. Determination of the tunnel barrier height Φ_T from measurements of the tunnel current I_t as a function of the tip approach Δz, which was externally enforced by applying a voltage pulse to the z-piezo. Each data point is the average of five pulses. The error bars represent the S.D. for these five pulses.

factor given for this instrument by the manufacturer. During this type of measurement, the feed-back circuit of the STM is almost completely switched off (integral and proportional gain were 0.03 and 0, respectively, as compared to 1.5 and 2.0 for typical imaging conditions). The data points in Fig. 9 were obtained by applying voltage pulses of various heights and 20 ms duration onto the z-piezo. Plotting the height of the resulting tunnel current as a function of distance change Δz for each tip approach, yields an exponential dependence over a wide range. From the slope of the straight line in Fig. 9, a tunnel barrier of 1.0±0.2 eV was determined for tunnelling from the tip to the substrate in 0.05 M H_2SO_4 + 1 mM Ag_2SO_4. The potential of the Au(111) substrate was held at + 0.25 V vs. Ag/Ag^+, that of the tip at + 100 mV vs. Ag/Ag^+. Under such conditions the Au(111) surface is covered by a monolayer of Ag [30].

Although the literature data for tunnel barriers in metal electrode–aqueous solution systems scatter widely, the values ranging from 0.2 [31,32] up to 3.8 eV [33], there seems to be a general agreement that the more recently published data which all jump between 1.0 and 1.5 eV [34,35], seem to be the most reliable ones. Hence, both values for the tunnel barrier determined by our method, 1.5 eV [26] for Cu

and 1.0 eV in the case of Ag, appear to be in the correct range of data.

References

[1] D.M. Eigler, E.K. Schweizer, Nature 344 (1990) 524.
[2] M.T. Cuberes, R.R. Schlitter, J.K. Gimzewski, Surf. Sci. 371 (1997) L231.
[3] Ph. Avouris, J.-W. Lyo, Appl. Surf. Sci. 60–61 (1992) 426.
[4] G. Meyer, S. Zöphel, K.H. Rieder, Appl. Phys. A 63 (1996) 557.
[5] C. Thirstrup, M. Sakurai, T. Nakayama, M. Aono, Surf. Sci. 411 (1998) 203.
[6] M.F. Crommie, C.P. Lutz, D.M. Eigler, Science 262 (1992) 218.
[7] W. Li, J.A. Virtanen, R.M. Penner, Appl. Phys. Lett. 60 (1992) 1181.
[8] W. Li, J.A. Virtanen, R.M. Penner, J. Phys. Chem. 96 (1992) 6529.

[9] X.H. Xia, R. Schuster, V. Kirchner, G. Ertl, J. Electroanal. Chem. 461 (1999) 102.

[10] D. Hofmann, W. Schindler, J. Kirschner, Appl. Phys. Lett. 73 (1998) 3279.

[11] R.T. Pötzschke, G. Staikov, W.J. Lorenz, W. Wiesbeck, J. Electrochem. Soc. 146 (1999) 141.

[12] R. Ullmann, T. Will, D.M. Kolb, Chem. Phys. Lett. 209 (1993) 238.

[13] D.M. Kolb, R. Ullmann, T. Will, Science 275 (1997) 1097.

[14] D.M. Kolb, R. Ullmann, J.C. Ziegler, Electrochim. Acta 43 (1998) 2751.

[15] G.E. Engelmann, J.C. Ziegler, D.M. Kolb, J. Electrochem. Soc. 145 (1998) L33.

[16] J.C. Ziegler, G.E. Engelmann, D.M. Kolb, Z. Phys. Chem. 208 (1999) 151.

[17] J. Wiechers, T. Twomey, D.M. Kolb, R.J. Behm, J. Electroanal. Chem. 248 (1988) 451.

[18] L.A. Nagahara, T. Thundat, S.M. Lindsay, Rev. Sci. Instrum. 60 (1989) 3128.

[19] C.E. Bach, R.J. Nichols, W. Beckmann, H. Meyer, A. Schulze, J.O. Besenhard, P.D. Jannakoudakis, J. Electrochem. Soc. 140 (1993) 1281.

[20] T. Will, M. Dietterle, D.M. Kolb, in: A.A. Gewirth, H. Siegenthaler (Eds.), Nanoscale Probes of the Solid–liquid Interface, NATO ASI, Vol. E 288, Kluwer, Dordrecht, 1995, p. 137.

[21] J. Clavilier, R. Faure, G. Guinet, R. Durand, J. Electroanal. Chem. 107 (1980) 205.

[22] H. Hagenström, M.A. Schneeweiß, D.M. Kolb, Langmuir 15 (1999) 7802.

[23] U. Landman, W.D. Luedtke, N.A. Burnham, R.J. Colton, Science 248 (1990) 454.

[24] U. Landman, W.D. Luedtke, in: R. Wiesendanger, H.-J. Güntherodt (Eds.), Scanning Tunnelling Microscopy III, Springer Series in Surface Science, Vol. 29, Springer, Berlin, 1993, p. 207.

[25] R. Ullmann, Ph.D. thesis, University of Ulm, 1997.

[26] G.E. Engelmann, J.C. Ziegler, D.M. Kolb, Surf. Sci. 401 (1998) L420.

[27] D.M. Kolb, G.E. Engelmann, J.C. Ziegler, Angew Chem. Int. Ed. 39 (2000) 1123; Angew Chem. 112 (2000) 1166.

[28] G.E. Engelmann, D.M. Kolb, to be published.

[29] K. Ogaki, K. Itaya, Electrochim. Acta 40 (1995) 1249.

[30] M.J. Esplandiu, M.A. Schneeweiß, D.M. Kolb, Phys. Chem. Chem. Phys. 1 (1999) 4847.

[31] M. Binggeli, D. Carnal, R. Nyffenegger, H. Siegenthaler, R. Christoph, H. Rohrer, J. Vac. Sci. Technol. B9 (1991) 1985.

[32] J. Halbritter, G. Repphun, S. Vinzelberg, G. Staikov, W.J. Lorenz, Electrochim. Acta 40 (1995) 1385.

[33] J. Pan, T.W. Jing, S.M. Lindsay, J. Phys. Chem. 98 (1993) 4205.

[34] S. Vinzelberg, Ph.D. thesis, University of Karlsruhe, 1995.

[35] A. Vaught, T.W. Jing, S.M. Lindsay, Chem. Phys. Lett. 236 (1995) 306.

Fabrication of thin electrolytes for second-generation solid oxide fuel cells

J. Will, A. Mitterdorfer, C. Kleinlogel, D. Perednis, L.J. Gauckler*

Department of Materials, ETH, Zurich, Sonneggstr. 5, CH-8092 Zürich, Switzerland

Abstract

This paper reviews different thin-film deposition methods for oxides, especially for stabilized zirconia and compares them with regard to SOFC applications. These methods will be classified into chemical, physical methods and ceramic powder processes. Each method is described with its special technical features and examples of components for fuel cells are given. PVD and CVD methods are specially suited to depositing high-quality films of simple chemical compositions. Liquid droplet methods and ceramic powder processes are more qualified for the deposition of complicated chemical compositions. © 2000 Elsevier Science B.V. All rights reserved.

Keywords: SOFC; Thin films; Zirconia; PVD; CVD; Liquid precursor methods

1. Introduction

Yttria-stabilized zirconia (YSZ) is the most commonly used electrolyte material for Solid Oxide Fuel Cells (SOFCs) because of its unique combination of properties such as high chemical and thermal stability and pure ionic conductivity over a wide range of conditions. As a result, YSZ today is still the standard electrolyte material in SOFCs. Due to the high operational temperatures (900–1000°C) the material demands upon SOFC components are quite stringent. It would be desirable to lower the operational temperatures (to 700–800°C) so that interconnect, heat exchangers, and structural components may be fabricated from relatively inexpensive metal components [1–6]. One problem associated with lowering the temperature is the increase of the YSZ electrolyte resistivity. This can be overcome by lowering the electrolyte resistance either by decreasing the electrolyte thickness or with alternative materials of higher ionic conductivity at lower temperatures (e.g. Sc-doped zirconia, ceria solid solutions, doped bismuth oxide, etc.). In addition, for both strategies reduced electrode/electrolyte interfacial losses are beneficial.

If the electrolyte thickness is reduced from today's 100–200 μm to a 5–10 μm range a new design for the electrode/electrolyte structure is needed. As the thin electrolyte can no longer be the mechanically supporting component, one of the porous electrodes must take over this function. Then a thin electrolyte film may be deposited on the electrode layer followed by the deposition of the other porous electrode. SOFCs based on thin electrolytes have already

been tested and exhibited excellent electrochemical performances (e.g. [7–10]).

We give a survey of the most commonly applied techniques for depositing thin electrolyte films with an emphasis on techniques, which are already used for SOFC processing. Most of the examples are for yttria-stabilized zirconia but are equally applicable to other oxide electrolytes.

2. Deposition of thin ceramic films

2.1. Chemical methods

2.1.1. Chemical vapor deposition techniques

2.1.1.1. General

There are two main chemical deposition techniques such as Chemical Vapor Deposition (CVD) and Electrochemical Vapor Deposition (EVD). Recently few related methods are also proposed and applied. These methods make it possible to control chemical composition and to form a dense film. They are also known to be suitable for mass production.

2.1.1.2. Chemical vapor deposition

CVD is a chemical process in which one or more gaseous precursors form a solid material by means of an activation process. The reactant vapors are (1) transported to the surface of a substrate and (2) adsorbed on the substrate surface where (3) the

chemical reaction leads to a solid product for (4) crystal growth.

CVD has been widely used for fabricating microelectronics. Therefore the underlying processes are well understood. Recently several modifications, which might become important for fabricating SOFC components, have been developed. Halogen compounds such as $ZrCl_4$ and YCl_3 [11,12], metal organic compounds such as metal alkoxides [13–15] or β-diketones ([16] and references therein) have been used as precursor materials. Growth rates of the film thickness are in the range of 1–10 $\mu m\,h^{-1}$, depending on the evaporation rate and substrate temperature.

A schematic diagram of a typical CVD apparatus is shown in Fig. 1. Typically fused-silica glass is used as the substrate material which is heated to deposition temperatures of 600–1200°C depending on the reactivity of the precursors.

Chour et al. [15] used butanol containing Zr- and Y-ions as a precursor material and pressed and sintered ceria pellets as substrates. The precursor was heated to 150°C whereas the substrate was heated to about 850°C. The deposition time was 4 h for a film thickness of 5 μm. After annealing at 1300°C for 10 h the YSZ phase in the deposited film became fully crystalline. An Open Cell Voltage (OCV) of 0.93 V at 650°C was reported.

The advantages of the CVD technique consist of producing uniform, pure, reproducible and adherent films at low or high rates. It is particularly useful in the deposition of coating in sites difficult to reach by
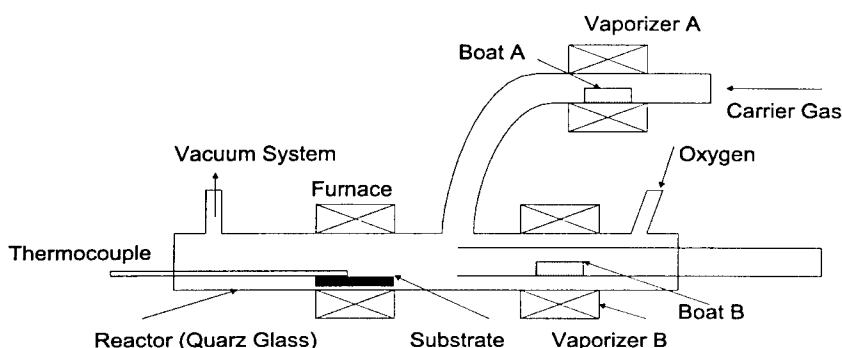

Fig. 1. Schematic diagram of a CVD apparatus for preparation of ZrO_2, Y_2O_3 and ZrO_2–Y_2O_3 films (after [16]).

other deposition techniques. Disadvantages are the high reaction temperature, the presence of corrosive gases (at least for halogenous compounds), and the relatively low deposition rates [17].

2.1.1.3. Electrochemical vapor deposition

EVD is a modified CVD process, originally developed by Westinghouse [18,19]. In these CVD-EVD processes, a porous ceramic substrate divides a reactor into two chambers, of which one is filled with a metal compound reactant and the other with an oxygen source reactant. EVD is a two-step process. The first step involves pore closure by a normal CVD type reaction between the reactant metal chloride vapors and water vapor (or oxygen). Film growth then proceeds due to the presence of an electrochemical potential gradient across the deposited film. In this step oxygen ions formed on the water vapor side of the substrate diffuse through the thin metal oxide layer to the metal chloride side. The oxygen ions react with the metal chloride vapors to form the metal oxide product. The solid product can be deposited as a thin film spreading over the internal pore surface in a desired region across the membrane substrate [20]. A schematic diagram of the basic principles of the CVD/EVD process is given in Fig. 2.

A single component cell, consisting of porous YSZ ceramics with an internally deposited dense film, could be produced at growth rates in the range 2.8–52 $\mu m\,h^{-1}$ [21]. Besides the temperature, the

morphology of the substrate pores and the chemical parameters influence growth rates. Detailed models of the EVD process have been proposed [7,22].

Modified EVD methods are vapor-phase-electrolytic deposition (VED) [7,23,24], thermophoresis assisted CVD (TA-CVD) [25,26], a combination of EVD and TA-CVD and chemical aerosol deposition technology (CADT) [27].

Ioroi et al. [28] produced fully dense YSZ electrolytes which were deposited on porous $La_{0.85}Sr_{0.15}MnO_3$ substrates. They used $ZrCl_4$ and YCl_3 vapor mixtures as the metal compound sources and water vapor as the oxygen source. An OCV of 1.04 V was reported for a $LaMnO_3/YSZ/Ni–YSZ$ with an EVD layer of YSZ, indicating that there was negligible gas leakage through the electrolyte [29]. Cao et al. [30] obtained thin zirconia layers on porous alumina substrates. $ZrCl_4$ and YCl_3 vapor with a ratio of 10:3 were used. After 40–50 min CVD/EVD a gas-tight YSZ layer was formed with a thickness of 0.5–1.5 μm depending on the experimental conditions. The thickness of the YSZ layer increased with the deposition temperature, e.g. 5 μm at 800°C and 19 μm at 1000°C. Sasaki et al. [31] deposited 18-μm thick YSZ layers on cathode tubes. They reported a power density of 0.8 W cm^{-2} with an active area of 1200 mm^2. Thin (2 μm) YSZ layers were deposited on pressed and sintered ceria substrates (20 mm $\varnothing$) by Nord-Varhaug et al. [32]. They used $ZrCl_4$ and YCl_3 metal–chloride precursors. The main problem was cracking of the substrate

(a)　　　　　　　　　　　　　　　　　　(b)

gas stream　Ar +ZrCl₄(g) + YCl₃ (g)

porous ceramic membrane

porous ceramic support

gas stream　air + H₂O

gas stream Ar + MeCl_x
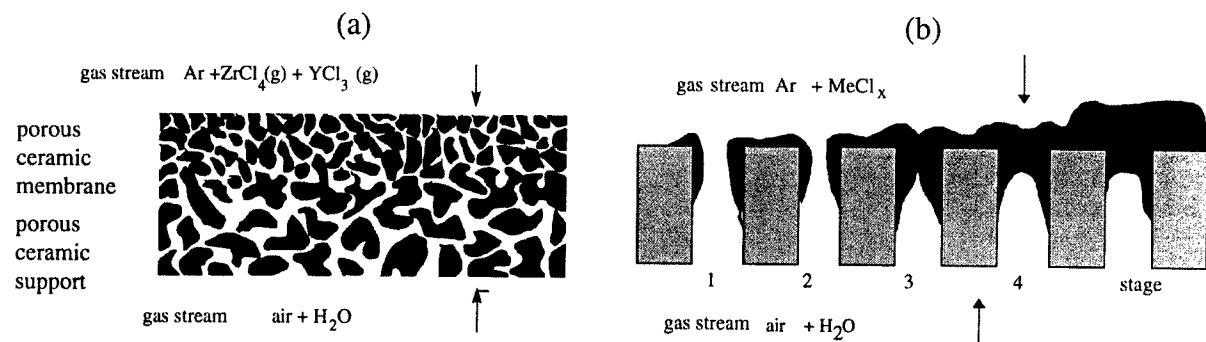
1　　2　　3　　4　　stage

gas stream　air + H₂O

Fig. 2. (a) A schematic diagram of the basic principles of the CVD/EVD processes. (b) Detailed view of the different stages during the CVD/EVD processes in which the solid product is mainly deposited at the chloride side (after [20]).

during heating at 770–950°C, which was probably due to the insufficient mechanical strength of the substrate.

The disadvantages of the EVD process are the high reaction temperature, the presence of corrosive gases, and the relatively low deposition rates. However, EVD is a widely used technique for depositing uniform and gas tight layers of YSZ and interconnect materials for SOFC.

2.1.2. Thin films by the liquid precursor route

2.1.2.1. General

Starting from a molecular precursor, one obtains a hydroxide or oxide network via inorganic polycondensation reactions. For this reason, extremely thin, dense, and well-defined films can be produced. Purity and uniformity are also easy to be controlled by the solution chemistry of the sol–gel process.

Metal alkoxides $M(OR)_n$, where R is usually an alkyl group, are generally the most versatile precursors. Alkoxides are known for almost all transition metals as well as for the rare earth metals [33] and are very reactive towards a reagent such as water. Up to now, zirconia films have been prepared from (1) zirconium propoxide [34–38], (2) zirconium tetrabutoxide [39,40], and (3) from a hydrosol prepared from a zirconium oxychloride solution [41].

2.1.2.2. Sol-gel route

Gelling occurs through the formation of a polymeric network. Fig. 3 shows the two steps of hydrolysis and polymerization by condensation where R is an alkyl group in case of Me = Zr. The desired amount of yttrium is achieved by addition of yttrium nitrate $(Y(NO_3)_3 - nH_2O)$.

The resulting network structures are strongly influenced by the respective kinetics of the reactions, which in turn depend on many parameters. The sol–gel transition occurs during deposition due to solvent evaporation that accelerates the reaction rates among the precursor oligomers. The desired microstructure is determined by the precursor reactivity and the deposition conditions [43,44]. The substrates are coated either by spin- or dip-coating techniques [45,46]. Once coated, the samples are dried at room temperature and heat treated for densification and
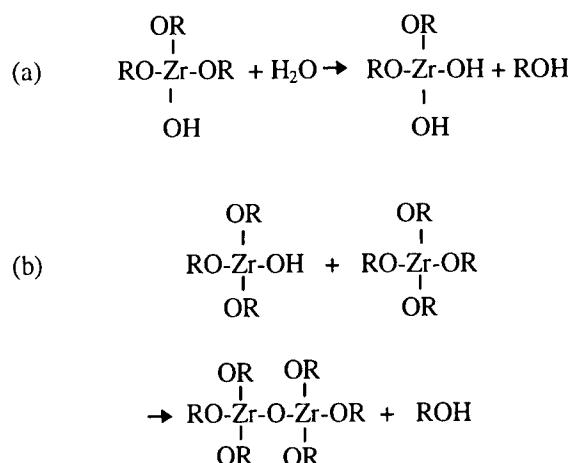

Fig. 3. Hydrolysis reaction and polymerization using the condensation mechanism [42].

crystallization of the film. The process of coating and drying/heating is usually repeated until the appropriate thickness is obtained. Sol-gel derived films, due to their fine structure and high density, can be sintered at much lower temperatures than those films made by conventional ceramic powder processing.

Alternatively the dilution of reactants can also influence the gelling time and finally the gel structure, as expected from simple laws of chemical kinetics. YSZ films described by Kueper et al. [38] were formed using a well-defined relative humidity during the deposition. They were about 0.2 mm thick and uncracked. Peshev et al. [36] showed that good-quality YSZ films of 120–150 nm thickness can be easily deposited on various smooth substrates (Si wafer, sapphire, optical silica glass, and alumina) using a sol–gel technique using zirconium propoxide $(Zr(O-C_3H_7)_4)$ and yttrium isopropoxide $(Y(CH_3)_2CHO)$ in isopropanol with ethyl aceto-acetate $(CH_3COCH_2CO_2C_2H_5)$ as chelating agent. By repeating the deposition steps the film thickness can be increased. Mehta et al. [47] deposited thin layers of YSZ with 11 mol.% Y_2O_3 on sintered disks of Gd-doped ceria electrolyte using spin coating alkoxide solutions. Dense films were obtained by this method on polished ceria substrates. After heat-treatment at 600°C the zirconia film thickness was 1–3 μm. At 600°C an OCV of 0.85 V was achieved after repeating the coating process three times. Nam et al. [48] used the sol–gel method combined with the

spin-coating technique to fabricate thin zirconia layers on pressed and sintered ceria electrolytes with a diameter up to 50 mm. The polymeric YSZ sol was synthesized using the partial hydrolysis of Zr–n-butoxide. Acetic and nitric acid were used as chelating agent and catalyst, respectively. Thin films of YSZ were deposited on the ceria substrates by spin coating of the sol at a spin rate of 2000 rpm for 20 s. After drying, the sample was heat-treated at 600°C. The coating, drying and heat treatment processes were repeated until the thickness of the coated film reached 2 μm. The sample was finally sintered at 1400°C for 2 h. Anderson et al. developed a solution-deposition technique [49,50]. The starting solution was prepared from zirconyl chloride hydrate and yttrium nitrate hydrate. A spin coating technique was used to form films onto either LSCF or LSM. Multiple coatings with drying and a subsequent heat treatment at 400–1000°C after each coating produced thicker films. The film thickness increased with increasing viscosity of the solution and decreasing spinning rate and time. Films of 0.1–0.3 μm thickness for each coating could be obtained with a spinning speeds of 2000 to 3000 rpm and a viscosity between 90 and 190 cp. Reiichi et al. [51] produced a composite electrolyte consisting of a zirconia film about 1 μm thick deposited using the sol–gel method onto a Ni–cermet substrate. A corresponding cell operated with moist H_2 and O_2 exhibited an OCV of 1.0 V at 800°C.

2.1.2.3. Spray pyrolysis method

A schematic diagram of a typical spray pyrolysis setup is shown in Fig. 4. A metal salt solution (usually aqueous or alcoholic) is sprayed onto a hot substrate to obtain the corresponding metal oxide films. Sprayed droplets reaching the substrate surface undergo pyrolytic (endothermic) decomposition. The substrate provides the thermal energy for the decomposition. A sufficiently high force applied to the surface of a liquid in the nozzle causes the emission of droplets. Three different groups of atomizers were employed for the generation of the spray: blast (using a stream of gas at high velocity) [52], ultrasonic (using an ultrasonic irradiation) [53,54] and electrostatic [55] (using a high voltage). The technique of atomization determines the droplet size distribution, efficiency and spray angle. The electrostatic atomization technique leads to almost mono-dispersed drops and also to finer droplets than can be produced by other techniques. Overspray is reduced due to the charged droplets, therefore the electrostatic atomization increases the deposition efficiency.

Spray pyrolysis usually has deposition rates of 1–5 μm h^{-1}. Choy et al. [52] however, report deposition rates of YSZ on porous LSM substrates as high as 60 μm h^{-1}. Dense 50-μm thick YSZ films were also deposited at 650°C. Thin films of calcia-stabilized zirconia (CSZ) were deposited on a LSM porous substrate by spray pyrolysis [56]. The OCV of the cell consisting of 33-μm thick CSZ film, LSM cathode, and Ni–YSZ cermet anode was 0.96 V and the maximum power density was 0.5 W cm^{-2} at 1000°C. Chen et al. [55] deposited YSZ films on GCO substrates. Dense thin YSZ layers of about 1 μm were only found under the several cracked and porous top layers. Such composite electrolyte structures are interesting for intermediate-temperature
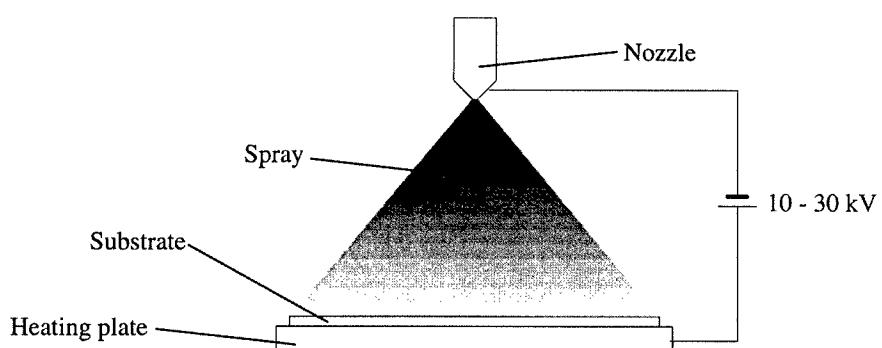

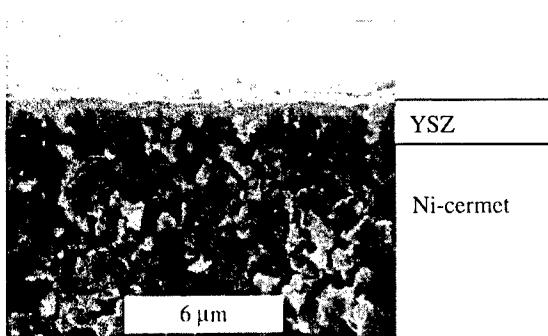Fig. 4. A schematic diagram of a typical spray pyrolysis setup.

Fig. 5. Cross-section of a YSZ film deposited on a porous Ni–cermet substrate [57].

SOFC, because the YSZ-coated ceria electrolytes were found to exhibit a higher open-circuit voltage compared to uncoated ceria [56]. Fig. 5 shows the microstructure of a YSZ layer sprayed on a porous substrate [57]. The zirconia layer was amorphous before heat-treatment. After a treatment at 600°C polycrystalline YSZ could be obtained.

2.2. Physical methods

2.2.1. Thermal spray technology

2.2.1.1. General

Thermal spraying is a generic term for thick (100–500 μm) overlay processes in which coating material is heated in a gaseous medium and projected at high velocity onto a component surface [58]. These processes are probably less applicable to produce thin electrolytes. They may be useful however for the deposition of porous electrodes [59] or electrolytes other than conventional YSZ, e.g. ceria or bismuth oxide, which show significant higher ionic conductivity at intermediate temperatures.

2.2.1.2. Conventional spray techniques

Various techniques can be used depending on material and desired coating performance. These include flame spraying (FS), air plasma spraying (APS), low-pressure plasma spraying (LPPS), detonation flame spraying (DFS), electric arc spraying (EAS), and more recently high-velocity oxyfuel (HVOF) spraying. Common to spraying processes are the high temperatures involved, the rapid quench-

ing of the melted ceramic particles on the cold substrate during deposition, and the thermal treatments required to improve the film density (and therefore to reduce the pore volume). All of them can affect the structure and modify the electrical properties of sprayed films with respect to sintered materials. Commercially available ZrO_2 and Y_2O_3 powders are used. They are manufactured by conventional processing techniques [60] such as mixing grinding, heating, and granulation [61,62].

Scagliotti et al. [63] produced plasma-sprayed yttria-stabilized zirconia films, which were dense, with a few large voids but no open porosity after high-temperature (> 2000 K) vacuum sintering and air annealing. The zirconia films were fully stabilized in the cubic phase with bulk conductivity and an activation energy similar to those of single crystals with the same composition. Varcalle et al. [60] found that only the powder feed rate and the traverse rate were significant factors affecting the deposition thickness. The key to maximize the economics of the zirconia coating deposition is to optimize the powder feed rate and the traverse rate. Injection angle, standoff distance, traverse rate and secondary flow all have a significant contribution to the variation in porosity. Thus, further study concerning porosity should be concentrated on these factors. Arai et al. [64,65] sprayed YSZ powder on porous electrode substrates consisting of LSM and Ni–cermet. The substrates could endure the thermal shock during the plasma-spraying process. The films were gas-tight, but still contained microcracks. Nicoll et al. [66] gave a survey of the critical parameters involved in VPS such as powder chemistry and morphology. Schiller et al. [67] manufactured a multilayer in one consecutive spray process. They produced an entirely plasma sprayed PEN (Positive electrode/Electrolyte/Negative electrode) consisting of the anode, electrolyte and cathode layer on a Ni felt. The anode, electrolyte and cathode layers had a thickness of 80, 70 and 100 μm, respectively. By applying optimized spray parameters with appropriate torches and nozzles, complex coatings, such as graded cermet layers, with a desired material and porosity can be realized. Aihara et al. [68] plasma-sprayed YSZ films on MnO_2 pre-coated lanthanum manganite substrates which were sintered at 1400°C. However, the thickness of the zirconia layer with 100 μm is rather high

and the sample size (15 mm ∅) is relatively small. An OCV of 1.05 V was measured at 1000°C. Henne [69] produced a whole PEN structure by vacuum plasma spraying in one consecutive process. Ni-felts, embedded in a porous sprayed Ni-matrix, served as base compounds and simultaneously as anodic electric contacts. The next layer consists of the Ni/ZrO_2 with gradually reduced content of Ni and decreasing porosity and pore size toward the dense and gas tight zirconia layer. The Perovskite layer was sprayed on the zirconia layer. Power densities of 230 mW cm^{-2} at an operational temperature of 910°C could be obtained. Gruner [70] also used the VPS method to produce a complete PEN-structure in a single run. The power density was 200 mW cm^{-2} at 910°C for an active area of 4.5 cm^2 with an electrolyte thickness of 250 μm.

2.2.2. Laser deposition techniques

2.2.2.1. General

Laser deposition has become a new and important technique for depositing thin films of a variety of materials. The ability to deposit almost any material, preserve the stoichiometry of multicomponent compounds and to carry out reactive deposition has finally been recognized and renewed the interest in this technology [71]. YZP (Yttria-stabilized Zirconia Polycrystals) thin films deposited by pulsed laser

deposition have been known for a couple of years, since the availability of high-energy pulsed UV lasers.

2.2.2.2. Pulsed laser deposition (PLD)

The basic set-up of a laser ablation equipment is shown in Fig. 6. The process involves a number of complex interactions among the process variables such as wavelength, power density, background gas, pressure, target composition, substrate–target distance, substrate temperature, substrate bias and gas–surface interactions. PLD requires temperatures of around 500 to 700°C to deposit high-quality crystalline films. It is relatively easy to produce multilayers by substitution of targets into the path of the laser beam. In a commercial setup the possibility of time-sharing a laser among a number of deposition/analysis chambers has been considered. One of the advantages of PLD is the potential for scaling up to production size and volume.

Murray et al. [72] used the frequency-doubled output (0.53 mm), of a Q-switched Nd:YAG laser (15 ns pulses at 5 Hz) to evaporate the YSZ target. The growth rate was relatively low (0.15–0.5 μm h^{-1}) because of the target's low quantum yield to 0.53-mm YAG radiation. Kokai et al. [73,74] deposited YSZ thin films by XeCl excimer laser ablation using a bulk YSZ target (20 ns pulses, 0.308 mm at 10 Hz). The deposition (1 μm h^{-1}) of dense
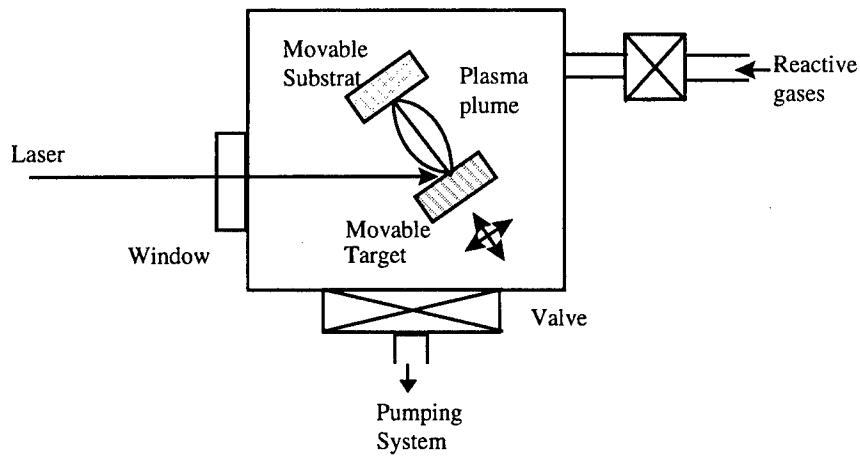

Fig. 6. Laser ablation equipment for deposition of advanced materials. The laser pulse passes through a window and impinges on the target material which is vaporized and deposited on the substrate in the form of a thin film [71].

YSZ films (0.5–2 μm) with excellent adhesive properties at 800°C was demonstrated on a CeO_2–Sm_2O_3 substrate maintained at 500°C in O_2 atmosphere. The post-deposition annealing of the YSZ film at 800°C resulted in the promotion of crystallinity. The film consisted of a cubic phase grown with a predominance of (200) orientation.

Surface melting (sealing) is a potential method to produce shiny surfaces of low roughness on a plasma-sprayed zirconia coating. But the problems of cracks, depressions, islands, etc. have not yet been solved [75,76].

2.2.2.3. Laser spraying

The laser spraying technique uses a carbon dioxide laser beam which is passed parallel to the substrate [77,78]. Thick YSZ layers of 60–150 μm were deposited. The powder, which is supplied through a special device (sometimes with the help of a carrier gas) melts in the laser beam and adheres to the substrate. The process is controlled by the laser power density, substrate temperature, reaction or carrier gases and reactor pressure.

2.2.3. PVD techniques

2.2.3.1. General

Physical vapor deposition (PVD) is a generic term for a variety of sputtering techniques. Radio frequency (RF) sputtering has been most widely used for YSZ film deposition in the production of SOFCs [79–81]. However, YSZ deposition rates during RF sputtering are generally relatively low due to the low sputtering yield of YSZ (0.25 μm h^{-1}). A schematic diagram of the apparatus is shown in Fig. 7. Reactive magnetron sputtering allows much higher deposition rates (2.5 μm h^{-1}) because of the higher sputtering yield. In addition, magnetron sputtering provides ion irradiation of the film during deposition, which has been shown to be crucial for obtaining high-density films at low temperature [82].

The ion-beam-assisted deposition (IBAD) techniques [83] resemble the reactive magnetron sputtering technique, where an ion beam and a reactive background gas are the primary components for producing the coating. Thin films may also be deposited by vacuum evaporation of a target using an electron beam heating device [84]. The deposition rates achieved are in general two orders of mag-
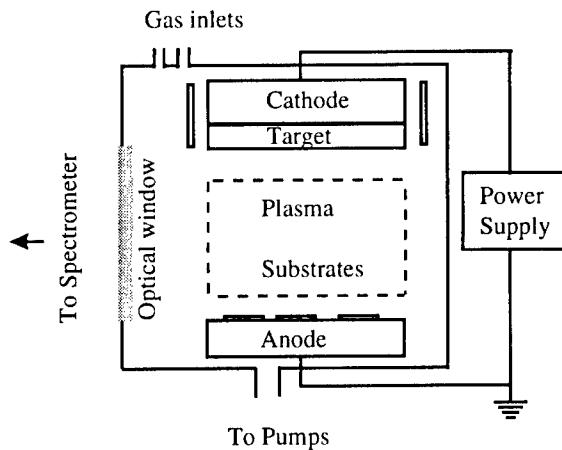

Fig. 7. RF-diode sputtering deposition apparatus [71].

nitude higher than for the above-mentioned methods (typically 1 μm min^{-1}).

2.2.3.2. RF-sputtering technique

Sputtering deposition is widely used to grow alloy and component films in which one or more of the constituent elements are volatile. Low-defect-density films of high-melting-point materials can be grown on unheated substrates because phase formation is primarily governed by kinetics, rather than by thermodynamics.

An evacuated chamber is filled with the sputtering gas. A large negative voltage is applied to the cathode. The sputtering gas forms a self-sustained glow discharge. RF-excitation allows use of a nonconducting target or a metal target surface that has become oxidized. Physical sputtering of the target occurs when positive ions from the plasma that are accelerated across the dark space strike the target surface. Material, which is ejected by a momentum transfer process, is mostly uncharged and moves between the electrodes where it becomes thermalized and condenses on any surface. A metal oxide film is grown by sputtering a metal target in a discharge containing oxygen, usually in conjunction with a noble gas. The sputtering process can dissociate an oxidized target surface. Therefore, the sputtered flux may consist of both metal atoms and metal oxide molecules. The metal, metal oxide and oxygen species that arrive at the substrate are adsorbed and ultimately incorporated into stable nuclei to form a

continuous film. These processes are the major factors determining film chemistry, short-range atom order, crystallography and microstructure.

Ceramic thin films may be deposited on various substrate materials. During sputtering the substrate temperature usually does not exceed 70°C. Annealing may be carried out after sputtering deposition both in order to repair damage from sputtering and to study effects of annealing temperature on the structural and electrical properties. Typical film growth rates are 0.15–0.5 μm h^{-1}.

YSZ films deposited on various substrates were found to be of cubic structure [69,70]. Annealing treatment at 800–900°C led to cracking of the YSZ films. However, thermal post-treatment at 1500°C improved the quality of the film by crack healing [69]. The authors found a severely cracked film, (after heating to $T = 900$°C) but no delimitation. Stress in the YSZ film is induced by differences in thermal expansion coefficients of YSZ ($\alpha = 10.5 \times 10^{-6}$ K^{-1}) and CeO$_2$ ($\alpha = 12.5 \times 10^{-6}$ K^{-1}). As the substrate is much thicker than the film, it is to be expected that the film will be under a large (biaxial) tensile stress at heating. The higher the temperature of the treatment, the greater was the crack density [85]. The problem of high tensile stress in thin films due to heat treatment may be avoided by introducing compressive stress in the film during or after sputtering.

A correlation between deposition rate and RF power was demonstrated by Charpentier et al. [86]. They deposited zirconia films on to dense nickel or silica substrates. Growth rates of 0.25 μm h^{-1}, 0.3 μm h^{-1}, and 0.5 μm h^{-1} for 400, 500 and 800 W, respectively, were obtained. They observed that heating of the substrate at 500°C results in a surface without apparent cracks compared to a situation without heating. Gao et al. [87] deposited zirconia thin films of about 0.5 μm on glass and silicon substrates. The film growth rate increased approximately linearly with power between 300 and 500 W but did not change with argon gas flow-rate or pressure. After deposition, the films were annealed in air at 500–700°C.

2.2.3.3. Reactive DC current magnetron sputtering

This method was first used by Konushi [88] to deposit YSZ for epitaxial growth. The principles for deposition of electrolyte films or Ag–cermets are straightforward. Deposition is initiated, after starting the oxygen flow by rotating the substrate into position over the target. The steady-state temperature of the substrate reaches 70°C during deposition. The substrate may be heated. By changing the sputter sources and sputter parameters a wide variety of different compositions and structures with specific properties may be obtained. Film deposition rates mainly depend on oxygen flow-rate. The decrease in deposition rate is attributed to the formation of oxides on the target surfaces, which are generally characterized by a much lower sputtering yield than the metals.

Jones [89] used this method to deposit ZrO$_2$ with a high deposition rate up to 9 μm h^{-1}. Wang and Barnett were successful in producing fully dense films at a deposition temperature of 350°C [90,91]. Their Ag–YSZ cermets had a high conductivity and a low overpotential during operation. Multilayer electrolytes for SOFCs were operated at temperatures around 750°C. Three-layer cells consisting of 1-μm thick Ag–YSZ cermet, a 14–20-μm thick YSZ electrolyte, and a 1–2.5-μm thick Ni–YSZ cermet were deposited on polished alumina disks. The cell exhibited an OCV of 0.8 V, less than the expected 1.1 V at 750°C and a maximum power density of 35 mW cm^{-2}.

Charpentier et al. [86] deposited a 4-μm thick YSZ film on a porous nickel substrate at 500°C. They found that the porosity of the substrate had a crucial influence on the quality of the films. The pore size of the substrate must be limited to 2 μm. The maximum deposition thickness which could be reached in one step is 4 μm. Honegger et al. [92] deposited a bilayer of YSZ (4 μm)/CYO (Y$_2$O$_3$ doped ceria) (1 μm) electrolytes on anode substrates (35 mm $\varnothing$). The cell showed maximum power densities of up to 1 W cm^{-2} at 720°C. OCV values of 0.98 V were obtained at 700°C. The low OCV values were attributed to leakage of oxygen from the cathode side to the anode chamber. The reported value of the deposition rate was 5 μm h^{-1} for YSZ. Badwal et al. [93] measured a power density of 350 mW cm^{-1} at 800°C for a cell (17 mm $\varnothing$) with YSZ thin electrolytes.

Kleinlogel et al. [94] used this method to deposit CYO–YSZ bilayers on cathode substrates (50 mm $\varnothing$). Thin 10 mol.% yttria-doped ceria solid solutions and 8 mol.% yttria-stabilized zirconia bilayers were

deposited on porous cathode substrates using DC magnetron sputtering in O_2–Ar plasmas using CeY-alloy and ZrY-alloy targets. Dense, microcolumnar film structures were already obtained at substrate temperatures as low as 250°C during deposition. Cell tests were performed using air as the oxidant and a humidified mixture of 70% N_2/30% H_2 as the fuel. An open-circuit voltage of 1.06 V was obtained at 700°C, indicating that the electronic conduction of the CYO layer was blocked by the YSZ layer. A maximum power output of 230 mW cm^{-2} (0.4 V 600 mA cm^{-2}) has been achieved. Fig. 8 shows a cross-sectional view of the sputtered electrolyte bilayer.

2.3. Ceramic powder processing methods

2.3.1. Thick film techniques

2.3.1.1. General

The tape casting, screen printing, and bulk sintering techniques have been extensively used for preparing electrolytes of a few tens of microns to >200 µm thickness. Although satisfactory results with SOFC prepared with the techniques described previously have been obtained at high temperatures (>950°C), the upscaling of component size still has remained as a major problem [95,96]. Tape-casting and screen-printing techniques could be potential candidates for producing electrolytes with diameters of 10–30 mm thicknesses in an inexpensive way.

2.3.1.2. Screen-printing

A highly viscous paste consisting of a mixture of ceramic powder, organic binder and plasticizer is forced through the open meshes of a screen using a squeegee. Parameters such as grain size, grain form, surface properties and packing density of the powder have to be optimized. The screen-printed films are dried and sintered at high temperatures. The sintering temperature, time and atmosphere are also important for good-quality films [97].

There are few publications on screen-printed dense films of stabilized zirconia. Bauza et al. [98] produced both porous and dense films, with a high ratio of electrode area to thickness which can be 1–2 orders of magnitude higher than that of conventional disks (pressed and sintered). Porosity arises mainly due to the agglomeration of the small particles in commercial powders. It was shown by Gödickemeier [99] (see Fig. 9) that electrolytes can be screen-printed on porous or dense substrates (Ni–YSZ cermets). More recently, Cassidy used the screen-printing technique as a method to deposit a zirconia layer onto a tape-cast anode support. The green anode–electrolyte bilayer was sintered resulting in an electrolyte thickness of around 8 µm. An OCV of 0.94 V has been achieved [100,101].

2.3.1.3. Tape casting

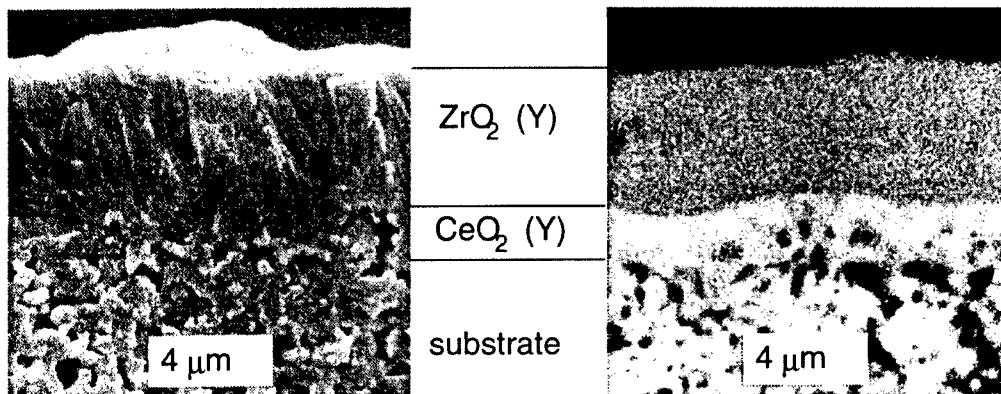Starting from ceramic powders, green tapes are produced which may be then cut into different

Fig. 8. SEM picture (left) and elemental analysis (right) of an electrolyte bilayer deposited via DC sputtering on top of a porous cathode substrate. It consists of a 1-µm thick CeO_2 (Y) chemical compatibility layer and a 4-µm thick ZrO_2 (Y) electrolyte layer [94].
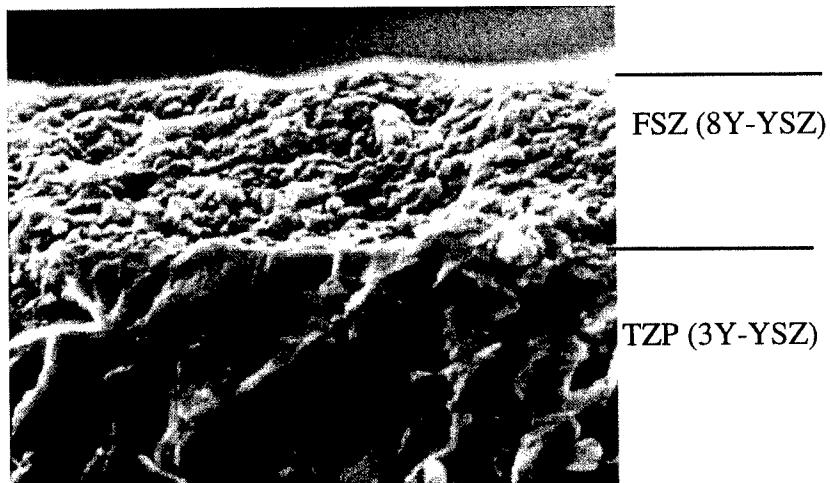
Fig. 9. SEM micrograph of a zirconia layer processed via screen-printing. Fracture surface: 8Y–YSZ layer on a 3Y–YSZ substrate [99].

shapes. The preparation of the slurry for this technique is similar to that of the paste for the screen printing method, and is achieved by conventional methods. By casting the slurry directly onto the joining substrate, unnecessary handling steps may be avoided and less binder and plasticizer have to be added [102]. Cermet fabrication (25–100 μm) is also possible by tape casting [103].

Tape casting has been developed to produce large-area, thin, flat ceramic layers for the monolithic and planar SOFC. Van Berkel et al. [104] used a multilayer tape casting technique, with which an electrode layer is tape-cast on top of a green thin electrode layer. A 50 × 50 mm² bilayer of 10 μm zirconia on a YSZ/Ni-anode tape could be manufactured. Ihringer et al. [105] used a water-based tape casting method and produced 0.6–10 μm YSZ layers which were cast on 200–250 μm NiO/YSZ anode substrates and co-sintered at 1350°C. After sintering, the complementary cathode was deposited. The cells (31 mm ∅) exhibited a power density of 580 mW cm⁻² with an OCV of 1.01 V at 760°C. Will [106] produced thin zirconia tapes and laminated them at 50°C with a separately produced green Ni–cermet tape. The resulting microstructure after sintering of the bilayer is shown in Fig. 10. The closed porosity of the zirconia layer was characterized by isolated round holes with diameters of 3–5 μm. They were proba-

bly formed due to the high organic content in the green tape.

2.3.1.4. Slurry coating technique

Thin film electrolytes may be fabricated also by the slurry coating method [60,95]. A water suspension with a small amount (< 5 wt.% of YSZ) is used to coat a substrate. The thin films were then dried at room temperature, pre-heated at elevated temperatures, and finally sintered. This cycle is normally repeated 5–10 times. Using an ethanol suspension of YSZ [95] may significantly shorten the drying step. Normally repeated coating may eliminate cracks. Thin and dense films with no observable crack were produced by Arai et al. [107]. Aizawa et al. [108] used the slurry coating technique to deposit a 20–30-μm thick zirconia film on tubular cathode substrates. The films were dense and such cells exhibited an OCV close to the theoretical value. Nam et al. [109] deposited YSZ films on pressed porous NiO/YSZ substrates. A 12 wt.% YSZ slurry was prepared and dip-coated on one side of the substrate. The film-coated anode was sintered at 1150°C for 1 h. The dipping–heating cycle was repeated to reach the desired thickness of the electrolyte followed by a final sintering step at 1430°C for 4 h. With two coatings the final electrolyte thickness was 10 μm. An YSZ suspension was deposited on partially
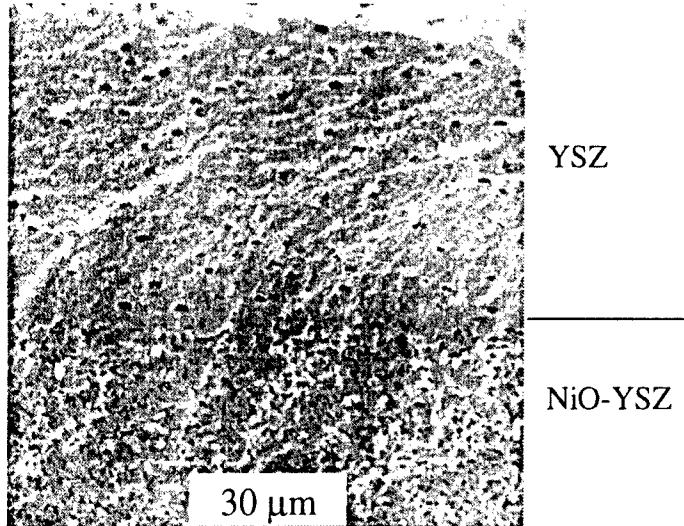
Fig. 10. SEM micrograph of a zirconia layer fabricated via transfer printing after sintering. Fracture surface: zirconia on top, Ni–cermet below [106].

sintered anode or cathode substrates by Visco and Souza [8,110,111]. The substrates (25 mm Ø) were pre-fired to the extent that the shrinkage profile of the substrate exceeds that of the YSZ film. In this way, the film is under compression rather than tension while sintering, and highly dense, crack-free films, 4–10 μm thick, were deposited in a single step. The cell exhibited a power output of 650 mW cm^{-2} at 800°C using a sputtered layer of Pt.

Ni–YSZ/YSZ/LSM cells built with this technique exhibited an exceptionally high power density of 1930 mW cm^{-2} at 800°C. Will [106] coated porous pre-sintered Ni–cermet tapes with zirconia suspensions. After drying, the coating was repeated. Fig. 11 shows the resulting microstructure after repeating the coating process five times followed by sintering of the bilayer. The zirconia layer (5 μm) adhered very well to the anodic substrate. Some of the zirconia
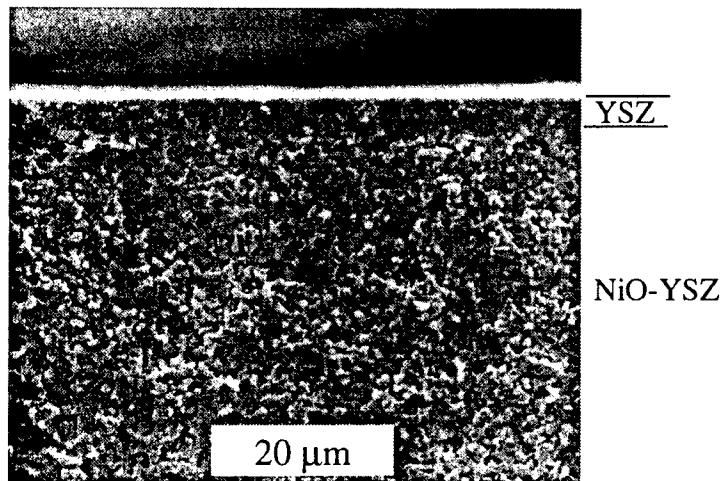

Fig. 11. SEM micrograph of a zirconia layer processed via slurry coating after sintering. The coating–drying cycle was repeated five times. Fracture surface: zirconia on top, Ni–cermet substrate below [106].

was deposited inside the porous substrate, which results in a very good mechanical interlocking.

2.3.1.5. Slip casting

Thick films may also be prepared using the slip casting process [112,113]. The slip (1:3 vol.% powder:water) was on a porous mold and the excess slurry was drained. After drying, the green compact was removed from the mold and then sintered. The density of the sintered samples was $<95\%$ and a small number of pores could be observed in SEM.

2.3.1.6. Filter pressing

The efficiency of the slip casting process normally is rather low. Using a low vacuum may enhance it. Förthmann et al. [114] coated gastight zirconia layers on presintered porous anode substrates with sizes up to 100×100 mm. Coating was performed in two steps: first, closing the open surface pores of the substrate using a 0.15–1.5 μm interlayer consisting of YSZ/NiO, and, second, preparing a 15–20 μm electrolyte layer by using a pure YSZ suspension. The anode substrate/electrolyte unit was subsequently sintered at 1500°C. After deposition of the cathode the cells exhibited a current density of 430 mW cm^{-2} at 800°C. Cells with a 15-μm thick electrolyte layer yield power densities of 230 W cm^{-2} at 750°C [1].

2.3.2. Thin film techniques

2.3.2.1. General

Recently, tape calendering and electrophoretic deposition techniques were applied to produce YSZ thin film electrolytes. Transfer printing is a new method for high-tech ceramics, however, like the other two methods, transfer printing is already known from conventional ceramic processing techniques.

2.3.2.2. Tape calendering

The process involves squeezing a softened thermoplastic polymer/ceramic powder mixture between two rollers to produce a continuous sheet of material. Individual sheets can be calendered and joined to form the multilayer tapes required for SOFCs. Tape calendering of YSZ ceramics was first successfully applied by Minh et al. [9,10] for the production of monolithic and flat plate SOFCs. Minh et al. pro-

duced thin (1–10 μm) zirconia electrolyte layers on porous Ni–YSZ cermet supports. Flat plate SOFCs with sizes of 100×100 mm^2 were operated at 600 to 800°C with a platinum paint cathode. A power density of 0.27 W cm^{-1} was achieved at 800°C. The OCV of the cell was 1.1 V, close to the theoretical value.

2.3.2.3. Electrophoretic deposition (EPD)

This technique is one of the colloidal processes in ceramic production and has advantages of short formation time, little restriction of the shape of substrate, and suitability for mass production. In EPD, charged powder particles are deposited from a suspension onto a metallic electrode or a conductive substrate by the application of a DC electric field. The rate of deposition is controllable via the applied potential and can be very fast (1 mm min^{-1}) [115]. Because the green coating contains few or no organics, no burnout procedures are required, and a deposit can be formed on the outside and/or the inside of the electrode. Various kinds of solvents have been applied. Ishihara et al. produced dense YSZ films with a uniform thickness using acetylacetone as solvent. Zirconia films were deposited on cathodic and anodic substrates with electroless plated Pt as anode or cathode [116]. The open-circuit voltage and the maximum power density achieved were 1.03 V and 1.84 W cm^{-2} (1000°C), respectively. The thickness of the YSZ films can be controlled easily by the time and applied voltage. Hruschka [117] and Will [106] deposited zirconia films on pressed or tape-cast anodic substrates with diameters of up to 120 mm. An open-circuit voltage of 0.9 V at 700°C and a power density of 200 mW cm^{-2} were reported. Fig. 12 shows a cross-section of a sintered EPD-derived zirconia layer. The substrate for the deposition was a tape cast Ni–cermet. After co-sintering of the two layers, the substrate exhibited a high porosity, whereas the zirconia layer was dense with a small amount of closed porosity.

2.3.2.4. Transfer printing

This method involves screen-printing a ceramic organic-based suspension onto a soluble gum paper and drying this layer. Subsequently, an acrylic resin covercoat is screen-printed over the electrolyte layer.
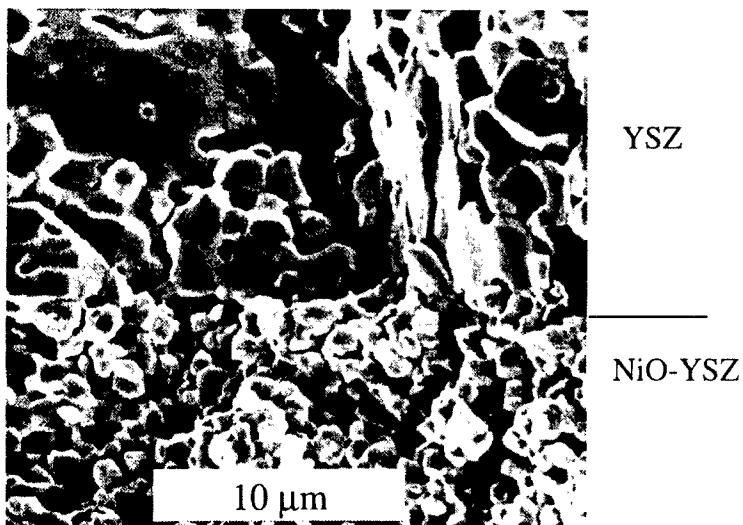
Fig. 12. SEM micrograph of a zirconia layer processed via electrophoretic deposition after sintering. Fracture surface: zirconia on top, Ni–cermet substrate below [117].

The electrolyte layer with the covercoat is released from the gum paper by immersion in water, which dissolves the gum. The layer with the covercoat is then squeezed over the appropriate substrate, dried and fired to full density.

Prica et al. [118] applied this method to fabricate a

1.2-mm layer of yttria-stabilized zirconia electrolyte deposited onto a cermet tube. An OCV of 0.95 V was reached at 1000°C. Will [106] applied transfer printing of zirconia layers on pre-sintered Ni–cermet tapes. A micrograph of the sintered bilayer is shown in Fig. 13.
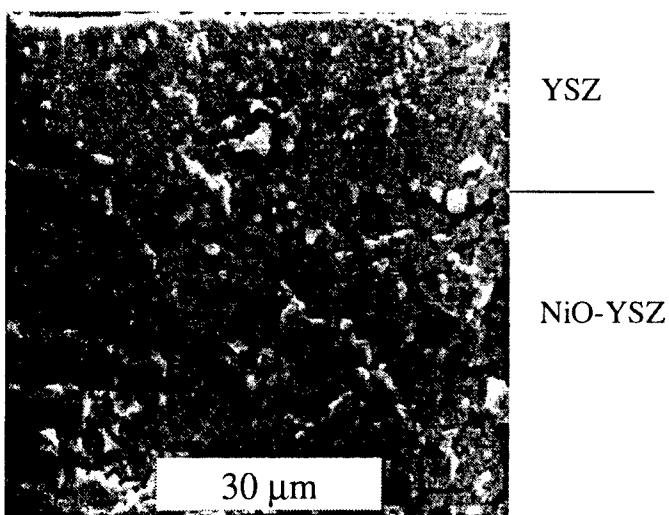

Fig. 13. SEM micrograph of a zirconia layer processed via transfer printing after sintering. Fracture surface: zirconia layer on top, Ni–cermet substrate below [106].

3. Summary and conclusions

This survey shows that many methods for depositing thin and dense YSZ films on dense or porous substrates exist that are based on ceramic powder techniques or chemical and physical processes.

These techniques mainly differ in deposition rates, substrate temperature during deposition, precursor materials, necessary equipment, expenditure, and in the quality of the resulting films. These described methods are compared and classified in Table 1.

Although methods such as CVD and PVD are well

Table 1
Comparison of the methods for producing thin and dense electrolytes for SOFC applications

Technique	Film characteristics		Process features	
	Microstructure	Deposition rate or thickness	Cost	Characteristics and limitations
Vapor phase				
Thermal spray technologies		$100–500 \ \mu m \ h^{-1}$		High deposition rates, various compositions possible, thick and porous coatings, high temperatures necessary
EVD	Columnar structures	$3–50 \ \mu m \ h^{-1}$	Expensive equipment and processing costs	High reaction temperatures necessary, corrosive gases
CVD	Columnar structures	$1–10 \ \mu m \ h^{-1}$	Expensive equipment	Various precursor materials possible, high reaction temperatures necessary, corrosive gases
PVD (RF and magnetron sputtering)	Columnar structures	$0.25–2.5 \ \mu m \ h^{-1}$	Expensive equipment	Tailor-made films, dense and crack-free films, low deposition temperatures, multipurpose technique, relatively small deposition rate
Laser ablation			Expensive equipment (laser)	Intermediate deposition temperatures, difficult upscaling, time-sharing of laser, relatively small deposition rate
Spray pyrolysis	Amorphous to polycrystalline	$5–60 \ \mu m \ h^{-1}$	Economical	Robust technology, upsealing possible, easy control of parameters, corrosive salts, post-thermal treatment usually necessary
Liquid phase				
Sol-gel, Liquid precursor route	Polycrystalline	$0.5–1 \ \mu m$ for each coating	Economical	Various precursors possible, very thin films, low temperature sintering, coating and drying/heating processes have to be repeated 5–10 times, crack formation during drying, many process parameters
Solid phase				
Tape casting	Polycrystalline slightly textured	$25–200 \ \mu m$		Robust technology, upscaling possible, crack formation
Slip casting and slurry coating	Polycrystalline	$25–200 \ \mu m$	Economical	Robust technology, crack formation, slow
Tape calendering	Polycrystalline	$5–200 \ \mu m$		Upscaling possible, co-calendering possible
EPD	Polycrystalline	$1–200 \ \mu m$		Short formation time, little restriction to shape of substrate, suitable for mass production, high deposition rates, inhomogeneous thickness
Transfer printing	Polycrystalline	$5–100 \ \mu m$	Economical	Robust technology, rough substrate surfaces possible, adhesion on smooth substrates difficult
Screen printing	Polycrystalline	$10–100 \ \mu m$	Economical	Robust technology, upscaling possible, crack formation

established, only simple stoichiometric compounds can be deposited, as each component has to be evaporated at different temperatures due to their different vapor pressures. The constituents have to be deposited from independently controlled sources, which add complexity to the system. Ceramic powder methods on the other hand have the potential to be good candidates for complicated stoichiometric compositions or for mixtures of materials.

It is assumed that CVD/EVD and spray pyrolysis will become key technologies for depositing thin electrolyte layers. The investment cost for the CVD apparatus is high [119] compared to droplet and powder techniques whereas the set-up for the spray pyrolysis is inexpensive and simple. This latter method has advantages of uniform coating of large areas, easy control of deposition rates and film thickness, inexpensive experimental set-up under atmospheric conditions [120]. On the other hand, all liquid precursor methods such as sol–gel, spray pyrolysis and slurry coating, are time-, labor- and energy-intensive because coating and drying/sintering has to be repeated in order to avoid crack-formation. Tape casting, electrophoresis, screen-printing, and transfer printing are considered very cost-effective and promising techniques. Whilst these methods may be appropriate for small area cells, the large shrinkage associated with the removal of polymeric binders and plasticizers in subsequent sintering steps reduces the quality of large (> 10 cm $\oslash$) area cells. Moreover, it is often difficult to retain adequate porosity within the supporting electrode structures during the cofiring stage for densification of the thick film electrolytes.

References

[1] H.P. Buchkremer, U. Dickmann, L.G.J. de Haart, H. Kabs, U. Stimming, D. Stöver, in: U. Stimming, S.C. Singhal, H. Tagawa, W. Lehnert (Eds.), Proc. 5th Int. Conf. Solid Oxide Fuel Cells, Electrochemical Society, Pennington, NJ, 1997, p. 160.

[2] B.C. Steele, in: U. Bossel (Ed.), Proc. 1st European Solid Oxide Fuel Cell Forum, European SOFC Forum, Oberrohrdorf, Switzerland, 1994, p. 375.

[3] K. Krist, J.D. Wright, in: S.C. Singhal, H. Iwahara (Eds.), Proc. 3rd Int. Symp. on Solid Oxide Fuel Cells, Electrochemical Society, Pennington, NJ, 1993, p. 782.

[4] L.G.J. de Haart, Th. Hauber, K. Mayer, U. Stimming, in: B. Thorstensen (Ed.), Proc. 2nd European Solid Oxide Fuel Cell Forum, European SOFC Forum, Oberrohrdorf, Switzerland, 1996, p. 229.

[5] N.Q. Minh, K. Montgomery, in: U. Stimming, S.C. Singhal, H. Tagawa, W. Lehnert (Eds.), Proc. 5th Int. Conf. Solid Oxide Fuel Cells, Electrochemical Society, Pennington, NJ, 1997, p. 153.

[6] K. Honegger, B. Batawi, Ch. Sprecher, R. Dietheim, in: U. Stimming, S.C. Singhal, H. Tagawa, W. Lehnert (Eds.), Proc. 5th Int. Conf. Solid Oxide Fuel Cells, Electrochemical Society, Pennington, NJ, 1997, p. 321.

[7] J. Schoonman, J.P. Dekker, J.W. Briers, N.J. Kiwiet, Solid State Ionics 46 (1991) 299.

[8] S. de Souza, S.J. Visco, L.C. de Jonghe, in: B. Thorstensen (Ed.), Proc. 2nd European Solid Oxide Fuel Cell Forum, European SOFC Forum, Oberrohrdorf, Switzerland, 1996, p. 677.

[9] N.Q. Minh, T.R. Armstrong, J.R. Esopa, J.V. Guiheen, C.R. Home, F.S. Liu, T.L. Stillwagon, J.J. Van Ackeren, in: F. Gross, P. Zegers, S.C. Singhal, O. Yamamoto (Eds.), Proc. 2nd Int. Symp. on Solid Oxide Fuel Cells, Commission of the European Communities, 1991, p. 93.

[10] N.Q. Minh, K. Montgomery, in: U. Stimming, S.C. Singhal, H. Tagawa, W. Lehnert (Eds.), Proc. 5th Int. Conf. Solid Oxide Fuel Cells, Electrochemical Society, Pennington, NJ, 1997, p. 153.

[11] H. Yamane, T. Hirai, J. Mater. Sci. Lett. 6 (1987) 1229.

[12] H. Yamane, T. Hirai, J. Cryst. Growth 94 (1989) 880.

[13] A.C. Jones, Chem. Vap. Deposition 4 (1998) 169.

[14] Y. Takahashi, T. Kawae, M. Nasu, J. Cryst. Growth 74 (1986) 409.

[15] K.-W. Chour, H. Chen, R. Xu, Thin Solid Films 304 (1997) 106.

[16] M. Aizawa, C. Kobayashi, H. Yamane, T. Hirai, J. Ceram. Soc. Jpn. 101 (1993) 283.

[17] D.A. Glocker, S.I. Shah (Eds.), Handbook of Thin Film Process Technology, Institute of Physics Publishing, 1995.

[18] A.O. Isenberg, in: J.D.E. McIntyre, S. Srinsvan, F.G. Will (Eds.), Proc. Symp. Electrode Materials Processes for Energy Conversion and Storage, Vol. 77, Electrochemical Society, Pennington, NJ, 1977, p. 572.

[19] U. Pal, S.C. Singhal, J. Electrochem. Soc. 137 (1990) 2937.

[20] Y.-S. Lin, Chemical and electrochemical vapor deposition of zirconia–yttria solid solutions in porous ceramic media, Ph.D. Thesis, University of Twente, The Netherlands, 1992.

[21] J.P. Dekker, V.E.J. van Dieten, J. Schoonman, Solid State Ionics 51 (1992) 143.

[22] L.G.J. de Haart, Y.S. Lin, K.J. de Vries, A.J. Burggraaf, Solid State Ionics 47 (1991) 331.

[23] Z. Ogumi, Y. Uchimoto, Y. Tsuji, Z. Takehara, J. Appl. Phys. 72 (1992) 1577.

[24] Z. Ogumi, Y. Uchimoto, Y. Tsuji, Z. Takehara, Solid State Ionics 58 (1992) 345.

[25] J.P. Dekker, P.J. van der Put, R.R. Nieuwenhuis, H.J. Veringa, J. Schoonman, in: Proc. Euro-CVD, Glasgow, Scotland, 1991.

[26] V.E.J. van Dieten, J. Schoonman, Solid State Ionics 57 (1992) 141.

[27] J.L. Deschanvres, F. Cellier, G. Delabouglise, M. Labeau, M. Langlet, J.C. Joubert, J. Appl. Phys. C5 (1989) 695.

[28] T. Ioroi, Y. Uchimoto, Z. Ogumi, Z.I. Takehara, in: M. Dokiya, O. Yamamoto, H. Tagawa, S.C. Singhal (Eds.), Proc. 4th Int. Symp. Solid Oxide Fuel Cells, Vol. 95-1, Electrochemical Society, Pennington, NJ, 1995, p. 603.

[29] A.O. Isenberg, in: Proc. ECS Symp. Electrode Materials, Processes for Energy Conversion and Storage, Vol. 77-6, 1977, p. 963.

[30] G.-Z. Cao, H.W. Brinkman, J. Meijerink, K.J. de Vries, A.J. Burggraaf, J. Am. Ceram. Soc. 76 (9) (1993) 2201.

[31] H. Sasaki, S. Otoshi, M. Suzuki, T. Sogi, A. Kajimura, N. Sugiuara, M. Ippommatsu, Solid State Ionics 72 (1994) 253.

[32] K. Nord-Varhaug, C.H. Chen, E.M. Kelder, F.P.F. van Berkel, J. Schoonman, in: B. Thorstensen (Ed.), Proc. 2nd European Solid Oxide Fuel Cell Forum, European SOFC Forum, Oberrohrdorf, Switzerland, 1996, p. 333.

[33] R.C. Mehrotra, J. Non-Cryst. Solids 100 (1988) 1.

[34] D. Ganguli, D. Kundu, J. Mater. Sci. Lett. 3 (1984) 503.

[35] D. Kundu, P.K. Biswas, D. Ganguli, J. Thin Solid Films 163 (1988) 273.

[36] P. Peshev et al., Mat. Res. Bull. 27 (1992) 1269.

[37] P. Papet et al., J. Mat. Sci. 24 (1989) 3850.

[38] T.W. Kueper, S.J. Visco, L.C. De Jonghe, Solid State Ionics 52 (1992) 251.

[39] C. Sakurai, T. Fukui, M. Okuyama, J. Am. Ceram. Soc. 76 (1993) 1061.

[40] K. Yamada, T.Y. Chow, T. Horihata, M. Nagata, J. Non-Cryst. Solids 100 (1989) 316.

[41] E. Kato, M. Ezoe, K. Daimon, in: S. Somiya, N. Yamamoto, H. Yanagida (Eds.), Science and Technology of Zirconia III, Proc. Advances in Ceramics, Vol. 24, American Ceramic Society, Westerville, OH, 1988, p. 975.

[42] P. Papet, J. Mat. Sci. 24 (1989) 3850.

[43] C.J. Brinker, A.J. Hurd, K.J. Ward, in: L.L. Hench, D.R. Ulrich (Eds.), Ultrastructure Processing of Advanced Ceramics, Wiley, New York, 1988, p. 223.

[44] A.J. Hurd, C.J. Brinker, in: B.J.J. Zelinski, C.J. Brinker, D.E. Clark, D.R. Ulrich (Eds.), Better Ceramics through Chemistry, Vol. IV, North-Holland, New York, 1990, p. 575.

[45] C.J. Brinker, G.W. Scherer, Sol-Gel Science, Academic Press, New York, 1990.

[46] W.J. Daughton, S.L. Givens, J. Electrochem. Soc. 129 (1982) 173.

[47] K. Mehta, R. Xu, Y.V. Virkar, J. Sol-Gel Science and Technology 11 (1998) 203.

[48] S.W. Nam, S.-G. Kim, S.-P. Yoon, S.-A. Hong, S.-H. Hyun, in: Proc. Fuel Cell Seminar, Palm Springs, Nov. 16–19, 1998, p. 60.

[49] C.C. Chen, M.M. Nasrallah, H.U. Anderson, Solid State Ionics 70/71 (1994) 101.

[50] H.U. Anderson, C.C. Chen, M.M. Nasrallah, Method of coating a substrate with a metal oxide film from an aqueous solution comprising a metal cation and a polymerizable organic solvent, US Patent No. 5,494,700, February 27, 1996.

[51] C. Reiichi, Y. Fumikatsu, Y. Junichi, in: Proc. MRS Fall Meeting, 496, Warrendale, PA, 1998, p. 181.

[52] K.L. Choy, in: W.E. Lee (Ed.), British Ceramic Proc., Vol. 54, 1995, p. 65.

[53] H. Ruiz, H. Vesteghem, A.R. Di Giampaolo, J. Lira, J. Surface and Coatings Technology 89 (1997) 77.

[54] J.L. Deschanvres et al., J. de Physique 50 (1989) 695.

[55] C.H. Chen, K. Nord-Varhaug, J. Schoonman, J. Mater. Synthesis and Processing 4 (1996) 189.

[56] T. Setoguchi, M. Sawano, K. Eguchi, H. Arai, Solid State Ionics 40–41 (1990) 502.

[57] D. Perednis, unpublish. results, Department of Materials, Nonmetallic Materials, ETH, Zurich, 1998.

[58] A.J. Sturgeon, Materials World June (1993) 351.

[59] L.W. Tai, P.A. Lessing, J. Am. Ceram. Soc. 74 (1991) 501.

[60] D.J. Varcalle Jr., G.R. Smolik, G.C. Wilson, G. Irons, J.A. Walter, Mater. Res. Soc. Symp. Proc. 155 (1989).

[61] G.M. Ingo Am., J. Am. Ceram. Soc. 74 (1991) 381.

[62] P.D. Harmsworth, R. Stevens, J. Mater. Sci. 27 (1992) 616.

[63] M. Scagliotti, F. Parmigiani, G. Samoggia, G. Lanzi, D. Richon, J. Mater. Sci. 23 (1988) 3764.

[64] T. Setoguchi, K. Eguchi, H. Arai, J. Vacuum 46 (1991) 1601.

[65] H. Arai, K. Eguchi, T. Setoguchi, R. Yamaguchi, in: S.C. Singhal, H. Iwahara (Eds.), Proc. 3rd Int. Conf. Solid Oxide Fuel Cells, Electrochemical Society, Pennington, NJ, 1991, p. 167.

[66] A.R. Nicoll, A. Salito, K. Honegger, Solid State Ionics 52 (1992) 269.

[67] G. Schiller, R. Henne, M. Lang, in: U. Stimming, S.C. Singhal, H. Tagawa, W. Lehnert (Eds.), Proc. 5th Int. Conf. Solid Oxide Fuel Cells, Electrochemical Society, Pennington, NJ, 1997, p. 635.

[68] Y. Aihara, S. Ito, S. Kawasaki, in: M. Dokiya, O. Yamamoto, H. Tagawa, S.C. Singhal (Eds.), Proc. 4th Int. Conf. Solid Oxide Fuel Cells, 1995, p. 180.

[69] R. Henne, E. Fendler, M. Lang, in: U. Bossel (Ed.), Proc. 1st European Solid Oxide Fuel Cell Forum, European SOFC Forum, Oberrohrdorf, Switzerland, 1994, p. 617.

[70] H.R. Gruner, H. Tannenberger, in: U. Bossel (Ed.), Proc. 1st European Solid Oxide Fuel Cell Forum, European SOFC Forum, Oberrohrdorf, Switzerland, 1994, p. 611.

[71] A. Ahmed, E. Ahmed, Materials World June (1993) 344.

[72] P.T. Murray, J.D. Wolf, J.A. Meseher, J.T. Grant, N.T. McDevitt, J. Mater. Lett. 5 (1987) 250.

[73] F. Kokai, K. Amano, H. Ota, F. Umemura, J. Appl. Phys. A54 (1992) 340.

[74] F. Kokai, K. Amano, H. Ota, Y. Ochiai, F. Umemura, J. Appl. Phys. 72 (1992) 699.

[75] K.M. Jasim, R.D. Rawlings, D.R.F. West, J. Mat. Sci. 26 (1991) 909.

[76] K.M. Jasim, R.D. Rawlings, D.R.F. West, J. Mat. Sci. 27 (1992) 3903.

[77] K. Tsukamoto, F. Uchiyama, Y. Ohno, Y. Kage, Surface Eng. 6 (1990) 45.

[78] K. Tsukamoto et al., Solid State Ionics 40/41 (1990) 1003.

[79] Y. Miyahara, J. Appl. Phys. 71 (1992) 2309.

[80] C.R. Aita, H.-K. Kwok, J. Am. Ceram. Soc. 73 (1990) 3209.

[81] K. Nakagawa, H. Yohioka, C. Kuroda, M. Ishida, Solid State Ionics 35 (1989) 249.

[82] J.A. Thornton, J. Vac. Sci. Technol. 11 (1974) 666.

[83] F.A. Smidt, Int. Mater. Rev. 35 (1990) 61.

[84] H. Michibata, T. Namikawa, Y. Yamazaki, Denki Kagaku 58 (11) (1990) 1070.

[85] K. Mehta, S.J. Hong, J.-F. Jue, A.V. Virkar, in: S.C. Singhal, H. Iwahara (Eds.), Proc 3rd Int. Symp. on Solid Oxide Fuel Cells, Electrochemical Society, Pennington, NJ, 1993, p. 92.

[86] P. Charpentier, P. Fragnaud, D.M. Schleich, C. Lunot, in: U. Stimming, S.C. Singhal, H. Tagawa, W. Lehnert (Eds.), Proc. 5th Int. Conf. Solid Oxide Fuel Cells, Electrochemical Society, 1997, p. 1169.

[87] Q.-H. Gao, R.E. Rocheaeau, B.Y. Liaw, in: S.C. Singhal, H. Iwahara (Eds.), Proc. 3rd Int. Conf. Solid Oxide Fuel Cells, Electrochemical Society, Pennington, NJ, 1993, p. 38.

[88] F. Konushi et al., in: J.M. Gibson, G.C. Osborn, R.M. Tromp (Eds.), Layered Structures and Epitaxy, Materials Research Society, Pittsburgh, 1985, p. 259.

[89] F. Jones, J. Vac. Sci. Technol. 6 (1988) 3088.

[90] L.S. Wang, S.A. Barnett, J. Electrochem. Soc. 139 (1992) 1134.

[91] L.S. Wang, S.A. Barnett, Solid State Ionics 61 (1993) 273.

[92] K. Honegger, E. Batawi, Ch. Sprecher, R. Diethelm, in: U. Stimming, S.C. Singhal, H. Tagawa, W. Lehnert (Eds.), Proc. 5th Int. Conf. Solid Oxide Fuel Cells, Electrochemical Society, 1997, p. 321.

[93] P.K. Srivastava et al., in: B. Thorstensen (Ed.), Proc. 2nd European Solid Oxide Fuel Cell Forum, European SOFC Forum, Oberrohrdorf, Switzerland, 1996, p. 761.

[94] C. Kleinlogel, M. Gödickemeier, K. Honegger, L.J. Gauckler, in: H.L. Tuller, A.C. Khandkar, M. Mogensen, W. Gopel (Eds.), Proc. Ionic and Mixed Conducting Ceramics, Vol. III, Electrochemical Society, Pennington, NJ, 1997, p. 97.

[95] T. Hikita, M. Kawashima, I. Yasuda, T. Koyama, Y. Matsuzaki, in: S.C. Singhal, H. Iwahara (Eds.), Proc. 3rd Int. Symp. on Solid Oxide Fuel Cells, Electrochemical Society, Pennington, NJ, 1993, p. 714.

[96] R. Diethelm, K. Honegger, in: S.C. Singhal, H. Iwahara (Eds.), Proc. 3rd Int. Symp. on Solid Oxide Fuel Cells, Electrochemical Society, Pennington, NJ, 1993, p. 822.

[97] W.F. Chu, Solid State Ionics 52 (1992) 243.

[98] D. Bauza, D. Especel, M. Gouet, British Ceramic Proc. 38 (1986) 197.

[99] M. Gödickemeier, unpublished results, Department of Materials, Nonmetallic Materials, ETH, Zurich, 1993.

[100] M. Cassidy, G. Lindsay, in: U. Bossel (Ed.), Proc. 1st European Solid Oxide Fuel Cell Forum, European SOFC Forum, Oberrohrdorf, Switzerland, 1994, p. 617.

[101] M. Cassidy, K. Kendall, C. Lindsay, in: B. Thorstensen (Ed.), Proc. 2nd European Solid Oxide Fuel Cell Forum, European SOFC Forum, Oberrohrdorf, Switzerland, 1996, p. 667.

[102] B.H. Rabin, J. Am. Ceram. Soc. 73 (1990) 2757.

[103] D.W. Dees, T.D. Claar, T.E. Easier, D.C. Fee, F.C. Mrazek, J. Electrochem. Soc. 134 (1987) 2141.

[104] F.P.F. van Berkel, G.M. Christie, F.H. van Heuveln, J.P.P. Huijsmans, in: M. Dokiya, O. Yamamoto, H. Tagawa, S.C. Singhal (Eds.), Proc. 4th Int. Conf. Solid Oxide Fuel Cells, 1995, p. 1062.

[105] R. Ihringer, J. Van Herle, A.J. McEvoy, in: U. Stimmung, S.C. Singhal, H. Tagawa, W. Lehnert (Eds.), Proc. 5th Int. Conf. Solid Oxide Fuel Cells, Electrochemical Society, Pennington, NJ, 1997, p. 340.

[106] J. Will, Porous support structures and sintered thin film electrolytes for solid oxide fuel cells, Diss. ETH No. 12876, ETH, Zurich, 1998.

[107] H. Arai, in: S.C. Singhal (Ed.), Proc. 1st Int. Symp. on Solid Oxide Fuel Cells, Electrochemical Society, Pennington, NJ, 1989, p. 10.

[108] M. Aizawa, H. Nishiyama, A. Ueno, M. Kuroishi, K. Eguchi, H. Arai, in: S.C. Singhal, H. Iwahara (Eds.), 3rd Int. Symp. on SOFC, Electrochemical Society, Pennington, NJ, 1993, p. 38.

[109] S.K. Nam, W.S. Seong, S.A. Hong, in: M. Dokiya, O. Yamamoto, H. Tagawa, S.C. Singhal (Eds.), Proc. 4th Int. Conf. Solid Oxide Fuel Cells, 1995, p. 318.

[110] S.J. Visco, S. de Souza, L.C. De Jonghe, in: Proc. EPORI/GRI Fuel Cell Workshop on Fuel Cell Technology Research and Development, April 4–5, 1995, p. 15.

[111] S. de Souza, S.J. Visco, L.C. de Jonghe, J. Electrochem. Soc. 144 (3) (1997) L35.

[112] T. Setoguchi, T. Inoue, H. Takebe, E. Eguchi, K. Morinaga, H. Arai, Solid State Ionics 37 (1990) 217.

[113] T. Setoguchi, K. Okamoto, K. Eguchi, H. Arai, J. Electrochem Soc. 139 (1992) 2875.

[114] R. Förthmann, G. Blaß, H.P. Buchkremer, in: U. Stimming, S.C. Singhal, H. Tagawa, W. Lehnert (Eds.), Proc. 5th Int. Conf. Solid Oxide Fuel Cells, Electrochemical Society, Pennington, NJ, 1997, p. 1003.

[115] P. Sarkar, P.S. Nicholson, J. Am. Ceram. Soc. 79 (8) (1996) 1987.

[116] T. Ishihara, K. Sato, Y. Takita, J. Am. Ceram. Soc. 79 (4) (1996) 913.

[117] M. Hruschka, Entwicklung der Elektrophoretischen fur die Herstellung dunner Elektrolytschichten, Ph.D. Thesis, University of Aachen, Berichte des Forschungszentrum Jülich, Germany, 1996.

[118] M. Prica, K. Kendall, M. Painter, in: M. Dokiya, O. Yamamoto, H. Tagawa, S.C. Singhal (Eds.), Proc. 4th Int. Conf. Solid Oxide Fuel Cells, 1995, p. 1056.

[119] H. Itoh, M. Mon, N. Mori, T. Abe, J. Power Sources 49 (1994) 315.

[120] M.H. Francombe, J.L. Vossen, in: Physics of Thin Films, Academic Press, NJ, 1982, p. 230.

Low-temperature electrodeposition of the high-temperature cubic polymorph of bismuth(III) oxide

Eric W. Bohannan, Christopher C. Jaynes, Mark G. Shumsky, Julie K. Barton, Jay A. Switzer*

University of Missouri-Rolla, Department of Chemistry and Graduate Center for Materials Research, Rolla, MO 65409-1170, USA

Received 1 September 1999; received in revised form 1 November 1999; accepted 1 December 1999

Abstract

Nanocrystalline films of δ-Bi_2O_3 were electrodeposited at 65°C directly from alkaline solutions of tartrate-complexed Bi(III). This face-centered-cubic polymorph of Bi_2O_3 is normally only stable at high temperatures (729–825°C). The material has the highest known oxide ion mobility. We propose that the high temperature form of the oxide is stabilized due to the nanocrystalline (70 nm) size of the particles in the film. The oxide also deposits epitaxially onto a single-crystal Au(110) substrate with strong in-plane and out-of-plane orientation. The large lattice mismatch (35.4%) is accommodated by forming a coincidence lattice, in which the δ-Bi_2O_3 is rotated 90° relative to the Au (110) substrate. The epitaxial relationship between film and substrate may also serve to stabilize the high-temperature structure. © 2000 Elsevier Science B.V. All rights reserved.

Keywords: Bismuth oxide; Electrodeposition; Epitaxial growth; Solid electrolyte

PACS: 81.15.P (Electrodeposition)

1. Introduction

Oxide-ion conducting solid electrolytes are of great interest for use in fuel cells, oxygen sensors, and oxygen pumps. The most widely used solid electrolytes with high oxide ion conductivity are those derived from zirconia, with yttria-stabilized zirconia being the most widely applied. However, zirconia-based solid electrolytes have an oxide ion conductivity that is up to two orders of magnitude

*Corresponding author. Tel.: +1-573-341-4383; fax: +1-573-341-4383.
E-mail address: jswitzer@umr.edu (J.A. Switzer)

lower than the cubic form of Bi_2O_3 [1]. A significant limitation of the bismuth oxide system is that the face-centered-cubic phase exists only between 729°C and the melting point of the material, 825°C [2]. Substitution of rare-earth oxides stabilizes δ-Bi_2O_3 down to room temperature, however there is a coincident lowering of the oxide ion conductivity by over two orders of magnitude [3].

The polymorphism of pure bismuth sesquioxide has been studied by several investigators [4–8] since the work of Sillén [9], who proposed that four polymorphs exist. Below 729°C Bi_2O_3 exists as the monoclinic α-phase. When cooling from temperatures above 729°C, the face-centered cubic (fcc)

δ-phase of Bi_2O_3 has been observed to undergo a transformation into one of two metastable phases, the tetragonal β-phase or the body centered cubic (bcc) γ-phase, before reverting to the monoclinic form. Sillen first described δ-Bi_2O_3 as having a pseudo-fluorite structure with one quarter of the oxygen atoms missing in an ordered defect oxygen lattice [9]. Gattow and Schröder showed by X-ray powder diffraction that δ-Bi_2O_3 is fcc and rejected the ordered defects in the oxygen lattice, preferring instead a statistical occupancy of 75% on each anion site [10]. Willis proposed a more complicated model in which each anion site is replaced by four equivalent sites displaced from their ideal positions, each site having an occupancy factor of 3/16 [11]. Battle et al. have shown by refinement of neutron diffraction patterns that δ-Bi_2O_3 has a highly defective fluorite structure where 43% of the regular anion sites are occupied, in addition to 8% occupancy of a second site displaced from the regular anion position [12]. The unusually high ionic conductivity of δ-Bi_2O_3 has been attributed to the highly disordered oxygen sublattice [13].

Electrodeposition as a means of materials synthesis offers the advantages of low processing temperatures, control of film thickness, deposition onto complex shapes, low capital investment and the production of nonequilibrium materials that cannot be accessed by traditional thermal processing. We have previously used electrodeposition to create superlattices of metal oxides [14–16] and nonequilibrium layered nanostructures of Cu_2O and Cu which showed quantum confinement effects in electrical properties [17–21]. Recently, we reported that epitaxial films of δ-Bi_2O_3 can be electrodeposited on Au single crystal substrates at 65°C, with the material stabilized by a template effect [22]. The production of room temperature stable epitaxial δ-Bi_2O_3 nanoscopic mesas grown by pulsed laser deposition has also been reported [23]. Nonequilibrium materials can be stabilized by the production of nanometer-scale crystallites, as in the case of ZrO_2 [24–27], or by epitaxially electrodepositing the material onto a substrate with a crystal structure similar to that of the desired product. In this work, we produce δ-Bi_2O_3 by electrodeposition that is stabilized at room temperature due to the nanoscale crystallites that are formed. We also show that the structure can be epitaxially stabilized by electrodepositing δ-Bi_2O_3 onto single crystal Au. The epitaxial films are shown to be oriented in-plane and out-of-plane by X-ray diffraction techniques.

2. Experimental procedure

Each 500-ml deposition solution consisted of 0.1 M Bi(III) nitrate pentahydrate, 0.25 M tartaric acid, and 2.5 M KOH prepared with water (> 18 MΩ) from a Barnstead NANOpure ultra pure water system. All chemicals were reagent grade and purchased from Aldrich. Temperature control was maintained with a Cole Palmer model 04644 digital hot plate/stirrer with temperature probe. A constant temperature of 65°C in the stirred solution was maintained during electrodeposition.

Electrodeposition was performed with an EG and G Princeton Applied Research Model 273A potentiostat/galvanostat. A three-electrode electrochemical cell was employed consisting of a working electrode (430 stainless steel, polycrystalline Au or single crystal Au), a saturated Ag/AgCl reference electrode and a Pt-wire counter electrode. The electropolished Au single crystal was purchased from Monocrystals Company. The single crystal had a 10-mm diameter and a 1-mm thickness. The purity of the Au was 99.99 + %. Commercially available 9-MHz AT-cut quartz crystals (Seiko EG and G model QA-AM9-AU) were used as the working electrode during electrochemical quartz crystal microbalance (EQCM) experiments. The quartz crystals have a coating on both sides consisting of a 500 Å Ti layer beneath a 3000 Å layer of Au. The quartz crystals were installed in a Teflon holder so that only one electrode face, with an area of 0.20 cm^2 was exposed to the solution. A quartz crystal analyzer (Seiko EG and G model QCA917) was used in conjunction with a Nicolet Pro10 oscilloscope to monitor changes in frequency during experiments. A gate time of 0.1 s and an output range of ±20 KHz/10 V was used with the analyzer. For all depositions a constant anodic current density of 5 mA/cm^2 was applied.

X-ray diffraction (XRD) experiments were performed with a Scintag 2000 diffractometer using CuKα radiation. Rietveld refinement of the powder

diffraction pattern of δ-Bi_2O_3, obtained from a series of films grown on 430 stainless steel, was performed with commercially available RIQAS software. Azimuthal scans of epitaxial films were obtained by the use of a texture goniometer accessory that had been fashioned in-house for the Scintag 2000. Particle size and strain measurements were obtained using the program SHADOW (Ver. 4.00, Materials Data). Instrumental broadening was determined with a LaB_6 standard (SRM 660) purchased from NIST.

A Hitachi S-570 scanning electron microscope (SEM) was used to obtain cross-sectional images of the δ-Bi_2O_3 films. The SEM was operated with an accelerating voltage of 25 kV and a magnification of 40 000 ×. Prior to imaging, the samples were sputter coated with ~100 Å of 60% Au/40% Pd to prevent sample charging. Energy dispersive spectroscopy (EDS) measurements were performed on uncoated samples with an EDAX Phoenix system in conjunction with a Hitachi S-4700 field emission SEM. Atomic force microscopy (AFM) images were obtained with a Digital Nanoscope E scanning probe microscope which was operated in the contact mode. The samples were imaged in air with Au-coated Si_3N_4 probes.

3. Results and discussion

The XRD powder pattern for electrodeposited δ-Bi_2O_3 is shown in Fig. 1. The powder sample was obtained from numerous thin films removed from 430 stainless steel substrates. A Rietveld fit to the powder pattern was performed with RIQAS software and is also shown. The Rietveld fit was performed with space group Fm3m, with the Bi atoms at (0,0,0), and oxygen atoms at (0.25,0.25,0.25) and (0.354,0.354,0.354) with occupancies of the oxygen sites of 0.43 and 0.08, respectively. Refinement of the pattern gave residual errors of 7.62% and 11.10% for R and R_{wp}. It is of note that a similar refinement performed with the same parameters except with the oxygens only at (0.25,0.25,0.25) and an occupancy of 0.75 gave similar residual errors ($R = 7.93\%$, $R_{wp} = 11.72\%$). The scattering factor for oxygen is much less than that of Bi, so very little can be learned about the precise placement of the oxygen atoms by XRD. A precision lattice parameter of 5.531 ± 0.001 Å was determined by high angle X-ray diffraction using a silicon reference standard. The lattice parameter for thermally prepared δ-Bi_2O_3 at 1047 K is 5.6595 Å [3]. Taking into account the
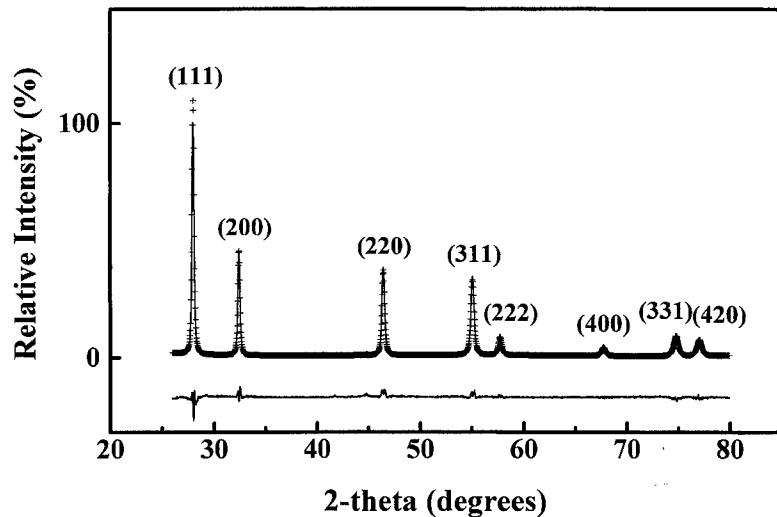

Fig. 1. XRD powder pattern (solid line), Rietveld fit (+), and difference pattern for δ-Bi_2O_3. A space group of *Fm3m* was assigned, with bismuth atoms at (0,0,0) and oxygen atoms on two sites, (0.25,0.25,0.25) and (0.354,0.354,0.354) with occupancies of 0.43 and 0.08, respectively.

thermal expansion coefficient for δ-Bi_2O_3 of 2.4×10^{-5} K^{-1} [5], the lattice parameter of our electrodeposited δ-Bi_2O_3 extrapolated to 1047 K is 5.6 Å. We view this as good agreement between the two materials, given the uncertainty in the expansion coefficient and the large degree of extrapolation required. The room-temperature positions and intensities of the observed reflections for electrodeposited δ-Bi_2O_3 powder are given in Table 1.

The cubic form of δ-Bi_2O_3 may be stabilized at these low temperatures by the small particle size of crystallites in the film. X-ray line broadening can be used to determine strain and particle size of a given crystalline material. Using the method developed by Williamson and Hall [28], the contributions of the particle size and strain to the observed X-ray line broadening, β, are considered to be additive.

$$\beta_{total} = \beta_{particle\ size} + \beta_{strain} \tag{1}$$

The contribution of broadening due to small particle size is given by the Scherrer equation while the broadening due to strain is represented by differentiation of the Bragg law.

$$\beta_{total} = \frac{0.94\lambda}{t \cos \theta} + 4 \tan \theta (\Delta d/d) \tag{2}$$

Table 1
Powder X-ray diffraction of electrodeposited δ-Bi_2O_3[a]

(hkl)	d-Spacing (Å)	2-Theta (degrees)	Relative intensity (%)
(111)	3.193	27.94	100
(200)	2.766	32.37	46
(220)	1.956	46.43	47
(311)	1.668	55.07	50
(222)	1.597	57.74	12
(400)	1.383	67.77	6
(331)	1.269	74.82	16
(420)	1.237	77.12	13
(422)	1.129	86.13	10
(511) (333)	1.064	92.81	13

[a] Positions calculated using crystallographically determined precision lattice parameter ($a = 5.531$ Å) and measured relative intensities observed in the room-temperature powder X-ray diffraction pattern for electrodeposited δ-Bi_2O_3 using a CuKα ($\lambda = 1.5418$ Å) source.
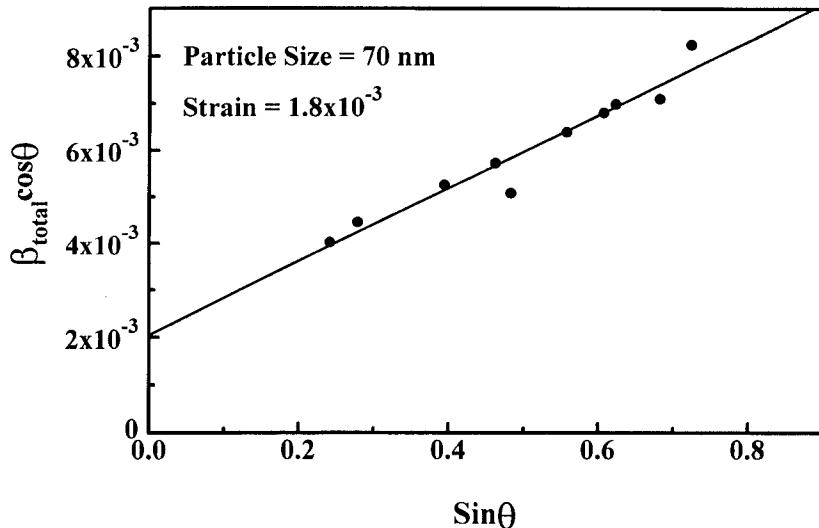

Fig. 2. Williamson–Hall plot for δ-Bi_2O_3 from X-ray powder pattern. A particle size of 70 nm was obtained from the y-intercept of the plot, while the strain ($\Delta d/d$) was determined from the slope of the line to be 1.8×10^{-3}. Linear regression gave a correlation coefficient of 0.97.

The total broadening (β_{total}) is the measured fwhm in radians, corrected for instrumental broadening. The X-ray wavelength of the source (CuKα = 0.154 nm) is given by λ, t is the particle size, and $\Delta d/d$ represents the strain. Multiplying both sides of Eq. (2) by cos θ gives the final form,

$$\beta_{total} \cos \theta = \frac{0.94\lambda}{t} + 4 \sin \theta (\Delta d/d) \qquad (3)$$

which is used to calculate the particle size and strain for δ-Bi$_2$O$_3$ from a plot of β_{total} cos θ versus sin θ, as shown in Fig. 2. Using the y-intercept obtained from linear regression of the broadening as a function of diffraction angle, we obtained a particle size of 70 nm. The slope of the fitted line gives a strain of 1.8×10^{-3} in the powder. The nanocrystalline nature of these films, as well as the strain observed, may help explain the stabilization of the fcc structure for Bi$_2$O$_3$ at room temperature.

We have also used the electrochemical chemical quartz crystal microbalance (EQCM) as an in situ monitor of δ-Bi$_2$O$_3$ film growth. The EQCM allows for the determination of minute mass changes, down to the sub-nanogram range, by monitoring the frequency response of a quartz oscillator during the electrodeposition process. The piezoelectric device, coated with Au, was used as the working electrode during the electrodeposition of δ-Bi$_2$O$_3$. The Sauerbrey equation [Eq. (4)] describes the mass-frequency relationship for the EQCM.

$$\Delta f = \frac{-2f_o^2 \Delta m}{(\rho\mu)^{1/2} A} \qquad (4)$$

The measured frequency shift is given by Δf, f_o is the resonant frequency of the oscillator (9 MHz), Δm is the mass change, ρ is the density of quartz (2.648 g/cm^3), μ is the shear modulus of quartz (2.947 $\times$ 10^{11} dyn/cm^2), and A is the piezoelectrically active area.

Fig. 3 shows the potential transient, the mass accumulated at the electrode, and the calculated thickness of a δ-Bi$_2$O$_3$ film during electrodeposition at a constant anodic current density of 5 mA/cm^2. The crystallographic density of δ-Bi$_2$O$_3$ (9.17 g/cm^3), was used in conjunction with the mass deposited to calculate the thickness of the film, assuming the film to be 100% dense. After an initial
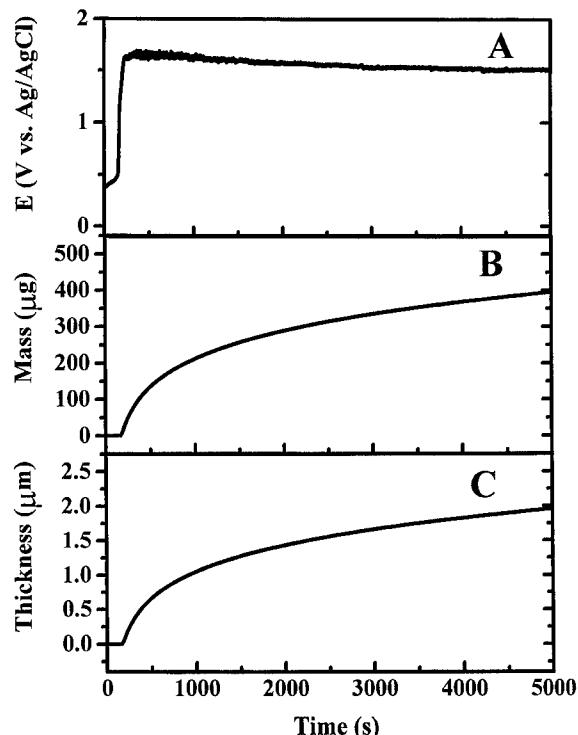

Fig. 3. In-situ monitoring of δ-Bi$_2$O$_3$ electrodeposition. Part A shows the potential transient vs. a Ag/AgCl reference electrode at a constant anodic current density of 5 mA/cm^2. Part B shows the mass accumulated at the electrode surface as a function of deposition time as determined with the EQCM. Part C shows the thickness of the electrodeposited δ-Bi$_2$O$_3$ film as calculated from the EQCM data and the crystallographic density of δ-Bi$_2$O$_3$ (9.17 g/cm^3).

induction period, the potential increases sharply as mass begins accumulating on the electrode. As the deposition proceeds there is a gradual decrease in the rate of deposition, as evidenced by the decrease in slope in parts B and C of Fig. 3. This is most likely due to a competing reaction of oxygen evolution at the working electrode.

At this point, the mechanism of δ-Bi$_2$O$_3$ deposition has not been clearly elucidated. Pourbaix has suggested that under strongly alkaline conditions the Bi(III) species existing in solution is BiO$_2^-$ and that Bi(III) can be oxidized to Bi(V) through electrolytic means [29]. We propose the following possible mechanism.

$$2BiO_2^- + 2OH^- \rightarrow Bi_2O_5 + H_2O + 4e^- \qquad (5)$$

$$Bi_2O_5 \rightarrow \delta\text{-}Bi_2O_3 + O_2 \qquad (6)$$
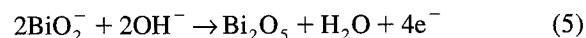
In Eq. (5) we show the oxidation of the solution species to bismuth(V) oxide. This film then undergoes an internal redox reaction, decomposing to form $\delta\text{-}Bi_2O_3$ while evolving oxygen gas. In agreement with this mechanism, if the deposition is carried out at temperatures between 50°C and room temperature, reddish-brown amorphous films are obtained on the electrode surface. The color is consistent with that of bismuth(V) oxide [30] and the films also give a positive iodometric response. Assuming this mechanism, the instantaneous current efficiency of the deposition process was calculated as a function of thickness as shown in Fig. 4. From a maximum current efficiency of approximately 55% during the early stages of deposition, the current efficiency falls off to a value of approximately 2% at 5000 s. This falloff may be due to a competing reaction, the evolution of oxygen at the working electrode, which is shown in Eq. (7).

$$4OH^- \rightarrow O_2 + 2H_2O + 4e^- \qquad (7)$$
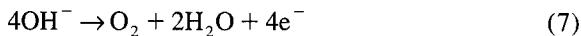
Vigorous gas evolution was observed at the working electrode surface during the later stage of film

deposition, consistent with Eq. (7). The nominal thickness of this film, grown for 5000 s, is 2 μm. Because the current efficiency decreases with deposition time, it is not possible under the present conditions to grow films with a thickness much larger than 2 μm.

The XRD pattern for the film used in the EQCM experiments is shown in Fig. 5. The substrate is a gold-coated EQCM electrode, used as received from the manufacturer. The gold film shows a strong (111) preferred orientation. Fig. 5 clearly shows that the $\delta\text{-}Bi_2O_3$ also has a strong (111) orientation suggestive of an epitaxial relationship between Au and the electrodeposited film. A SEM micrograph of a cross-section of the $\delta\text{-}Bi_2O_3$ film is shown in Fig. 6. The cross-section reveals a columnar microstructure, consistent with a highly oriented thin film. Several cross-sectional images, obtained from different regions of the film, revealed that the film has good thickness uniformity. The film thickness, determined from the SEM micrograph, is approximately 2 μm. This is in good agreement with the value calculated from the EQCM data. In order to determine the crystallite sizes present in the film, an image of the surface of the film was obtained with an AFM operated in the contact mode as shown in Fig.
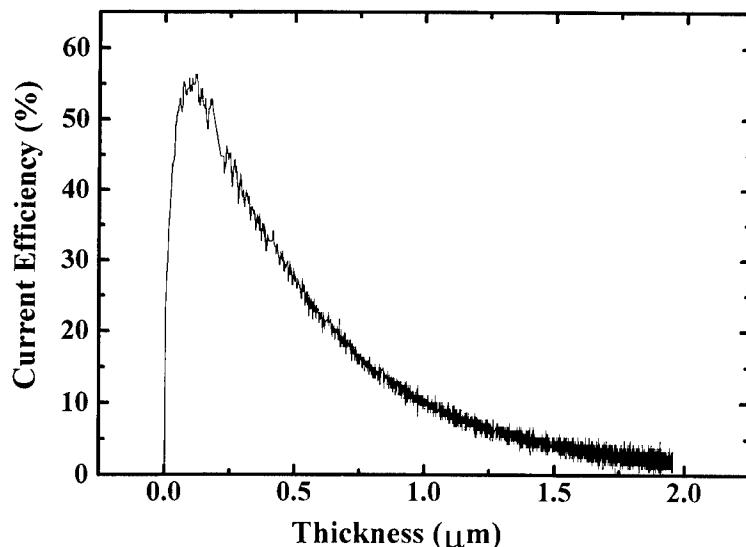

Fig. 4. Current efficiency of the $\delta\text{-}Bi_2O_3$ electrodeposition process as a function of film thickness. The current efficiency was determined using EQCM data, the applied current density, and the proposed mechanism given in the text. The fall off in current efficiency reveals that the films can be grown only to a nominal thickness of 2 μm.

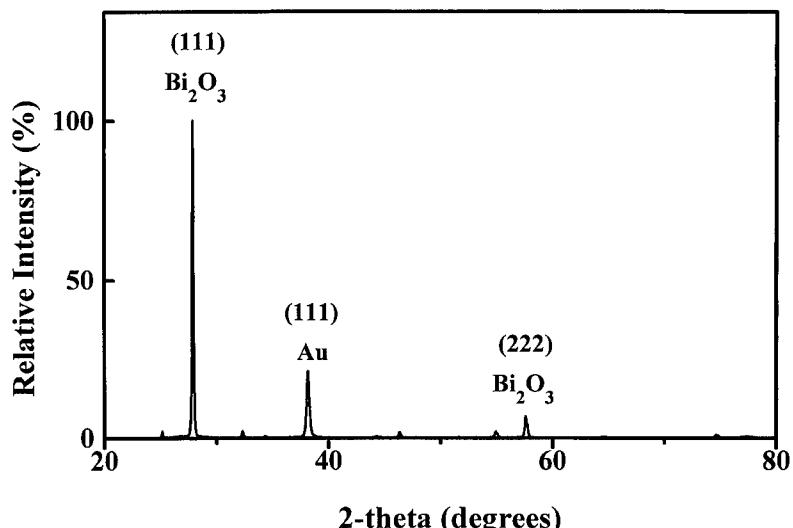Fig. 5. XRD pattern of a δ-Bi_2O_3 deposited onto a (111)-textured Au EQCM electrode. Comparison of this pattern with that shown in Fig. 1 reveals that the δ-Bi_2O_3 has a strong (111) preferred orientation, suggestive of an epitaxial relationship between Au and δ-Bi_2O_3.

Fig. 6. SEM cross-sectional image of δ-Bi_2O_3 electrodeposited onto a (111)-textured Au EQCM electrode. The image shows a high degree of columnar growth, typical of textured films. The thickness of the film as determined by SEM agrees well with that calculated from the EQCM. The bar marker is 750 nm.

7. The average crystallite size was 65 ± 6 nm, which is in agreement with the particle size obtained from Williamson–Hall analysis of the δ-Bi_2O_3 powder sample discussed earlier. EDS showed no evidence of K incorporation in the δ-Bi_2O_3 film, consistent with the structure being stabilized due to small crystallite size and not to the presence of dopants. Standardless quantification of the O/Bi ratio by EDS gave a stoichiometry of $Bi_2O_{2.9}$.

Although there is the hint of an epitaxial relationship between Au and δ-Bi_2O_3 seen in Fig. 5, in order to confirm this relationship it is necessary to show that the two materials have both in-plane and out-of-plane alignment. This was accomplished by electrodepositing δ-Bi_2O_3 onto a Au(110) single crystal substrate. The θ–2θ pattern for a δ-Bi_2O_3 film grown on a Au(110) single crystal is shown in Fig. 8. For the Au substrate, only the (220) reflection is observed over the diffraction angles shown. The δ-Bi_2O_3 shows mainly the (220) and (440) reflections, indicating that there is a strong out-of-plane epitaxial relationship. It has been suggested that the high-temperature form of δ-Bi_2O_3 has a primitive cubic as opposed to a face centered cubic structure [31]. The observation of mixed index reflections would preclude a face centered cubic structure for our material, as these reflections are symmetry
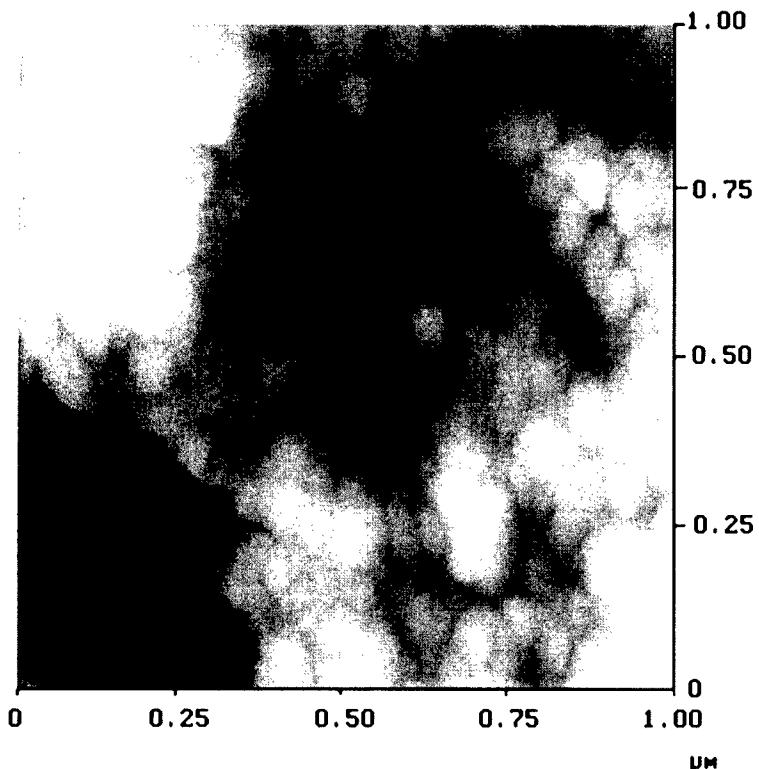
Fig. 7. Contact AFM image of the surface of an electrodeposited δ-Bi$_2$O$_3$ film grown on a (111) textured Au EQCM electrode. The scan size is 1.0 μm in both directions. The average particle size is 65±6 nm.

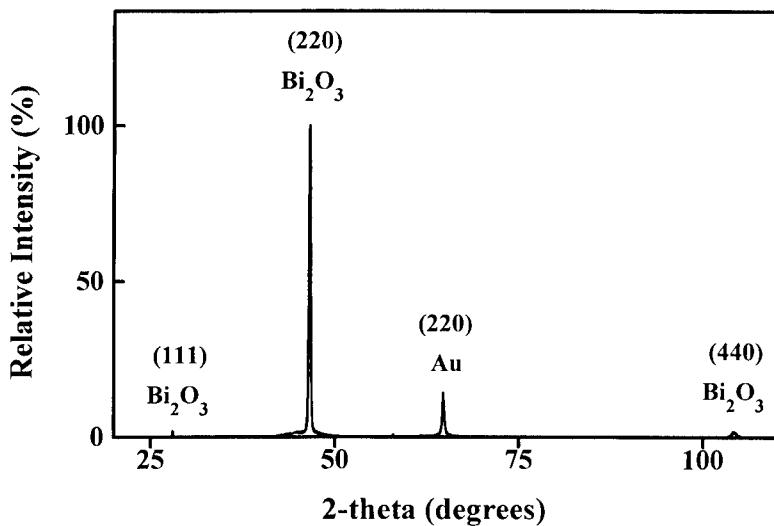Fig. 8. XRD pattern of a δ-Bi$_2$O$_3$ film electrodeposited onto a Au(110) single crystal. The δ-Bi$_2$O$_3$ shows a strong (110) out-of-plane orientation, following the orientation of the Au single crystal. The absence of the (110) reflection for Bi$_2$O$_3$ precludes the δ-Bi$_2$O$_3$ structure from being primitive cubic.
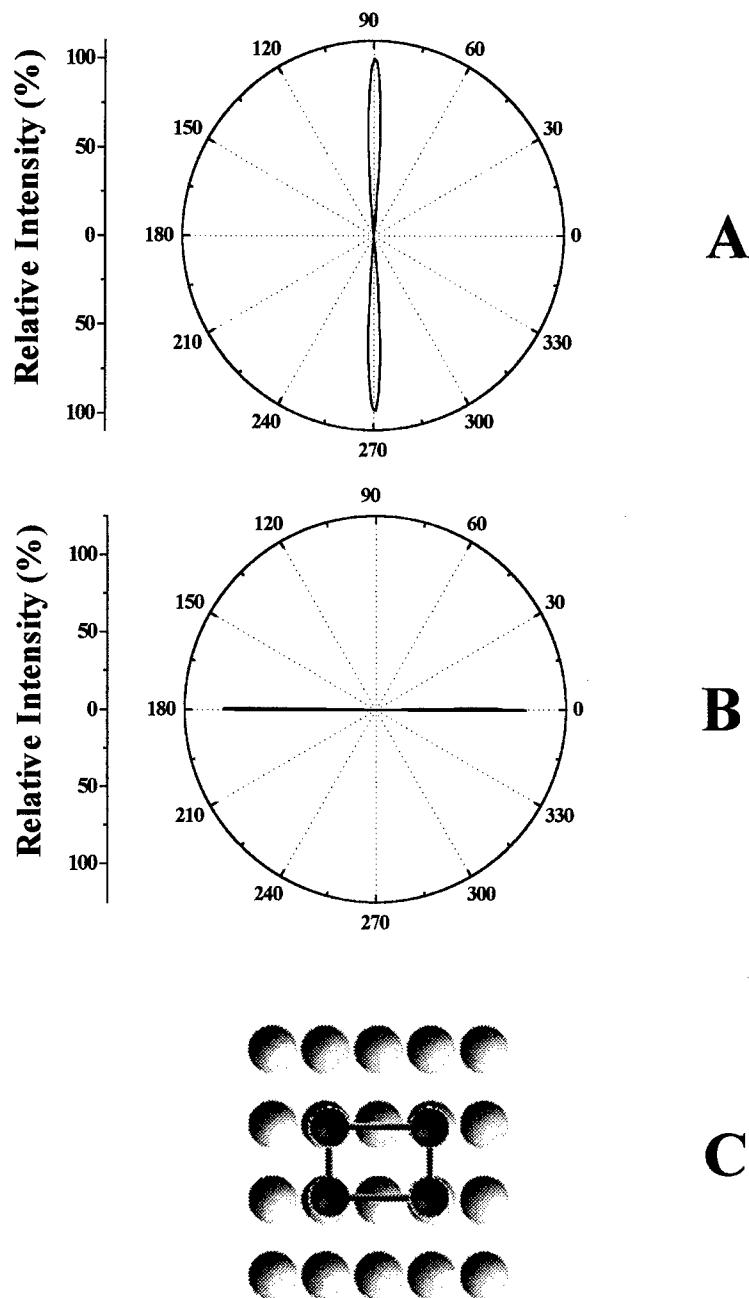
Fig. 9. Evidence for in-plane orientation in electrodeposited δ-Bi_2O_3. Part A shows the azimuthal scan for the (200) δ-Bi_2O_3 reflection for a film deposited onto single crystal Au(110). The azimuthal scan shows the expected two-fold symmetry and shows a high degree of in-plane orientation. Part B shows the azimuthal scan for the (200) reflection of the Au(110) single crystal substrate. Two-fold symmetry is again observed, although, comparing parts A and B, the peaks of δ-Bi_2O_3 are rotated 90° relative to the Au substrate. For both azimuthal scans, the sample was tilted at an angle of 45° to bring the (200) reflections into the Bragg condition. Part C shows an interface model for epitaxial growth of δ-Bi_2O_3 on Au. The δ-Bi_2O_3 overlayer (bismuth atoms represented as dark balls) is rotated 90° relative to the Au substrate. This $(1\times1)Bi_2O_3(110)[110]//(2\times1)Au(110)[100]$ coincidence lattice reduces the lattice mismatch from 35.4% to −4.2%.

forbidden. However, there is no evidence of a (110) reflection for epitaxial δ-Bi_2O_3 as the baseline noise at the expected spacing for the (110) reflection is less than 0.1% of the intensity seen for the (220) δ-Bi_2O_3 reflection. Therefore, our material is rigorously face-centered-cubic.

If there is a true epitaxial relationship between film and sample, the film grown on single crystal Au should also show evidence of in-plane orientation. The in-plane (parallel to the substrate) orientation of the δ-Bi_2O_3 film on (110) single crystal Au was examined by performing azimuthal (ϕ) X-ray scans. In order to bring other reflections, besides the (110) family, into the Bragg condition, it is necessary to tilt the sample at an appropriate angle. For the present sample, in order to observe the (100) family of reflections, it is necessary to tilt the sample at an angle of 45°, which corresponds to the angle between the [100] and [110] directions. By setting 2θ equal to 32.39°, which corresponds to the (200) reflection for δ-Bi_2O_3, and rotating the tilted sample, an azimuthal scan is obtained as shown in Fig. 9. The azimuthal scan is essentially a cross-section of the pole figure at a given tilt angle. Part A of Fig. 9 shows the azimuthal scan for the (200) reflection of δ-Bi_2O_3. The two-fold symmetry that is observed is proof of in-plane orientation and hence the epitaxial relationship between film and substrate. Part B shows the azimuthal scan for the (200) reflection of Au ($2\theta = 44.39°$), which was also obtained at a tilt angle of 45°. As expected, two-fold symmetry is observed in the ϕ scan, however the film peaks of part A are rotated 90° relative to the substrate peaks of part B. This is explained by examining closely the lattice mismatch of the system. By only comparing the lattice parameters of Au and δ-Bi_2O_3, a lattice mismatch of 35.4% is calculated. This mismatch is so large that any epitaxial relationship between the two would be extremely unlikely. However, if we compare the spacing between Au atoms along the [100] direction (0.40786 nm), and the spacing of Bi atoms along the [110] direction (0.3907 nm), the lattice mismatch is much smaller (−4.2%). This situation requires rotation of the film 90° relative to the substrate, forming a $(1 \times 1)Bi_2O_3(110)[110]/$ $/(2 \times 1)Au(110)[100]$ coincidence lattice, a representation of which is shown in Fig. 9c. We have examined other samples grown on the other low-index faces of single crystal Au substrates, with these revealing much more complicated epitaxial relationships [22]. The epitaxial relationship between fcc Au and δ-Bi_2O_3 may stabilize the fcc phase at room temperature by a template effect.

4. Conclusions

We have shown that thin films of δ-Bi_2O_3 can be electrodeposited directly from an alkaline Bi(III) tartrate solution. Normally observed only between the temperatures of 729 and 825°C, the electrodeposited δ-Bi_2O_3 films in this study are stable at room temperature. This unexpected stability of the high temperature phase may be due to the nanocrystalline nature of the films. The films may also be epitaxially stabilized, as observed by the formation of a coincidence lattice of δ-Bi_2O_3 on single-crystal Au(110). These films should be of great interest, since δ-Bi_2O_3 has the highest oxide ion conductivity of any material studied to date.

Acknowledgements

References

[1] T. Takahashi, H. Iwahara, Mat. Res. Bull. 13 (1978) 1447.
[2] H.A. Harwig, A.G. Gerards, Thermochim. Acta 28 (1979) 121.
[3] P. Shuk, H.D. Wiemhöfer, U. Guth, W. Göpel, M. Greenblatt, Solid State Ionics 89 (1996) 179.
[4] W.C. Schumb, E.S. Rittner, J. Am. Chem. Soc. 65 (1943) 1055.
[5] E.M. Levin, R.S. Roth, J. Res. Natl. Bur. Std. 68A (2) (1964) 189.
[6] E.M. Levin, R.S. Roth, J. Res. Natl. Bur. Std. 68A (2) (1964) 197.
[7] C.N.R. Rao, G.V. Subba Rao, S. Ramdas, J. Phys. Chem 73 (3) (1969).
[8] H.A. Harwig, Z. Anorg. Allg. Chem. 444 (1978) 151.
[9] L.G. Sillén, Ark. Kemi Mineral. Geol. 12A (18) (1937) 1.

[10] G. Gattow, H. Schröder, Z. Anorg. Allg. Chem. 318 (1962) 176.

[11] B.T.M. Willis, Acta Crystallogr. 18 (1965) 75.

[12] P.D. Battle, C.R.A. Catlow, J. Drennan, A.D. Murray, J. Phys. C 16 (1983) L561.

[13] L.A. Depero, L. Sangaletti, J. Solid State Chem. 122 (1996) 439.

[14] J.A. Switzer, M.J. Shane, R.J. Phillips, Science 247 (1990) 444.

[15] J.A. Switzer, R.P. Raffaelle, R.J. Phillips, C.-J. Hung, T.D. Golden, Science 258 (1992) 1918.

[16] J.A. Switzer, C.-J. Hung, B.E. Breyfogle, M.G. Shumsky, R. Van Leeuwen, T.D. Golden, Science 264 (1994) 1573.

[17] J.A. Switzer, C.-J. Hung, L.-Y. Huang, E.R. Switzer, D.R. Kammler, T.D. Golden, E.W. Bohannan, J. Am. Chem. Soc. 120 (1998) 3530.

[18] J.A. Switzer, B.M. Maune, E.R. Raub, E.W. Bohannan, J. Phys. Chem. B 103 (1999) 395.

[19] E.W. Bohannan, L.-Y. Huang, F.S. Miller, M.G. Shumsky, J.A. Switzer, Langmuir 15 (1999) 813.

[20] J.A. Switzer, C.-J. Hung, L.-Y. Huang, F.S. Miller, Y. Zhou, E.R. Raub et al., J. Mater. Res. 13 (1998) 909.

[21] J.A. Switzer, C.-J. Hung, E.W. Bohannan, M.G. Shumsky, T.D. Golden, D.C. Van Aken, Adv. Mater. 9 (1997) 334.

[22] J.A. Switzer, M.G. Shumsky, E.W. Bohannan, Science 284 (1999) 293.

[23] M. Alexe, J.F. Scott, C. Curran, N.D. Zakharov, D. Hesse, A. Pignolet, Appl. Phys. Lett. 73 (1998) 1592.

[24] R.C. Garvie, J. Phys. Chem. 69 (1965) 1238.

[25] K.S. Mazdiyasni, C.T. Lynch, J.S. Smith, J. Am. Ceram. Soc. 48 (1964) 372.

[26] T. Mitsuhashi, M. Ichihara, U. Tatsuke, J. Am. Ceram. Soc. 57 (1974) 97.

[27] J.A. Switzer, R.J. Phillips, Mat. Res. Soc. Symp. Proc. 121 (1988) 111.

[28] G.K. Williamson, W.H. Hall, Acta Metallurgica 1 (1953) 22.

[29] J. Van Muylder, M. Pourbaix, in: Atlas of Electrochemical Equilibria in Aqueous Solutions, Pergamon Press, New York, 1966, pp. 533–539.

[30] F.G. Cotton, G. Wilkinson, in: Advanced Inorganic Chemistry, 5th Edition, John Wiley and Sons, New York, 1988, pp. 401–402.

[31] J.W. Medernach, R.L. Snyder, J. Am. Ceram. Soc. 61 (1978) 494.

Manganese dioxides as cathodes for lithium rechargeable cells: the stability challenge

M. Stanley Whittingham*, Peter Y. Zavalij

Chemistry Department and Institute for Materials Research, State University of New York at Binghamton, Binghamton, New York, NY 19602, USA

Abstract

A wide range of manganese oxides is under study for possible use as the cathode of high energy density batteries. The spinel, $LiMn_2O_4$, although the most studied has a relatively low energy density and appears unstable under charge. This review emphasizes non-spinel oxides, in particular those with layered or tunnel structures that offer enhanced behavior in lithium ion and lithium polymer cells. A major focus is on stabilizing these manganese oxide structures against conversion to the spinel phase. © 2000 Elsevier Science B.V. All rights reserved.

Keywords: Manganese oxide; Spinel; Cubic close packing; Metastable phase; Pillars

1. Introduction

The use of intercalation compounds as electrodes in lithium batteries began about 20 years ago. The prototypical intercalation compound is titanium disulfide, which has been extensively studied [1,2] as the cathode in high energy density lithium batteries. However, even though TiS_2 is one of the few solid cathode materials that can sustain current densities of the order of 5–10 ma/cm^2, as required for many applications, its voltage is insufficiently high when combined with a lithium alloy or carbon anode even for the new generation of 2 volt electronic devices. $LiCoO_2$ [3], as used in the commercial SONY Li-ION cell, can provide the desired voltage, but is too expensive for large scale applications and only

cycles 0.5 Li. Thus, new cathode materials, which combine the reversibility and current drain capabilities of TiS_2 with the electrode potential of oxides such as $LiCoO_2$ are desired.

In the last 10 years much effort has been focussed on manganese because of its low cost, low toxicity and familiarity to the battery field. This has centered on the spinel phase, $LiMn_2O_4$ and on several layered manganese oxides. The spinel phase cycles well only for 0.5 Li/Mn, and has stability problems at elevated temperatures; work in this area has been the subject of reviews by Thackeray [4] and Tarascon [5]. The layered manganates, with the same structure as $LiCoO_2$ have been studied by Piffard [6,7], Whittingham [8–12], Bruce [13], Delmas [14,15] and Bach et al. [16–18]. The lithium content of the synthesized material can vary from $x = 0$ to 1 in Li_xMnO_2, depending on the synthesis approach used; x is around 0.5 in aqueous based preparations and can approach unity in non-aqueous based ion-exchange

*Corresponding author. Tel.: + 1-607-777-4623; fax: + 1-607-777-4623.
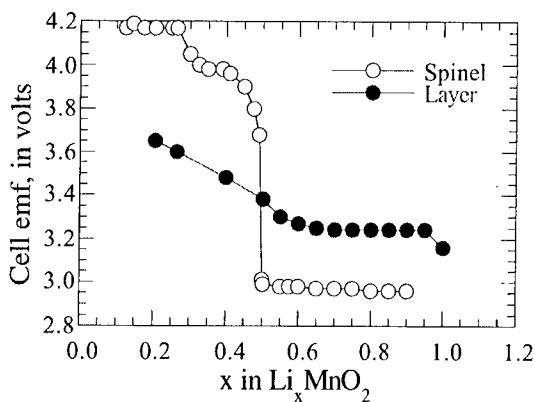
E-mail address: stanwhit@binghamton.edu (M.S. Whittingham)

Fig. 1. Cell voltages of the layered and spinel phases of manganese oxide, data from Bruce and Whittingham labs, from [19].

reactions from Na_xMnO_2. These researchers all showed that these layered phases can be cycled, but that the capacity fades with time. This appears to be due to diffusion of manganese leading to the spinel, or spinel-like phases [10]. Fig. 1 shows the variation of potential with lithium content, which indicates the higher stability of the spinel phase at low lithium contents [19]. Critically it indicates that in the layered material more than 0.8 Li can be cycled over less than a 0.5 volt range. Recent studies [10] suggest that layered manganates can be stabilized by pillaring with cations that are larger than both lithium and manganese; these pillars appear to impede the diffusion of manganese ions into the interlayer region because of the energetically unfavorable sites present.
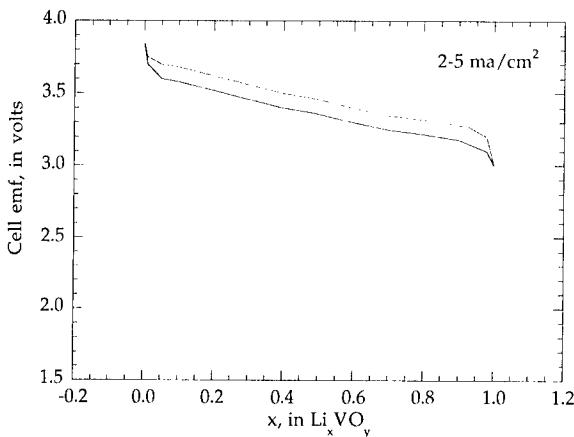
Fig. 2. Ideal behavior for a lithium battery cathode, from [19].

Thus, a search is on to find manganese oxides that are stable over the full range from MnO_2 to $LiMnO_2$, and that exhibit the ideal cycling characteristics shown in Fig. 2 [19].

2. Manganese dioxides

Manganese oxides, with the approximate Mn:O ratio of 1:2, form a wide range of crystalline structures as shown in Fig. 3. Many of these structures are stabilized by other ions, such as lithium in the spinel $LiMn_2O_4$, barium in the hollandite $BaMn_8O_{16}$, or potassium in cryptomelane KMn_8O_{16} — both of which have the 2×2 tunnel structure. Many of these structures are also stabilized by the presence of protonic species. This large variety of structures almost certainly means that in the compound Li_xMnO_2, a variety of structures will become the thermodynamically stable phase as the lithium content is changed over the range of $0 \le x \le 1$. Moreover, the stable phase will also change with temperature, so that the phase formed under elevated temperature conditions may not be stable at room temperature. In addition, the oxygen content will in some cases also be a function of temperature as pointed out by Delmas [20]. In the following sections, recent electrochemical data is discussed for a cross-section of these structures.

3. Layered structure manganese dioxides

Fig. 4 shows the cycling behavior of layer structure K_xMnO_2 in lithium cells, and Fig. 5 compares the capacity on cycling of Li_xMnO_2, Na_xMnO_2 and K_xMnO_2 [10]. We found that the magnesium and rubidium analogs have inferior behavior. In similar cells the spinel $LiMn_2O_4$, loses capacity even faster when cycled in the 3 volt regime than layered $LiMnO_2$. Whereas lithium ions are in octahedral coordination between the MnO_2 sheets in Li_xMnO_2, potassium ions are not, thus the oxygen ion arrangement is no longer cubic close packed as in the spinel phase. Thus, it will be necessary for the oxygen ions as well as the manganese ions to diffuse in order for the structure to convert to the spinel structure on cycling in lithium cells. This may explain in part the
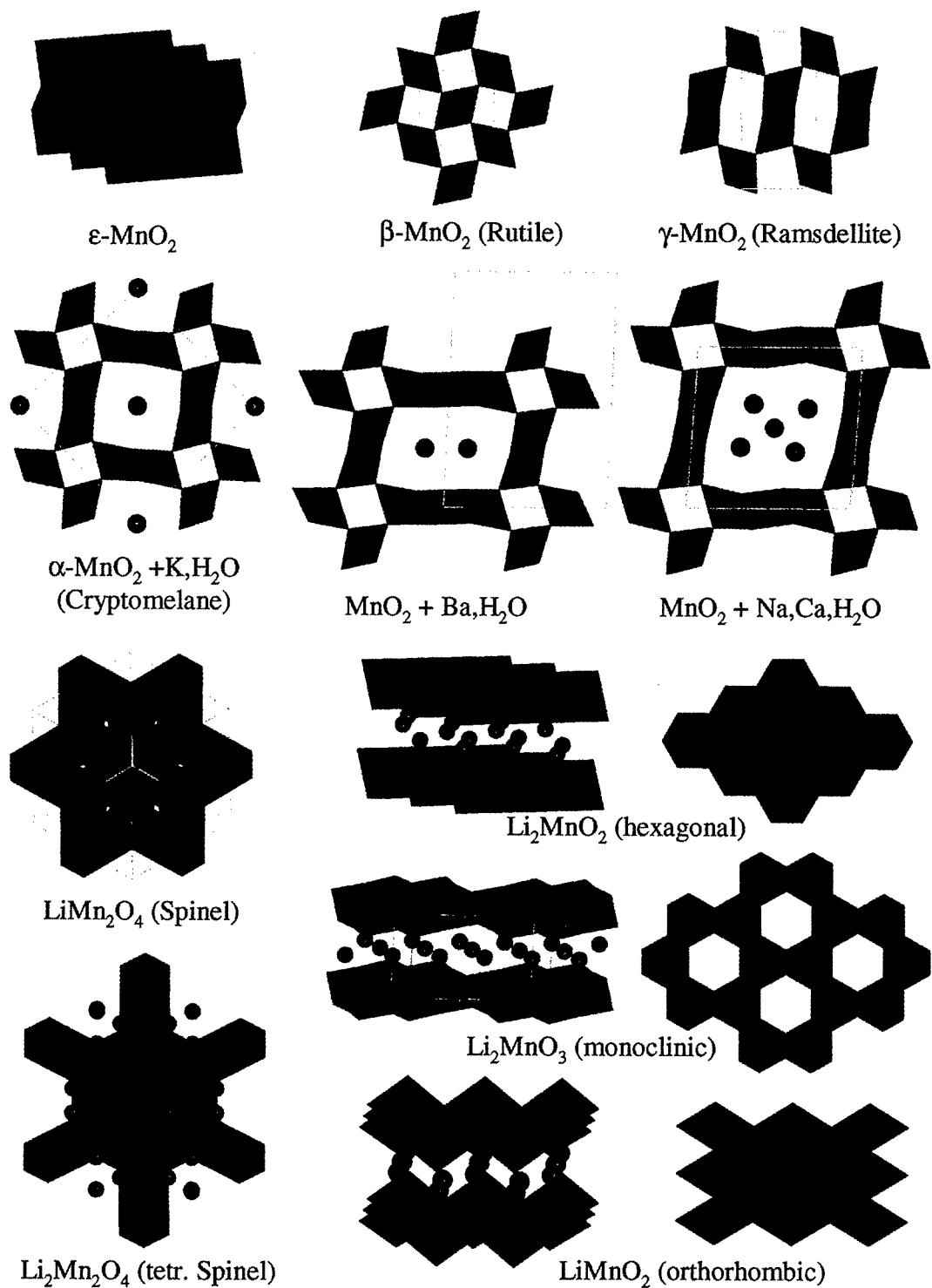
ε-MnO$_2$ β-MnO$_2$ (Rutile)   γ-MnO$_2$ (Ramsdellite)

α-MnO$_2$ +K,H$_2$O
(Cryptomelane)   MnO$_2$ + Ba,H$_2$O   MnO$_2$ + Na,Ca,H$_2$O

LiMn$_2$O$_4$ (Spinel)

Li$_2$MnO$_2$ (hexagonal)

Li$_2$MnO$_3$ (monoclinic)

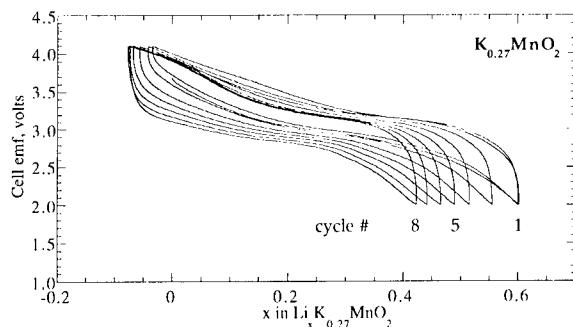Li$_2$Mn$_2$O$_4$ (tetr. Spinel)   LiMnO$_2$ (orthorhombic)

Fig. 3. Structures of some MnO$_2$ phases.

Fig. 4. Cycling behavior of layered potassium manganate, from [10].
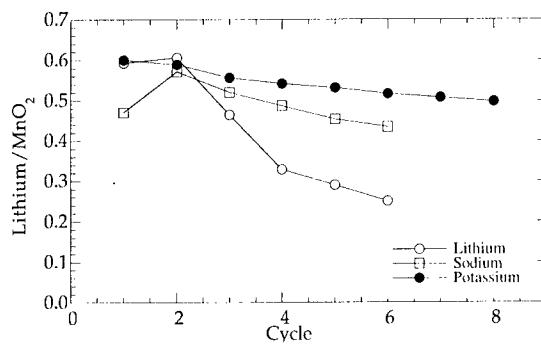
Fig. 5. Capacity as a function of cycle for Li_xMnO_2, Na_xMnO_2 and K_xMnO_2, from [10].

added stability of the K_xMnO_2 structure relative to spinel. As noted earlier, an array of hexagonal close packed oxygen layers in Li_xMnO_2 would certainly inhibit conversion to the cubic close-packed oxygen layers.

This K_xMnO_2 was formed hydrothermally by reaction of aqueous potassium permanganate solutions at 170°C. We have determined the structure of this $K_{0.27}MnO_2 \cdot nH_2O$ [8]. The manganese ions are in octahedral coordination, just like the titanium in $KTiS_2$, and the oxygen sheets shift to give trigonal prismatic sites in the interlayer region unlike in Li_xTiS_2 or Li_xMnO_2 where the anion sheets give octahedral coordination for the lithium. The structure is trigonal, space group $R\bar{3}m$, with hexagonal axes $a = 2.849(8)$, $c = 21.536(7)$ Å; 3 Mn in 3a 0 0 0 and 6 O in 6c 0 0 0.039(3). The K and H_2O mix with a fixed ratio of 1:2 on position 9d 1/2 0 1/2 between the MnO_2 layers; thus, this atom is placed not in the center of a trigonal prism but on its face.

Potassium forms a range of compounds with manganese dioxide, K_xMnO_2 that depend on potassium content temperature of preparation and oxygen content [20]. These phases are shown in Fig. 6. At the highest temperatures, $KMnO_2$ is formed but in contrast to the Na_xMnO_2 and K_xTiS_2 systems the 1:1 composition is not a layered compound but rather is composed of MnO_2 chains held together by potassium ions [21]. Studies are underway to determine its ion-exchange and electrochemical behavior in lithium cells [22]. The $K_{0.7}MnO_2$ phase appears to be a line phase. At $x = 0.25$ the cryptomelane (hollandite) framework is formed, $K_{.2}Mn_8O_{16}$. However, under hydrothermal conditions a layered structure is formed in this same composition range [8]. At intermediate values two layered phases are formed, a three block structure and a two-block structure. In both, the manganese ions are in octahedral sites, whereas the potassium ions are in trigonal prismatic sites. The stacking sequence is AbAc-BaBcA or AbAcBcBaCaCbA, with the former having no cations immediately above or below each other in neighboring layers.

The hydrothermally formed hydrated $K_xMnO_2 \cdot nH_2O$ is a three block structure. However, a 2-block hydrated structure has been formed by heating $KMnO_4$ with MnO_2 at elevated temperatures followed by a water wash to remove soluble phases [23]. Almost certainly the Delmas $K_{0.5}MnO_2$ phase [20] is formed first, and in the subsequent water wash potassium is leached out just as noted for Na_xMnO_2 [10] and Li_xTiS_2 [2].

Delmas reported [20] that there is a reduced oxygen content in K_xMnO_2 and Na_xMnO_2 phases formed above 400°C. When these high temperature formed materials are annealed in oxygen below
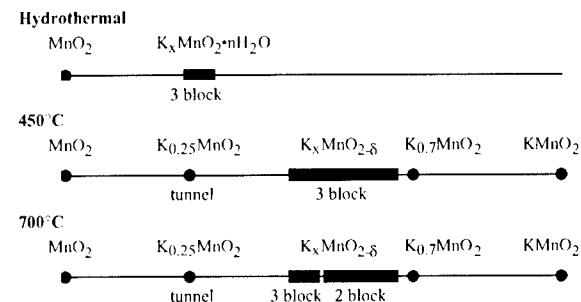

Fig. 6. Phases formed by K_xMnO_2, after [20].

400°C, there is an oxygen uptake of 0.12 O/Mn for $K_{0.5}MnO_2$ (3 block) formed at 450°C and 0.16 for $K_{0.55}MnO_2$ (2 block) formed at 700°C

Thus, if manganese oxides are made by ion-exchange from the sodium or potassium analogs from samples synthesized at high temperatures then the oxygen composition will depend on the precursor synthesis conditions. Fig. 7 [9] shows a range of synthetic approaches to the synthesis and reactions of manganates. The central reaction schemes represent the hydrothermal approach. The initially formed one water layer structure can be swelled incorporating a second water layer for ions like sodium or magnesium. These two compounds have the mineralogical names birnessite and buserite. The two layer swelled structure can then readily exchange its cations for long chain alkylammonium ions [24], much like the vermiculites and the layered disulfides.

The left side of Fig. 7 shows what has become known as the sol–gel synthesis approach. An amorphous manganese oxide is first made by the reduction of permanganate by organics such as fumaric acid [18,25] and sugars [26] or by inorganics such as iodides [8]. This gel is then heated to an elevated temperature, 500–800°C forming a layered manganate. The Bordeaux group [20,27] first formed these

anhydrous manganates by a high temperature reaction between MnO_2, Mn_2O_3 and A_2O and showed that they had a range of composition, e.g. $Na_xMn_{1-\delta}O_2$ where $0.45 = x = 0.67$. At these temperatures, the manganese oxide lattice is oxygen 'deficient', which deficiency can be diminished by an oxygen anneal around 400°C, which increases the Mn^{IV} content and converts the lattice from monoclinic to hexagonal.

We have discussed the use of pillars to stabilize the MnO_2 layer structure. Another option is to make the layered lithium manganese oxide more like $LiCoO_2$, possibly by doping with cobalt, iron or nickel to give for example $Li_xMn_{1-y}Co_yO_2$. Several workers have very recently shown enhanced behavior using this approach. Thus Armstrong [28] showed enhanced cycling behavior for $LiMn_{1-y}Co_yO_2$ with $y = 10\%$, with a capacity maintained at 200 mAh/g over 20 cycles which corresponds to 0.7Li/Mn. These cobalt substituted samples were made by ion-exchange from $NaMnO_2$ synthesized at 670°C; the Mn:O ratio in the starting material was not reported. The substitution of cobalt or iron for manganese in potassium manganese dioxides, K_xMnO_2, caused a marked enhancement by two orders of magnitude of the conductivity of the manganese oxide [29,30], as shown in Fig. 8. The conductivity enhancement was independent of whether the sample was prepared under hydrothermal conditions at 170°C or by solid state synthesis at over 700°C. This conductivity enhancement may be the cause for the suppression of the Jahn–Teller distortion.

3.1. Tunnel structures

Manganese oxide forms several tunnel structures, as shown in Fig. 3; these have 2×2 ($BaMn_8O_{16}$-hollandite, KMn_8O_{16}-cryptomelane, Mn_8O_{16}-α-MnO_2), 2×3, and 3×3 (todorokite) tunnels.

One interesting tunnel structure is that commonly known as hollandite, with the unit formula $M_xMn_8O_{16} \cdot nH_2O$. This is the same 2×2 tunnel structure that is also taken up by α-MnO_2. M is typically a large cation such as potassium or barium. These cations, however, inhibit the in-diffusion of lithium ions. Feng et al. [31] have succeeded in forming the hollandite structure with just protons and
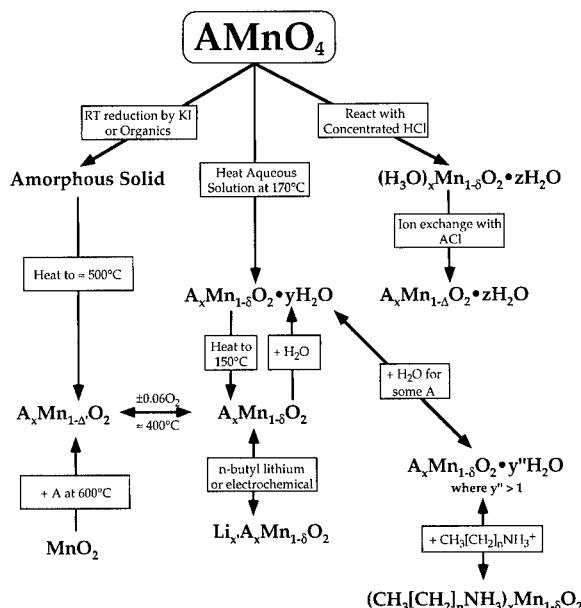

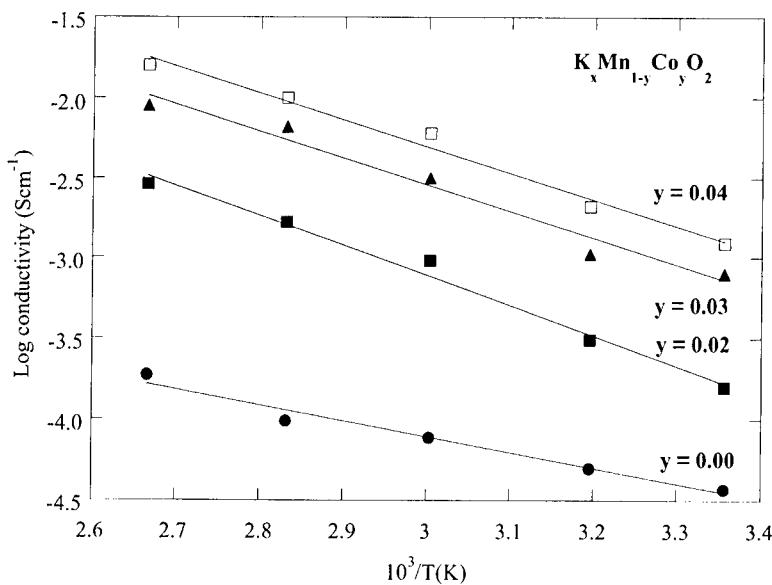Fig. 7. Synthetic routes to A_xMnO_2, from [9].

Fig. 8. Conductivity of cobalt doped layered manganese oxides, from [30].

water in the tunnel by the reaction between lithium permanganate and manganese (II) nitrate in strong, ≥ 8 M, sulfuric acid at 100°C. The structure is maintained after annealing at 300°C. In an electrochemical cell, 0.7 Li can be reversibly intercalated at 0.25 mA/cm^2 at an average potential of around 3 volts giving an capacity of 230 mAh/g to a cut-off of 2.0 volts; this decays to about 170 mAh/g for the 3rd to 10th cycles. This is much better stability than that observed in samples formed by sulfuric acid leaching of Li$_2$MnO$_3$ at 90°C [32]. This result on the 2×2 structure shows the inherent reversibility of manganese oxides when conversion to the spinel phase is inhibited.

The 3×3 todorokite structure of Mg$_{0.2}$MnO$_{1.9}$ · 0.6H$_2$O, has been shown by Nazar [33] to cycle around 0.5 Li/Mn at low current densities and cathodes containing 50% carbon. This is close to the theoretical capacity of 0.6 Li/Mn.

In addition, manganese oxide forms a complex tunnel structure with sodium, Na$_{0.44}$MnO$_2$, first reported by Parant et al. [27], which has the structure of Na$_4$Mn$_4$Ti$_5$O$_{18}$ [34]. Some recent work on this group of manganese oxides suggests that excellent cycling behavior can be obtained in manganese oxides. The tunnel compound, Na$_{0.44}$MnO$_2$, has been studied in sodium and lithium cells by Doeff et al.

[35,36] and shown to exhibit good reversibility. At 85°C in a polymer electrolyte cell Na$_{0.14}$MnO$_2$ attained 140 mAh/g. The coordination around the manganese changes somewhat as sodium is replaced by lithium [37]. In Na$_{0.44}$MnO$_2$ the manganese has square pyramidal coordination with the pyramidal Mn–O bond being somewhat long at 2.33 Å compared with the 1.73 and 1.86 in the basal plane, whereas in the exchanged and partially oxidized Li$_{0.27}$MnO$_2$ a sixth oxygen comes within bonding distance at 2.49 Å. Most recently, Armstrong et al. [38] have made the corresponding lithium compound by complete ion-exchange, Li$_{0.44}$MnO$_2$, and reported a capacity of 85 mAh/g without fade over 100 cycles when cycled between 3.6 and 2.8 volts. These results clearly show that manganese oxides can be stabilized against reversion to the spinel structure. However, a doubling of the capacity is needed for a viable system.

3.2. Disordered structures

Another option to avoid reversion to the spinel structure is to start with a disordered manganese oxide structure, akin to the aerogel vanadium oxides. Smyrl [39] and Manthiram [40] have begun studying such materials.

4. Conclusions

A range of pure and doped manganese oxides have been synthesized in an attempt to form the next generation cathode for high energy density lithium batteries. Some clues have been found to stabilize MnO_2 over a range of lithium content. These include pillaring of the lattice with larger cations such as potassium, doping the lattice with other transition elements such as Co or Fe, forming stable tunnel structures, and amorphous structures. Doping of the manganese lattice with elements to enhance its notoriously poor electrical conductivity appears promising but still needs studying in the tunnel and amorphous materials.

Acknowledgements

References

[1] M.S. Whittingham, Science 192 (1976) 1126.
[2] M.S. Whittingham, Prog. Solid State Chem. 12 (1978) 41.
[3] K. Mitzushima, P.C. Jones, P.J. Wiseman, J.B. Goodenough, Mat. Res. Bull. 17 (1980) 785.
[4] M.M. Thackeray, Prog. Solid State Chem. 25 (1997) 1.
[5] J.-M. Tarascon and editor, Solid State Ionics 69 (1994).
[6] F. Leroux, D. Guyomard, Y. Piffard, Solid State Ionics 80 (1995) 299.
[7] F. Leroux, D. Guyomard, Y. Piffard, Solid State Ionics 80 (1995) 307.
[8] R. Chen, P. Zavalij, M.S. Whittingham, Chem. Mater. 8 (1996) 1275.
[9] R. Chen, T. Chirayil, M.S. Whittingham, Proceedings of the 10th International Symposium on Solid State Ionics, Singapore, December 1995, Solid State Ionics 86–88 (1996) 1.
[10] R. Chen, M.S. Whittingham, J. Electrochem. Soc. 144 (1997) L64.
[11] R. Chen, M.S. Whittingham, Proc. Annual Automotive Technology Development Customers Coordination Meeting, DOE-OTT (Dearborn, MI, Oct. 27–30, 1997), III (1997) 301.
[12] M.S. Whittingham, R. Chen, T. Chirayil, P. Zavalij, Electrochem. Soc. Proc. 96–5 (1996) 76.
[13] A.R. Armstrong, P.G. Bruce, Nature 381 (1996) 499.
[14] F. Capitaine, P. Gravereau, C. Delmas, Solid State Ionics 89 (1996) 197.
[15] C. Delmas, F. Capitaine, Abstracts 8th Int. Meeting Lithium Batteries, 8 (1996) 470.
[16] S. Bach, J.P. Pereira-Ramos, N. Baffier, J. Solid State Chem. 120 (1995) 70.
[17] S. Bach, J.P. Pereiraramos, C. Cachet, M. Bode, L.T. Yu, Electrochim. Acta 40 (1995) 785.
[18] J.P. Pereira-Ramos, R. Baddour, S. Bach, N. Baffier, Solid State Ionics 53–56 (1992) 701.
[19] M.S. Whittingham, The relationship between structure and cell properties of the cathode for lithium batteries, in: O. Yamamoto, M. Wakihara (Eds.), Lithium Batteries, Kodansha, Tokyo, 1998.
[20] C. Delmas, C. Fouassier, Z. Anorg. Allg. Chem. 420 (1976) 184.
[21] M. Jansen, F.M. Chang, R. Hoppe, Z. Anorg. Allgem. Chemie 490 (1982) 101.
[22] F. Zhang, P.Y. Zavalij, M.S. Whittingham, Unpublished data. (1999)
[23] S.H. Kim, S.J. Kim, S.M. Oh, Chem. Mater. 11 (1999) 557.
[24] D.C. Golden, J.B. Dixon, C.C. Chen, Clays and Clay Minerals 5 (1986) 511.
[25] P. LeGoff, N. Baffier, S. Bach, J.P. Pereiara-Ramos, R. Messina, Solid State Ionics 61 (1993) 309.
[26] S. Ching, J.A. Landrigan, M.L. Jorgenson, N. Duan, S.L. Suib, C.-L. O'Young, Chem. Mater. 7 (1995) 1604.
[27] J.-P. Parant, R. Olazcuaga, M. Delalette, C. Fouassier, P. Hagenmuller, J. Solid State Chem. 3 (1971) 1.
[28] A.R. Armstrong, R. Gitzendanner, A.D. Robertson, P.G. Bruce, Chem. Commun. (1998) 1833.
[29] P. Sharma, G. Moore, F. Zhang, P.Y. Zavalij, M.S. Whittingham, Electrochem. Solid-State Lett. 2 (1999) 494.
[30] M.S. Whittingham, P. Zavalij, F. Zhang, P. Sharma, G. Moore, Electrochem. Soc. Proc. 99–13 (1999) 1.
[31] Q. Feng, H. Kanoh, K. Ooi, M. Tani, Y. Nakacho, J. Electrochem. Soc. 141 (1994) L135.
[32] M.H. Rossouw, D.C. Liles, M.M. Thackeray, W.I.F. David, S. Hull, Mater. Res. Bull. 27 (1992) 221.
[33] M.J. Duncan, F. Leroux, J.M. Corbett, L.F. Nazar, J. Electrochem. Soc. 145 (1998) 3746.
[34] W.G. Mumme, Acta Cryst. B24 (1968) 1114.
[35] M.M. Doeff, M.Y. Peng, Y. Ma, L.C. DeJonghe, J. Electrochem. Soc. 141 (1994) L145.
[36] M.M. Doeff, T.J. Richardson, L. Kepley, J. Electrochem. Soc. 143 (1996) 2507.
[37] T.J. Richardson, P.N. Ross, M.M. Doeff, Electrochem. Soc. Abstr. 98–2 (1998) 122.
[38] A.R. Armstrong, H. Huang, R.A. Jennings, P.G. Bruce, J. Mater. Chem. 8 (1998) 255.
[39] W. Smyrl, Abstracts Advanced Non-Aqueous Battery Technology Research and Development Workshop (Hunt Valley, MD, Oct 15–17, 1997), (1997)
[40] J. Kim, A. Manthiram, Nature 390 (1997) 265.

The influence of non-ideal microstructures on the analysis of grain boundary impedances

J. Fleig*

Max-Planck-Institut für Festkörperforschung, Stuttgart, Germany

Abstract

The so-called brick layer model is frequently used to analyze impedance spectra of polycrystalline samples with highly resistive grain boundaries. However, the basic assumptions of the model (cubic grains, laterally homogeneous grain boundaries, identical properties of all grain boundaries) are usually violated in real ceramics. To investigate the impact of some deviations from the brick layer model, the potential distributions, and thus the impedance of polycrystals, have been calculated by the finite element method. The results show that bulk properties can distinctly influence the size and shape of the so-called 'grain boundary semicircle', particularly for laterally inhomogeneous grain boundaries and for properties varying from boundary to boundary. Depressions of the grain boundary semicircle solely due to a non-brick-layer microstructure are observed. The validity and limits of the brick layer model are discussed. © 2000 Elsevier Science B.V. All rights reserved.

Keywords: Grain boundaries; Microstructure; Impedance; Electrical properties; Brick layer model; Potential distribution

1. Introduction

Highly resistive grain boundaries are of great technological importance with regard to the overall electrical properties of polycrystalline materials and can play a desired functional role in semiconducting electroceramic devices such as varistors, thermistors and capacitors [1,2]. On the other hand, for many applications of solid electrolytes (e.g. fuel cells, oxygen pumps or electrochemical reactors) the overall conductivity of the electroceramic material should be as high as possible and highly resistive grain boundaries, such as those found in oxygen conduct-

ing membranes of zirconia [3–7], are distinctly unwelcome.

Impedance spectroscopy is an important tool to investigate the electrical properties of highly resistive grain boundaries since the grain boundaries frequently cause an additional semicircle in the complex impedance plane [3–7]. In order to analyze and interpret the spectra a brick layer model (Fig. 1a) is usually applied assuming cubic grains and laterally homogeneous as well as identical grain boundaries. However, these brick layer assumptions are more or less violated in real ceramics and a detailed investigation of the impact of such deviations on the overall impedance is still missing.

In this contribution an overview of impedance effects caused by some important deviations from the

*Tel.: +49-711-689-1770; fax: +49-711-689-1722.
E-mail address: fleig@chemix.mpi-stuttgart.mpg.de (J. Fleig)
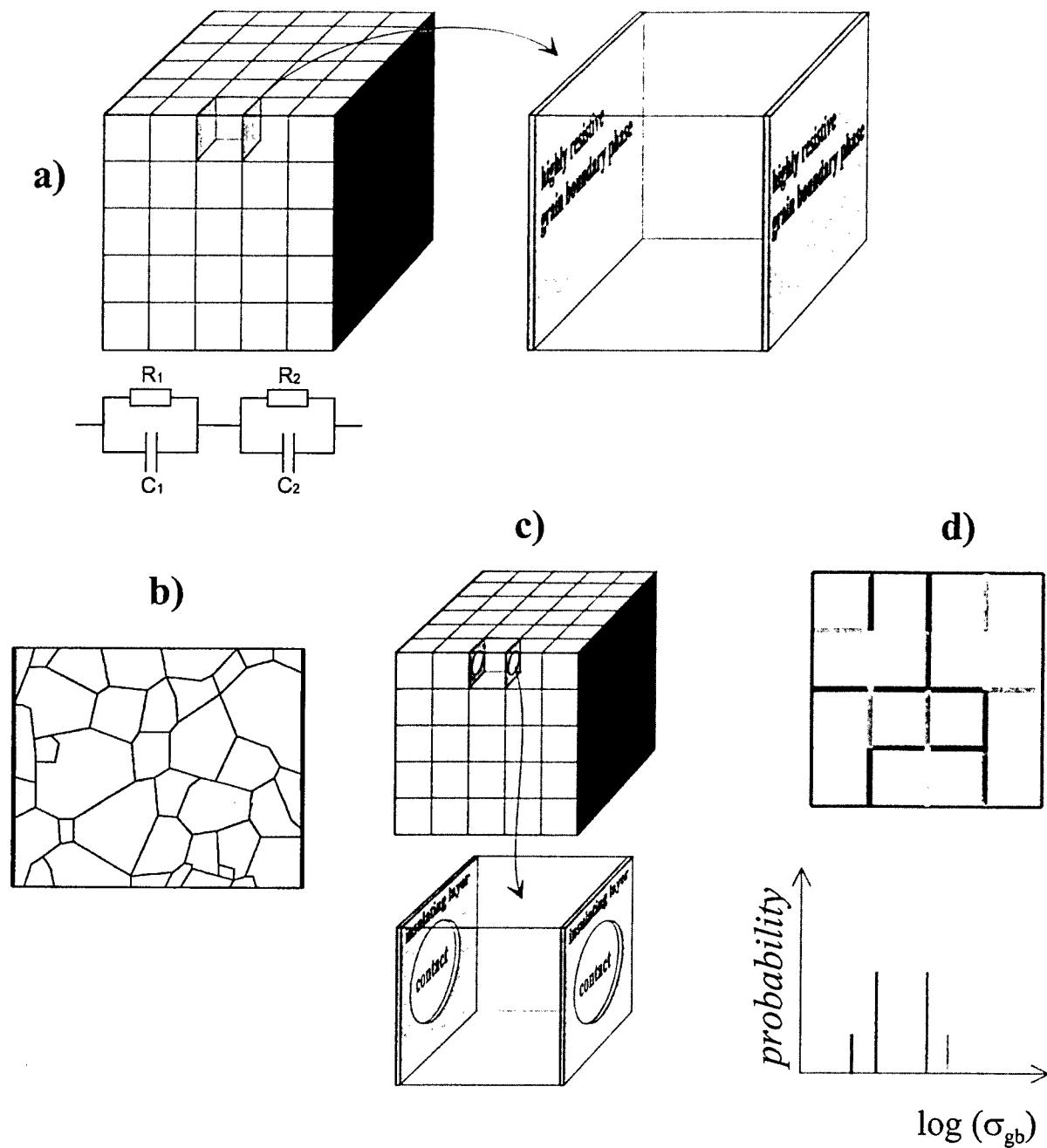
Fig. 1. Sketch of the brick layer model (a) and important deviations in real materials as considered in this contribution: (b) non-cubic grains (here in 2D); (c) laterally inhomogeneous grain boundaries (here in 3D); (d) grain boundary properties differing from grain to grain according to the probability distribution of the grain boundary conductivity (here in 2D). In the brick layer approach (a) highly resistive grain boundaries perpendicular to the electrodes can be neglected leading to the equilvalent circuit shown in (a).

brick layer model is given, while a detailed analysis of some special aspects is presented elsewhere [8–10]. Particularly, we consider: (i) deviations from the cubic grain shape; (ii) the influence of imperfect contacts between the grains; and (iii) the impact of a distribution of different grain boundaries in the crystal (Fig. 1). Moreover, some conditions are discussed within which the brick layer model is a useful tool to estimate electrical properties of grain boundaries.

2. Model considerations

The potential distribution within a polycrystal is obtained by solving Laplace's equation for the electrical potential (φ). The impedance in a sample with bulk conductivity σ_{bulk} and permittivity ε_{bulk} can be calculated by integrating the complex current density, $j = -(\sigma + i\omega\varepsilon)\mathrm{grad}(\varphi)$, along an electrode. Grain boundaries are assumed to exhibit an effective thickness w_{gb} and an effective conductivity σ_{gb}. The microscopic reason for the blocking character of the grain boundary (e.g. core effects, space charge effects or a second phase) is not considered in this work.

In the case of the two-dimensional calculations of different grain boundary patterns (Section 3.1) identical grain boundary conductivity and thickness were assumed for all grain boundaries. In Section 3.2, in which the three-dimensional simulations of imperfect grain-to-grain contacts are discussed, the properties vary along a single grain boundary: the grain boundary conductivity is assumed to be zero for an insulating grain boundary phase (e.g. a solid phase or pores, Fig. 1c) and non-zero for the contacted region. In Section 3.3 (two-dimensional simulations) a variation in the conductivity from grain boundary to grain boundary was considered, using different probability distributions of σ_{gb} (cf. Fig. 1d).

The numerical solution was computed using the finite element software 'FLUX-EXPERT' from Simulog (1 Rue James Joule, 78280 Guyancourt Cedex, France). The grain boundaries may be taken into account via so-called 'interfacial elements' [9,11]. Further details on such calculations are given in Refs. [9,12].

3. Results and discussion

3.1. The influence of different grain boundary patterns

To examine the influence of the microstructure, FE-calculations in two dimensions were performed. A general principle may improve the experimentalists' prediction of the possible impact a given microstructure will have on the impedance: if possible, current lines make detours around hindrances, i.e. resistive grain boundaries. This leads to an interesting observation. Detours are 'easy' for high bulk conductivity, and excess grain boundaries are avoided. However, detours are 'difficult' for low bulk conductivity, and additional grain boundaries must be passed, leading to a greater grain boundary resistance than for the case of high σ_{bulk} [9]. Hence, the low-frequency semicircle of the impedance spectrum, which is usually exclusively interpreted in terms of grain boundary properties, can also be influenced by properties of the grain interior.

Such detour-effects can play an important role in real ceramics, particularly if broad grain size distributions exist or if the grain size distribution is spatially inhomogeneous. This is illustrated for a sample with inhomogeneous grain size distribution, as shown in Fig. 2 (consisting of some 7-μm large grains and agglomerations of smaller grains with 1-μm grain size). A simple calculation of an average grain size by counting the grains per area leads to a value of 1.94 μm. The low-frequency semicircle as obtained by finite element calculations is considerably smaller than predicted by the brick layer model for a grain size of 1.94 μm (see Fig. 2). As a consequence, the calculation of a meaningful average grain size requires a weighting in favour of large grains.

This can easily be understood from a plot of the magnitude of the d.c. current density (Fig. 3a): the current by-passes the regions of high grain boundary density and thus the inhomogeneous current distribution prefers large grains. However, this changes for relatively low bulk conductivity since detours become more difficult and a much more homogeneous current distribution results as shown in Fig. 3b. Hence the 'grain boundary resistance' as obtained from the low-frequency semicircle, depends
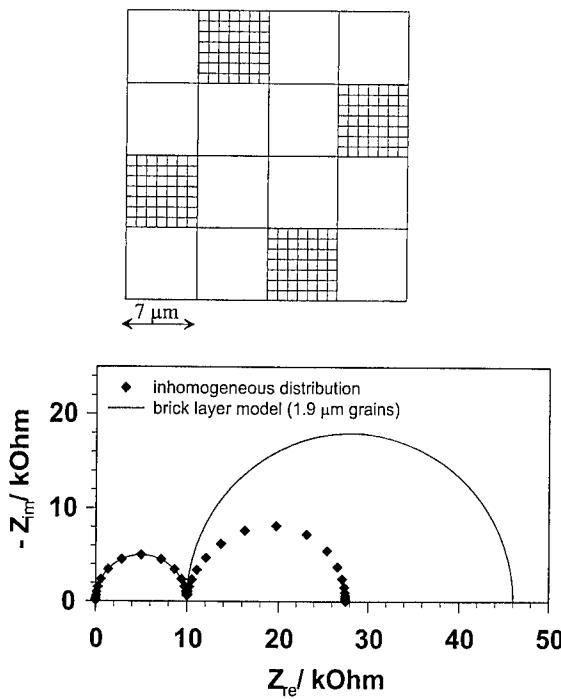
Fig. 2. Artificial microstructure representing the case of an inhomogeneous grain size distribution (agglomeration of smaller grains) and the resulting impedance spectrum as calculated by the finite element method. For comparison the spectrum calculated by assuming a brick layer model of 1.94 μm grain size is plotted as well. The grain boundary properties are: $\sigma_{gb} = 4 \times 10^{-8}$ $1/\Omega$, grain boundary thickness = 2.8 nm, permittivity $\varepsilon_{gb} = \varepsilon_{bulk}$, bulk conductivity $\sigma_{bulk} = 10^{-4}$ $1/\Omega$. (Please note, that in 2D the unit of a conductivity is $1/\Omega$.)

not only on the conductivity of the highly resistive grain boundaries but also on the bulk conductivity (Fig. 3c). As a consequence, the temperature-dependence of the low-frequency semicircle ('grain boundary semicircle') yields an apparent activation energy which can differ slightly from the true grain boundary activation energy. We give a numerical example for the case considered in Figs. 2 and 3: (i) if $E_{act,bulk} = 0.9$ eV and $E_{act,gb} = 1.8$ eV there is a 'medium' temperature regime with an apparent grain boundary activation energy of 1.7 eV. ('Medium' temperature regime means temperatures for which the sizes of the two semicircles are of the same order of magnitude.) The relative deviation from $E_{act,gb}$ can be shown to be approximately proportional to $(1 - E_{act,bulk}/E_{act,gb})$ and thus can be rather large for small $E_{act,gb}$.

Moreover, the low frequency semicircle is not ideal but asymmetrically distorted. A fit using a resistor in parallel with a constant phase element with impedance $Q^{-1}(i\omega)^{-n}$ (Q,n = fit parameters, ω = angular frequency) yields a value of $n = 0.916$ for the left half of the low-frequency semicircle while the right half results in $n = 0.99$. It has to be emphasized that the depression is not due to a distribution of relaxation times (only one grain boundary relaxation time exists) but is instead a consequence of the frequency-dependence of the current lines: for low frequencies the current detours the excess grain boundaries, while for high frequencies the interfaces are nearly dielectrically short-circuited and a homogeneous current distribution results. This frequency-dependent switching of the current lines leads to modifications in the spectra shape and has no counterpart in quasi-one-dimensional systems as the simple brick layer model. The high-frequency semicircle, on the other hand, is not affected by the microstructural pattern and reveals the true bulk properties.

On the other hand, in many cases the brick layer model does allow reasonable estimates of the grain boundary properties. This is discussed in more detail in Ref. [9]. From the calculations therein (e.g. a pattern as shown in Fig. 1b) and other calculations for two-dimensional grain boundary patterns we expect that the brick layer model is a reasonable approximation for homogeneous and relatively narrow distributions of grain sizes and grain shapes. Serious problems are expected, for example, for a very broad grain size distribution with very large and very small grains or a spatially inhomogeneous grain size distribution as sketched in Fig. 3.

3.2. The influence of imperfect contacts

Grain boundaries are often laterally inhomogeneous (i.e. 'imperfect') in the sense that ideally conducting as well as totally insulating interface regions are present. To give two examples: (i) solid grain boundary phases frequently only partially wet the grains establishing a diminished grain-to-grain contact, and (ii) nanopores along grain boundaries can cause an imperfect contact between two grains. In such cases an insulating layer partly separates neighboring grains (Fig. 1c) and the d.c. current is
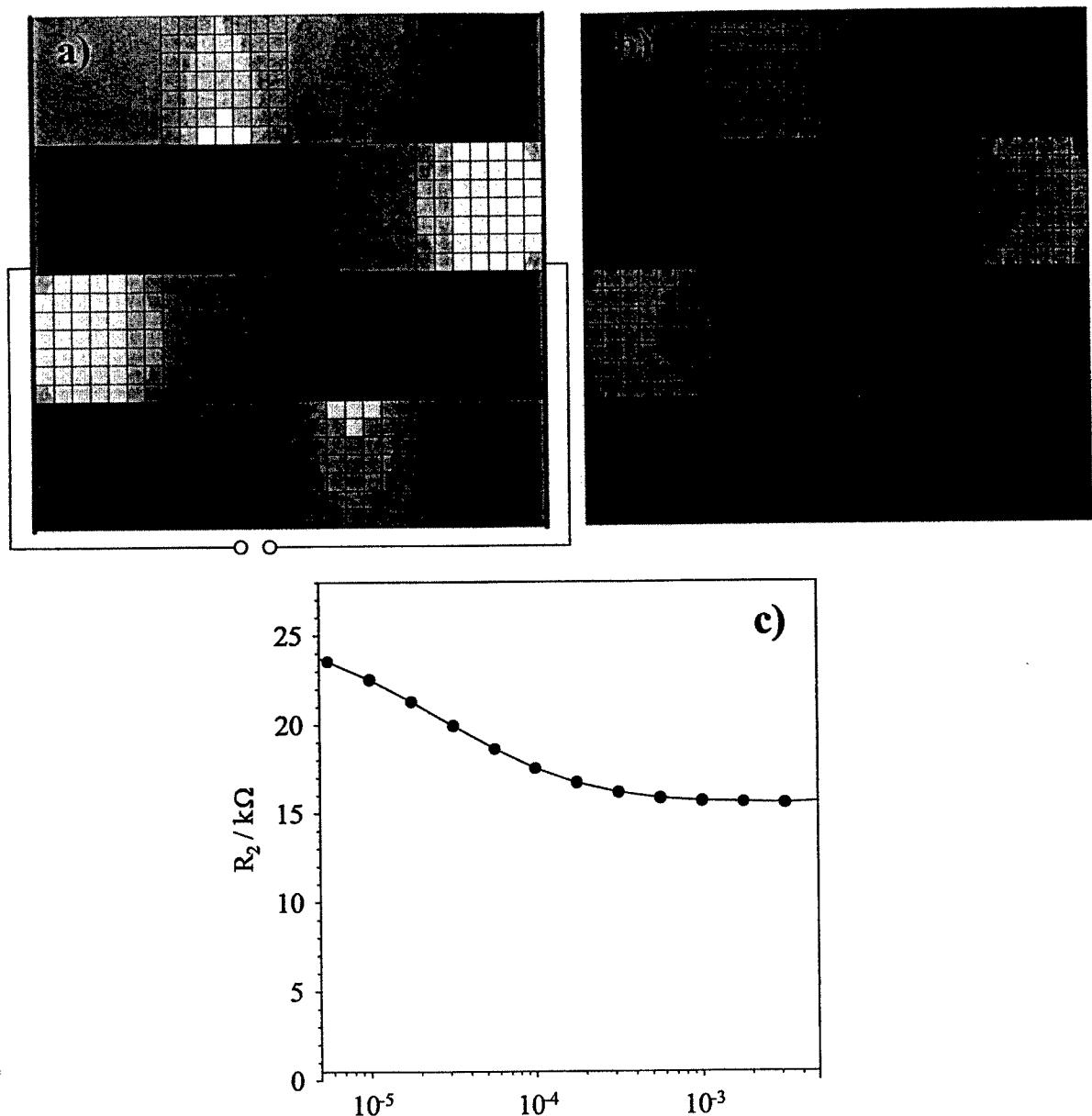
Fig. 3. Top: magnitude of the d.c. current density within the two-dimensional polycrystal of Fig. 2 for two different bulk conductivities: (a) $\sigma_{bulk} = 2 \times 10^{-4}$ $1/\Omega$; (b) $\sigma_{bulk} = 10^{-5}$ $1/\Omega$. For other parameters see Fig. 2. Dark indicates high current density and light low current density. Bottom: resistance from the low-frequency semicircle R_2 as a function of bulk conductivity.

constricted close to the conducting grain-to-grain contacts. Consequently the d.c. bulk resistance is higher than the ideal bulk resistance. Such imperfect contacts give rise to a low-frequency semicircle in the complex impedance plane (Fig. 4) which can be

interpreted in terms of a transition of the bulk resistance from the d.c. value to the a.c. (ideal) value due to the dielectric 'opening' of the insulating grain boundary phase capacitor [8]. Hence it is not the sequence of two serial regions of different conduc-

J. Fleig / Solid State Ionics 131 (2000) 117–127
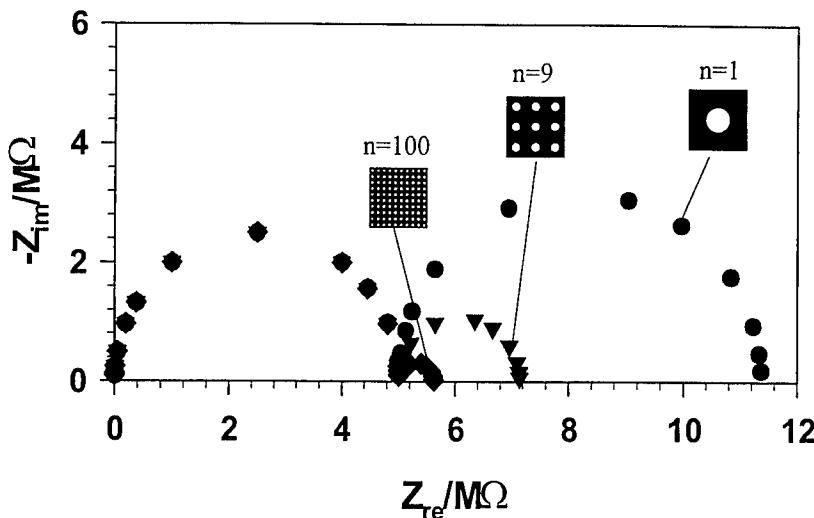
Fig. 4. Impedance spectra for a three-dimensional polycrystal (bulk conductivity $\sigma_{bulk} = 10^{-7}$ $1/\Omega$ cm) with an electrode area of 1 cm^2 and a thickness of 5 mm. All grain boundaries are identical but laterally inhomogeneous, consisting of an insulating phase (thickness $= 2$ nm, permittivity $= \varepsilon_{bulk}$) and different amounts (n) of circular perfectly conducting spots (cf. Fig. 1c). The insets sketch cross-sections of the grain boundaries between two grains (cf. Fig. 1c) with contacted (white) and insulating (black) regions. In all three cases the fraction of contacted area per grain boundary is kept constant at 12.6%. The dc resistance (11.4 mΩ) is a pure bulk resistance and is larger than the ideal bulk resistance (5 MΩ) because of the current constriction close to the contacted spots.

tivities but the frequency-dependent shift of the current lines that leads to the low-frequency semicircle. Fig. 4 shows the resulting impedance spectra for different grain boundary contact geometries, all of them exhibiting the same area fraction of insulating grain boundary phase ($-\alpha_{contact}$) but different numbers of contact spots carrying the d.c. current. The so-called 'grain boundary resistance' R_2 (diameter of the low-frequency arc) strongly depends on the number of contacts while the high-frequency semicircle is not influenced by grain boundary properties and still reveals the 'ideal' bulk values as expected for a single crystal. It has to be emphasized that the additional resistance is not due to the contact 'bridge' which connects two grains (cf. Fig. 1c) but is caused by the current constriction in the grain bulk close to the conducting grain-to-grain contacts.

A quantitative estimate of the magnitude of the 'grain boundary resistance' R_2 is possible according to Ref. [8]

$$R_2 \approx \frac{1}{\sigma_{bulk}} \frac{1}{\sqrt{4\alpha_{contact}}n} \frac{L_{sample}}{A_{sample}} \qquad (1)$$

In Eq. (1) n is the number of grain-to-grain

contacts per grain boundary and $\alpha_{contact}$ the fraction of established contact area (contacted area/complete area), σ_{bulk} denotes the bulk conductivity and L_{sample}, A_{sample} are the sample thickness and area, respectively. Thus R_2 is determined by two independent parameters ($\alpha_{contact}$, n), and an evaluation of the contacted area (or of the fraction of 'blocked' current) solely from the impedance spectrum is not possible. The 'grain boundary capacitance', on the other hand, allows an estimate of the thickness of the insulating grain boundary phase [8].

To help estimate to what extent current constriction might cause grain boundary impedances in real electroceramic materials, a plot is given (Fig. 5) which relates R_2/R_1 (i.e. the ratio of the semicircle diameters) to the fraction of contacted area ($\alpha_{contact}$) for varying contact numbers per grain boundary. From Fig. 5 and also from the estimate according to Eq. (1), it can be seen that pronounced low-frequency semicircles require rather small contact areas, particularly if many contact spots are involved. In many cases we expect the grain boundary resistance due to current constriction to be of the order of magnitude of the ideal bulk resistance or even
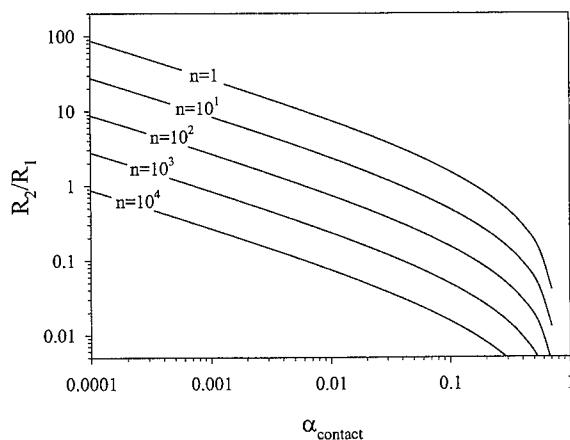
Fig. 5. Ratio of R_2/R_1 ('grain boundary resistance'/ideal bulk resistance) depending on the fraction of contacted area $\alpha_{contact}$, for different numbers of contacts per grain boundary n. The plots are calculated using a more generally valid estimate than Eq. (1) as given in Ref. [8].

smaller. However, in porous material (e.g. freshly pressed samples) or if there are only very few gaps (pin-holes) in a highly resistive grain boundary phase current constriction effects can be considerably larger.

Indications that current constriction effects are relevant can be obtained from the temperature, partial pressure, bias and grain size dependence of R_2. If current constriction plays a role, the temperature and partial pressure dependence of R_2 should be close to that of the bulk as already predicted by intuitive models [3,5–7,13]. A bias-dependent 'grain boundary resistance', on the other hand, suggests other mechanisms than current constriction. The grain size dependence of the grain boundary resistance, finally, is expected to deviate from the inverse linear relationship suggested by the brick layer model. Further information is given in Refs. [8,12].

However, the situation becomes more complicated if partially blocking and totally blocking interface regions exist simultaneously. For example, an insulating grain boundary phase partially wets the grains while at the established grain-to-grain contacts an additional transfer resistivity exists. Current constriction effects and 'true' grain boundary contributions due to the transfer process superimpose and lead to a rather complex situation.

To get a first insight into this topic we consider the following grain boundary case. A solid grain boundary phase (thickness 2 nm) partially wets the grains, leaving a circular grain-to-grain contact with a diameter of 54% of the grain boundary length (2 μm) (as sketched in Fig. 1c). At the established contact we assume a transfer hindrance which can be described by a 2-nm thick 'layer' of conductivity σ_{gb} and permittivity ε_{bulk}. As shown in Fig. 6, again one low-frequency semicircle arises in the complex impedance plane. However, this low-frequency semicircle includes both bulk contributions (due to current constriction) and 'true' grain boundary contributions owing to the partial blocking at the established contact. Hence a 'mixed' activation energy results and even a change of the activation energy with temperature from the bulk value to a higher or lower value (non-Arrhenius-behaviour) is possible. Nevertheless, the contribution of current constriction within the grains can be estimated by Eq. (1).

Such ambiguous situations arise if the capacitance of the insulating grain boundary phase is larger than the capacitance related to the transfer process at the established contact. Since relevant current constriction effects require relatively small contacted areas (see Fig. 5) we expect that this condition for the two
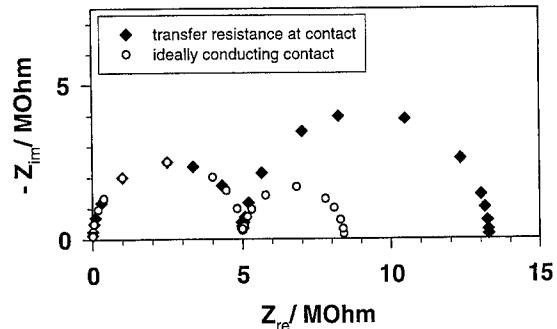

Fig. 6. Impedance spectra for a three-dimensional crystal (bulk conductivity $\sigma_{bulk} = 10^{-7}$ $1/\Omega$ cm) with and without an additional transfer resistance at the established grain-to-grain contact. All grain boundaries are identical and exhibit one contact spot with contact area $\alpha_{contact} = 0.23$. Parameters: electrode area, 1 cm²; sample thickness, 5 mm; thickness of the insulating phase, 2 nm; permittivity of the insulating phase, ε_{bulk}; partial blocking at the established contact according to a 2-nm thick 'layer' of conductivity, σ_{gb}; and permittivity, ε_{bulk}.

capacitances is often fulfilled at real grain boundaries. However, if the opposite situation is valid (capacitance of the insulating layer smaller than the transfer capacitance) a third semicircle appears, and an approximate separation of current constriction and true grain boundary resistance is possible, as shown for a similar problem (fuel cell cathode with the current being constricted close to the three phase boundary region) in Ref. [14].

3.3. The influence of the distribution of different grain boundaries in space

Even if each individual grain boundary is laterally homogeneous, the structural and chemical qualities, and thus the electrical properties, may vary from boundary to boundary leading to a certain distribution of grain boundary conductivities as sketched in Fig. 1d. One example where such a distribution is expected is for the case when the grain boundary resistance is caused by a space charge depletion layer. Due to an exponential relation, relatively small variations of the space charge potential result in strong variations of the effective grain boundary resistivity.

We probed the influence of distributions of different grain boundaries in two dimensions for some probability distributions of the grain boundary conductivity σ_{gb} (Figs. 7–9). Following the given distribution the grain boundary conductivities were randomly distributed in the square microstructural pattern (cf. Fig. 1d, the calculations are performed for a sample consisting of 10×10 grains).

Fig. 7 shows the spectrum for a discrete Gaussian distribution of $\log(\sigma_{gb})$ calculated by the finite element method and a spectrum according to the brick layer model using the 'mean' grain boundary conductivity $(10^{-7}\ 1/\Omega)$. Such a distribution of $\log(\sigma_{gb})$ corresponds to a Gaussian distribution of the space charge potential. Even though the extreme conductivity values of the distribution differ by a factor of 100 the brick layer model allows a rather satisfying estimate of the 'mean' grain boundary properties. However, again an inhomogeneous current distribution results which depends weakly on the bulk conductivity. Therefore, bulk properties slightly influence the 'grain boundary semicircle' (cf. Fig. 3), and a minor difference between the activation energy
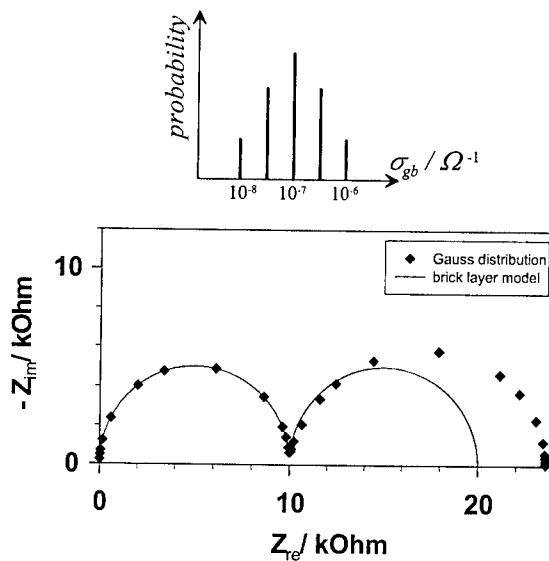

Fig. 7. Calculated impedance spectrum of a polycrystal (10×10 grains) for a discrete Gaussian distribution of the grain boundary conductivities (cf. Fig. 1d). The Gaussian distribution is on a logarithmic scale. The corresponding brick layer model assumes a conductivity according to the 'mean' value of the distribution $(10^{-7}\ 1/\Omega)$. Parameters: two-dimensional bulk conductivity, 10^{-4} $1/\Omega$; grain size, 2 μm; grain boundary thickness, 2 nm.
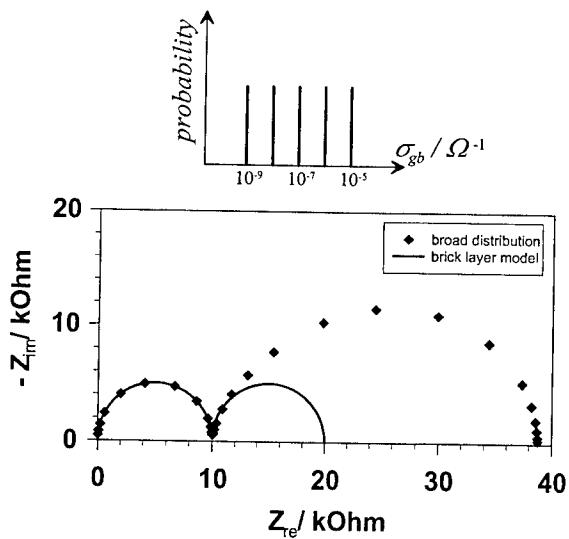

Fig. 8. Calculated impedance spectrum of a polycrystal (10×10 grains) for a very broad distribution of the grain boundary conductivity (cf. Fig. 1d). The corresponding brick layer model assumes a conductivity according to the center of the distribution $(10^{-7}\ 1/\Omega)$. Other parameters as in Fig. 7.
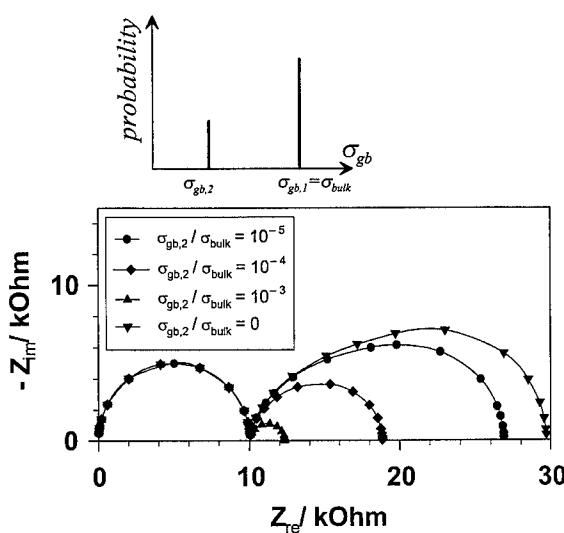
Fig. 9. Calculated impedance spectra of a polycrystal (10×10 grains) for different bimodal distributions of the grain boundary conductivity (cf. Fig. 1d). While 70% of the grain boundaries exhibit bulk conductivity $\sigma_{bulk} = \sigma_{gb,1} = 10^{-4}$ $1/\Omega$, $\sigma_{gb,2}$ varies between 10^{-7} $1/\Omega$ and zero. Other parameters as in Fig. 7.

of the low-frequency semicircle and the true activation energy of the grain boundary resistivity can occur. Moreover, the low-frequency semicircle exhibits a weak asymmetric depression (Fig. 7).

The situation becomes more difficult for a very broad conductivity distribution of constant probability (Fig. 8). A strongly deformed 'grain boundary semicircle' results and a brick layer model using the conductivity of the center of the distribution (10^{-7} $1/\Omega$) underestimates the 'grain boundary resistance' considerably. On the other hand, a serial connection of grain boundaries according to the given probability distribution yields a much larger value of R_2 than the two-dimensional distribution (222 kΩ). This again demonstrates the influence of detours around high-resistive grain boundaries to lower the resistance but also the problems to deduce a meaningful parameter from the 'grain boundary resistance'. Furthermore, the 'grain boundary resistance' is distinctly influenced by the bulk conductivity. As in the case of different grain boundary patterns (see Section 3.1), detour effects around very blocking grain boundaries contribute to the low-frequency 'semicircle'. Consequently the apparent activation energy no

longer reflects the activation energy of the grain boundary conductivity even if all σ_{gb} of the distribution have identical activation energies.

Let us finally discuss the extreme case in which 70% of the grain boundaries are ideal and exhibit bulk conductivity while 30% are highly resistive (bimodal distribution). Fig. 9 demonstrates, how the 'grain boundary arc' depends on the conductivity of the highly resistive interfaces ($\sigma_{gb,2}$). For moderate grain boundary conductivity the arc is semicircle-like and depends mainly on $\sigma_{gb,2}$ but only slightly on the bulk conductivity. For highly blocking grain boundaries, on the other hand, the low-frequency 'semicircle' becomes distinctly distorted and its size depends only weakly on $\sigma_{gb,2}$ but mainly on the bulk conductivity. In the extreme case of 30% totally insulating grain boundaries the low-frequency arc reaches a maximum and the so-called 'grain boundary resistance' turns out to be a part of the d.c. bulk resistance caused by detours around the very blocking grain boundaries. Hence the mechanism determining the resistance of the low-frequency arc changes with decreasing grain boundary conductivity and the apparent activation energy varies from the activation energy of $\sigma_{gb,2}$ to the bulk value for decreasing $\sigma_{gb,2}/\sigma_{bulk}$ ratio. This is demonstrated in Fig. 10 for bulk and grain boundary activation energies of 0.6 and 1.2 eV, respectively.

These examples demonstrate that, on one hand, a brick layer analysis can yield meaningful values as long as relatively narrow Gauss distributions of grain boundary properties are considered, while it can completely fail in other cases. A more detailed investigation in three dimensions is in progress [10] and will reveal more quantitatively the conditions under which a brick layer analysis is useful.

Finally we can conclude from Sections 3.1 to 3.3 that two- or three-dimensional current lines can depend on bulk conductivity and a.c. frequency. This leads to new features which do not exist in related one-dimensional problems as for example to bulk-dependent 'grain boundary semicircles' and to distorted or additional arcs only due to a change of the current lines with increasing frequency. As a consequence, the resistance of the low-frequency semicircle (R_2) does frequently not represent the exact resistance of the grain boundaries themselves. On the other hand, the term 'grain boundary resistance' is
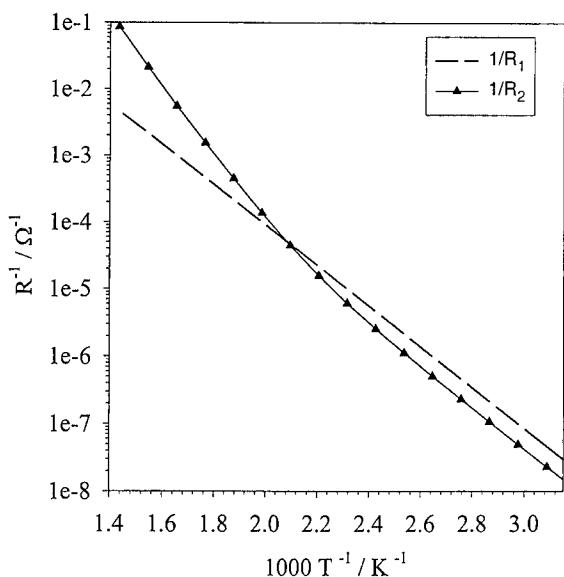
Fig. 10. Bulk (R_1) and 'grain boundary resistance' (R_2) for the bimodal distribution of grain boundary properties as shown in Fig. 9. The bulk conductivity σ_{bulk} has an activation energy of 0.6 eV while $\sigma_{gb,2}$ is activated with 1.2 eV. Notice that $R_2^{-1}(T)$ reflects the activation energy of $\sigma_{gb,2}$ at high temperatures, but $R_2^{-1}(T)$ approaches bulk activation at low temperatures.

still meaningful in the sense that R_2 is caused by the grain boundaries and does not exist in a corresponding single crystal.

However, in all cases the high-frequency semicircle reveals the ideal bulk values as expected for a single crystal, since for the entire high-frequency arc the grain boundaries are dielectrically conducting and hence negligible. This is even true if the d.c. resistance is a pure bulk resistance, i.e. if the low-frequency semicircle is caused by detours around blocking grain boundaries.

4. Conclusions

- Deviations from the cubic grain size are acceptable for a brick layer analysis as long as the grain size distribution is relatively narrow and spatially homogeneously, and as long as no pronounced anisotropy in the grain shape distribution exists. However, agglomerates of small grains or very

broad distributions can lead to considerable errors.

- If imperfect contacts (lateral inhomogeneities) between grains occur, current constriction in the grain becomes important. This leads to an apparent grain boundary semicircle, the resistance of which is purely bulk-dependent. An estimate of the additional resistance can be given according to Eq. (1), however, a quantitative determination of the fraction of blocked grain boundary area solely from the impedance spectrum is not possible. A simple brick layer analysis fails in such cases.

- The brick layer model can be used to estimate mean grain boundary properties if a relatively narrow (Gaussian) distribution of grain boundary conductivities is given. However, very broad or bimodal distributions lead to large deviations and a meaningful analysis using the brick layer model fails. In such cases the low-frequency arc can be distinctly influenced by bulk properties and considerably distorted. This can lead to apparent activation energies which differ from the true grain boundary activation energy.

- Grain boundary arcs deviating from ideal semicircles do not only occur for distributions of relaxation times, but also for microstructures which differ from the brick layer model even if only a single grain boundary relaxation time is involved.

- In all cases considered the high-frequency semicircle still reveals the ideal bulk resistance and capacitance as expected for a single crystal.

References

[1] F. Greuter, G. Blatter, Semiconduct. Sci. Tech. 5 (1990) 111.
[2] G. Pike, Mater. Sci. Tech. 11 (1994) 731.
[3] J.E. Bauerle, J. Phys. Chem. Solids 30 (1969) 2657–2670.
[4] T. van Dijk, A.J. Burggraaf, Phys. Stat. Sol. (a) 63 (1981) 229–240.
[5] M.J. Verkerk, B.J. Middelhuis, A.J. Burggraaf, Solid State Ionics 6 (1982) 159.
[6] S.P.S. Badwal, Solid State Ionics 76 (1995) 67.
[7] M. Kleitz, H. Bernard, E. Fernandez, E. Schouler, Advances in ceramics, in: A.H. Heuer, L.W. Hobbs (Eds.), Science and Technology of Zirconia, Vol. 3, The American Ceramic Society, Washington, DC, 1981, p. 310.

[8] J. Fleig, J. Maier, J. Am Ceram. Soc. 82 (1999) 3485.

[9] J. Fleig, J. Maier, J. Electrochem. Soc. 145 (1998) 2081.

[10] J. Fleig, J. Maier, (in preparation).

[11] Les element interfaciaux dans FLUX-EXPERT Version 2.0, Simulog, 60 rue Lavoisier, 38330 Montbonnot, France, 1996.

[12] J. Fleig, J. Maier, J. Electroceramics 1 (1997) 73.

[13] P.G. Bruce, A.R. West, J. Electrochem. Soc. 130 (1983) 662.

[14] J. Fleig, J. Maier, J. Electrochem. Soc. 144 (1997) L302.

Oscillatory kinetics at solid/solid phase boundaries in ionic crystals

Jürgen Janek*

Institut für Physikalische Chemie und Elektrochemie, Universität Hannover, Callinstr. 3-3A, 30167 Hannover, Germany

Abstract

The transfer of matter and charge across interfaces between two solids is related to defect relaxation in the regions near the interface. A transfer rate which exceeds the rate of defect relaxation may lead to degradation of the interface, causing a feedback effect for the transfer process itself. As a consequence, non-linear phenomena (dissipative structures) like periodic oscillations of the interfacial properties can occur under conditions far from equilibrium. Possible mechanisms and experimental examples are discussed. © 2000 Elsevier Science B.V. All rights reserved.

Keywords: Dissipative structures; Electrochemical oscillations; Interfaces; Ionic conductors; Point defects

1. Introduction

The transfer of ions across boundaries between two solid materials plays an important role in solid-state reactions [1], in solid-state electrochemical devices [2] and in advanced ionic materials [3,4]. It is of basic interest for the understanding of solid-state kinetics [5,6]. An increasing number of theoretical and experimental studies, mainly driven by development of micro- and nanocrystalline materials, as also solid-state batteries and fuel cells, can be attributed to this strong interest (e.g. Refs. [7–21]).

The main aspect in most studies of ionic interface kinetics concerns the relation between an ionic flux across a boundary and the corresponding (electro) chemical driving force, i.e. the current/voltage characteristics (e.g. Refs. [7–9,11,16,17]). Thus,

experimental studies usually aim for the determination of the transfer resistance which a given boundary represents for the transfer of ions, and concepts which have been established in the description of solid/liquid interfaces (e.g. the Butler–Volmer equation) are transferred without serious discussion. Despite an increasing number of experimental studies, the corresponding knowledge is yet still restricted, due to many experimental problems. Most critical are the preparation of structurally and chemically well-defined interfaces which allow reproducible kinetic studies and the application of suitable local probes. The situation becomes even worse by the fact that, as yet, no experimental techniques exist for the direct local observation and analysis of solid/solid interfaces in situ [22]. Recently, microelectrodes with high spatial resolution have been applied in the study of grain boundaries in ionic conductors [23].

An additional and inherent problem in the experimental study of ion transfer across solid/solid

*Fax: + 49-641-99-34509.

E-mail address: juergen.janek@phys.chemie.unie-giessen.de (J. Janek)

boundaries, creating a major difference to electron transfer, is the possibility of both structural and morphological changes within the boundary region, driven by the transfer process itself [1,6]. The present paper focusses on these reactive aspects of ionic interface kinetics which complicate the study of ion transfer. It presents examples for non-linear kinetics observed in simple model systems, thereby emphasizing the importance of defect reactions and relaxation in boundary regions.

The paper is organized as follows: in Section 2 some general aspects of interface kinetics and possible instabilities are summarized. In Section 3 follows a short discussion of feedback mechanisms at inner boundaries, which may lead to strong non-linear or even oscillating kinetics. The electrochemical dissolution of a metal into a solid electrolyte (Section 4) and the electrolysis of a mixed conductor at an inert metal electrode (Section 5) are presented as two experimental examples visualizing a number of important aspects of ionic interface kinetics.

2. Interfacial instabilities

In order to present a more systematic picture, some general aspects related to non-equilibrium interfaces will be discussed in this section. The structure of a solid/solid interface may depend both on the intrinsic properties of the system under study and on its preparation. In general, coherent and semicoherent interfaces (e.g. low angle grain boundaries) are well defined and provide reproducible experimental model systems [13,24,25]. The coherent Ni/Ni_2Si-interface which forms during the course of the reaction between Ni and Si provides an excellent example [13].

Most boundaries, however, which are of practical interest are incoherent, and the results of kinetics studies may depend also on the preparation of the boundary. As high angle grain boundaries (cf. nanocrystalline materials [26,27]), incoherent interfaces have to be considered as strongly disordered regions with high atomic mobility.

The focus of the present paper is directed toward non-linear and oscillatory kinetics at solid/solid interfaces. Non-equilibrium interfaces can be characterized in a rather general scheme by their velocity

relative to a given reference. We distinguish resting and moving boundaries. At resting boundaries, at least one of the two neighboring lattices remains intact and the transfer of ions does not lead to a shift of the boundary itself, i.e. transport processes in the neighboring phases supply and consume the transferring species. Typical examples for resting boundaries are provided by systems of the type AX/AY (AX, AY = cation conductors) or BX/CX (BX, CX = anion conductors). If either the electronic transference number of both phases equals zero or if the electronic flux is inhibited by suitable experimental means, the transfer of cations or anions is the only possible interfacial process. The system should remain stable even under non-equilibrium conditions, and time-independent transfer kinetics are observed.

Real systems always exhibit electronic conductivity, in its magnitude depending on the intrinsic band structure and the degree of doping. Strictly, ionic conductors have always to be considered as mixed conductors, with a more or less significant electronic contribution to the total conductivity. Real systems range from solid electrolytes with very low electronic conductivities (e.g. AgCl, AgI, CaF_2) to mixed conductors with comparable partial ionic and electronic conductivities (e.g. Ag_2S, CeO_2) and semiconducting crystals with dominating electronic conductivity (e.g. CoO, NiO). Thus, a boundary between two ionic conductors always represents a region where not only the total conductivity changes, rather the transference numbers of ions and electrons, will also change, as emphasized by Schmalzried and co-workers [1,28,29]. If an electric current is drawn across such boundary by the use of reversible metal electrodes (in the case of cation conductors) or gas electrodes (in the case of anion conductors), this difference in charge transference may lead to 'internal' electrochemical reactions at the boundary ([1], pp. 226) (see Fig. 1a). One will observe the continuous decomposition of one phase at the boundary and the corresponding deposition of either the metal or the metalloid component. Corresponding experiments have been performed by Riess and Schmalzried [30] at boundaries of the type AgBr/AgCl, leading to the growth of metal dendrites within the boundary.

A situation which corresponds closely to the electrode processes at ion-blocking anodes (see
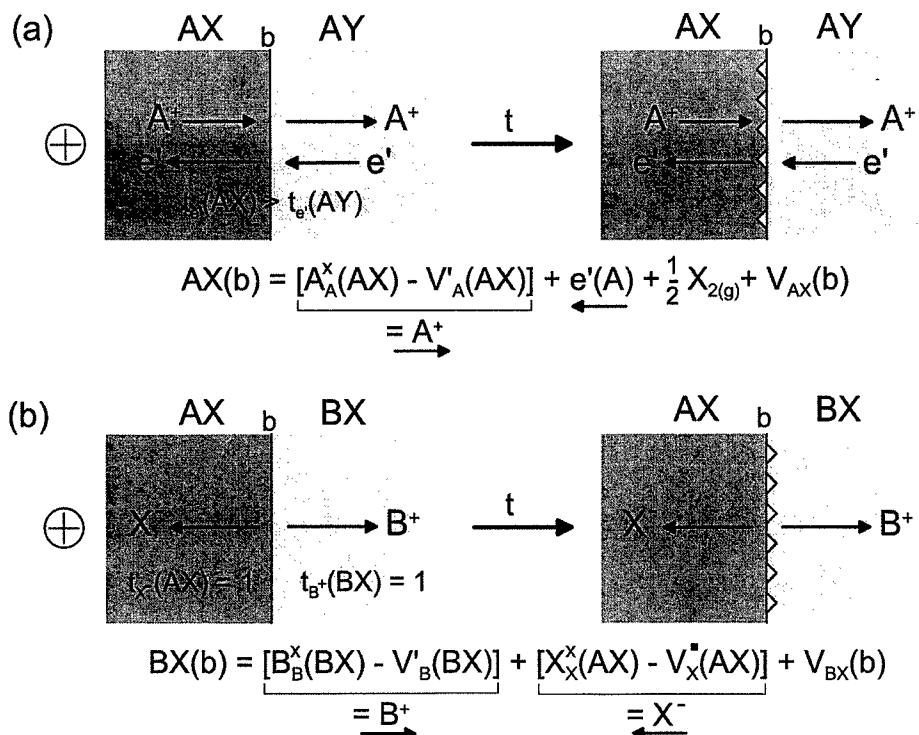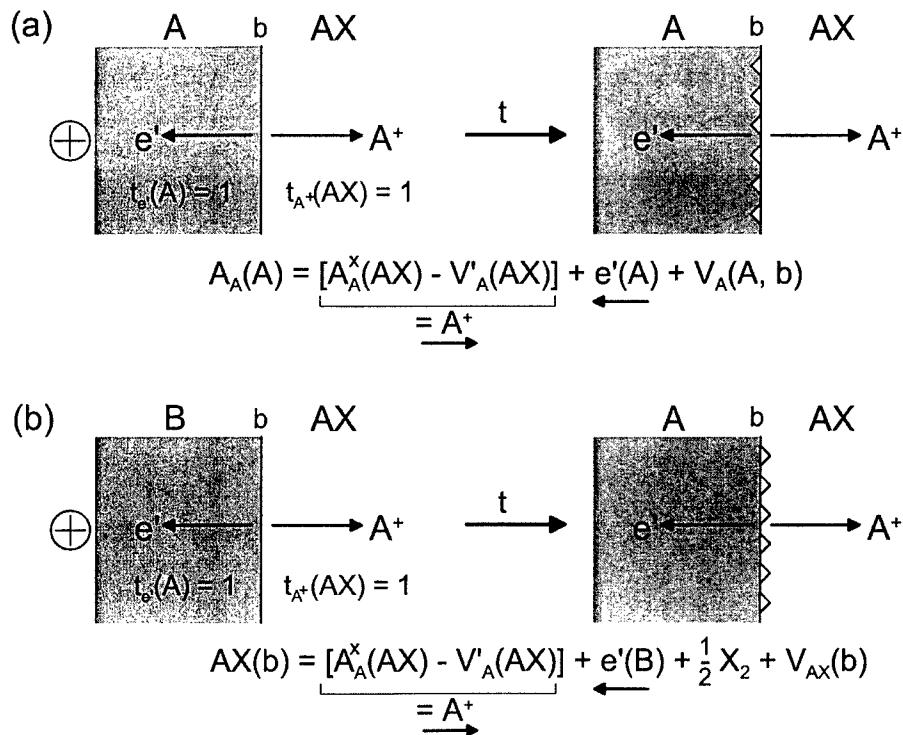
Fig. 1. Different basic experimental situations related to interfacial instabilities at resting boundaries: (a) ion transfer across a boundary AX/AY, (b) ion transfer across a boundary AX/BX.

below) is given if the non-metal potential is increased at the boundary under kinetic load (see Fig. 1a). In this case, the lattice of that electrolyte which contains the less oxidizing non-metal suffers from continuous decomposition, in its magnitude depending on the transport properties of both electrolytes, on the current load and on the rate of non-metal loss from the decomposition (boundary) region. The decomposition reduces the contact area of both phases by the formation of micropores (surface vacancies) and their aggregation and will give rise to strong non-linear kinetics, even at low current densities. Mechanical pressure which is exerted to the interface will have strong influence on the kinetics. So far, no experimental example for this particular kinetic effect has been reported.

If these reactive processes are suppressed at the boundary (e.g. due to a high degree of coherency) the chemical potential of the components of the electrolytes will change locally. Chemical potential gradients are established which compensate the

differing partial fluxes in both phases in the stationary state. If the transition between crystal regions with different transference numbers takes place in a single lattice ('coherent' transition), extremely high chemical potential gradients can be induced. As Virkar and co-workers [31,32] demonstrated in the case of zirconia, exhibiting a steep gradient in the electronic transference number produced by inhomogeneous doping, internal oxygen activities (pressures) can be induced by electric currents that lead to the complete destruction of the lattice.

A second group of resting solid/solid interfaces is provided by metal/electrolyte boundaries. Due to strong technological interest these have been investigated for many years [33–38]. From the kinetic point of view, metal/electrolyte boundaries can be distinguished by their degree of 'reversibility': reversible electrodes with low polarisation resistance are given by parent metal electrodes of the type A/AX or alloy electrodes (A,B)/AX. Blocking electrodes B/AX are composed of a virtually inert metal B and

an electrolyte. Intermediate cases are possible if the electrode metal is not inert against anodic dissolution. All electrodes are subject to dissolution or growth processes at sufficiently high electric potentials. At reversible electrodes the electrolyte lattice remains intact, and the metal phase is either dissolved anodically (see Fig. 2a) or grows cathodically. At ion-blocking electrodes, either the electrolyte is dissolved anodically (electrolysis, see Fig. 2b) or the metal component of the electrolyte is deposited cathodically. These processes generally lead to time-dependent behaviour of the interface, since its structure and morphology is changing continuously. In Section 4, examples of both reversible and blocking electrodes are presented which show that strong non-linear kinetics at electrodes is rather the usual case than an exception.

Still another situation at a resting interface is provided by the combination of two electrolytes which only allow charge transfer by the electrolysis of one electrolyte (see Fig. 1b). An example of such

system is well represented by the couple YSZ/CoO. If the semiconducting CoO is used as the cathode, it decomposes in order to produce oxygen ions which are then dragged across the YSZ toward the anode. The cobalt ions will move in the counter direction, leading to the dissolution of CoO at the boundary. If the CoO lattice is not dissolved layer by layer, one again expects structuring of the surface by the formation of surface vacancies and pores. A strong decrease of the contact area is the consequence, leading to an oscillating interface kinetics (C. Korte, personal communication).

Regarding Figs. 1 and 2, a number of different kinetic situations at interfaces can be realized which all lead to the dissolution (destruction) of one lattice. In the case of reversible and ion-blocking metal/ electrolyte boundaries, electrochemical oscillations have already been observed. A study of the dissolution of one electrolyte lattice at an electrolyte/electrolyte interface has not yet been reported. The reverse case, i.e. the deposition of metal at an

Fig. 2. Different basic experimental situations related to interfacial instabilities at resting electrodes: (a) ion transfer across a reversible electrode A/AX; (b) electrolysis at an ion-blocking electrode B/AX.

electrolyte/electrolyte interface, has been investigated by Riess and Schmalzried [30].

Moving boundaries require the simultaneous growth of one phase and annihilation of the second phase. Typical examples can be found in crystals which undergo a phase transition. Schmalzried and co-workers studied the phase transition between the α- and β-phases of silver sulfide and silver selenide, which induces characteristic chemical potential oscillations if the α/β-boundary is moving through the crystal [15,39]. An important macroscopic aspect of moving boundaries is the question whether a boundary moves in a morphologically stable manner, or whether it becomes morphologically unstable. A number of theoretical and experimental studies on the problem of morphological stability have been reported by Schmalzried ([1], p. 11) and Martin and co-workers [40,41]. In many cases, relatively simple rules can be applied in order to decide whether a moving boundary will remain stable or will become unstable. The morphology of an unstable boundary itself, however, can usually not be predicted by simple arguments. Rather computer simulations [42] or sophisticated theoretical arguments have to be applied [43].

An example for a morphologically unstable boundary is depicted in Fig. 3. If YSZ is polarized cathodically with a platinum electrode, the reduction advances with an unstable front through the crystal starting from the cathode. Corresponding experiments and more details can be found in Ref. [44].

Clearly, internal electrochemical reactions and related instabilities can also occur at moving boundaries. Yet no examples have been reported.

3. Feedback mechanisms

The occurrence of oscillatory electrochemical reactions, as one example of dissipative structures, requires at least one positive feedback step in the kinetics [45–47]. For chemical oscillators, Franck analysed different cases of positive and negative feedback and defined the principle of a so-called antagonistic feedback [46]. Simply speaking, any oscillating system contains both de-stabilizing positive feedback steps and stabilizing negative feedback steps. So far, a number of different feedback mecha-

nisms have been exemplified in various oscillating systems. Thus, the strong non-linear voltage dependence of an electric resistance, a membrane resistance or the tunnel effect may provide a feedback step. Other typical cases are feedback steps based on the temperature dependence of rate constants or on the concentration dependence of heterogeneous catalysis. During recent years, the study of related dissipative structures has found enormous theoretical and practical interest, and a number of excellent books and reviews are available (e.g. Refs. [48,49]).

Dealing with the kinetics of solid/solid interfaces, the question of possible feedback mechanisms as possible causes for the occurrence of oscillatory kinetics arises. To date only a few experimental examples for oscillatory kinetics in solid-state systems have been investigated (e.g. Refs. [50–55]), and the understanding of the underlying mechanisms is generally poor. Well known examples of oscillatory behaviour—at least from a phenomenological point of view—are the formation of multilayered reaction products during high-temperature oxidation (e.g. of Ti–Zr alloys) based on a thermal feedback [50], the formation of layered tarnishing films during high-temperature corrosion of titanium based on a mechanical (elastic) feedback [51,52], and chemical potential oscillations during the phase transformation of certain non-stoichiometric phases [15,39,56]. The feedback mechanism of the latter phenomenon has not yet been definitely identified. Our own experiments on the anodic dissolution of metal electrodes and the electrolysis of solid electrolytes, as depicted schematically in Figs. 1 and 2, provide additional examples for a mechanical feedback caused by the accumulation, i.e. the slow relaxation, of lattice defects at a boundary.

Often found in many chemical oscillators is thermal feedback by the evolution of reaction heat. An example for such thermal feedback in a solid-state reaction is provided by the oxidation of Ti/Zr alloys in oxygen atmosphere [50]. If the oxidation is run within a definite temperature range, the reaction leads to a layered product consisting of two different phases. The surface temperature of the oxidizing specimen oscillates simultaneously with the growth process. Generally, thermal feedback will be less important in inorganic solid-state kinetics than in molecular chemistry. Most inorganic solid-state re-
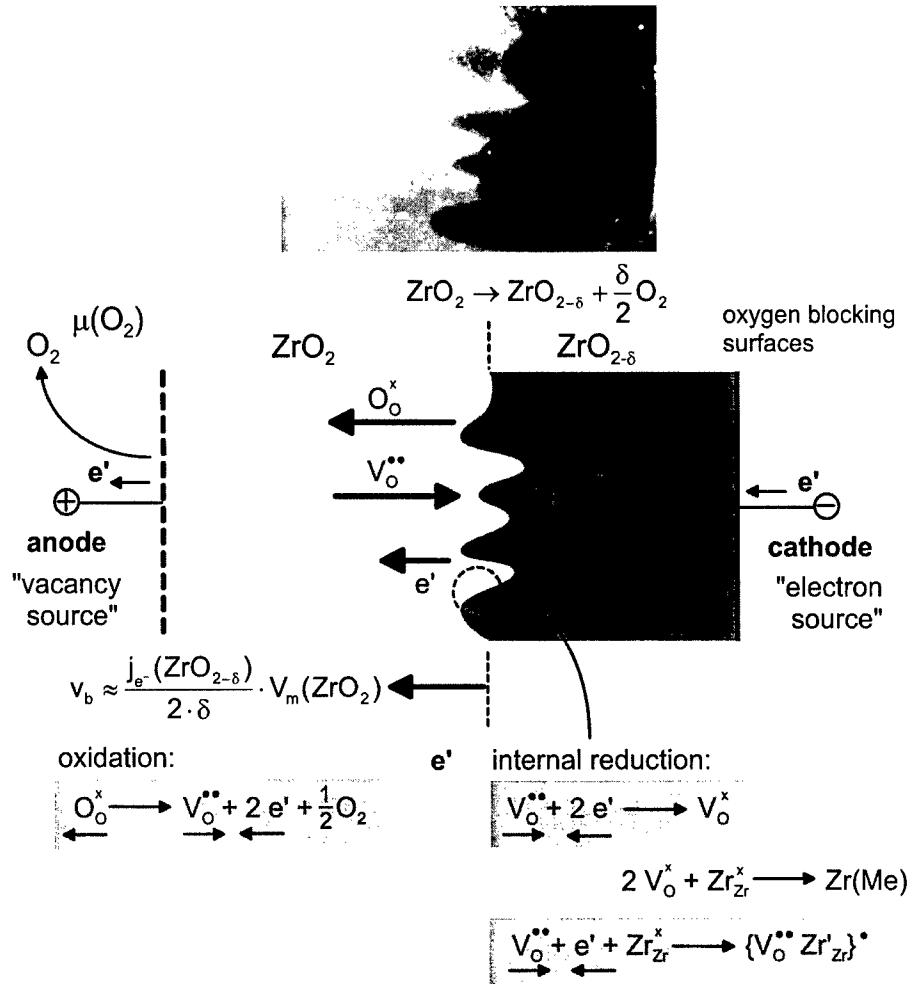
Fig. 3. Processes at the moving internal reduction front in YSZ. The top figure shows a photograph of a reduction front in single crystalline YSZ [44]. The bottom box notes the stability criterion for the moving boundary (φ = electric potential).

actions require high temperatures in order to obtain sufficiently high reaction rates (transport coefficients), and thus, enthalpic effects become less important.

In the solid state mechanical effects are much more important, i.e. interaction by elastic distortions of a lattice and plastic deformation by the generation and motion of dislocations. Coherent and semicoherent interfaces induce elastic distortions in the neighboring lattice regions, which influence local defect equilibria. Pierraggi and Rapp discuss the Ni dissolution at the inner (resting) interface Ni/NiO during high-temperature corrosion of nickel by the model of an semicoherent interface. As an explanation for the

strong adhesion of the growing oxide film to the metal substrate, despite the formation of metal vacancies during the oxidation process, they suggest periodic dislocation climbing as a possible mechanism for the complete relaxation of metal vacancies (cf. metal dissolution in Section 4) [25]. In the oxidation of titanium which leads to an inward growth of TiO_2, a periodic rupture of the oxide film from the metal substrate is observed [51,52]. Under suitable experimental conditions one observes the periodic growth of hundreds of similar appearing oxide layers (thickness of approximately 1 μm) (see Fig. 4). Detailed experiments show that relatively thin titania films (less than 1 μm) still adhere to the substrate. With increasing thickness the film starts to peel off locally, and finally the contact breaks completely. Obviously, only thin titania films allow a sufficient relaxation of the elastic distortion which is induced by the lattice mismatch at the boundary. If a critical thickness is approached, the relaxation of the elastic stress is not efficient enough and the contact of both phases breaks.

Low frequent oscillations (time period in the order of 60 s) of the chemical potential of silver metal have been observed during the spatially controlled phase transformations $\beta\text{-}Ag_2S \rightleftarrows \alpha\text{-}Ag_2S$ [15,56] and $\beta\text{-}Ag_2Se \rightleftarrows \alpha\text{-}Ag_2Se$ [57]. A suitable temperature dif-

Fig. 4. SEM picture (cross-section) of the reaction product of titanium oxidation ($T = 900°C$, $a(O_2) = 0.01$, $t = 24$ h).

ference across the sample includes the transformation temperature, and an inhomogeneous crystal with a well-defined interface is thereby obtained. By shifting the temperature gradient along the sample, the phase boundary is driven along it and leaves the transformed crystal behind the moving boundary. Since the silver excess in both phases differs by orders of magnitude, the boundary has to act as a source or sink for the silver component. Chemical diffusion is thus induced. If the chemical potential of silver metal is measured at fixed positions along the sample, characteristic oscillations of the potential are observed. Schmalzried and co-workers discuss three different mechanisms for the observed chemical oscillations: (a) non-linear coupling of different defect relaxation and transport steps at the boundary (see comment below); (b) discontinuous boundary motion by the periodic rupture of dislocation networks from the semicoherent interface; and (c) discontinuous boundary drag by impurities. For more details, the reader is referred to Refs. [15,56,57].

Finally, the possible occurrence of chemical or electrochemical oscillators on the basis of coupled point defect reactions at boundaries, as proposed in Ref. [1] (p. 254), shall be discussed briefly. Schmalzried suggests that the coupling of both non-linear transfer and relaxation steps of point defects together with transport processes in the neighboring phases may lead to oscillatory kinetics, even at the interface between two different ionic conductors with simple Frenkel disorder. So far, no quantitative formal treatment or experimental study supports that idea. Rather one has to realize that the main difference between typical chemical oscillators and possible solid-state oscillators bases on the fact that molecular reactions allow autocatalytic steps (non-systemic positive feedback [46]). Considering point defect kinetics, no equivalent type of an autocatalytic reaction appears to be possible. Rather site conservation in the crystalline state prevents autocatalytic steps. Thus, one major source of positive feedback is generally missing in the solid state. However, if atom transfer across a solid/solid boundary is related to the dissolution of a lattice, i.e. to the creation of spatial interface (surface) instabilities (vacancies and pores), positive feedback becomes possible, as outlined above and as exemplified below.

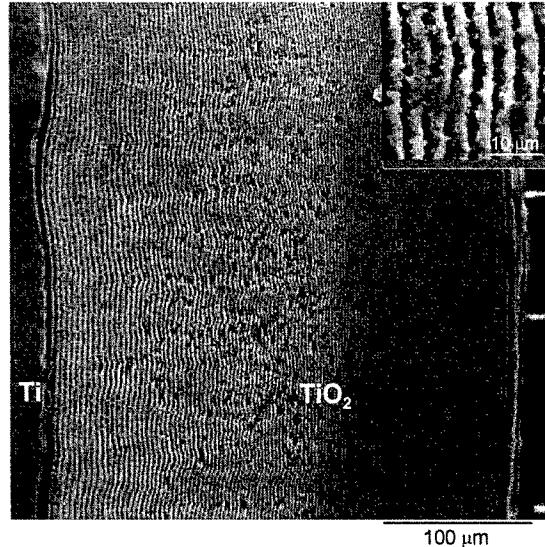In conclusion, we have to expect other feedback

mechanisms in solid-state kinetics than in fluid-phase kinetics. At coherent and semicoherent boundaries we expect an influence of elastic effects, and we have to take the motion of dislocations and their interaction with point defects into account. As a consequence of slow defect relaxation, non-equilibrium boundaries may accumulate point defects and thus may suffer from serious structural and morphological changes. In the next two sections, corresponding experimental observations are summarized.

4. The anodic dissolution of a metal into a solid electrolyte

The anodic dissolution of a metal A into a cation-conducting compound AX represents an important kinetic step during the deloading of solid-state batteries and during high-temperature corrosion. Therefore, the kinetics of metal dissolution has been investigated for many years. Primarily, interfaces of the type Ag/AgX_ν (X = Cl, Br, I, S, Se) have been studied due to the stability of the silver ion-conducting compounds and their high ionic conductivity [5,7,9,19,21,33–38].

As discussed above, a virtually reversible metal electrode may be subject to kinetic degradation by the accumulation of metal vacancies and the creation of pores. In Fig. 5, the experimental setup together with a schematic picture of the microscopic processes at the anodic boundary are shown, assuming an unrealistically proper (coherent) boundary at this point. According to the reaction equation in Fig. 2a, metal vacancies are formed in the metal (on the metal surface) during the transfer of ions into the electrolyte. Correspondingly, the transferring ions occupy vacant sites in the electrolyte lattice. Thus, the transfer process in total, as suggested in Fig. 5, comprises at least three different steps: (a) the formation and relaxation of a vacancy on the metal surface; (b) the jump of the ionized metal atom into the electrolyte lattice; and (c) the relaxation of the new ion in the electrolyte lattice. If we assume that all ionic relaxation and transport steps in the solid electrolyte occur sufficiently fast, it is the relaxation of vacancies in the metal which controls the interface kinetics.

If we assume that the relaxation of metal vac-

ancies proceeds by bulk diffusion into the metal electrode, we estimate an anodic limiting current density of a silver electrode of approximately 50 $\mu A/cm^2$ at $T = 800°C$ [6]. Typical current densities in anodic dissolution experiments at much lower temperatures are in the order of 1 mA/cm^2, and thus, bulk diffusion of vacancies will definitely not be able to provide a sufficiently high relaxation rate.

As a consequence of the slow relaxation of metal vacancies, the vacancies accumulate and form pores at the boundary. The formation of pores has been proven indirectly by dilatometric measurements in situ (cf. Ref. [38]). In Fig. 6, the results of an experiment at the interface Ag/AgI are depicted. The anodic overvoltage (see Fig. 6a) oscillates periodically with a rather low frequency. Simultaneously, the length change of the anode/electrolyte couple shows step-like oscillations with an identical frequency. If one assumes that (in a first-order approximation) the formation of vacancies in the boundary and their accumulation to pores produces no measurable length change, the oscillatory dilatometer signal can be interpreted as a consequence of alternating pore growth and annihilation. In Fig. 6c, the corresponding pore volume normalized by the geometric interface area (V_p/A) is shown as a function of time. (V_p/A) has the dimension of a length and can be interpreted as the thickness of a porous boundary region produced kinetically during the dissolution process. The zero pore volume at $t = 0$ represents an arbitrary value, since the pore volume in the beginning of the experiment is not known. Only the change in pore volume can be determined from the experiment. However, from the analysis of an initial transient in the dilatometer signal one can estimate an initial thickness of the porous region in the order of 10 μm. Fig. 6 shows that this thickness oscillates with an amplitude of less than 1 μm. Thus, during anodic dissolution, a porous boundary region is formed which exhibits slight oscillations of its width in the order of 10%.

The picture is complicated by the fact that at least three different transfer processes can be distinguished in dynamic voltammograms (see Fig. 7b). Characteristic maxima indicate these individual transfer steps which occur at different overvoltages. Thus, process (a) takes place at relatively low overvoltages in the order of a few mV and is
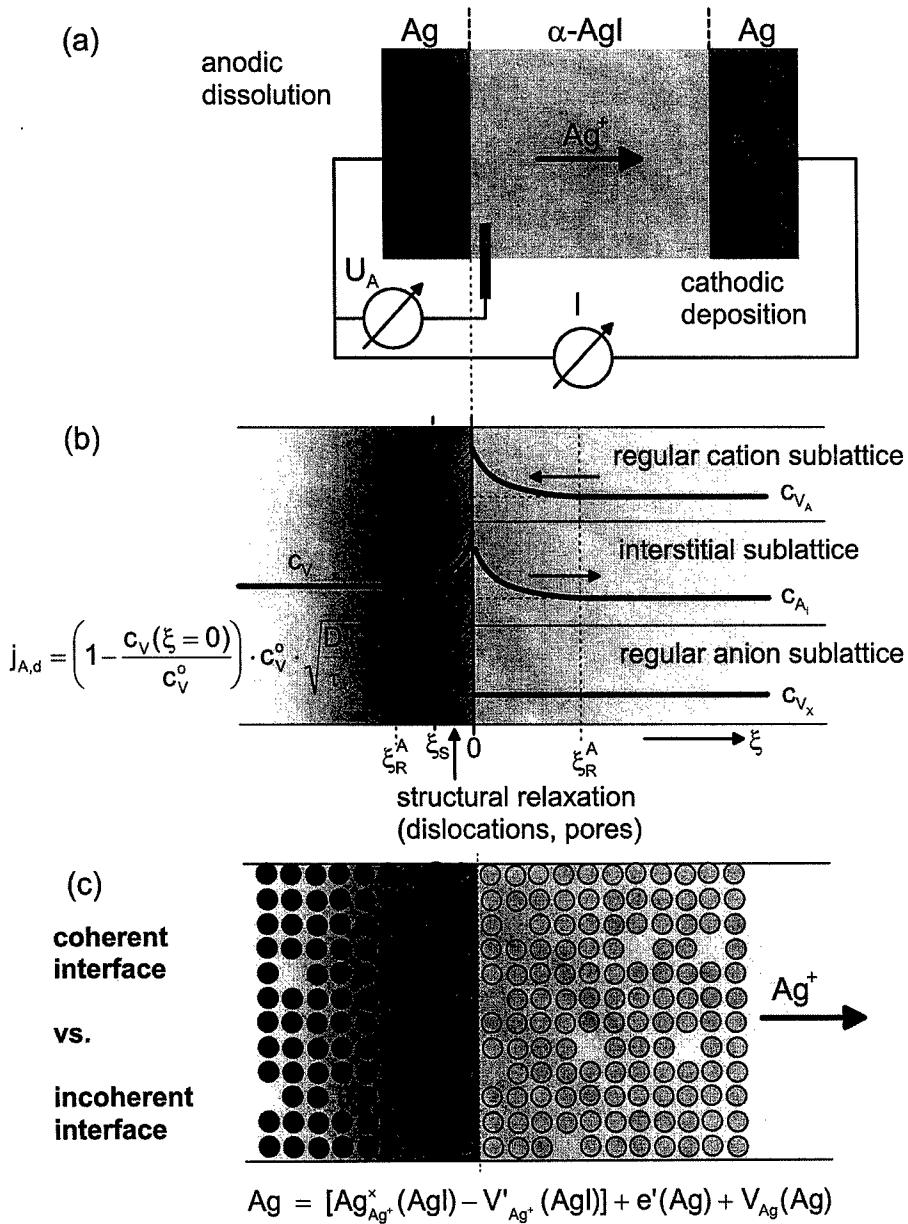
Fig. 5. General scheme of processes at a metal/solid electrolyte boundary: (a) schematic experimental setup, (b) defect relaxation, (c) schematic and simplified representation of the microscopic situation.

responsible for the base line in the galvanostatic time series. Process (b) takes place at overvoltages of approximately 50 mV and is responsible for the small shoulder in the galvanostatic voltage peaks. Process (c) requires relatively high overvoltages in the order

of some 100 mV and corresponds to the broad maxima of the galvanostatic time series which are superposed by high-frequency oscillations with small amplitude.

Since no analytic tools for a direct local study of
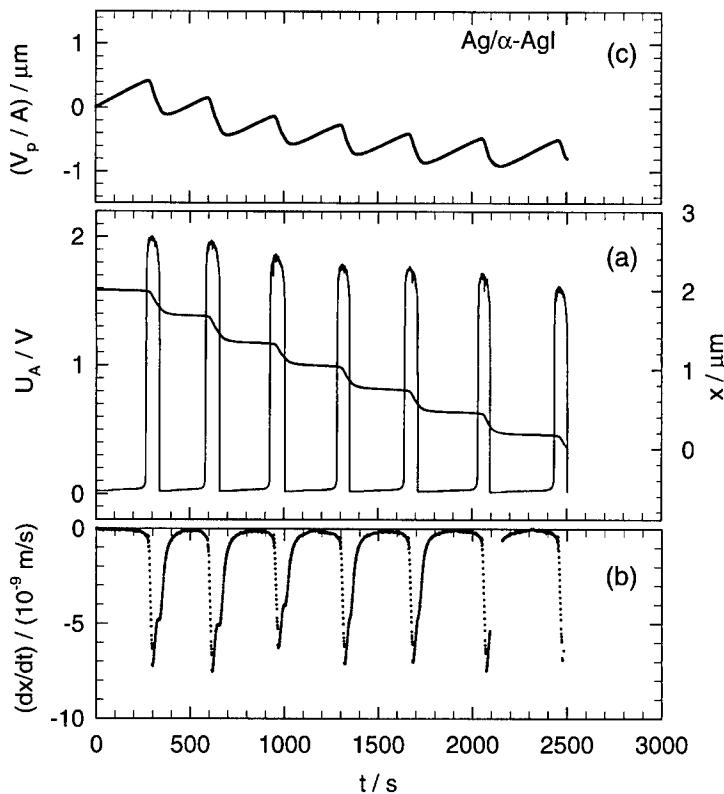
Fig. 6. Anodic galvanostatic dissolution of Ag at an Ag/AgI-electrode ($T = 260°C$): (a) overvoltage and the corresponding dilatometer signal (step-like line) as a function of time; (b) rate of length change of the Ag/AgI-couple; (c) pore volume in the interface region normalized by the geometric interface area as a function of time (see Ref. [38] for details).

the interfacial processes are available, the identification of these individual transfer steps is difficult. However, process (a) is probably related to the metal dissolution at small interface areas with very high exchange current densities. Comparable high exchange current densities are observed in the study of metal whisker/electrolyte interfaces and might be caused by a virtually coherent contact around a screw dislocation in the metal surface. Thus, process (a) gives some indication of locally restricted coherent contacts at the interface. Process (c) shows the characteristic features of oscillations during the electrolysis of solid electrolytes, thus it might be related to the decomposition of AgI and corresponding pore formation in the electrolyte surface. Process (b), which takes place at intermediate overvoltages, might be due to the transfer of silver adatoms. These are supplied by surface diffusion on the surfaces of pores and probably play a crucial role

in the formation of the porous structure during the dissolution process.

Summarizing, a number of individual processes take place simultaneously and are coupled through the complicated porous structure of the boundary region to each other. The transfer itself causes the porosity and, thus, a complicated network of feedback steps is set up. The mechanical pressure orthonormal to the interface plays the role of a control parameter [21]. Its strong influence on the kinetics gives additional evidence for the macroscopic character of the interfacial instabilities. In terms of Franck's analysis, both systemic and non-systemic feedback steps are involved. A systematic physico-chemical model of the oscillatory kinetics still has to be developed.

Electrochemical oscillations have also been observed at ion-blocking interfaces (anodic polarisation) of the type Pt/AgX (X = Cl, Br, I) [5,57] and
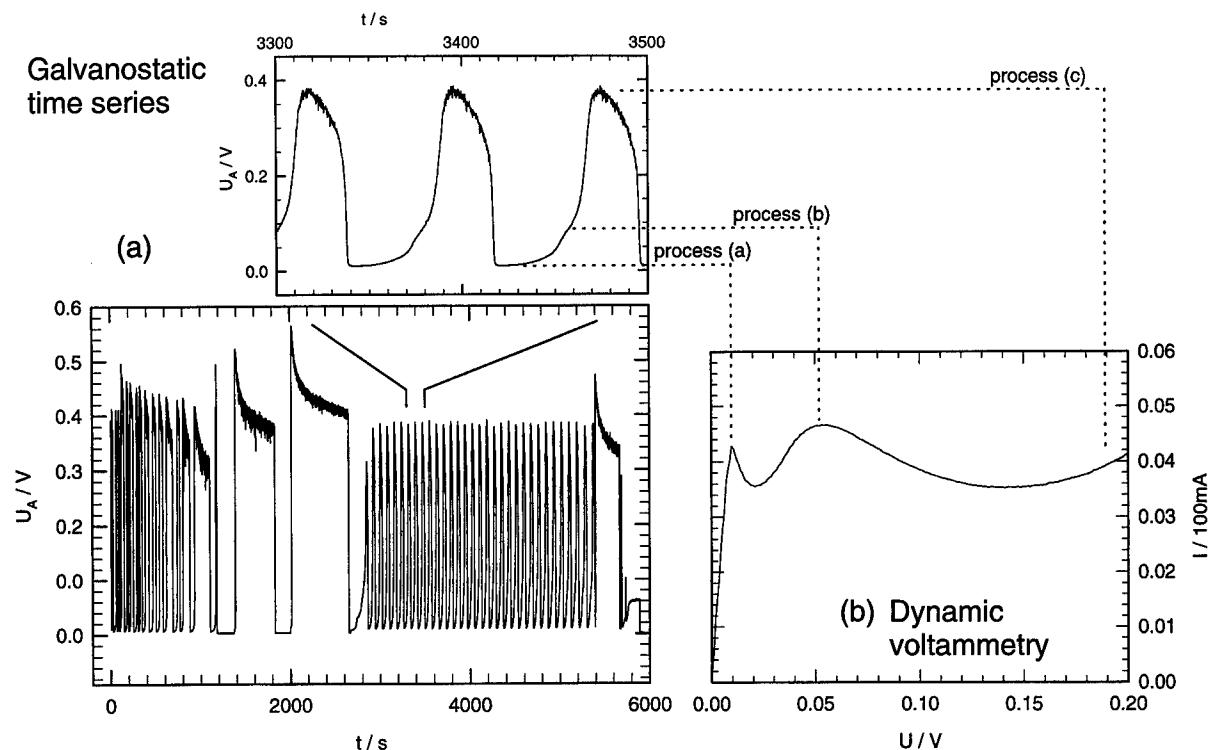
Fig. 7. Anodic galvanostatic dissolution of Ag at an Ag/AgI-electrode ($T = 260°C$, $I = 1.56$ mA/cm^2): (a) overvoltage as a function of time; (b) dynamic current/voltage characteristics of the electrode from a cyclic voltammogram (sweep rate, 0.1 V/min).

Pt/Ag$_4$RbI$_5$ [58]. So far, no oscillations with well-defined modes have been observed in these systems. As depicted schematically in Fig. 8, the galvanostatic voltage oscillations are caused by the local decomposition of the electrolyte and the corresponding pore formation. Thus, again a mechanical feedback is operating.

5. The anodic electrolysis of an ionic conductor

The anodic electrolysis of a cation-conducting solid electrolyte at an inert electrode leads to the annihilation of negatively charged vacancies, which migrate toward the anode driven by the electric field, and to the oxidation of the non-metal anions. The corresponding reaction equation is shown in Fig. 2b. Each non-metal molecule which is formed leaves two vacant lattice molecule sites at the boundary, i. e. the contact area is continuously reduced during the electrolysis. In Fig. 8, the electrolysis of semicon-

ducting Co$_{1-\delta}$O at a platinum point electrode is depicted schematically. Co$_{1-\delta}$O contains mobile cation vacancies which are negatively charged relative to the cation sublattice, but due to a small ionic transference number in the order of 10^{-4}, the electric current is primarily maintained by electronic charge carriers (electron holes). Applying a constant current of 1 mA to the electrode with a geometric contact area of 100 μm^2, the oxide is thus dissolved with a relatively large rate of approximately 0.1 μm/s. As already reported in Ref. [37], quasi-periodic oscillations of the anodic overvoltage with a frequency of roughly 0.5 s^{-1} are observed, being equivalent to the annihilation of approximately 0.2 μm oxide per oscillation period. This length is in surprisingly good correspondence to the typical length per oscillation period, which has been observed at Ag/AgI-electrodes. It shows that the oscillatory kinetics is rather caused by macroscopic morphological changes than by structural changes on an atomic scale.

Fig. 9 shows the result of a typical galvanostatic
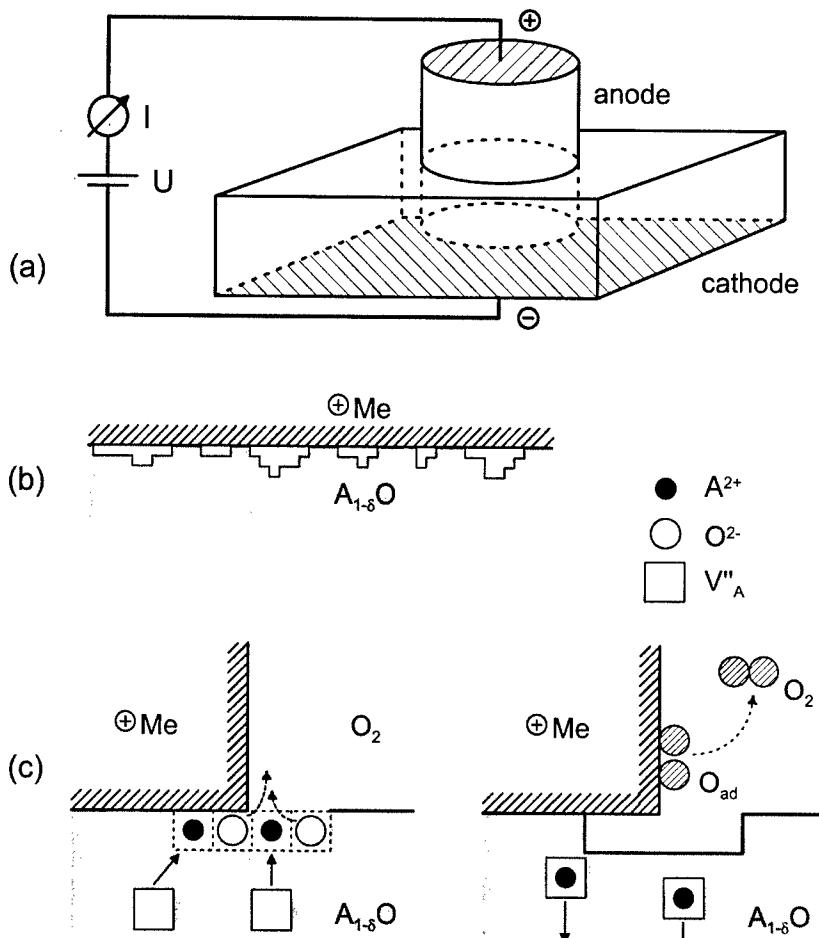
Fig. 8. Electrolysis of a semiconducting oxide $A_{1-\delta}O$ at an inert metal (point) electrode. (b) Interfacial morphology, (c) anodic electrode process and formation of surface defects.

experiment. Experiments on the dissolution and growth of CoO and other oxides at YSZ anodes will be performed in a forthcoming study, in order to realize the kinetic situation which is depicted schematically in Fig. 1b. The build-up of high oxygen pressures in closed pores within the boundary is avoided by the use of an oxygen ion-conducting anode, and it will be interesting whether oscillatory kinetics is observed.

exemplified by electrodes of the type Ag/AgX and Pt/CoO, these reactive processes will generally lead to morphological changes of the boundary and the surrounding region. These morphological changes cause mechanical instabilities and may lead to the complete destruction of initially well-defined boundaries. Furthermore, the ion transfer induces a strong feedback via the structural and morphological consequences of the transfer process.

6. Conclusions

It is demonstrated that ion transfer across a solid/ solid boundary is often related to reactive processes which may cause strong non-linear effects. As

Acknowledgements
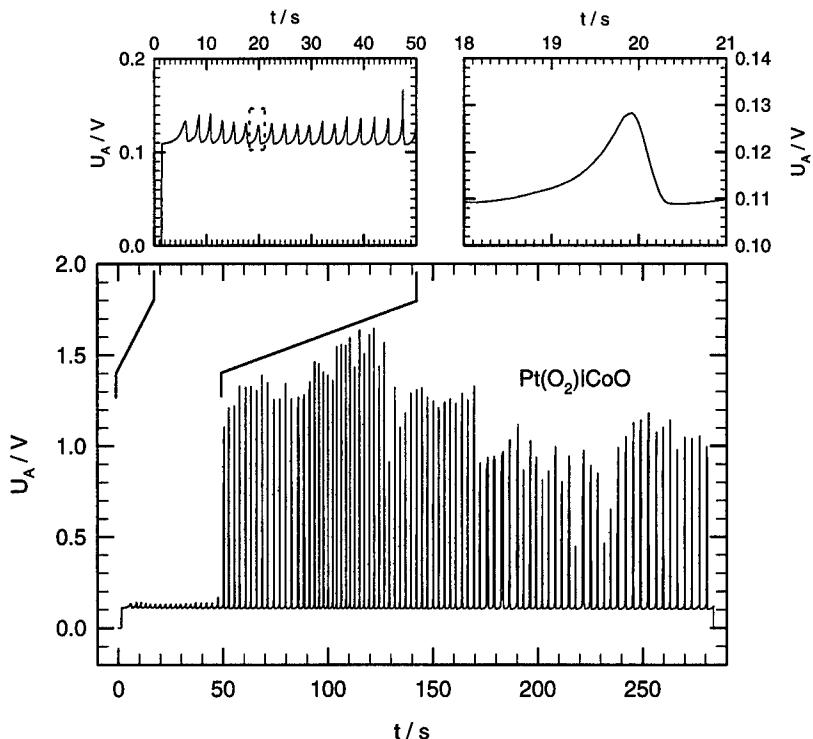
Fig. 9. Electrochemical oscillations at the anodic interface Pt/CoO: voltage U_A across the interface during galvanostatic dissolution of CoO ($T = 1100°C$, $a(O_2) = 0.21$, $I = 8$ mA).

References

[1] H. Schmalzried, in: Chemical Kinetics of Solids, Verlag Chemie, Weinheim, 1995.

[2] C. Deportes et al., in: Electrochimie des Solides, Presses Universitaire de Grenoble, Grenoble, France, 1994.

[3] J. Maier, Solid State Ionics 70/71 (1994) 43.

[4] W. Puin, P. Heitjans, Nanostruct. Mater. 6 (1995) 885.

[5] J. Janek, Zum Ladungsdurchtritt an Phasengrenzen in Festkörpern, Habilitation thesis, University of Hannover, Hannover 1997.

[6] H. Schmalzried, J. Janek, Ber. Bunsenges. Phys. Chem. 102 (1998) 127–143.

[7] J.C. Bazán, L.E. Fasano, Electrochim. Acta 34 (1989) 309.

[8] R.Z.D. Fernandes, S. Aleonard, J. Ilali, A. Hammou, M. Kleitz, Solid State Ionics 34 (1989) 253.

[9] A.M. Mikhailova, Sov. Electrochem. 26 (1990) 1505.

[10] H. Schmalzried, React. Solids 8 (1990) 247.

[11] H. Schmalzried, M. Ullrich, H. Wysk, Solid State Ionics 51 (1992) 91.

[12] H. Schmalzried, Pol. J. Chem. 67 (1993) 167.

[13] D. Hesse, P. Werner, R. Mattheis, J. Heydenreich, Appl. Phys. A 57 (1993) 415.

[14] G. Noetzel, Elektrochemische Charakterisierung von Elektroden und Mikrokontakten an festen Ionenleitern, Ph. D. thesis, University of Tübingen, Tübingen, 1994.

[15] H. Wysk, Kinetische Untersuchungen an fest/fest-Phasengrenzen mit Mikrosensoren, Ph. D. thesis, University of Hannover, Hannover, 1995.

[16] C. Rosenkranz, J. Janek, Solid State Ionics 82 (1995) 95–106.

[17] S. Villain, J. Cabané, D. Roux, L. Roussel, P. Knauth, Solid State Ionics 76 (1995) 229.

[18] M. Kleitz, L. Dessemond, M.C. Steil, Solid State Ionics 75 (1995) 107.

[19] J. Janek, S. Majoni, Ber. Bunsenges. Phys. Chem. 99 (1995) 14–20.

[20] R. Hagenbeck, L. Schneider-Stoermann, M. Vollmann, R. Waser, Mater. Sci. Eng. B 39 (1996) 179.

[21] J. Janek, S. Majoni, Defects Diff. Forum 129–130 (1996) 243–252.

[22] G. Langer, Chemische Reaktion, Transport atomarer Sonden und PAC-Messungen an der polarisierbaren Metall-Oxid Grenzfläche Pt/ZrO$_2$(Y$_2$O$_3$), Ph.D. thesis, University of Hannover, Hannover, 1998.

[23] J. Fleig, S. Rodewald, J. Maier, J. Appl. Phys. 87 (2000) 2372.

[24] A.P. Sutton, R.W. Balluffi, Interfaces in Crystalline Materials, Clarendon Press, Oxford, 1995.

[25] B. Pierraggi, R.A. Rapp, Acta Met. Mater. 36 (1988) 1281.

[26] H. Gleiter, Nanostruct. Mater. 1 (1992) 1.

[27] R.W. Siegel, Nanophase materials, Encycl. Appl. Phys. 11 (1994) 173.

[28] H. Schmalzried, M. Backhaus-Ricoult, Progr. Solid State Chem. 22 (1993) 1.

[29] U. Stilkenböhmer, H. Schmalzried, Phys. Stat. Sol. (A) 146 (1994) 31.

[30] I. Riess, H. Schmalzried (personal communication).

[31] A.V. Virkar, L. Viswanathan, D.R. Biswas, J. Mater. Sci. 15 (1980) 302.

[32] A.V. Virkar, J. Mater. Sci. 20 (1985) 552.

[33] D.O. Raleigh, Electrode processes in solid electrolyte systems, in: A.J. Bard (Ed.), Electroanalytical Chemistry, Vol. 6, Marcel Dekker, New York, 1973, p. 87.

[34] J. Corish, C.D. O'Briain, J. Crystal Growth 13/14 (1972) 62.

[35] S. Toshima, T. Ohsaki, N. Kimura, Electrochim. Acta 21 (1976) 469.

[36] H. Fischbach, Z. Metallkd. 71 (1980) 115.

[37] J. Janek, Solid State Ionics 101–103 (1997) 721–727.

[38] S. Majoni, J. Janek, Ber. Bunsenges. Phys. Chem. 102 (1998) 756–762.

[39] H. Schmalzried, H. Reye, Ber. Bunsenges. Phys. Chem. 38 (1979) 53.

[40] S. Schimschal-Tölke, H. Schmalzried, M. Martin, Ber. Bunsenges. Phys. Chem. 99 (1995) 1, 10.

[41] M. Martin, P. Tigelmann, S. Schimschal-Tölke, G. Schulz, Solid State Ionics 75 (1995) 219.

[42] G. Schulz, M. Martin, Solid State Ionics 101–103 (1997) 417.

[43] E. Brener, H. Müller-Krumbhaar, D. Temkin, T. Abel, Solid State Ionics 131 (2000) 23–33.

[44] J. Janek, C. Korte, Solid State Ionics 116 (1999) 181.

[45] U.F. Franck, Faraday Symp. Chem. Soc. 9 (1974) 137.

[46] U.F. Franck, Ber. Bunsenges. Phys. Chem. 84 (1980) 334.

[47] A. Sanfeld, Pure Appl. Chem. 56 (1984) 1727.

[48] S.K. Scott, in: Chemical Chaos, Clarendon Press, Oxford, 1991.

[49] F.W. Schneider, A.F. Münster, in: Nichtlineare Dynamik in der Chemie, Spektrum-Verlag, Heidelberg, 1996.

[50] M. Lallemant, G. Bertrand, J.C. Cannot, J.P. Larpin, N. Roudergues, React. Solids 3 (1987) 227.

[51] M. Lallemant, G. Bertrand, J.C. Cannot, J.P. Larpin, N. Roudergues, React. Solids 3 (1987) 227.

[52] G. Bertrand, Pattern formation during dry corrosion of of metals and alloys, in: D. Walgraef (Ed.), Patterns, Defects and Microstructures in Non-equilibrium Systems, Martinus Nijhoff, Dordrecht, The Netherlands, 1987.

[53] K. Osinski, A.W. Vriend, G.F. Bastin, F.J.J. van Loo, Z. Metallkd. 73 (1982) 258.

[54] M.R. Rijnders, A.A. Kodentsov, C. Cserhati, J. van den Akker, F.J.J. van Loo, Defects Diff. Forum 129–130 (1996) 253.

[55] J. Salazar, M. Lallemant, Solid State Ionics 50 (1992) 233.

[56] U.V. Oehsen, Thermodynamische und kinetische Untersuchungen an kristasllinem Silberselenid, Ph.D. thesis, University of Hannover, Hannover, 1980.

[57] C. Rosenkranz, Zur oszillierenden Elektrodenkinetik an der fest/fest-Phasengrenze Me/AgX, Ph.D. thesis, University of Hannover, Hannover, 1998.

[58] S.I. Bredikhin, V.N. Bondarev, A.V. Boris, P.V. Pikhits, W. Weppner, Solid State Ionics 81 (1995) 19.

Ionic conduction in nanocrystalline materials

Harry L. Tuller*

Crystal Physics & Electroceramics Laboratory, Department of Materials Science & Engineering, Massachusetts Institute of Technology, 77 Massachusetts Ave, Room 13-3126, Cambridge, MA 02139, USA

Abstract

The potential impact of high densities of interfaces in nanocrystalline solids on ionic conduction and defect formation are examined. The literature on three oxides; cubic zirconia, ceria and titania, is reviewed. While it remains too early to make firm conclusions, the following observations are made. Additives which contribute to ion blocking at grain boundaries are diluted in nanocrystalline oxides giving rise to substantial reductions in specific grain boundary resistivities. The case for enhanced ionic conduction in nanocrystalline oxides remains unresolved due to conflicting reports and inadequate efforts to isolate the ionic from the total conductivity. There is strong support for the notion that the energetics for defect formation may be substantially reduced in nanocrystalline oxides leading to markedly increased levels of nonstoichiometry and electronic carrier generation. © 2000 Elsevier Science B.V. All rights reserved.

1. Introduction

The influence of grain boundaries on the electrical, diffusive and defect properties of electroceramics has been recognized for some time. In ZnO varistors, for example, grain boundaries, depleted of free electrons, serve to increase the overall resistance of the device, at low fields, by a factor of $\approx 10^{10}$ [1]. Similarly, impurities such as SiO_2, known to segregate to the grain boundaries in stabilized zirconia and ceria, reduce the effective oxygen ion conductivity by as much as several orders of magnitude [2–5]. Alternatively, grain boundaries may serve as 'short circuiting pathways' as they do in LiI–Al_2O_3 composites leading to enhancements in Li ion conduc-

tivity by nearly two orders of magnitude [6]. Given the recent and rapidly growing interest in nanocrystalline solids, one logically questions the impact that this change in scale may have on the properties of solid state ionic materials. In this article, we consider why transport across or along grain boundaries in solids with nanometer-sized grains may differ distinctly from that in conventional polycrystalline solids. We also consider how defect generation may be influenced by the change in scale and the impact this may have on mixed ionic-electronic conduction (MIEC) in solids.

2. Impact of interfaces on ionic conduction

Since ions move by a thermally activated 'hopping' motion between near equivalent sites, high

*Tel.: +1-617-253-6890; fax: +1-617-258-5749.
E-mail address: hltuller@mit.edu (H.L. Tuller)

temperature operation is normally required to achieve reasonably high levels of ionic conductivity in most ionic solids. Well-known exceptions exist such as αAgI and some Ag and Li-based oxide and sulfide glasses [7] which exhibit high levels of ionic conductivity at or in the near vicinity of room temperature. This follows from the fact that they are simultaneously highly disordered and exhibit continuous, open channels between ion sites.

In contrast to the above two examples, in which the source of ionic disorder is intrinsic in nature, stabilized cubic zirconia (e.g. $Zr_{1-x}Y_xO_{2-x/2}$) is a well-known example in which disorder is induced by the addition of aliovalent elements. Nevertheless, temperatures of the order of 900–1000°C are required to reach levels of ionic conductivity of ≈ 0.1 S/cm, given the much larger ionic radius of oxygen and consequently lower mobility.

A number of oxygen ion conductors, largely stabilized zirconia, ceria and lanthanum gallate are prime candidates to serve as the solid electrolyte in the solid oxide fuel cell. For reasons related to long-term stability and cost, one would like to drop the operating temperature of these devices by at least several hundred degrees. Decreased temperatures, however, require increased electrolyte conductance and enhanced gas/electrode reaction kinetics. An intriguing question is whether polycrystalline ceramics, with nanosize grains, would exhibit enhanced ionic conduction due to transport along the grain boundaries.

It is indeed well-known in the materials community that grain boundary diffusion is often orders of magnitude greater than corresponding 'bulk' diffusion through the grains. This is illustrated in the classic diffusion studies on NiO [8] as illustrated in Fig. 1 in which, for example, the oxygen grain boundary diffusivity at ≈ 1300°C is reported to be approximately six orders of magnitude higher than that in the lattice. Presumably, the source of enhanced diffusion results from the fact that a high percentage of displaced atoms with corresponding strained bonds and excess volume exist at the interface between the misaligned adjacent grains. Grain boundaries thus intrinsically appear to possess the two key characteristics necessary for enhanced ionic diffusion: high defect densities (displaced atoms) and high mobilities (interconnected excess
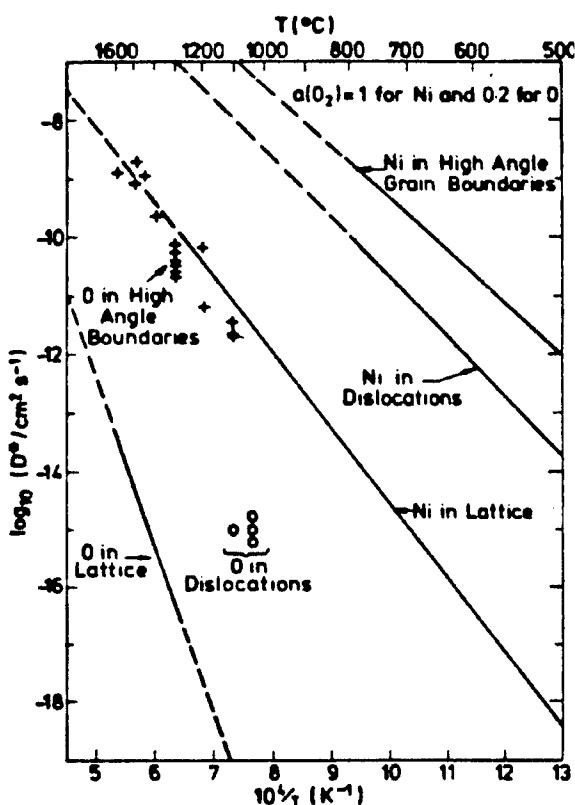
Fig. 1. Nickel and oxygen self-diffusion in bulk, in dislocation and in grain boundaries of nickel oxide [8].

free volume). There are, however, surprisingly few cases in which the source of the enhanced diffusion at grain boundaries has been well established.

High ionic diffusivities are insufficient by themselves to insure high ionic conductivities. Indeed, in conventional polycrystalline materials, the fractional cross-sectional area of grain boundaries lying parallel to the current flux is very small. Consider the idealized 'brick model' schematic in Fig. 2, in which cubic grains with dimension L on each side are separated from each other by grain boundaries of width $2b$. Ignoring blocking effects of boundaries perpendicular to current flow, the relative ratio of cross-sectional areas is

$$\frac{A(\text{grains})}{A(\text{boundaries})} = \frac{L}{4b} \tag{1}$$

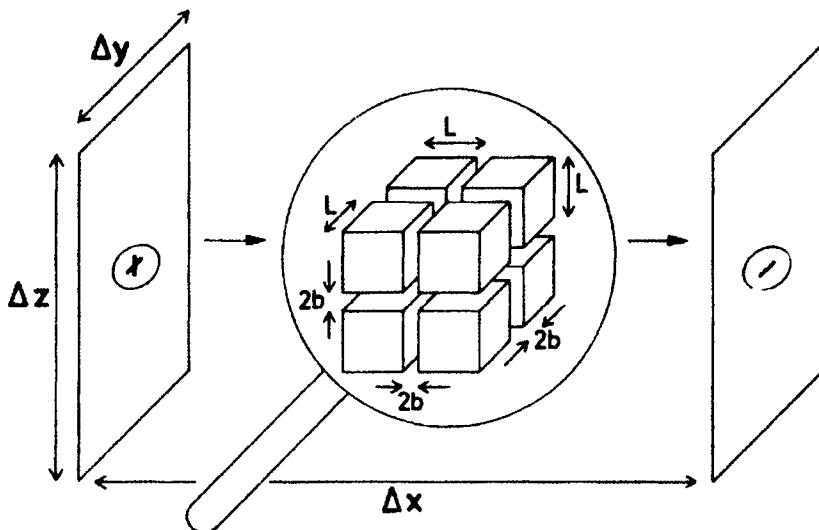Thus to achieve equal conductance, the grain bound-

Fig. 2. Brick layer model of idealized polycrystalline structure in which grains of dimensions L^3 are separated by grain boundaries of width $2b$ [6].

ary conductivity σ_{gb} must be larger than the grain conductivity σ_B by

$$\sigma_{GB} = \sigma_B(L/4b) \qquad (2)$$

For a typical polycrystalline material with average grain size of 1 μm and a grain boundary core width of 1 nm, $\sigma_{GB} \approx 500\sigma_B$ is required to merely double the overall conductance of the material.

Consider instead the schematic of a nanocrystalline solid in Fig. 3 in which the dimensions of the grain boundaries become comparable to those of the grains. Here a significant fraction of the atoms lie in the disordered region of the boundaries and can be expected to contribute to enhanced conductivity. Thus for geometries for which $L \approx 4b$, a grain boundary conductivity which is, say, several orders of magnitude greater than that in the bulk will translate into a similar enhancement (less a factor of 2) in the overall ionic conductivity of the specimen.

The intuitive image of a highly disordered grain boundary region, as depicted in Fig. 3, is not born out by high resolution transmission electron microscopy. It is instructive to examine the high resolution microscopy images of NiO obtained by Merkle [10] and reproduced in Fig. 4. One observes that structural disorder in the grain boundary 'core' is accomo-

dated within several atomic planes of the boundary and rather than being randomly dispersed, 'defects' organize themselves and create a new periodic structure at the interface. Indeed, recent TEM observations of nanocrystalline ceria [11] show crystallites with high levels of perfection separated by atomically sharp boundaries with no indication of the glass-like disorder discussed in the early diffusion literature.

An additional explanation for enhanced conduction at boundaries is related to the formation of space charge regions in the grains adjacent to the boundaries. Charged species, impurities and/or defects, tend to segregate to the grain boundaries in order to lower the strain and electrostatic energies of the system. These boundary charges are compensated by the formation of space charge in the adjoining grains. Thus, bulk ionic defects with like charge to that of the boundary will be depleted while those with opposite charge will be accumulated in the space charge region. If the bulk defect with high mobility is accumulated in the space charge region, the overall conductivity of the solid should increase. The width of this space charge region is tied to the Debye screening length, L_D

$$L_D = \left(\epsilon_r \epsilon_0 k/Tq^2 C_b\right)^{1/2} \qquad (3)$$
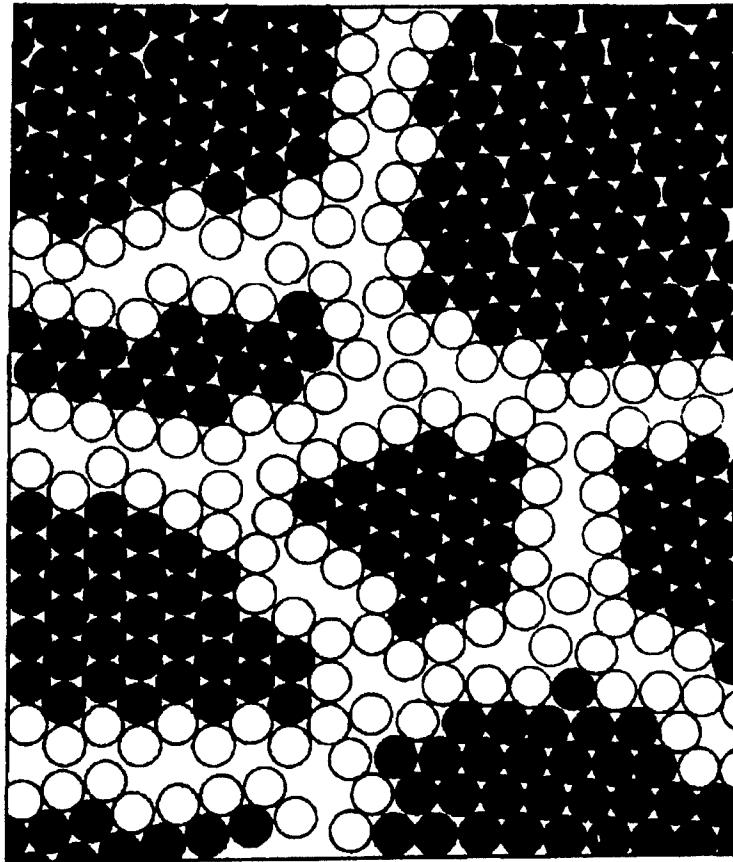
Fig. 3. Schematic of grains (dark circles) separated by grain boundary regions (open circles) of comparable dimensions [9].

in which C_b is the concentration of the bulk majority carrier. For a solid with $\epsilon_r = 10$ and $C_b = 10^{22}$ m^{-3} at 600 K, this leads to a Debye length of ≈ 50 nm and a space charge width of approximately two times that value. Thus, the effective boundary width contributing to enhanced conductivity may be many times greater than the boundary core width.

Maier [6] has calculated the additional boundary contribution, $\Delta\sigma_m$, to be

$$\Delta\sigma^m = (4L_D/d)(\sigma_{v,sc} + \sigma_{i,sc}) \qquad (4)$$

in which d is the average grain size and $\sigma_{v,sc}$ and $\sigma_{i,sc}$ are the mean space charge conductivities due to vacancies and interstitials respectively. The boundary contribution is, thus, given by the product of the areal fraction of the interface and the mean space

charge conductivity. Obviously, as L_D approaches d, as it does in nanocrystalline solids, this contribution can become significant. However, an additional factor must be taken into account under these circumstances.

As illustrated in Fig. 5, as d approaches L_D, the defect density at the center of the grain no longer reverts back to the background value C_b. Thus, in the limit of small grains, local charge neutrality is nowhere satisfied. Under these circumstances, Maier has shown that an additional nano-size factor g, given by [12]

$$g = (4L_D/d)[(C^\circ - C_b)/C^\circ]^{1/2} \qquad (5)$$

where C° is the concentration of the majority mobile defect at the first layer adjacent to the interface core,
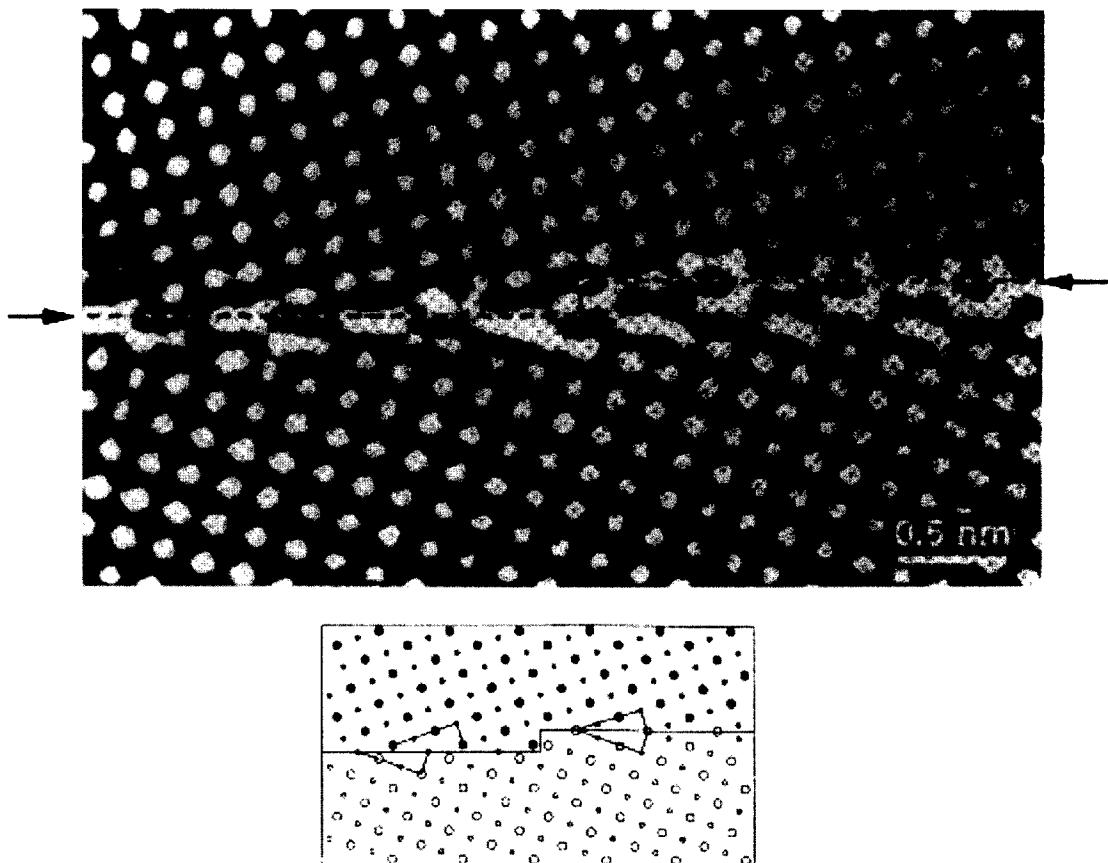
Fig. 4. High resolution electron micrograph, above, and a calculated image, below, of a (310) symmetric <100> tilt boundary in NiO [10].

further enhances the grain boundary contribution to the conductivity compared to the case where $d \gg L_D$. For large $C°$ ($\gg C_b$), $g \approx (4L_D/d)$ which reaches an order of magnitude for $d = 0.4L_D$ [12].

In the last few years, a number of oxides known to exhibit ionic conductivity, such as stabilized zirconia and ceria, have been prepared in nanocrystalline form and their transport properties have been reported. In the following, we review these results, focusing particularly on the trend in magnitude of both ionic and electronic conductivity as the average grain size is reduced to the nanometer regime. Our interest in the electronic conductivity derives from the apparent change in defect thermodynamics at the nanometer scale. This translates into reduced defect formation energies and, under certain circumstances, markedly enhanced electronic conductivities which

may mask increases in the ionic conductivity. This may be detrimental for applications in which one wishes to utilize the material as a solid electrolyte or beneficial where the requirement is for high levels of mixed ionic-electronic conductivity as in fuel cell electrodes or in oxygen permeation membranes [13].

Another feature which deserves particular attention is the influence of grain boundaries lying perpendicular to the flow of current. As mentioned at the beginning of this article, such boundaries often block the flow of current, and as the grain size decreases, could contribute to an overall decrease in conductivity. Thus, in analyzing the effects of grain size on conductivity, it is important to able to comment on the relative effects of boundaries both parallel and perpendicular to the flow of current. In the literature published to date, this information is
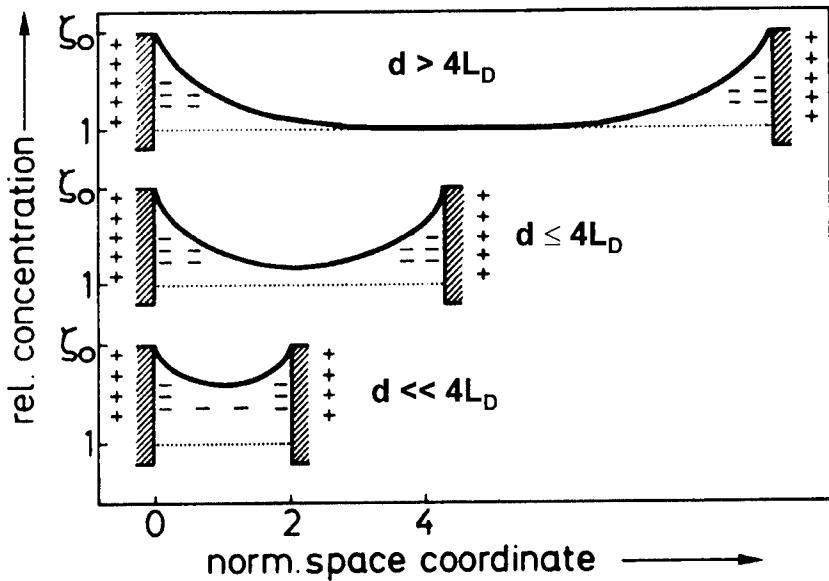
Fig. 5. Defect profiles in structures with dimension, d. The build defect concentration is not reached when $d \ll 4L_D$, where L_D is the debye length [12].

often difficult to assess. Finally, we consider recent evidence for ionic conductivity in nano-crystalline TiO_2, an oxide normally viewed as a semiconductor.

3. Ion transport in nanocrystalline oxides

3.1. Stabilized zirconia

A recent study by Aoki et al. [5] reports perhaps the clearest correlation between grain size and ionic conductivity. In this study of high purity 15 mol% CaO-stabilized zirconia, a clear correlation was established between the amount of Si segregated to grain boundaries, as established by high resolution STEM, and the corresponding grain boundary resistivity, as derived by complex impedance measurements. The solute coverage in this high purity material could be systematically varied by changing the grain size over a 0.1–10 μm range at constant impurity and doping levels.

Of particular interest to this work are the results shown in Fig. 6, which show that the specific grain boundary conductivity drops sharply initially with increasing grain size and ultimately saturates above ~4 μm. This drop in specific grain boundary con-
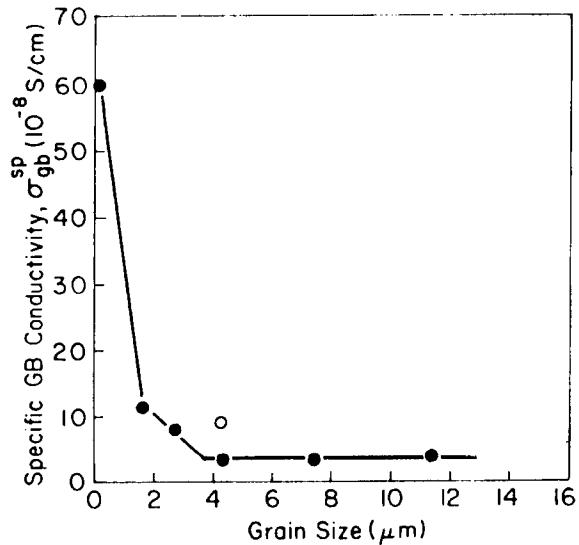
Fig. 6. Specific grain boundary conductivity in calcia stabilized zirconia at 500°C vs. grain size [5].

ductivity by about a factor of 15 is correlated with a corresponding increase in silicate ($Si_2Ca_3O_7$) coverage of the grain boundaries. Note, first, that in the regime of these studies, the solute coverage averages below a monolayer, and second, that the strongest dependence of grain boundary resistance on silicate

coverage occurs at low coverage levels. These results suggest that grain boundary resistance due to blocking effects at perpendicular boundaries may drop to exceptionally low values in relatively pure (relative to segregants such as Si) nanocrystalline conductors. This seems to be born out, at least, in some subsequent studies.

While the work by Aoki et al. [5] demonstrated a clear dependence of grain boundary conductance on grain size, the smallest grain size examined, 140 nm, was larger than that normally associated with nanocrystalline solids, i.e. typically several to 100 nm. In the following, we review studies performed on stabilized zirconia ceramics with grain sizes falling into this category.

Mondal and Hahn [14] prepared nanocrystalline zirconia stabilized with 2–3 mol% yttria beginning with powders processed by the inert-gas condensation technique and followed by sintering. The resultant specimens had grain sizes between 35 and 50 nm and relative densities between 82 and 93%. Activation energies for bulk (0.85±0.05 eV) and grain boundary conductivity (1.0±0.1 eV) as well as absolute values of conductivity coincided with that of conventional ceramics as illustrated in Fig. 7. The absence of significant effects was attributed to the insufficiently small grain sizes of their samples. Jiang et al. [15] reached similar conclusions. They

prepared ultra-fine grained yttria-stabilized zirconia by combustion synthesis using metal nitrates as precursors. Compressed pellets were sintered by fast-firing at 1200–1400°C. Relative density was less than 95% for average grain sizes less than 200 nm. They also found activation energies for grain and grain boundary conduction (0.95 and 1.2 eV) to be in agreement with values for materials with micron-sized grains. Here, the grain size was even larger; over 90 nm in all cases.

On the contrary, Kosacki et al. [16], who investigated yttria (16%)-stabilized zirconia (YSZ) thin films prepared by a polymer precursor process on alumina substrates, found that the nanocrystalline materials exhibited a two order of magnitude increase in conductivity compared to polycrystalline and single crystalline materials. Fig. 8 compares the impedance spectra obtained for single, poly and nanocrystalline YSZ. A clear grain boundary (gb) contribution at intermediate frequencies is evident in the impedance spectra of polycrystalline YSZ with grain size above 1 μm. For nanocrystalline YSZ, a single semicircle, obtained at high frequency is attributed to the superposition of bulk and grain boundary effects. The bulk conductivities, as determined from the high frequency intercepts on the real axis for single and polycrystalline YSZ (grain size ≥ 1.3 μm) show no dependence on grain size as
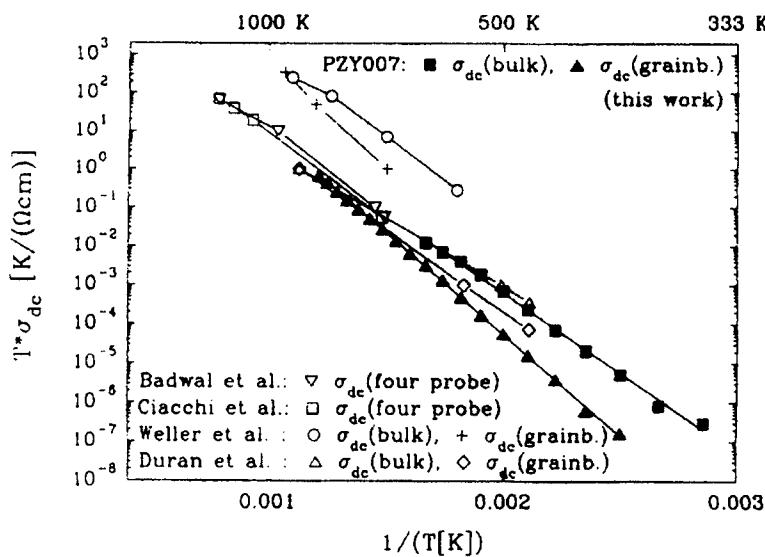
Fig. 7. Comparison of bulk and grain boundary conductivities of nano- and micro-crystalline YSZ [14].
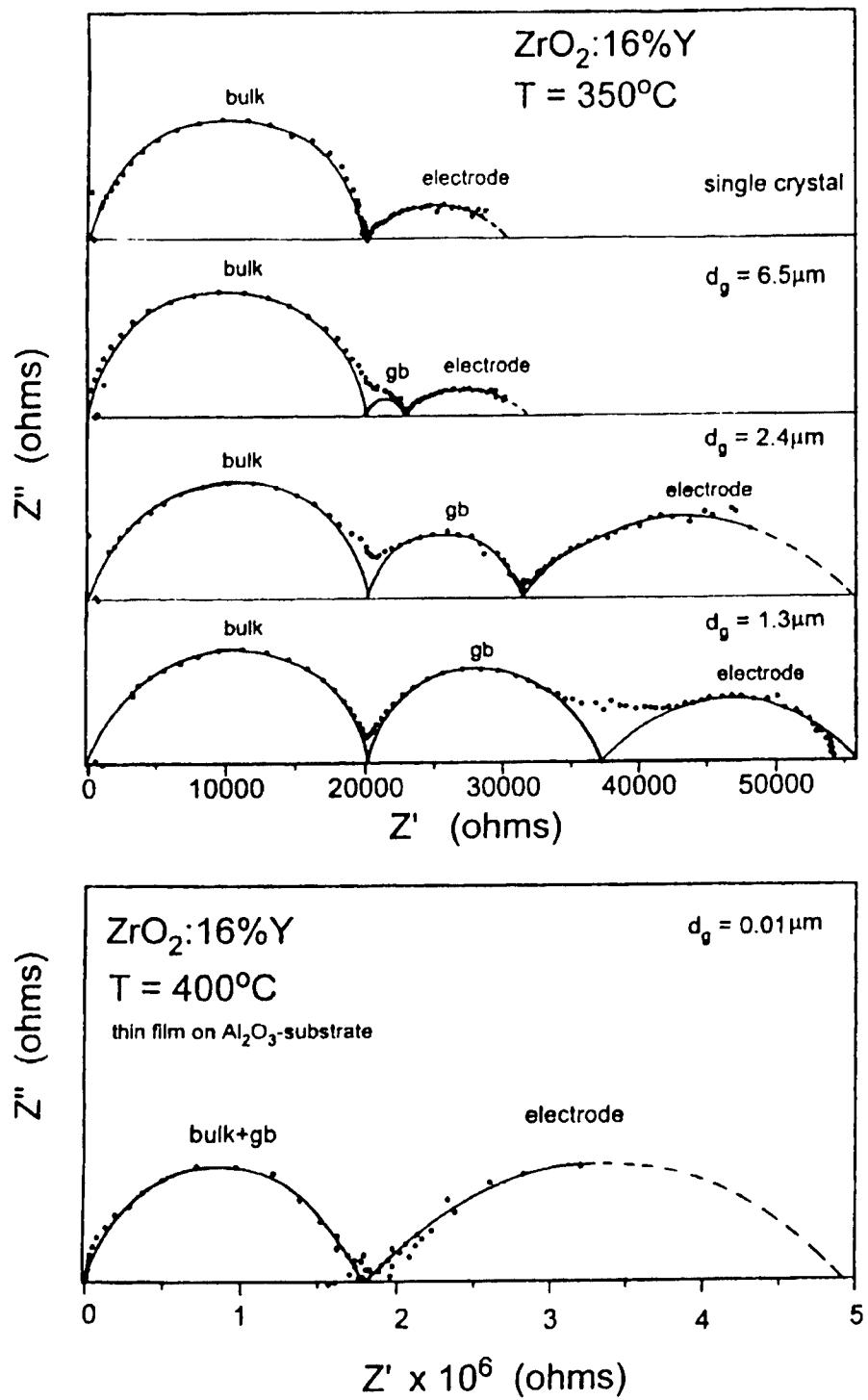
Fig. 8. Complex impedance spectra obtained for (a) single crystal microcrystalline YSZ bulk specimens and (b) for nanocrystalline YSZ films [16].
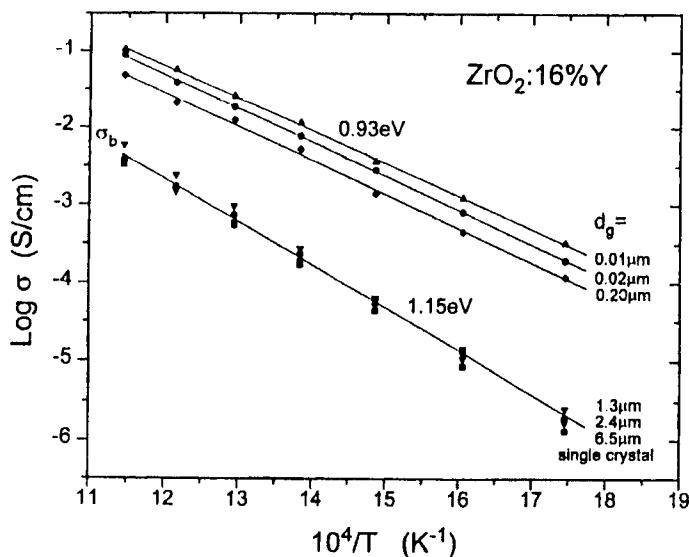
Fig. 9. Comparison of electrical conductivity for single crystal, bulk microcrystalline specimens and nanocrystalline thin films of YSZ [16].

evident from Fig. 9. On the other hand, the corresponding data for polycrystalline YSZ with submicron size grains show a substantial enhancement in conductivity above that of the larger grain materials. This increase in conductivity is associated with a reduction of the activation energy from 1.15 to 0.93 eV. The authors suggest that the high frequency resistance of the nanocrystalline YSZ is largely determined by the grain boundary resistance and attribute the sharp drop in the specific grain boundary resistance to a decrease in the level of impurities segregating to the boundaries as in Ref. [5]. It must be noted, however, if much of the high frequency resistance is attributed to grain boundary blocking, this would imply even higher bulk conductivity enhancements than those suggested in Fig. 9.

At this time, one can only speculate about the origin of the large discrepancy between the study of Kosacki et al. [16] and those of Mondal and Han [14] and Jiang et al. [15]. The key difference between these studies is the manner in which the nanocrystalline specimens were prepared. In Ref. [16], thin films of about 1 μm thickness were prepared by a polymer precursor spin coating process, while in Refs. [14,15], bulk specimens were prepared by pressing and sintering ultra-fine powders prepared by combustion synthesis or inert-gas condensation. Since films have a large surface to volume

ratio, they tend to be more susceptible to the influence of humidity on the exposed side and film-substrate interactions on the opposite side. Control experiments in which alternate substrates are used and the relative humidity is varied under controlled conditions would help in clarifying the source of enhanced ionic conduction in thim film nanocrystalline YSZ.

3.2. Ceria

3.2.1. Undoped ceria

In contrast to stabilized zirconia, ceria (CeO_2) is stable in the cubic fluorite phase without the need for additives. Ce^{4+} reduces to Ce^{3+} at elevated temperatures and reducing atmospheres resulting in a high degree of oxygen deficiency and n-type semiconductivity [17,18]. Doping with acceptors such as Y^{3+} or Gd^{3+}, like YSZ, transforms ceria into an excellent solid oxide electrolyte [19]. These features appear to contribute to ceria's unusual catalytic activity. In particular, high surface area nanocrystalline CeO_{2-x} exhibits exceptionally high catalytic activity already at low temperatures in redox reactions such as CO oxidation and SO_2 reduction by CO [20].

It is of interest to establish the source of the enhanced catalytic activity of nanocrystalline ceria. To that end, Tschope et al. [21] examined the

electrical properties of porous nanocrystalline ceria as a function of temperature and at several different atmospheres. A typical complex impedance plot, which exhibits strong overlap between two semicircles, is shown in Fig. 10. Also shown is the fitted equivalent R–C circuit. The two capacitances were found to be within an order of magnitude of each other, not surprising given that the grain size in nanocrystalline solids approaches the same order of magnitude as the space charge width. This illustrates that the distinction between bulk and grain boundary regions tends to vanish as the grain size is reduced to the nanometer regime [21], consistent with observations for YSZ [16] as well as for other studies of CeO_2 [11] and TiO_2 [22].

The activation energy for conduction in porous nancrystalline CeO_2 (0.7 eV) was found to be less than half of that reported for single crystalline CeO_2 (1.97 eV) [8] pointing to a reduced enthalpy of defect formation. Because porous materials are more difficult to interpret due to uncertainties related to open porosity, surface adsorption and constrictions at particle contacts, Chiang et al. [11] prepared CeO_{2-x} polycrystals of ~10 nm grain size with densities of

greater than 95% by several processing routes. These included powders prepared by inert gas condensation and by a chemical route. Both sets of powders were densified at 1.1 GPa pressure at 600°C for ~1 h thereby maintaining an average grain size of ~10 nm. Reference specimens of ~5 μm grain size were prepared by firing identical nanocrystalline pellets at 1200°C for 12–15 h. This allowed for one-to-one comparison between specimens which differed ideally only in microstructure.

The bulk conductivity $(T=600°C)$, as derived from the high frequency part of the impedance spectra, is shown plotted in Fig. 11 as a function of P_{O_2} for the 10 nm and 5 μm grain size materials. Note that while the large grained material is P_{O_2}-independent at high P_{O_2} suggesting ionic conduction, nanosized material is P_{O_2} dependent, indicative of n-type semiconducting behavior. Furthermore, if one extrapolates the electronic conductivity of the 5 μm material to 10^5 Pa (1 atm), one observes ~10^4 enhancement in electronic conductivity for the nanocrysatlline material. As in the above study [21], the activation energy for electronic conduction is much reduced in nanocrystalline CeO_2 (0.99–1.16 eV) as compared to the coarsened material (2.45 eV). Kosacki et al. [23] found similar results for thin film CeO_2.
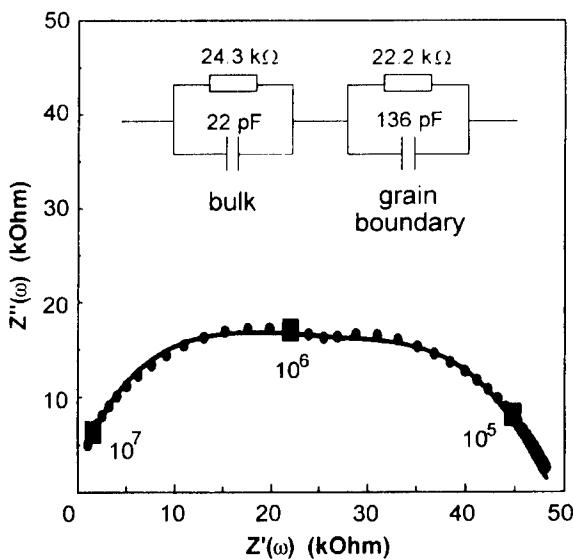
Fig. 10. Complex impedance spectrum of nanocrystalline CeO_{2-x} at 130°C in a hydrogen atmosphere and equivalent circuit [21]. Note strong overlap of high and low frequency semicircles.
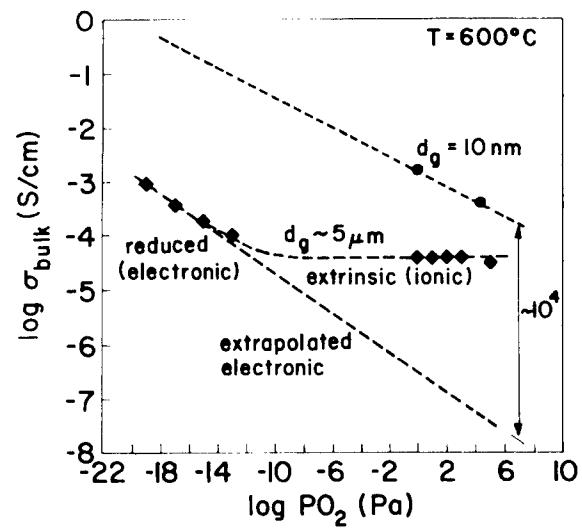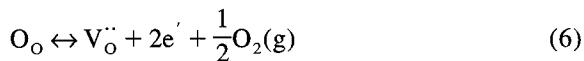
Fig. 11. The bulk conductivity of nanocrystalline (d~10 nm) and coarsened microcrystalline (d~5 mm) CeO_{2-x} measured at 600°C as a function of oxygen partial pressure [11].

One may relate these energies to the enthalpy of reduction by considering the appropriate reduction reaction

$$O_O \leftrightarrow V_O^{\cdot\cdot} + 2e' + \frac{1}{2}O_2(g) \tag{6}$$

which for dilute concentrations has the mass action relation

$$K_R(T) = K_R^{\circ} \exp\left(-\frac{\Delta H_R}{kT}\right) = [V_O^{\cdot\cdot}]n^2 P_{O_2}^{1/2} \tag{7}$$

Assuming the vacancy density is fixed by acceptor impurities as evident in Fig. 11 for the coarsened material and noting that the activation energy for conduction is given by

$$E_a = \left(\frac{\Delta H_R}{2}\right) + E_h \tag{8}$$

where E_h ($=0.4$ eV) is the hopping energy of electrons [18], one derives ΔH_R values of 1.18–1.52 eV for nanocrystalline CeO_2 versus 4.10 eV for coarsened CeO_2. This large dependence of the effective reduction enthalpy on grain size suggests, as in Ref. [20], that defect generation at grain boundaries and surfaces becomes predominant as these interfaces become more predominant.

Porat et al. [24] investigated the non-stoichiometry of nanocrystalline CeO_2 by coulometric titration. Large apparent deviations from stoichiometry of up to 10^{-3} were found. The oxygen deficiency follows an oxygen pressure dependence with an exponent of $-1/2$. This can be understood if neutral oxygen vacancies are majority defects in nanocrystalline CeO_2 or that oxygen losses upon reduction are largely due to oxygen desorption from particle surfaces. The latter interpretation corroborates the conclusions of Tschöpe and Birringer [25], who investigated chemically precipitated cerium dioxide annealed at 550 and 600°C by thermogravimetry. Pressure/composition isotherms at 500, 550 and 660°C of nanocrystalline and conventional polycrystals showed a two-phase region only at the highest temperature, where bulk reduction was observed. At lower temperature, surface oxygen was desorbed with the larger apparent oxygen deficiency of nanocrystalline materials correlated with the larger surface area.

3.2.2. CeO_2 solid solutions

Large deviations from stoichiometry were also found in nanocrystalline CeO_2–PrO_x solid solutions by Knauth and Tuller [26]. Of special note was the observation of chemical diffusivities with low activation energy of 0.3 eV. This is suspected to reflect the presence of fast diffusion pathways.

Chiang and coworkers [27,28] investigated highly dense gadolinium-doped cerium dioxide samples with about 10 nm average crystallite size. With a relatively small gadolinium concentration (1.5 mol%), qualitatively similar results with the nominally undoped samples were found: a strongly enhanced electronic conductivity and a small reduction enthalpy. This is experimental support for 'undoping' of grains due to the small grain size [5]. The grain boundary resistance was higher, likely because of gadolinium segregation. In heavily doped nanocrystalline CeO_2 samples (26 mol%), no significant increase in bulk ionic conductivity compared with a conventional sample was found. It appears that transport along grain boundaries, which is likely to be seen together with the bulk response, did not play a significant role, neither by ionic diffusion in interface cores nor in space charge regions due to carrier accumulation. In total, reduction of grain size resulted in an increase of total resistance and the grain boundaries remained highly blocking, even in nanocrystalline samples.

3.3. Titania

Nanocrystalline titanium dioxide is being exploited as the active element in inexpensive photovoltaic cells and as the photocatalyst in water treatment plants to oxidize dissolved organics [29,30]. It is also one of a number of semiconducting oxides which has been considered as a potential oxygen sensor. It is therefore of interest to establish if nanostructured titania exhibits enhanced ionic diffusion and/or defect generation.

Knauth and Tuller [22] prepared dense (~95%) compacts of TiO_2 with the anatase phase. The average grain size was 35 ± 10 nm. The P_{O_2} dependence of the electrical conductivity is shown plotted

in Fig. 12. In contrast to the p-to-n transition exhibited by coarsened titania at intermediate P_{O_2}, one observes an apparent ionic plateau at high P_{O_2} and an n-type regime at low P_{O_2}. The $P_{O_2}^{-1/2}$ dependence of the n-type conductivity is distinctly stronger than the $P_{O_2}^{-1/4}$ dependence exhibited by the coarsened material.

The ionic conductivity is shown plotted in Fig. 13 as a function of reciprocal temperature. The ionic conductivity is described by

$$\sigma_{ion} = \left(\frac{2.2 \times 10^3}{T}\right) \exp\left(-\frac{1\ eV}{kT}\right) \text{S/cm} \qquad (9)$$

This corresponds to an ionic conductivity of ~2× 10^{-5} S/cm at 1000 K. In a recent study on single

crystalline titania, Nowotny et al. [31] were able to extract the ionic conductivity from the P_{O_2} dependence of the total conductivity. Interestingly enough, they obtained a similar value of σ_{ion} ~3×10^{-5} S/cm at 1000 K but report a considerably larger activation energy of ~1.5 eV. This comparison suggests that while the effective doping level in the nanocrystalline material is lower due to segregation of dopants to the grain boundaries, the increased density of interfaces, at the same time, provides higher diffusive pathways than available in the single crystal material. This latter factor is presumably the source of the lower activation energy in the nanocrystalline material.

Demetry and Shi [32] found P_{O_2} independent conductivity plateaus at 500°C for rutile nanocrystal-
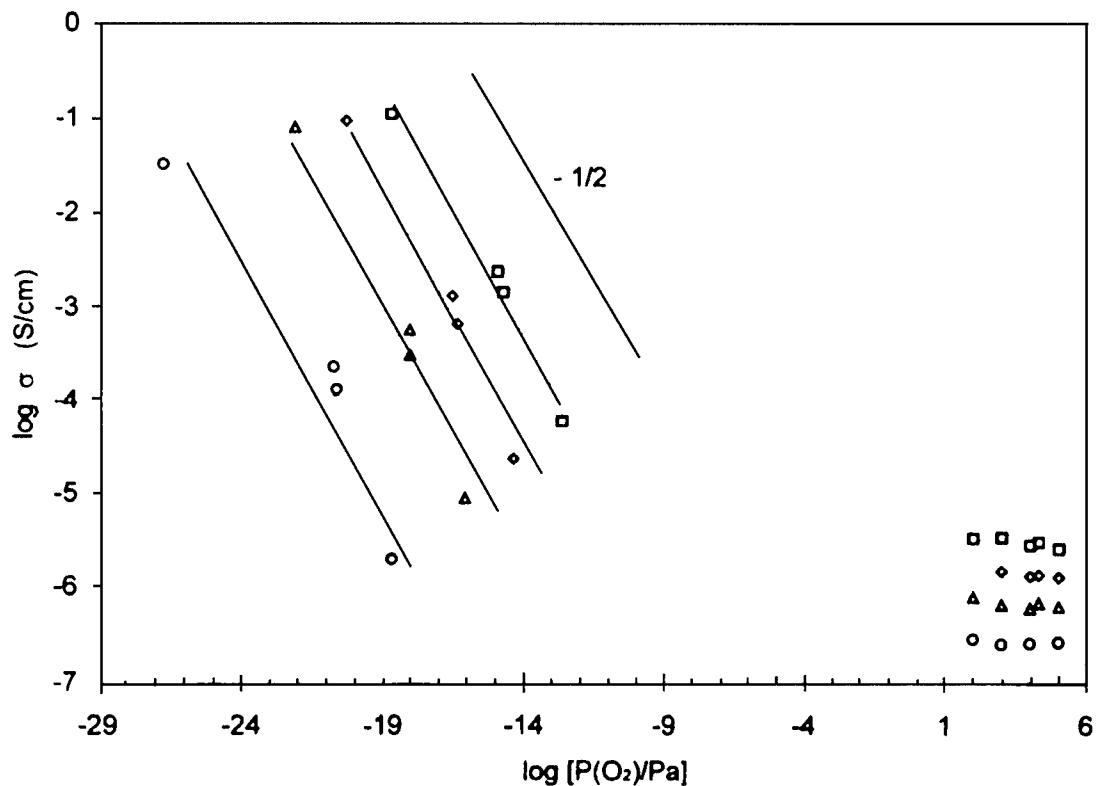
Fig. 12. Oxygen partial pressure dependence of the electrical conductivity of nanocrystalline TiO$_2$ (d~35 nm): □, 580°C; ◇, 530°C; △, 500°C; ○, 450°C [22].
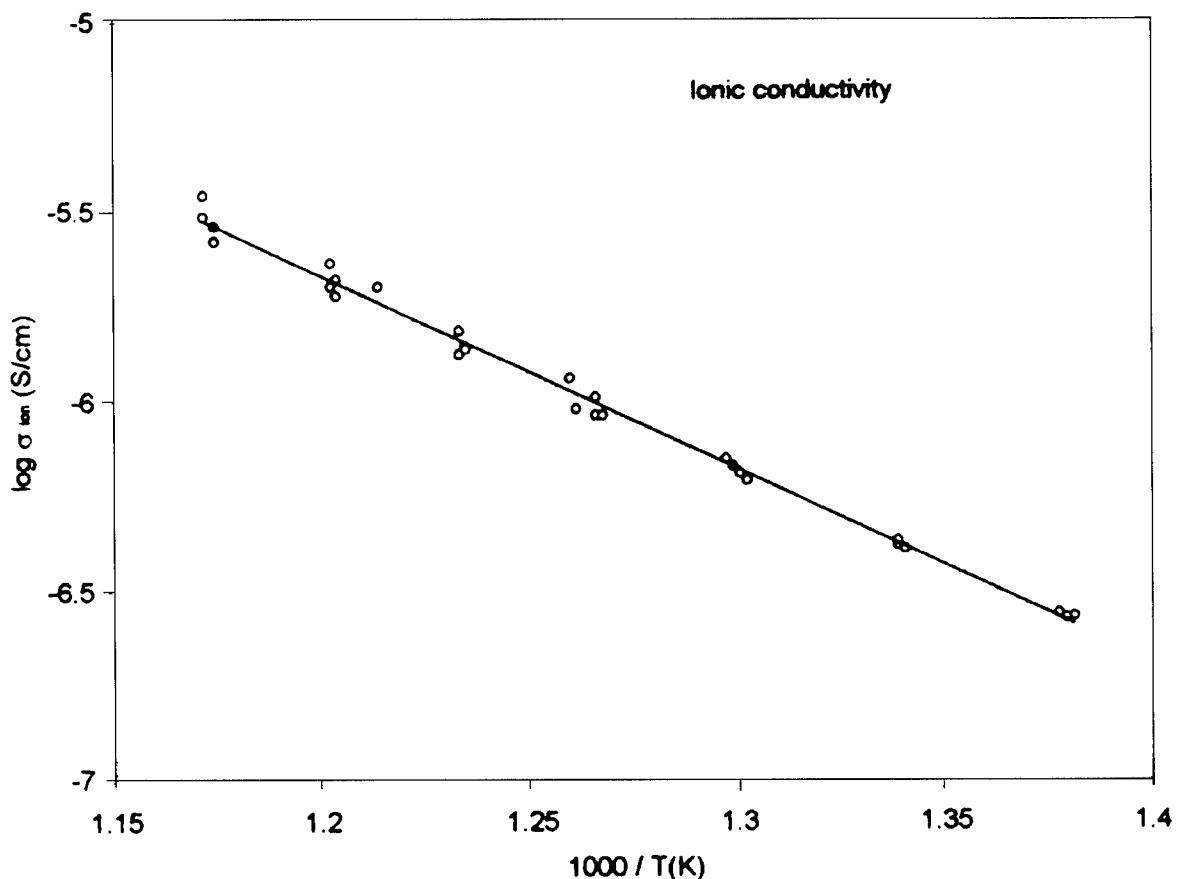
Fig. 13. The ionic conductivity of nanocrystalline TiO_2 as a function of reciprocal temperature [22].

line specimens with 50 and 260 nm grain size. They report activation energies of 0.96 and 1.23 eV respectively and considerably higher magnitudes of conductivity. It should be noted that the authors were able to stabilize the rutile phase by the addition of 1 mol% SnO_2 while the specimens of Knauth and Tuller [22] were prepared in the anatase phase. While one might wish to conclude that ionic conduction in the rutile phase is much higher than in the anatase phase, it must be remembered that the P_{O_2} independence of the conductivity suggests impurity control and at this point we have no clear means for comparing the effective dopant levels in the two sets of materials. On the contrary, the activation energies of the two sets of materials are similar (rutile 0.96 eV

versus anatase 1.0 eV) for materials with similar grain size suggesting carrier rather than mobility control. Furthermore, more direct means for confirming the ionic nature of the conductivity in the P_{O_2} independent conductivity plateaus would be most desirable.

4. Conclusions

We have focused in this article on the question of whether and to what extent ionic conduction and/or defect formation are modified in nanocrystalline oxides. We have reviewed the literature on three systems; cubic zirconia, ceria and titania, for which

experimental data has become available. At this time, it is too early to make firm conclusions but we can make some useful observations. These include:

1. Additives which contribute to ion blocking at grain boundaries are diluted in nanocrystalline oxides giving rise to substantial reductions in specific grain boundary resistivities. This leads, in some cases, to an overall decrease in grain boundary resistance.
2. The case for enhanced ionic conduction in nominally undoped nanocrystalline oxides remains unresolved. In the case of CeO_2, enhanced electronic conductivity (see (4) below) masks any changes in ionic conductivity. In TiO_2, evidence is mixed. Nanocrystalline rutile appears to exhibit higher ionic conductivity than single crystal rutile while nanocrystalline anatase exhibits comparable levels of conductivity. In any case, more direct methods of measuring ionic conduction are necessary before even these tentative observations are taken too seriously.
3. There is mixed evidence in support of enhanced ionic conduction in doped electrolytes. No increases in ionic conduction are reported for either bulk stabilized ZrO_2 or doped CeO_2. In thin films, enhancements of several orders of magnitude are reported. It remains to be seen if this discrepancy is related to differences in the manner in which the dopants are distributed between grain and grain boundary during processing or, in the case of the films, are due to spurious effects such as humidity or film substrate interactions.
4. In CeO_2 or CeO_2-based solid solutions, there is strong support for the notion that the energetics for defect formation may be substantially reduced in nanocrystalline oxides. This results in markedly increased levels of nonstoichiometry and electronic carrier generation, likely important contributors to the enhanced catalytic activity reported for these materials. Similar observations, while less dramatic, have also been reported for TiO_2 [22].

One may confidently conclude that there remains much interesting work still to be done. Given recent improvements in the processing and characterization of nanocrystalline materials and structures, progress in this field can be expected to be rapid.

References

[1] H.L. Tuller, J. Electroceram. 4 (Suppl. 1) (1999) 33.
[2] S.P.S. Badwal, S. Rajendran, Solid State Ionics 70–71 (1994) 83.
[3] R. Gerhardt, A.S. Nowick, J. Am. Ceram. Soc. 69 (1986) 641.
[4] R. Gerhardt, A.S. Nowick, M.E. Mochel, I. Dumler, J. Am. Ceram. Soc. 69 (1986) 646.
[5] M. Aoki, Y.-M. Chiang, I. Kosacki, J.-R. Lee, H.L. Tuller, Y.J. Liu, J. Am. Ceram. Soc. 79 (1996) 1169.
[6] J. Maier, Prog. Solid State Chem. 23 (1995) 171.
[7] H.L. Tuller, P.K. Moon, Mat. Sci. Eng. B 1 (1988) 171.
[8] A. Atkinson, C. Monty, in: L.C. Dufour et al. (Ed.), Surfaces and Interfaces of Ceramic Materials, Kluwer Academic, Dordrecht, The Netherlands, 1989, p. 273.
[9] J.A. Cusumano, in: J.M. Thomas, K.I. Zmarev (Eds.), Perspectives in Catalysis, Blackwell Scientific, Boston, 1992.
[10] K.L. Merkle, Phys. Chem. Sol. 55 (1994) 991.
[11] Y.-M. Chiang, E.B. Lavik, I. Kosacki, H.L. Tuller, J.Y. Ying, J. Electroceramics 1 (1997) 7–14.
[12] J. Maier, Solid State Ionics 23 (1987) 59.
[13] H.L. Tuller, in: F.W. Poulsen, N. Bonanos, S. Linderoth, M. Mogensen, B. Zachau-Christiansen (Eds.), High Temperature Electrochemistry: Ceramics and Metals, Risø National Laboratory, Roskilde, 1996, p. 139.
[14] P. Mondal, H. Hahn, Ber. Bunsenges Phys. Chem. 101 (1997) 1765–1766.
[15] S. Jiang, J. Mat. Res. 12 (1997) 2374.
[16] I. Kosacki, B. Gorman, H.U. Anderson, in: T.A. Ramanarayanan, W.L. Worrell, H.L. Tuller, A.C. Kandkar, M. Mogensen, W. Gopel (Eds.), Ionic and Mixed Conductors, Vol. III, Electrochemical Society, Pennington, NJ, 1998, p. 631.
[17] H.L. Tuller, A.S. Nowick, J. Electrochem. Soc. 126 (1979) 209–217.

[18] H.L. Tuller, A.S. Nowick, J. Phys. Chem. Solids 38 (1977) 859–867.

[19] H.L. Tuller, Solid State Ionics 52 (1992) 135–146.

[20] A. Tschope, W. Liu, M. Flytzani-Stephanopolous, J.Y. Ying, J. Catal. 157 (1995) 42.

[21] A. Tschope, J.Y. Ying, H.L. Tuller, Sensors and Actuators B 31 (1996) 111.

[22] P. Knauth, H.L. Tuller, J. Appl. Phys. 85 (1999) 897–902.

[23] I. Kosacki, H. Anderson, Mat. Res. Proc. 453 (1997) 537.

[24] O. Porat, E.B. Lavik, H.L. Tuller, Y.-M. Chiang, in: S. Komarneni, J. Parker, H. Wollenberger (Eds.), Nanophase and Nanocomposite Materials, Vol. II, Materials Research Society, Pittsburgh, PA, 1997, p. 99.

[25] A. Tschöpe, R. Birringer, Nanostructured Mater. 9 (1997) 59.

[26] P. Knauth, H.L. Tuller, J. Euro. Ceram. Soc. 19 (1999) 831.

[27] E.B. Lavik, Y.M. Chiang, Mat. Res. Proc 457 (1997).

[28] Y.M. Chiang, E.B. Lavik, D.A. Blom, Nanostructured Mater. 9 (1997) 633.

[29] C.J. Barbe, F. Arendse, P. Compte et al., J. Am. Ceram. Soc. 80 (1997) 3157.

[30] J.Y. Ying, T. Sun, J. Electroceramics 1 (1997) 219.

[31] J. Nowotny, M. Redecka, M. Rekes, S. Sugihara, E.R. Vance, W. Weppner, Ceramics Int. 24 (1998) 571.

[32] C. Demetry, V. Shi, Solid State Ionics 118 (1999) 271.

Local and overall ionic conductivity in nanocrystalline CaF_2

W. Puin[a], S. Rodewald[b,*], R. Ramlau[b], P. Heitjans[a], J. Maier[b]

[a]*Institut für Physikalische Chemie und Elektrochemie, Universität Hannover, Callinstraße 3-3A, D-30167 Hannover, Germany*
[b]*Max-Planck-Institut für Festkörperforschung, Heisenbergstraße 1, D-70569 Stuttgart, Germany*

Abstract

Ionic conductivity data on nanocrystalline CaF_2 is evaluated. The d.c. conductivity is distinctly larger than in coarse-grained materials. The impedance plot exhibits two regimes: a high- and a low-frequency semicircle, the diameters of which increase with increasing grain size. The high-frequency semicircle reflects both bulk transport plus transport along the boundaries while the low-frequency semicircle describes the blocking effect of the grain boundaries. Absolute values and activation energy of the conductivity suggest dominating transport along space charge layers. The increase of the low frequency semicircle is due to increased current constriction because of the appearance of large pores. © 2000 Elsevier Science B.V. All rights reserved.

Keywords: Ionic conductivity; Nanocrystalline; CaF_2

1. Introduction

The consideration of nanocrystalline materials has become very popular recently and many properties, in particular mechanical and electronic properties, have been studied intensively. An overview of studies related to nanocrystalline electroceramics is given in Ref. [1]. Surprisingly, not very much work has been done with respect to ionic or mixed conductors even though ionic transport is intimately related to atomistic aspects [1–3]. An overview on the expected effects is given in [4]. The most obvious one is the enhancement of interfacial contributions due just to the increased density of interfaces. The impact on the overall conductivity may thus stem from the interface core which exhibits a structure different from the grain interior directly or indirectly via space charge effects. In addition the effects of 'edges and corners' will grow correspondingly. If the grain size is of the order of characteristic decay lengths or smaller we have to face mesoscopic effects. One is the change from semi-infinite to finite space charge conditions [5] which means that the space charge distribution of one interface is not decaying to a zero (bulk) value but influenced by one other interface. Also modifications of the ground-state structure in the grain interior must be considered which change the standard term in the chemical potential of the carriers. (Size effects due to delocalisation of the wave

*Corresponding author. Tel.: +49-711-689-1736; fax: +49-711-689-1722.

E-mail address: rodewald@chemix.mpi-stuttgart.mpg.de (S. Rodewald)

functions should be relevant only for proton conduc-
tors under very special conditions.)

CaF$_2$ is well-suited as a model material for such
studies, since its macroscopic properties are widely
known, it is chemically stable and exhibits well
defined grain boundary effects on the ionic con-
ductivity as studied by Saito et al. [6]. Nuclear
magnetic resonance (NMR) work on nanocrystalline
CaF$_2$ [7,8] allowed one to differentiate between two
F-ion types of distinct diffusivities. The faster ions
were ascribed to the grain boundaries, and the slower
ones to the grains. The overall diffusivity was found
to be considerably enhanced as compared to that in
single crystal CaF$_2$. Similar NMR results were
recently obtained for nanocrystalline LiNbO$_3$ [8,9].
The increased diffusivity in nanocrystalline CaF$_2$
corresponds to the results of conductivity measure-
ments on the same material by impedance spec-
troscopy [10]. The present contribution is essentially
an evaluation of the data in Ref. [10] by using the
model developed in Ref. [11] to deconvolute the
different conductivity contributions in a polycrystal-
line sample including space charge phenomena. In
addition TEM studies are employed to take proper
account of morphological variations.

2. Impedance analysis of micro- and nanocrystalline materials

In general the impedance analysis of polycrystal-
line materials is complex. The grain boundary net-
work topology can be complicated and, thus, also the
percolation behaviour. Different types of grain
boundaries can exist in the same material according
to type, structure, misfit angle, inclusions (glasses or
pores) etc. Additional complications occur if the
crystallites are not homogeneous. In the following
we assume that the grain boundary effect can be
mimicked by a brick layer model with one kind of
grain boundary and follow Ref. [11]. It is shown in
Ref. [12] that results of the brick-layer model are
expected to be a good approximation for this materi-
al even if the microstructure deviates substantially
from the model. In other words we assume a cubic
primitive microstructure consisting of cubic grains
(thickness L) separated by identical boundaries. The
equivalent circuit then approximately reduces to the
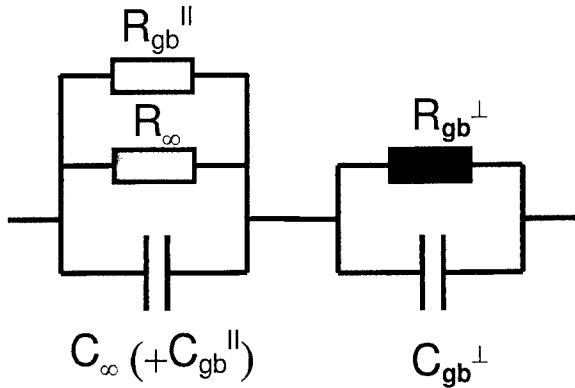
Fig. 1. Equivalent circuit model assuming the different contribu-
tions to the impedance spectra in the brick layer approximation. It
is assumed that the parallel interfacial pathway is also blocked by
$R_{gb}\perp$ [10].

circuit given in Fig. 1. The equivalent circuit in Fig.
1 consists of two parallel circuit-elements which are
denoted by resistance and capacitance values in a
series circuit. R_∞, C_∞ refer to the bulk, $R^\parallel_{gb}$, $C^\parallel_{gb}$, and
$R^\perp_{gb}$, $C^\perp_{gb}$ to the boundary values. In terms of the
complex conductivities the superposition is given by
Eq. (1):

$$\hat{\sigma}_m = \frac{\hat{\sigma}_\infty \hat{\sigma}^\parallel_L + \beta^\parallel_L \varphi_L \hat{\sigma}^\parallel_L \hat{\sigma}^\perp_L}{\hat{\sigma}^\perp_L + \beta^\perp_L \varphi_L \hat{\sigma}_\infty} \tag{1}$$

The total complex conductivity $\hat{\sigma}_m$ has contributions
from the complex bulk conductivity $\hat{\sigma}_\infty$ and the
interfacial layer parallel and perpendicular complex
conductivities $\hat{\sigma}^\parallel_L$ and $\hat{\sigma}^\perp_L$. Both $\hat{\sigma}^\perp$ and $\hat{\sigma}^\parallel$ consists
of core and space charge effects. A more detailed
analysis is given in Ref. [11]. In an impedance plot,
the circuit of Fig. 1 should lead to two semicircles.
Usually the low frequency semicircle, corresponding
to a higher capacitance, reflects the series effect the
at grain boundaries, whereas the high frequency
semicircle, in which $C^\parallel$ is normally negligible com-
pared to C_∞, refers to bulk plus parallel layers. This
simple model allows one to take account of the grain
boundary anisotropy. The anisotropy may be due to
the sandwich structure (space charge region | core |
space charge region) and/or to the profile character
of the space charge regions themselves (e.g. inver-
sion layers). Thus, in the same material, blocking and
short-circuiting behaviour of the grain boundary may

be perceived [11]: The grain boundary can provide fast pathways but can also (in the direction of measurement) act as an obstacle for the transport from grain to grain as indicated in Fig. 1. Also series blocking effects can often simply be traced back to current constrictions due to insufficient contact [13,14]. In this case the measured activation energy roughly corresponds to the bulk value. In the case of highly conducting layers via space charges the activation energy is usually somewhat higher than the migration enthalpy of the enriched defect type. The difference is smaller, the larger the interfacial effect. The effective series and parallel space charge contributions can be derived from the profile [11,15]. In the following we are especially interested in the second contribution. Thus the conductivity of the parallel interfacial layer $\sigma_L^{\parallel}$ [11], [16] to be inserted in Eq. 1 is given by:

$$\sigma_L^{\parallel} \cong \Delta\sigma_L^{\parallel} = u_V F c_{V\infty} \frac{2\vartheta_V}{1 - \vartheta_V} \cong u_V F \sqrt{c_{V0} c_{V\infty}}. \qquad (2)$$

In the brick layer model the volume fraction of the space charge layers is

$$\varphi_L = 6(2\lambda/L) = \frac{12}{L} \sqrt{\frac{\varepsilon_0 \varepsilon_r RT}{2F^2 c_{V\infty}}} \qquad (3)$$

with $\beta_L^{\parallel} = 2/3$. The result is

$$\sigma_m^{\parallel} \cong 4u_V \sqrt{2\varepsilon_r \varepsilon_0 RT c_{V0}}/L. \qquad (4)$$

The quantities u_V, $c_{V\infty}$, c_{V0} denote mobility, bulk defect concentration and defect concentration in the first layer adjacent to the interface core of the enhanced carriers (here taken as the vacancy). The enhancement is characterized by the 'degree of influence' (on the vacancies) ϑ_V as defined in Ref. [11]. L is the thickness of the grain, $\beta_L^{\parallel}$ the fraction of interfaces contributing to the conduction.

In nano-crystalline materials the fraction of interfacial regions is much more pronounced and consequently their impact on the overall electrical conductivity is enhanced. In addition, there is the possibility that the Debye-length is comparable or even larger than the crystallite sizes. In these cases, space charge effects may be extremely high, the crystallites may be charged everywhere and no bulk profiles may be attained within the mesoscopic

sample [5]. In these cases, it was derived that for large effects [5]:

$$\sigma_m^{\parallel} \cong f u_V \sqrt{2\varepsilon_r \varepsilon_0 RT(c_{V0} - c_V^*)}/L \qquad (5)$$

(c_V^*: concentration in the centre). The dependence of c_V^* on c_{V0} and L necessary for an explicit treatment is given in Ref. [5]. To be precise Eq. (5) was derived for nano-sized films with $f=2$. The value $f \cong 4$ should give a first rough estimate for nano-crystalline (cubic) grains, even though for precise considerations the simultaneous influence of all six interfaces should be considered.

3. Experimental

Nanocrystalline powder of CaF_2 (n-CaF_2) with an average particle diameter of 9 nm was prepared by the inert gas condensation method. The impurity level was determined to be ≤ 30 ppm except for Na (400 ppm). Cylindrical pellets (with a density of about 96%) were formed under a pressure of 2 GPa, coated with Ag on both sides and placed between the electrodes of an air tight measurement cell. The impedance of the sample was measured using a HP 4192A impedance analyser from 5 to 13 MHz at temperatures in the range 390–500 K. More details on the preparation and measurement can be found in reference [10]. Transmission Electron Microscopy (TEM) investigations were carried out with a PHILIPS CM30/ST electron microscope operating at 300 kV (point resolution 0.19 nm). The slightly sintered nano-crystalline powder was dispersed in n-butanol and then dropped on a specimen grid which was a perforated carbon film. TEM images were taken in the bright-field mode to determine the grain sizes, and in the high resolution mode to investigate the pore sizes.

4. Results and discussion

The impedance spectra of the freshly prepared samples show three semicircles. These impedance spectra can be interpreted in terms of the equivalent circuit given in (Fig. 1) taking the additional contributions of blocking electrode effects into account.

The semicircle at very low frequencies is caused by electrode polarisation effects and will not be further discussed in this contribution. The two other partly overlapping depressed semicircles can be assigned to bulk and grain boundaries. As discussed above the high frequency contribution can be attributed to the parallel combination of bulk and parallel boundary pathways '‖' while the low frequency semicircle describes the blocking of these pathways by perpendicular boundary effects '⊥' [11]. The resistance obtained from the low-frequency semicircle is about 10 times larger than the resistance of the high-frequency semicircle. Nevertheless the total d.c. contribution is far greater than the pure bulk contribution of coarse grained material. By annealing the sample for 30 min at 505 K the resistance of the low-frequency semicircle increases by almost one order of magnitude, whereas the high-frequency semicircle shows only an increase of a factor of two (Fig. 2).

The very low resistance of the high-frequency semicircle compared to the normally measured bulk resistances (Fig. 3) of CaF_2 may be simply interpreted in terms of space charge effects as the following arguments suggest: Measurements on m-CaF_2 (CaF_2 with grain size in the micron-region) by Saito et al. [6] showed that space charge effects play
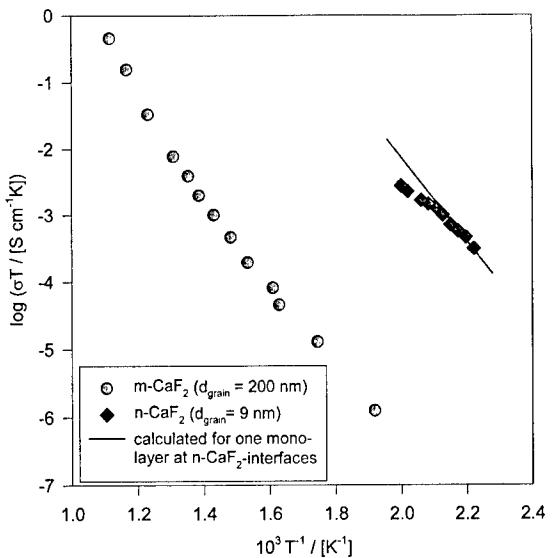
Fig. 3. Temperature dependence of the conductivities of nano- and micro-crystalline CaF_2 derived from the high-frequency semicircles [5,9]. The line represents the estimated conductivities assuming a pronounced space charge effect [5].

Fig. 2. Impedance spectra for nanocrystalline CaF_2 samples (a) 'freshly prepared' and (b) 'annealed' [9].

a significant role in polycrystalline materials. The space charge potential can be increased by special chemical treatment (heterogeneous doping by SiO_2, contamination by SbF_5 or BF_3). This behaviour is completely analogous to the experiments on Ag-halides (heterogeneous doping by Al_2O_3 [17], contamination with NH_3 or $(CN)_2$ [18]). The solid line indicated in Fig. 3 is obtained simply by scaling up the space charge effects of Saito et al. according to the increased interfacial density. The slope of the line is approximately the activation energy of the vacancies and suggests, accumulation in the grain boundary core. Assuming that the increased vacancy concentration is responsible for the enhancement, the line meets the correct order of magnitude. The systematic deviation at increased temperature is definitely due to sintering and coarsening.

If the grain size of the material becomes smaller than four times the Debye length, even the core of the grains becomes fully charged. In that case, an additional enhancement factor comes into play. As the results show, this 'nano size' effect [5] is obviously not observed here (however see results obtained for $AgI:Al_2O_3$ composite [4]). This is in agreement with the fact that the computed Debye

length (~1 nm) is much below the grain size (~9 nm) owing to the high impurity concentration of Na+-ions.

The second semicircle can be explained in the following way. Both bulk and space charge transport perceive the perpendicular boundaries. This may be due to core effects or due to current constriction. The comparably low capacitance points towards the second effect. It is also supported by the activation energy of 0.8 eV which is close to the bulk value [14]. Increased current constriction is certainly responsible for the fact that the low frequency semicircle increases with temperature. TEM images (Fig. 4) reveal a coarsening of the grains connected with the generation of significant pores causing serious constriction effects [5]. The generation of large pores is understandable since no pressure is applied during the grain growth process.

Therefore two effects, both caused by annealing, have to be considered: (i) The diminishing of the volume fraction of highly conducting parallel pathways (space charge layers) leading to an increase of the resistance of the high-frequency semicircle and (ii) current constriction effects which become more serious due to the formation of large pores. Applying pressure would lead to densification and probably eliminate the second effect. The grain coarsening itself is an inherent problem in nanocrystalline materials due to high interfacial energy. In particular, in ionic conductors this may be an even more serious problem due to facilitated kinetics. A way-out can be the use of nano-composites, e.g. heterogeneous doping of fluorides by silica [19], in which the phase distribution makes grain growth much more difficult.

5. Conclusions

Nanocrystalline CaF_2 shows a significantly higher overall conductivity than the micro-crystalline material. This behaviour can be completely understood in terms of the large fraction of interface regions in the nanocrystalline material. By assuming a pronounced space charge effect (one monolayer of absorbed at the grain boundary interface) the order of magnitude and temperature dependence of the overall conductivity in n-CaF_2 can be explained. The appearance of the mesoscopic space charge effect predicted in Ref. [5] demands the preparation of highly pure n-CaF_2. The significant porosity leads to current constriction.
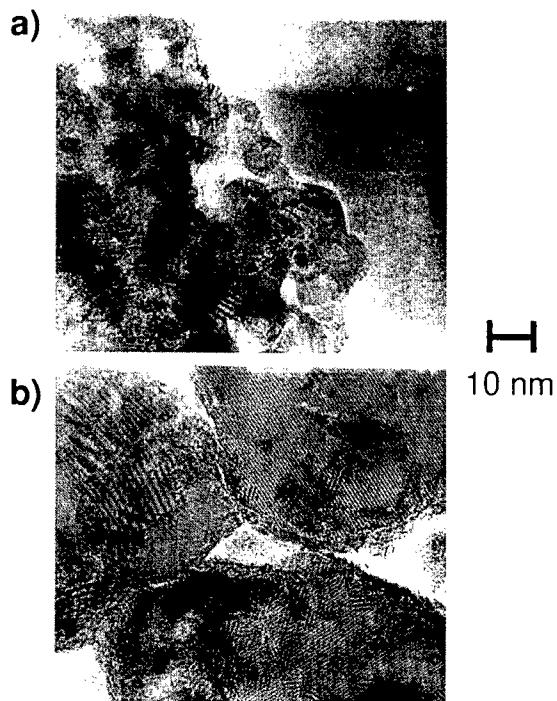
Fig. 4. TEM image of the nano-crystalline CaF_2 powder: (a) The 'freshly prepared' sample exhibits a small grain size and only little pores, (b) The 'annealed' sample (at 870 K for 90 min) shows larger grain sizes (d_{grain} >50 nm) and the formation of large pores.

References

[1] Y.-M. Chiang, J. Electroceramics 3 (1997) 205.
[2] H.L. Tuller, J. Electroceramics 3 (1997) 211.
[3] Y.-M. Chiang, E.B. Chiang, I. Lavik, H. Kosacki, H.L. Tuller, J. Electroceramics 1 (1997) 7.
[4] J.-S. Lee, J. Maier, Solid State Ionics 131 (2000).
[5] J. Maier, Solid State Ionics 23 (1987) 59.
[6] Y. Saito, J. Maier, J. Electrochem. Soc. 142 (1995) 3078.

[7] W. Puin, P. Heitjans, W. Dickenscheid, H. Gleiter, in: O. Kanert, J.-M. Spaeth (Eds.), Defects in Insulating Materials, World Scientific, Singapore, 1993, p. 137.

[8] P. Heitjans, A. Schirmer, in: J. Kärger, P. Heitjans, R. Haberlandt (Eds.), Diffusion in Condensed Matter, Vieweg, Wiesbaden, 1998, p. 116.

[9] D. Bork, P. Heitjans, J. Phys. Chem. B 102 (1998) 7303.

[10] W. Puin, P. Heitjans, NanoStructured Mater. 6 (1995) 885.

[11] J. Maier, Ber. Bunsenges. Phys. Chem. 90 (1986) 26.

[12] J. Fleig, J. Maier, J. Electrochem. Soc. 145 (1998) 2081.

[13] J.E. Bauerle, J. Phys. Chem. Solids 30 (1969) 2657.

[14] J. Fleig, J. Maier, in this issue

[15] J. Maier, Prog. Solid State Chem. 23 (1995) 171.

[16] J. Maier, J. Electrochem. Soc. 134 (1987) 1524.

[17] J. Maier, S. Prill, B. Reichert, Solid State Ionics 28–30 (1988) 1465.

[18] U. Lauer, J. Maier, Sensors and Actuators B2 (1990) 125.

[19] K. Hariharan, J. Maier, J. Electrochem. Soc. 142 (1995) 3469.

Potentiometrical investigations of nanocrystalline copper

Ch.P. Gräf, U. Heim, G. Schwitzgebel*

FB11.3 Physical Chemistry, Saarland University, 66041 Saarbrücken, Germany

Abstract

Various samples of nanocrystalline copper have been investigated as electrodes in acid $CuSO_4$ solutions, with the objective of examining growth and relaxation processes by studying the time dependence of the potential E. During the dissolution of Cu_2O the disproportionation of Cu^+ ions and the formation of nanocrystalline copper was detected in the $E(t)$ curve. A simple model for estimating the surface relaxation according to the Gibbs–Wulff theorem was applied to crystals with shapes varying between cube and octahedron. When the edge atoms are included in the energetic calculations, the excess surface energy becomes dependent on the size of the crystals. Surface relaxation then interferes with crystal growing. In agreement with these results, no separate time region of relaxation could be found for the $E(t)$ of nanocrystalline copper. It was shown that the accurate measurement of electrode potentials of copper requires attention to the specific electrochemical properties of copper, above all its extreme sensitivity to O_2 traces. A simple procedure has been developed for trapping O_2 in the cell and monitoring its absence electrochemically. © 2000 Elsevier Science B.V. All rights reserved.

Keywords: Nanocrystalline copper electrodes; Cu growth and relaxation; Surface energy calculation

1. Introduction

The surface Gibbs energy of small particles increases with decreasing diameter for a constant amount of substance. This excess free energy, ΔG_{GT}^{ex}, is the driving force for recrystallization of the growing of particles at the expense of smaller ones. The degree of the non-equilibrium state can be determined by ΔG_{GT}^{ex}, e.g.: in the case of small liquid droplets as the excess vapour pressure (Gibbs–Thomson) and in the case of small solid particles or nanocrystalline samples in contact with appropriate

ionic conductors by measuring the excess EMF, ΔE^{ex} [1–4]. In these techniques there is an active exchange of atoms or molecules between the liquid and the gas phase or of atoms or ions between the solid and ion-conducting phase. This means that the local exchange equilibrium, and thus the measurement, is not or not markedly influenced by the global non-equilibrium.

Another type of non-equilibrium (ΔG_{GW}^{ex}) has to be taken into account in the case of crystals. The Gibbs–Wulff theorem states that the equilibrium shape of a free crystal is characterized by a minimum of free surface energy, which requires constancy of the fractions σ_i/h_i for all faces of the crystal (σ_i: specific free surface energy of face i; h_i: vertical distance from the Wulff centre). Faces of different σ_i of a metal crystal should exhibit different electrode

*Corresponding author. Tel.: +49-681-302-2913; fax: +49-681-302-4833.

E-mail address: g.schwitzgebel@rz.uni-sb.de (G. Schwitzgebel)

potentials, E_i, when in electrochemical exchange with a ion conducting phase. But this has never been proved unequivocally and probably it cannot be proved, because no defined reversible electrode potential exists on a defect-free face of a single crystal of macroscopic dimensions (>100 μm^2) [5]. The measurement process itself is based on the presence of defects – ad-atoms, steps, kinks and screw dislocations – but there is no guarantee that new face types do not appear when steps degenerate.

A better chance for indirect evidence of E_i differences can be expected from investigations of nanocrystalline metals, which are normally prepared in non-equilibrium shapes. Since ΔG_{GW}^{ex} like ΔG_{GT}^{ex} is inversely proportional to the particle diameter (Section 2.3), differences in E_i will be magnified according to the same proportionality. The fraction of edge atoms increases even more greatly, so that the measuring process is facilitated. Thus, the process of equilibration of the shape of crystals, which we call surface relaxation, is in principle superimposed on the growth process and it is an interesting question, if it can be detected by EMF or other phenomenological measurements, e.g. calorimetry [6,7].

The literature on recrystallization in contact with a neighbouring phase only seldom refers the Ostwald ripening [8]. One example of a quantitative time law of EMF change has been published [1], but there are more examples of qualitative observations [9–11]. Relaxation under the influence of stored excess free energy of strain, ΔG_s^{ex}, is a general phenomenon in solid state science, which has often been supposed to be also detectable and determinable potentiometrically [13–15].

Kinetic laws of relaxation have not been studied by EMF techniques hitherto. Some features of $\Delta E^{ex}(t)$ curves in our previous work on nanocrystalline copper (Cu_{nc}) [12] seemed to suggest relaxation effects. However, because of the peculiarities of the two-step electrode reaction of Cu and its extreme sensitivity against O_2, other interpretations must be taken into account. Therefore one of the objectives of this work was to scrutinize $\Delta E^{ex}(t)$ curves. The other was to treat surface relaxation from a very simplified point of view, in order to foresee how this type of relaxation could proceed.

2. Theory

2.1. Excess EMF of nanocrystalline metals

The Gibbs energy change of a chemical reaction, $\Delta_R G$, can be determined in a electrochemical cell, if this reaction is the cell reaction and if the electrode reactions with the electrolyte are reversible.

$$\Delta_R G = - z_e F \Delta E \tag{1}$$

In the specific cell,

$$M_{nc} / \text{solution with } M^{z+} / M_{mc}, \tag{2}$$

the metal in its microcrystalline state M_{mc} is in equilibrium with metal ions M^{z+},

$$M^{z+} + z_+ e^- = M_{mc} \text{ (right side)} \tag{3}$$

(z_+: charge number). A similar equilibrium is supposed for the nanocrystalline metal M_{nc},

$$M^{z+} + z_+ e^- = M_{nc} \text{ (left side)} \tag{4}$$

so that the cell reaction is given by

$$M_{nc} \rightarrow M_{mc} \tag{5}$$

and its EMF by

$$\Delta E^{ex} = E_{mc} - E_{nc}. \tag{6}$$

With Eq. (1) one obtains (F: Faraday constant)

$$- \Delta_R G = \Delta G^{ex} = z_e F \Delta E^{ex}. \tag{7}$$

In general ΔG^{ex} can be made up from different non-equilibrium contributions.

$$\Delta_R G^{ex} = \Delta G_{GT}^{ex} + \Delta G_s^{ex} + \Delta G_{GW}^{ex} \tag{8}$$

A generalized Gibbs–Thomson equation,

$$\Delta G_{GT} = g \, \sigma V_M / \bar{r} \tag{9}$$

($\bar{r}$: mean radius; σ: specific interfacial energy; V_M: molar volume of M; g: geometrical factor of the order of 1, describing the shape of the particles) is valid for the excess surface free energy ΔG_{GT}^{ex} [16]. The excess free energy of strain ΔG_s^{ex} has been calculated using the micro strain ϵ and mechanical stress laws [3,15] and for ΔG_{GW} an exemplary estimation will be given below (Section 2.3).

2.2. Grain growth

An increase of $\bar{r}$, i.e. grain growth, lowers the Gibbs energy ΔG_{GT}^{ex} of an assembly of crystals. The literature on this phenomenon is enormous [17], but one must distinguish between several types of growth. The growth of M_{nc} crystals in contact with a solution, which exchanges ions with the metal, is more than one order of magnitude faster than intrinsic grain growth [3]. Furthermore, this contact growth may proceed conservatively, i.e. all material which dissolves (from smaller crystals) is deposited on bigger ones, or non-conservatively, when material is lost into the solution by corrosion. All forced growth processes, induced by electrochemical deposition techniques [18], are also non-conservative.

The early results of Wagner [8] on contact growth of free spherical particles (Ostwald ripening) have been confirmed for surface layers [19]. Diffusion control of the elementary steps leads to

$$\bar{r}(t) = r_0 \left(1 - \gamma_d t\right)^{-1/3} \tag{10}$$

and reaction control to

$$\bar{r}(t) = r_0 \left(1 - \gamma_r t\right)^{-1/2} \tag{11}$$

where γ_i contains informations about the grain size distribution. With different meanings of γ_i the time laws of Eqs. (10) and (11) can also be derived in the case of non-conservative growth. But this condition has not yet been treated exhaustively and other time laws may exist [19].

Eqs. (10) and (11) can be combined with Eq. (9). With Eq. (11) for instance, one obtains

$$\Delta E^{ex} = \left(\gamma + \gamma' t\right)^{-1/2} \tag{12}$$

which has been found for Ag_{nc} in Ag^{+} complex solutions [1].

2.3. Surface relaxation

In his derivation of growth laws Wagner [8] explicitly starts from particle shapes, which are already in the Gibbs–Wulff equilibrium. For an approximate estimation of surface energy differences, we may consider fcc crystals composed of only two types of planes (100) and (111), i.e. the

cube, the octahedron and the mixed forms which are predominant for Cu [20]. The shape of the crystals can be described by normal distances of the planes from the centre, r_{100} and r_{111}, or by a single parameter α, defined in Eq. (13).

$$\alpha = r_{111}/r_{100} \sqrt{3}\,(\text{cube}) \ge \alpha \ge 1/\sqrt{3}\,(\text{octahedron}) \tag{13}$$

According to the simplest model [21], the surface energy per surface atom is the sum of the energies of the free bonds. The bond energy for closed-packed metals, ι, comes from the sublimation energy, $\Delta_s U$ (N_A: Avogadro number)

$$\psi = \Delta_s U / 6 N_A \tag{14}$$

The specific surface energies (σ_{100} and σ_{111}) are obtained by reference to the surface area using the atomic radius r_a

$$\sigma_{111} = \psi \sqrt{3}/2\, r_a^2 \tag{15a}$$

$$\sigma_{100} = \psi/r_a^2 \tag{15b}$$

Neglecting entropic and volume contributions ($G \cong U$), the molar excess Gibbs energy of the surface is written in the form of

$$\Delta G_{GW}^{ex} = (M\,\Delta_s H/N_A\, \rho\, r_a^2\, r_s)\,\{f(\alpha) + r_a\, k(\alpha)/r_s\} \tag{16}$$

(M: molar mass; ρ: density; r_s: radius of a sphere with identical volume).

The functions $f(\alpha)$ and $k(\alpha)$ contain geometrical terms for the calculation of the surface and of the edge length (see Appendix A). The expression in braces of Eq. (16) (see Fig. 1) exhibits a minimum at $\alpha = 0.145$ for $f(\alpha)$ (neglecting edge atoms) and a small shift of this minimum for decreasing crystal size. This minimum corresponds to the Gibbs–Wulff equilibrium shape with minimal surface energy.

With Eq. (16) the energetic difference between high (non-equilibrium) and low energy (relaxed) crystals and with Eq. (7) the excess EMF can be calculated. Taking the maximal differences on the ordinate of Fig. 1 between a macroscopic single crystal ($r_s = 1$ mm) and a nanocrystal ($r_s = 20$ nm), one obtains
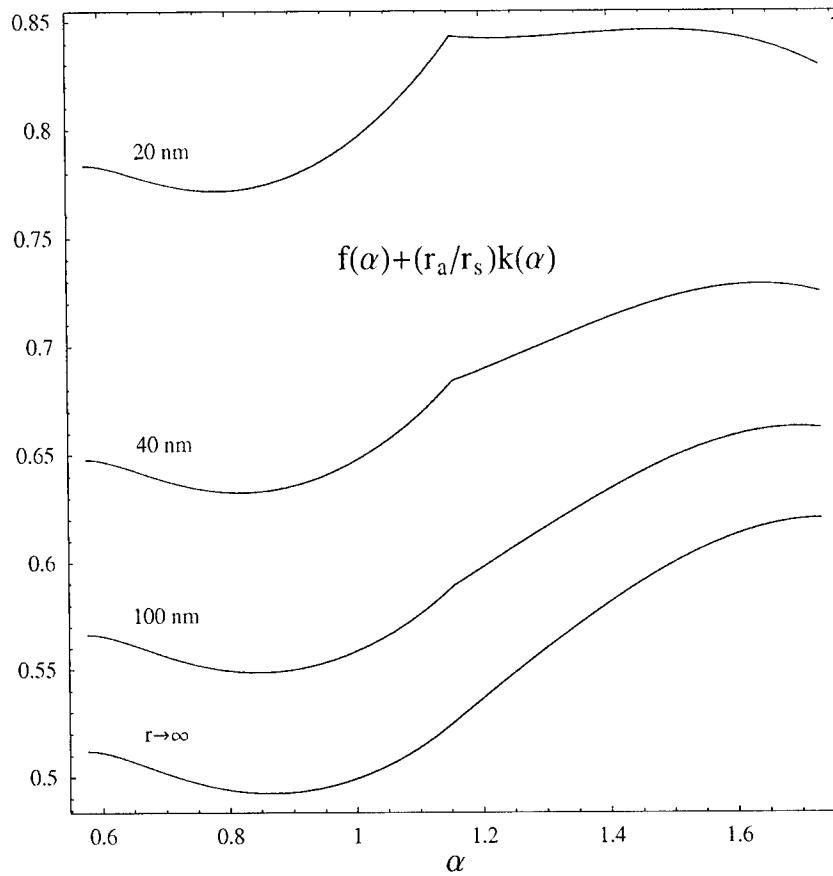
Fig. 1. Shape-dependent factor of molar Gibbs–Wulff energy ΔG_{GW}^{ex} (cf. Eq. (16)).

$\Delta U_{GW}^{ex}(1 \text{ mm}) \approx 3 \text{ mJ mol}^{-1}$ $\Delta U_{GW}^{ex}(20 \text{ nm}) \approx 1 \text{ kJ mol}^{-1}$

$\Delta E_{GW}^{ex} \approx 16 \text{ nV}$ $\Delta E_{GW}^{ex} \approx 5 \text{ mV}$

In principle these quantities are in a measurable range for nanocrystals, but they can rarely be distinguished from other excess energies.

Another interesting fact is that when edge energy is included, nanocrystals ($r_s = 20$ nm) with α values between $\sqrt{3}$ (cube) and $2/\sqrt{3}$ (cubooctahedron) have nearly constant surface energies and might be rather stable towards small fluctuations, whereas relaxation in the region $1/\sqrt{3}$ (octahedron)$\geq \alpha \geq 2/\sqrt{3}$ always ends in the minimum.

With the assumption that the relaxation kinetics $d\alpha/dt$ is driven by the gradient of ΔG_{GW}^{ex},

$$d\alpha/dt = -k'(\partial \Delta G_{GW}^{ex}(\alpha)/\partial \alpha)_{r_s = const} \qquad (17)$$

it is easy to see that the rate law not only depends on the starting point α, but also on the size of r_s of the crystal. Relaxation of shapes between cube and cubooctahedron will only begin when $\partial \Delta G_{GW}^{ex}/\partial \alpha > 0$ i.e. when r_s will have grown over 20 nm. The important consequence is that relaxation is coupled with growing. Our treatment is simplified and only approximate, because for polycrystalline materials the shape equilibrium must in principle be discussed according to the Gibbs–Wulff–Kaischew theorem (c.f. [18] p. 152) and because in the solution the specific surface energy must be replaced by the interfacial energy. Nevertheless, one can conclude (even from Fig. 1) that there is no simple and characteristic time law for surface relaxation processes. The kinetics of a whole assembly of nanocrystals can not be predicted, which means that a direct experimental detection is not possible. Its

measurement would require that other equilibrium processes are excluded.

2.4. Electrochemistry of copper

Fig. 2 summarizes in a simplified scheme the processes occurring at a Cu electrode in a solution with Cu ions. It is well known that the Cu oxidation follows a two-step mechanism,

$$Cu^+ + e^- = Cu$$

$$E_I = E_I^0 + (RT/F) \ln[a(Cu^+)/a(Cu)] \tag{I}$$

$$Cu^{2+} + e^- = Cu^+$$

$$E_{II} = E_{II}^0 + (RT/F) \ln[a(Cu^{2+})/a(Cu^+)] \tag{II}$$
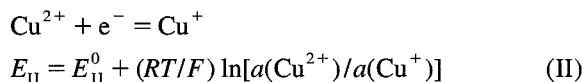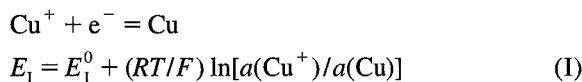
in which the exchange current of electrode reaction (I) is orders of magnitude higher than that of reaction (II). In the electrochemical equilibrium the electrode potentials E_I and E_{II} are equal, so that the chemical reaction of Cu^+ disproportionation (III) is also in equilibrium.

$$2Cu^+ = Cu^{2+} + Cu$$

$$K = a(Cu^{2+}) a(Cu)/a(Cu^+)^2$$

$$= 2 \times 10^6 \, l \, mol^{-1} \tag{III}$$
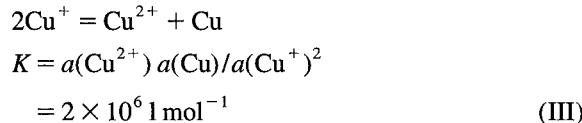
This equilibrium can easily be disturbed by traces of oxygen, which oxidize Cu^+ (see Fig. 2). Then, the backward displacement of reaction (III) leads to a (positive) open circuit overvoltage [22], i.e. a corrosion potential is measured.

From electrode kinetics it has been concluded that in Eq. (I) Cu probably reacts mainly out of step positions (Cu_{step}) rather than as ad-atom (Cu_{ad}) [23]. Then it is easily understandable that the exchange

current of reaction (I) has been found to be more than five times higher for Cu_{nc} than for Cu_{mc} [21], because the surface density of step atoms increases with decreasing crystal size. The electrode potential $E(Cu_{nc})$ is more negative than $E(Cu_{mc})$, so that ΔE^{ex} in Eq. (6) is positive. The Nernst equations (I) and (II) are applied by expressing ΔG^{ex} as

$$a^*(Cu) = a(Cu_{nc}) = \exp(-\Delta G^{ex}/RT) \tag{18}$$

using an activity $a^* > 1$ for Cu_{nc}. In the local equilibrium between Cu_{nc} and the ions Cu^+ and Cu^{2+}, Eq. (II) shows that $a^*(Cu^+)$ in contact with Cu_{nc} will be enhanced, whereas $a(Cu^{2+})$ is normally fixed by the Cu(II) salt contained in the solution.

The local equilibrium will not be established if $a(Cu^+) \neq a^*(Cu^+)$, for instance in the presence of O_2 traces: $a(Cu^+) < a^*(Cu^+)$ (see above). The same inequality arises when normal Cu_{mc} and Cu_{nc} are present in the same solution. In the case of large surfaces of Cu_{mc} this metallic state will impose its $a(Cu^+)$ value on Cu_{nc}, so that reaction (III) is reversed, which means that Cu^{2+} oxidizes Cu_{nc}. Therefore, it is necessary to measure $E(Cu_{mc})$ and $E(Cu_{nc})$ separately against an inert reference electrode and to subtract the values according to Eq. (6). The converse situation must arise, when Cu_2O is added to an acid copper salt solution. The oxide dissolves and $a(Cu^+)$ reaches values even higher than in contact with Cu_{nc}. Then reaction (III) proceeds in the forward direction, meanwhile $E_I = E_{II}$ can no longer be valid. Reaction (I) will then determine the potential because of its higher exchange current.

3. Experimental

The cells were totally made of glass, so that a N_2 gas flow which had only contact with glass could be passed through the cell or short-circuited by two three-way valves, completely sealing the cell under a standing N_2 atmosphere. The covers were designed for at least four electrodes, which could be immersed in or taken out of the cell solution. A magnetic device could be fixed to the cover, in order to pour small quantities of Cu_2O into the solution without opening the cell.

Fig. 2. Simplified scheme of the electrode processes on copper.
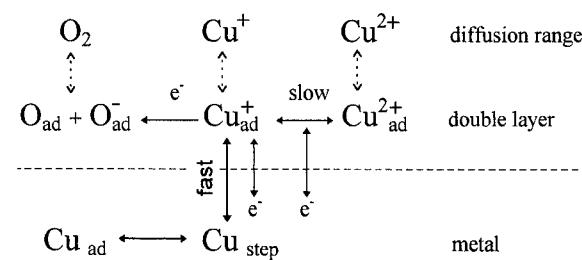
Cu_{nc} samples were prepared by inert-gas con-
densation [24]. Electrodes consisted of manually
broken pieces of the Cu_{nc} tablets, coming from the
preparation apparatus. Contacts to the electrode leads
consisted of a conducting silver lacquer (Conrad)
and an insulation of picein wax (Roth). Commercial
Cu wire (99.99%), pre-treated by electrochemical
polishing, was used for Cu_{mc} electrodes. Blank Pt
electrodes were wires or small foil strips and cleaned
in a H_2 flame. A $Hg/HgSO_4$ electrode with a
diaphragm, but filled with the cell solution, was used
as reference electrode. Its potential referred to NHE
is not exactly known (~0.65 V), so our results are
referred to this reference electrode, i.e. they are
reported as the (negative) EMF values of the cell
$Hg/HgSO_4$, H_2SO_4, $CuSO_4/Cu$.

The cell solutions were 0.5 M $CuSO_4$ in 0.5 M
H_2SO_4 or 0.1 M $CuSO_4$ in 0.05 M H_2SO_4 (all
analytical purity grade) in bidistilled water. For some
purposes Cu powder (99.99%) was added to the
solutions.

The grain size of the Cu_{nc} was determined from
XRD (Siemens D500) patterns. The (111) and (222)
reflections were used for the peak analysis. The
area-weighted mean diameter and the average micro

strain $\bar{\varepsilon}$ were obtained by a Warren–Averbach
evaluation, assuming spherical grain shape and log-
normal size distribution [25]. The cell voltages were
measured using computer-controlled electrometers
(Bank, Prema).

4. Results and discussion

Three types of experiments were performed in
order to study the changes in the EMF of cells with
Cu_{nc} electrodes: They differ with respect to their
closeness to the conditions of the local equilibrium.

When nitrogen (99.996%) was used for protection
against oxygen, it was found that a small but
reproducible corrosion of copper occurred, which
shifted the electrical potentials of Cu_{mc} by about 10
mV in the positive direction, whereas Cu_{nc} is less
affected, the effect decreasing with grain size e.g.
with =4 nm no shift at all was detected. This
behaviour is a consequence of the higher exchange
current density of Cu_{nc} [22]. Two EMF curves of
different Cu_{nc} samples under the slight O_2 corrosion
(streaming N_2) were compared with the time law of
Eq. (12) (Fig. 3). The comparison must be restricted
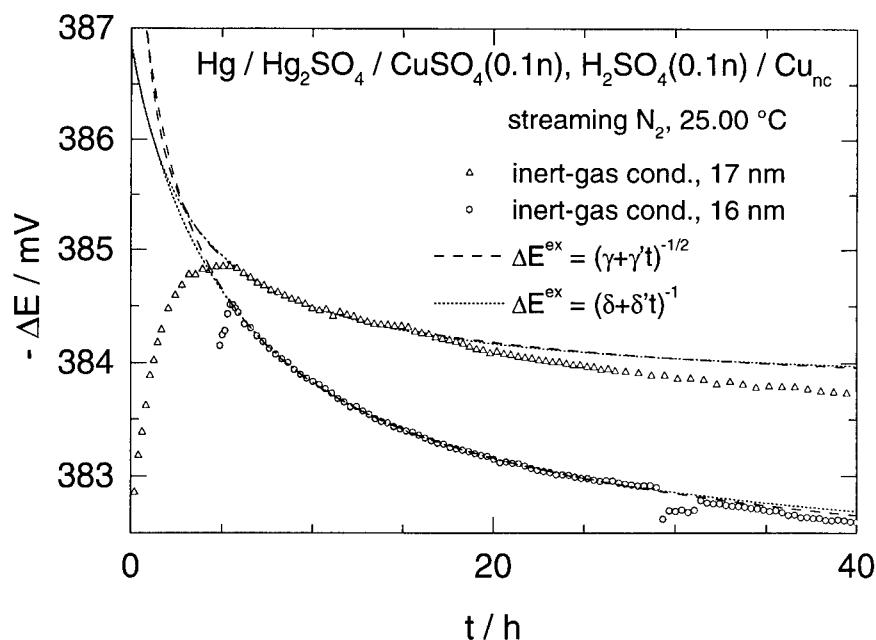
Fig. 3. Electrodes of nanocrystalline copper under slow corrosion by O_2.

to 5 h$<t<$15 h for sample 1, and to $t<$24 h for sample 2 because of some typical irregularities (cf. Section 5). The extrapolation with Eq. (12) to $t=0$ yields ΔE^{ex} values not fulfilling Eq. (9), which has been well corroborated with many Cu_{nc} samples of various sizes [3]. An extrapolation using the empirical law $\Delta E^{ex}=f(t^{-1})$ gives results which fit Eq. (9).

An example of the second type of experiments is shown in Fig. 4. Here the solution in the closed cell was completely freed from O_2 by Cu powder and the Cu_{nc} electrode was immersed thereafter. A comparatively fast change of the EMF was found with a very good global fulfillment of Eq. (12), although short regions of enhanced deviations occur (Section 5).

Traces of oxygen could also be completely removed over a long period by the action of the Cu_{mc} electrode itself (Fig. 5). The best proof of the absence of corrosion is the equality of the potential, measured at Cu_{mc}, and at Pt. When the Cu_{nc} electrode was dipped in the solution (tilting of the cell) and Cu_{mc} taken out of the solution, the potentials of Cu_{nc} (E_I) and Pt (E_{II}) decreased, but in a diverging manner. The explanation – according to the Nernst Eq. (I) E_I should increase with $a(Cu^+)$, when Cu_{mc} is exchanged by Cu_{nc} – will be given in Section 4.

Another obvious peculiarity is that during the first hour two different processes are occurring at the Cu_{nc} electrode, where the faster one produces a short minimum in the curve, which is reproducible within slight variations of shape. We were able to show that both effects were caused by the dissolution of the Cu_2O, which had formed at the surface of Cu_{nc} since the time of its preparation (see below).

When a small quantity of Cu_2O was added to the stirred O_2-free cell solution, the electrical potentials of Cu_{mc} and Pt electrodes changed significantly (Fig. 6). A sharp minimum appeared followed by a flat maximum and a rather slow decrease afterwards. A certain quantity of Cu_2O remains undissolved, mixed with Cu_{nc} nanocrystals ($\geq$20 nm). It has long been known, that Cu_2O reacts in sulphuric acid to Cu^{2+} ions and Cu_{nc} with intermediate formation of Cu^+ ions. However, the mechanism has never been studied in detail. From our experiments we deduce that Cu_{nc} forms at least partially at the metal surfaces of both electrodes, Cu_{mc} and Pt, but probably more rapidly at Cu_{mc}, which would explain the deviations in the time range 142.5 h$<t<$144 h. The size of these crystals just grown over the state of nuclei yields large ΔG_{GT}^{ex} and (negative) ΔE^{ex} values, but it
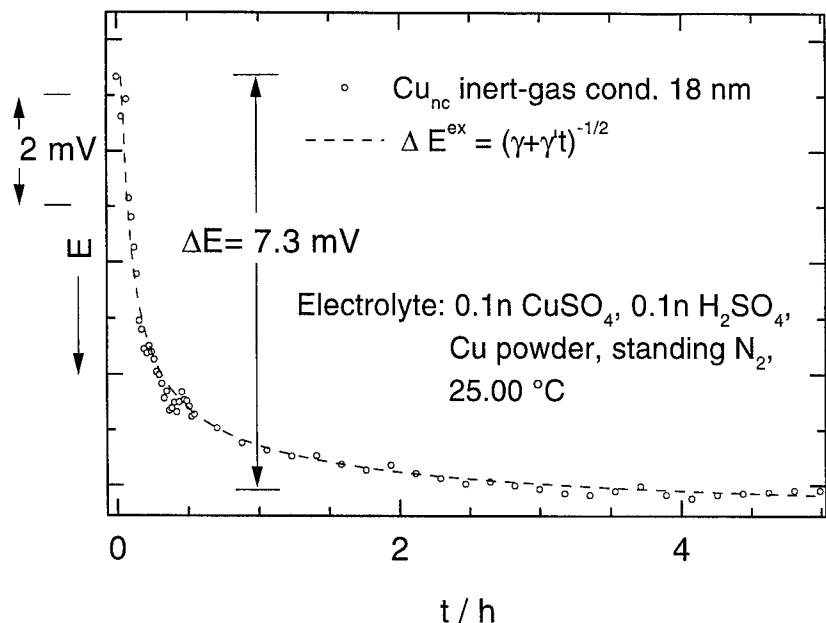

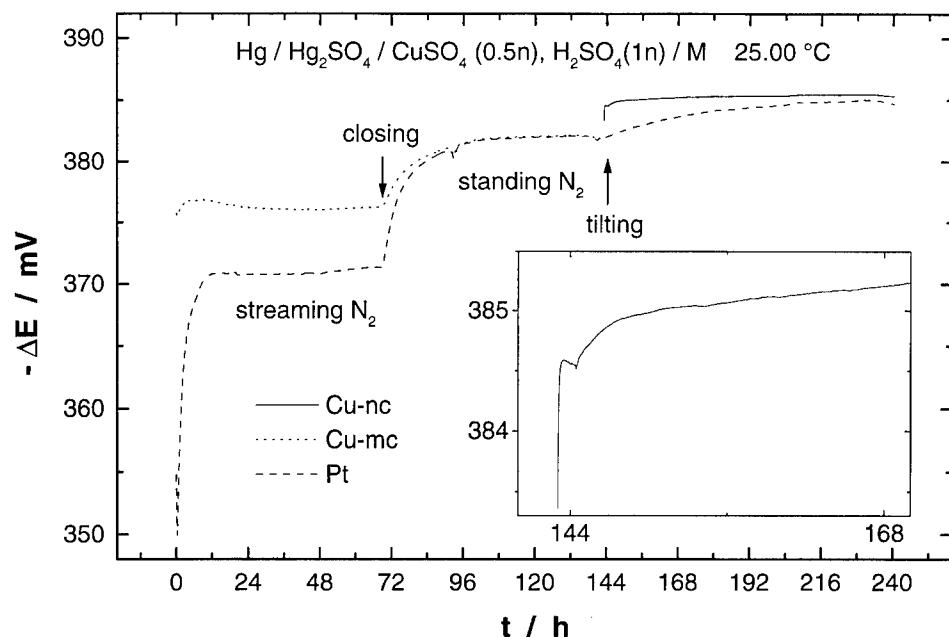Fig. 4. Electrode of nanocrystalline copper corroded by Cu^{2+} ions.

Fig. 5. Electrodes of Pt, micro- and nanocrystalline (r=45 nm) copper in a tiltable cell. N_2 contains 40 ppm O_2; in the closed cell O_2 is trapped by Cu_{mc}; by tilting Cu_{mc} is pulled out and Cu_{nc} dipped into the solution.
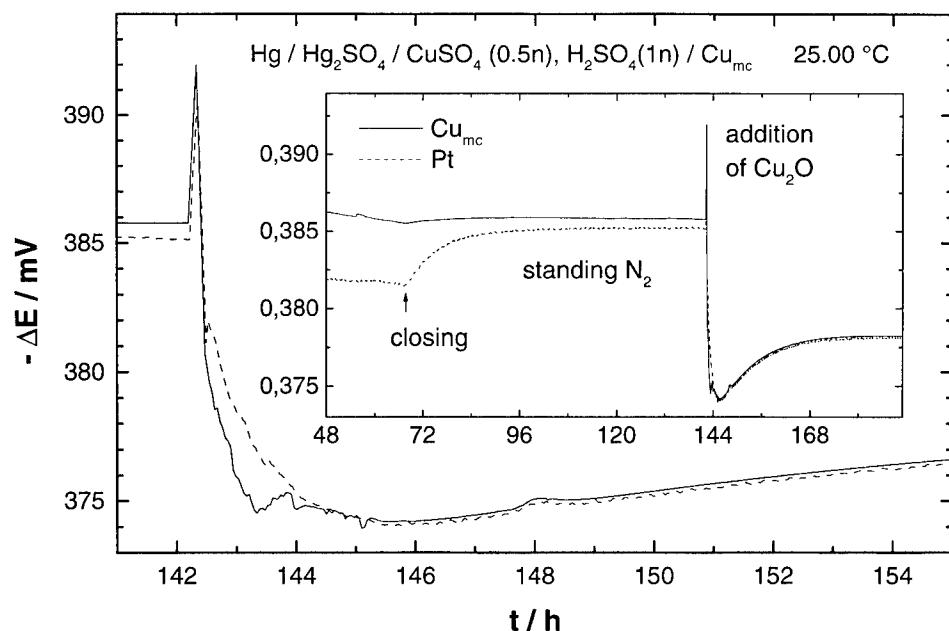

Fig. 6. Potentiometric study of the dissolution of 0.4 mg Cu_2O in 45 ml of the solution.

entails fast growth. The potential rises to a flat maximum determined by the superelevated Cu^+ ion concentration. The following decrease of ΔE^{ex} could be well described by a 1st order rate law in accordance with a catalytic decay of Cu^+ on the metallic surfaces. (Further EMF and kinetic studies on the Cu^+ disproportionation are underway). The same reaction order was found for the increase of the potential of the Pt electrode after the immersion of Cu_{nc} in Fig. 5. Obviously the small minimum in this Cu_{nc} curve is due to a slight reactive deposition of supplementary Cu_{nc} on Cu_{nc} and the following decrease of both potentials, of Cu_{nc} and Pt, by the Cu^+ diproportionation.

5. Conclusion

In the experiments without any corrosion, for which Fig. 6 gives an example, there is only one identifiable operative process: The initial dissolution of Cu_2O, which induces the decomposition of Cu^+. Over a period of nearly 100 h the Cu_{nc} curve shows no other marked phenomena than small fluctuation (<0.1 mV), best seen in the inlet of Fig. 6. No relaxation of any type can be observed. When slow corrosion processes are active, either by O_2 (Fig. 3) or by Cu^{2+} (Fig. 4), short positive (1 mV) deviations from the elsewhere smooth $E(t)$ courses appeared after irregular time intervals. Sometimes they were accompanied by similar features of the Pt potential (not shown in Figs. 4 and 5), which means that Cu_2O particles had been liberated in the nanocrystalline electrode, with a subsequent change of the Cu^+ concentration. The irregular course was only visible in the Cu_{nc} potential in few cases. Then it can be concluded that relaxation takes place, but until now no distinction between surface or strain relaxation is possible. These negative results are not in contrast to the theoretical considerations, which showed that no general time dependence and no prediction of the time of appearence can be expected for surface relaxation.

On the other hand, we demonstrated by this work that under total exclusion of O_2, which can be reached by trapping it within the cell, potentials of Cu_{mc} and Cu_{nc} can be measured with satisfactory precision. Therefore it would be possible and interesting to repeat some of the experiments with other types of Cu_{nc} (e.g. electrodeposition, ball-milling).

Appendix A

The molar free surface energy ΔG_{GW}^{ex} is composed of the contributions from the two types (i) of surfaces $\sigma_i\, A_i(\alpha, r_s)$, where the total area A_i of the type i depends on the spherical shape α and the effective spherical radius r_s, and of the three types (j) of edges $\kappa_j\, L_j(\alpha, r_s)$, where κ_j stands for the specific edge energy ($\kappa_{111/100}$, $\kappa_{111/111}$, $\kappa_{100/100}$) and L_j for the total length of the edge type. After referring these contributions to the amount of the crystal (V: its volume) a transformation of Eq. (14) leads to Eq. (16), where $f(\alpha)$ and $k(\alpha)$ are given by Eq. (A.2) and Eq. (A.3).

$$\Delta G_{GW} = M\,\{\sum_i \sigma_i A_i(\alpha, r_s) + \sum_j \kappa_j L_j(\alpha, r_s)\}/V(r_s)\,\rho \tag{A.1}$$

$$f(\alpha) = \begin{cases} \dfrac{3^{1/3}}{4\pi^{1/3}}\dfrac{-5 + 2\,3^{3/2}\,\alpha - 3\alpha^2}{(-7 + 3^{5/2}\,\alpha - 9\alpha^2 + 3^{1/2}\alpha^3)^{2/3}} & \sqrt{3} \geq \alpha \geq \dfrac{2}{\sqrt{3}} \\[2ex] \dfrac{3^{1/3}}{4\pi^{1/3}}\dfrac{-1 = 2\,3^{1/2}\,\alpha}{(1 - 3^{3/2}\,\alpha + 9\alpha - 2\,3^{1/2}\alpha^3)^{2/3}} & \dfrac{2}{\sqrt{3}} \geq \alpha \geq \dfrac{1}{\sqrt{3}} \end{cases} \tag{A.2}$$

$$k(\alpha) = \begin{cases} \dfrac{30\,6^{1/2}\,\alpha}{(3^{3/2}\alpha^3 - (3^{1/2}\alpha - 1)^3)^{1/3}} & \sqrt{3} \geq \alpha \geq \dfrac{2}{\sqrt{3}} \\[2ex] \dfrac{96\,2^{1/2} + 18\,6^{1/2}\,\alpha}{(6 - (3 - 3^{1/2}\alpha)^3)^{1/3}} & \dfrac{2}{\sqrt{3}} \geq \alpha \geq \dfrac{1}{\sqrt{3}} \end{cases} \tag{A.3}$$

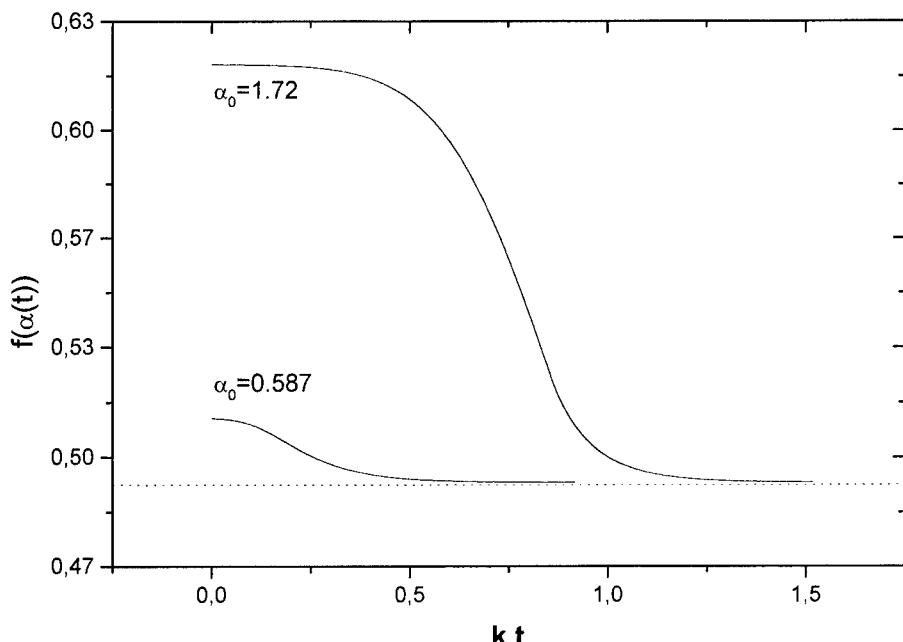When Eq. (17) is valid for the relaxation kinetics one obtains $\alpha(t)$ by numerical integration of Eq. (A.4).

Fig. 7. Factor $f(\alpha(t))$ as a measure of surface energy in its time dependence; starting near cube: $\alpha_0 = 1.72$; starting near octahedron: $\alpha_0 = 0.587$.

$$\mathrm{d}\alpha/\mathrm{d}t = -k'\,(\partial\Delta G_s(\alpha)/\partial\alpha)_{r_s=\mathrm{const}}$$

$$= -k\,\partial\{f(\alpha) + r_a k(\alpha)/r_s\}/\partial\alpha \qquad (A.4)$$

$$\int_{\alpha_o}^{a(t)} \frac{\mathrm{d}\alpha}{\partial\{f(\alpha) + r_a k(\alpha)/r_s\}/\partial\alpha} = -kt \qquad (A.5)$$

Then $\Delta G_{GW}^{ex}(t)$ can be calculated. As an example we plot in Fig. 7 the factor $f(\alpha(t))$, which determines the rate for $r_s > 100$ nm.

References

[1] S. Villain, P. Knauth, G. Schwitzgebel, Phys. Chem. B101 (1997) 7452.

[2] P. Knauth, G. Schwitzgebel, A. Tschöpe, S. Villain, J. Solid State Chem. 140 (1998) 295.

[3] U. Heim, G. Schwitzgebel, Nanostruct. Mater. 12 (1999) 19.

[4] G. Schwitzgebel, R. Mildenberger, Ber. Bunsenges. Phys. Chem. 101 (1997) 1742.

[5] E. Budevski, V. Bostanov, Electrochim. Acta 9 (1964) 477.

[6] J. Rupp, R. Birringer, Phys. Rev. B36 (1987) 7888.

[7] K.-St. Werkmeister, F. Rullang, M. Koch, M. Heyer, G. Schwitzgebel, Nanostruct. Mater. 12 (1999) 229.

[8] C. Wagner, Z. Elektrochem. 65 (1961) 581.

[9] D. Henning, K.G. Weil, Ber. Bunsenges. Phys. Chem. 82 (1978) 265.

[10] F. Gärtner, R. Bormann, R. Birringer, A. Tschöpe, Scripta Mater. 35 (1996) 805.

[11] U. Heim, Thesis, Saarbrücken, 2000.

[12] C.P. Gräf, Diploma Work, Saarbrücken, 1998.

[13] G. Schwitzgebel, Z. phys. Chem. NF 95 (1975) 15.

[14] G.B. Rais, M.J. Bromberg, E.M. Gugel, Fizika Tverdogo Tela 8 (1966) 3700.

[15] D. Lewis, C.E. Pearce, Electrochim. Acta 16 (1971) 747.

[16] L.E. Chen, F. Spaepen, J. Appl. Phys. 69 (1991) 689.

[17] F.J. Humphreys, M. Hatherly, Recrystallization and Related Annealing Phenomena, Pergamon (Elsevier Science Ltd), Oxford, 1996.

[18] E. Budevski, G. Staikov, W.J. Lorenz, Electrochemical Phase Formation and Growth, Wiley, Weinheim-New York, 1996.

[19] B.K. Chakraverty, J. Phys. Chem. Solids 28 (1967) 2401.

[20] B. Honigmann, Gleichgewichts- und Wachstumsformen von Kristallen, Steinkopf Verlag, Darmstadt, 1958.

[21] W. Romanowski, Surface Science 18 (1969) 373.

[22] C.P. Gräf, U. Heim, G. Schwitzgebel, in preparation

[23] A. De Agostini, E. Schmidt, W.J. Lorenz, Electrochim. Acta 34 (1989) 1243.

[24] H. Gleiter, Phase Transition 24 (1990) 15.

[25] H. Natter, R. Hempelmann, Ber. Bunsenges. Phys. Chem. 100 (1996) 55.

Zeolites and catalysis

Jens Weitkamp*

Institute of Chemical Technology, University of Stuttgart, D-70550 Stuttgart, Germany

Abstract

This review covers the fundamentals of zeolite materials science and their application as catalysts. After a brief introduction into their structures, the most important parameters are discussed which allow the preparation of an almost infinite variety of zeolitic materials tailored for a given catalytic application. Zeolites are solid acids, and the chemical nature, the density, strength and location of the acid sites in zeolites are discussed. Shape-selective catalysis, which is a unique feature of zeolites, is briefly addressed. © 2000 Elsevier Science B.V. All rights reserved.

Keywords: Zeolites; Catalysis; Microporous materials; Mesoporous materials; Acidity of solids; Shape-selective catalyst; Ion-exchange

1. Introduction

Zeolites occur in nature and have been known for almost 250 years as aluminosilicate minerals. Examples are faujasite, mordenite, offretite, ferrierite, erionite and chabazite. Today, these and other zeolite structures are of great interest in catalysis, yet their naturally occurring forms are of limited value, because (i) they almost always contain undesired impurity phases, (ii) their chemical composition varies from one deposit to another and even from one stratum to another in the same deposit, and (iii) nature did not optimize their properties for catalytic applications.

It was only with the advent of synthetic zeolites from ca. 1948 to 1955 (thanks, mostly, to the pioneering work of Barrer and Milton) that this class of porous materials began to play a role in catalysis. A landmark event was the introduction of synthetic faujasites (zeolites X and Y) on an industrial scale in fluid catalytic cracking (FCC) of heavy petroleum distillates in 1962, one of the most important chemical processes worldwide. The new zeolitic catalysts were not only orders of magnitude more active than the previously used amorphous silica–alumina catalysts (which enabled drastic process engineering improvements [1]), but they also brought about a significant increase in the yield of gasoline, the most valuable product from FCC plants. It can be estimated [1,2] that this yield enhancement alone resulted in an added value in the order of at least several billion US dollars per year. It has further been estimated [3] that, as a whole, the cost of petroleum refining worldwide would be higher by at least 10 billion US dollars per year, if zeolite catalysts were not available today.

In the period after 1962, zeolite catalysts rapidly conquered additional processes in the fields of

---

*Tel.: +49-711-685-4060; fax: +49-711-685-4065.

E-mail address: jens.weitkamp@po.uni-stuttgart.de (J. Weitkamp)

petroleum refining and basic petrochemistry. The most important of these processes are hydrocracking of heavy petroleum distillates [4], octane number enhancement of light gasoline by isomerization [5], the synthesis of ethylbenzene (the precursor of styrene and polystyrene) from benzene and ethene after the Mobil–Badger process [6], the disproportionation of toluene into benzene and xylenes [7] and the isomerization of xylenes (to produce *para*-xylene, the precursor chemical for terephthalic acid). In the manufacture of fine chemicals, the application of zeolite catalysts is still limited, even though their potential is considered to be very high in this area as well [8,9]. Altogether, catalysis is the single most important application of zeolites in terms of financial market size (not in terms of tonnage) with an estimated market volume around 1 billion US dollars per year [3].

This review will cover the basic principles of zeolite chemistry and catalysis. After a brief treatment of their structures, those properties of zeolites will be addressed which are of utmost importance in their use as catalysts, viz. surface acidity and shape selectivity.

2. Structures and definitions

The elementary building units of zeolites are SiO_4 and AlO_4 tetrahedra. Adjacent tetrahedra are linked at their corners via a common oxygen atom, and this results in an inorganic macromolecule with a structurally distinct three-dimensional framework. It is evident from this building principle that the net formulae of the tetrahedra are SiO_2 and AlO_2^-, i.e. one negative charge resides at each tetrahedron in the framework which has aluminum in its center. The framework of a zeolite contains channels, channel intersections and/or cages with dimensions from ca. 0.2 to 1 nm. Inside these voids are water molecules and small cations which compensate the negative framework charge. The chemical composition of a zeolite can hence be represented by a formula of the type

$$A^{m+}_{y/m}[(SiO_2)_x \cdot (AlO_2^-)_y] \cdot zH_2O \tag{1}$$
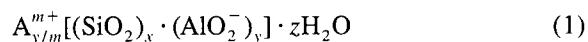
where A is a cation with the charge m, $(x+y)$ is the

number of tetrahedra per crystallographic unit cell and x/y is the so-called framework silicon/aluminum ratio n_{Si}/n_{Al} (or simply Si/Al). Löwenstein's rule [10] precludes that two contiguous tetrahedra contain aluminum on tetrahedral positions, i.e. Al–O–Al linkages are forbidden, or $n_{Si}/n_{Al} \geq 1$. Silicon and aluminum in aluminosilicate zeolites are referred to as the T-atoms.

Fig. 1 shows the structures of four selected zeolites along with their respective void systems and pore dimensions. In these commonly used representations, the T-atoms are located at the vertices, and the lines connecting them stand for T–O–T bonds. For example, if 24 tetrahedra are linked together as shown in the top line of Fig. 1, the cubo-octahedron, also referred to as a sodalite unit or β-cage, results. It is an important secondary building unit from which various zeolite structures derive. If sodalite units are connected via their hexagonal faces as shown in Fig. 1, the structure of the mineral faujasite results. It is identical with the structures of the synthetic zeolites X ($1 \leq n_{Si}/n_{Al} \leq 1.5$) and Y ($n_{Si}/n_{Al} > 1.5$). Zeolite Y is of utmost importance in heterogeneous catalysis, for example it is the active component in catalysts for fluid catalytic cracking [1,2]. Its pore system is relatively spacious and consists of spherical cages, referred to as supercages, with a diameter of 1.3 nm connected tetrahedrally with four neighboring cages through windows with a diameter of 0.74 nm formed by 12 TO_4-tetrahedra. Zeolite Y is therefore classified to possess a three-dimensional, 12-membered-ring pore system.

An example of a zeolite with unidimensional, 12-membered-ring pores is zeolite ZSM-12 (Fig. 1, line 2). Its pores are slightly elliptical with dimensions of 0.57×0.61 nm. Zeolite ZSM-5 (Fig. 1, line 3) and its all-silica analogue silicalite-1 ($n_{Si}/n_{Al} = \infty$) are built from the pentasil unit. They contain intersecting systems of ten-membered-ring pores, one being straight and one sinusoidal. ZSM-5 is another example of a zeolite which has gained huge importance in heterogeneous catalysis. It is used industrially in the synthesis of ethylbenzene, the isomerization of xylenes and the disproportionation of toluene, and it is often looked upon as the prototype of shape-selective catalysts (vide infra). Several zeolites with unidimensional, ten-membered-ring pores exist as well, one example being Theta-1 which is isostruc-
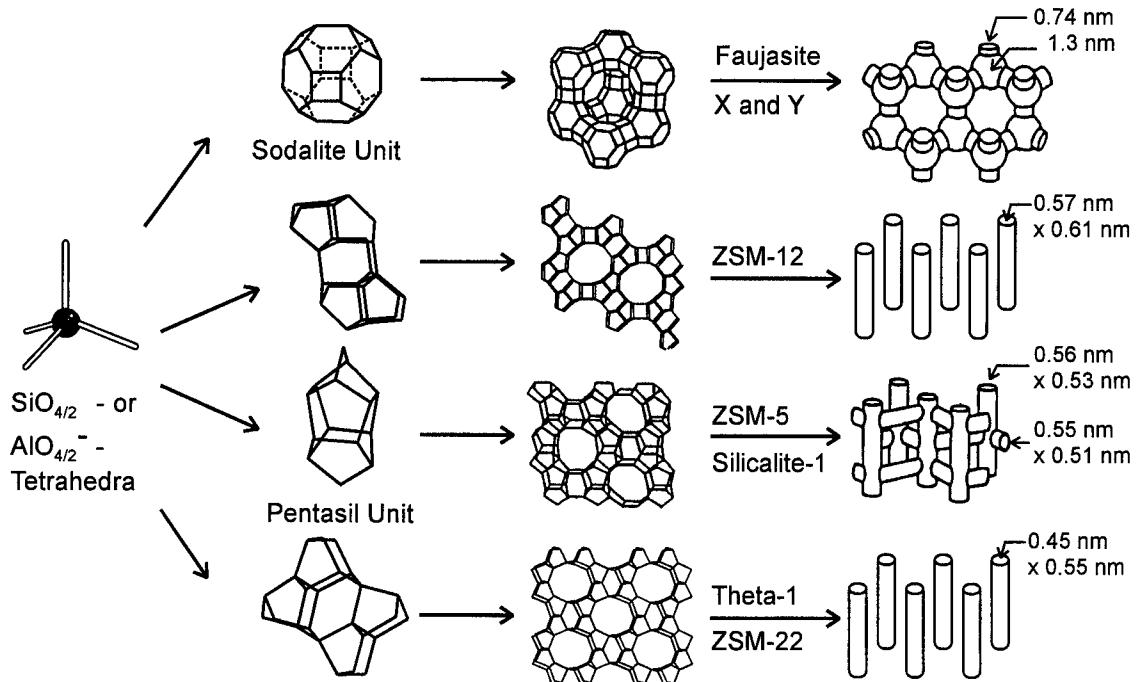
Fig. 1. Structures of four selected zeolites (from top to bottom: faujasite or zeolites X, Y; zeolite ZSM-12; zeolite ZSM-5 or silicalite-1; zeolite Theta-1 or ZSM-22) and their micropore systems and dimensions.

tural to zeolite ZSM-22 (Fig. 1, bottom line). An assortment of zeolite catalysts as shown in Fig. 1 is often a good starting point for a coarse investigation of the influence of the pore width and/or dimensionality on the selectivity of the reaction to be studied.

Among the unique features of zeolites compared to more conventional solid catalysts or catalyst supports are (i) their strictly uniform pore diameters and (ii) pore widths in the order of molecular dimensions (Fig. 2). Bearing in mind the pertinent IUPAC classification [11] for

micropores: $2.0\,\mathrm{nm} \geq d_\mathrm{p}$,

mesopores: $2.0\,\mathrm{nm} < d_\mathrm{p} \leq 50\,\mathrm{nm}$ and

macropores: $d_\mathrm{p} > 50\,\mathrm{nm}$

with d_p being the pore diameter, zeolites are typical microporous materials. More conventional porous solids have their range of pore diameters from ca. 10

nm onwards (cf. Fig. 2), and for some time there was a gap in the lower mesopore range.

This gap was filled recently with the discovery of mesoporous materials of the M41S family [12], the most prominent and most extensively investigated member of this family being MCM-41. MCM-41 is a hexagonal material containing a regular array of mesopores with uniform diameter. By proper synthesis procedures, the pore diameter can be varied from ca. 2 to 10 nm. The M41S materials are often referred to as 'mesoporous zeolites'. Indeed, MCM-41 resembles a zeolite with respect to its regular system of pores with their uniform width. There is, however, one significant difference, namely the non-crystallinity of the silica or silica–alumina pore walls in MCM-41.

The most appropriate definition of the term *zeolite* is a matter of ongoing debate. Mineralogists tend to restrict it to aluminosilicates according to Eq. (1). Zeolites are then crystalline aluminosilicates with a framework forming regular channels with a diameter of up to ca. 1 nm. These channels contain cations (frequently Na^+ ions), which compensate the nega-
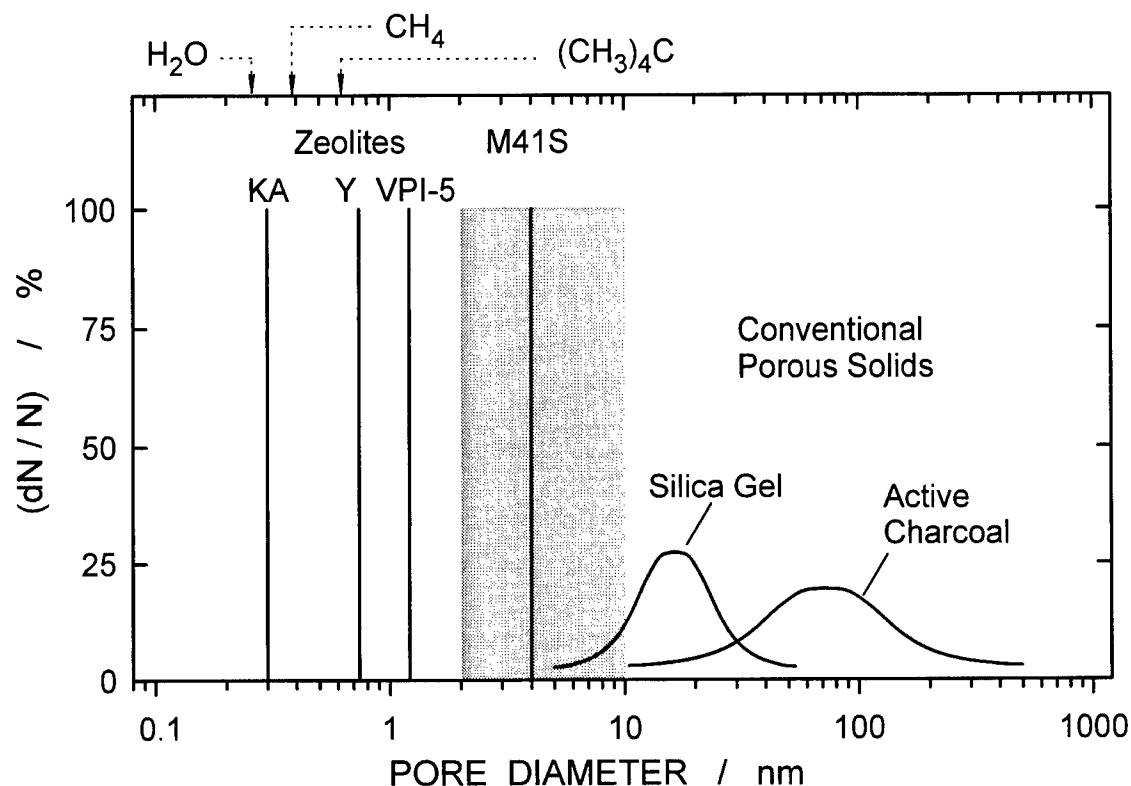
Fig. 2. Typical pore diameter distributions of porous solids (KA is the K^+ form of zeolite A; VPI-5 is a microporous aluminophosphate with 18-membered-ring pores; for the description of M41S materials see Section 2). For comparison, the kinetic diameters of water, methane and neopentane are also indicated.

tive framework charge and are very mobile, and water which desorbs upon heating without destruction of the crystalline structure.

Liebau et al. [13,14] suggested the classification of the materials in the large group of tectosilicates according to their chemical composition (aluminosilicates: *tectolites*; SiO_2: *tectosils*) and their framework or tetrahedral density ρ_T defined as the number of TO_4 tetrahedra n_T per nm^3. Tectosilicates with $\rho_T \geq 21$ n_T/nm^3 are referred to as *dense* and divided into *pyknolites* (aluminosilicates, e.g. nepheline, cordierite or feldspars) and *pyknosils* (SiO_2, e.g. quartz or cristobalite). These materials lack porosity and are, hence, of no interest by themselves as catalysts (though sometimes as catalyst carriers). Tectosilicates with $\rho_T < 21$ n_T/nm^3 are called *porous* and divided into *porolites* (aluminosilicates) and *porosils* (SiO_2). Sub-classes of the porolites are *clathralites* (e.g. sodalite or ZSM-39) and

zeolites. Clathralites possess voids with windows (usually formed by six TO_4 tetrahedra) which are too small to let the void-filling guests pass. Such tectosilicates have the characteristics of clathrates and are not of interest in catalysis. In zeolites, by contrast, the cavities possess windows large enough for guest molecules to diffuse through. In much the same way, sub-classes of porosils are *clathrasils* (e.g. silica–sodalite or melanophlogite) and *zeosils* (e.g. silicalite-1 or silica-ZSM-22). Liebau's nomenclature, though very straightforward and systematic, has unfortunately found limited acceptance, though its salient terms are being used occasionally in the literature [15].

Today, a broad variety of zeolite-like microporous materials are known with T-atoms other than silicon and aluminum. For these materials, Dyer proposed the term *zeotypes* [16]. The best known examples are microporous aluminophosphates ($AlPO_4s$) and ma-

terials derived from them by incorporation of T-atoms other than aluminum and phosphorus [17,18]. All these and related microporous materials with still other T-atoms like titanium, vanadium, cobalt, etc. are of considerable interest in catalysis and routinely dealt with at the International Zeolite Conferences. The terms *zeolites*, *microporous materials* and *molecular sieves* are therefore often used as synonyms indicating that the regular array of micropores with well-defined dimensions is the unifying principle which renders this wealth of materials attractive for catalysis (and other applications).

3. Broad variety of zeolitic materials available

3.1. Structure and pore size

Four selected zeolite structures were shown in Fig. 1, but many more are available today. A huge number of zeolitic materials has been described in the literature, and a great deal of these in the patent

literature. It is sometimes difficult, especially for researchers whose prime interest lies in catalysis, to find out whether such reported materials possess truly new structures or whether they represent variants of structures already known. In this context, the work of the Structure Commission of the International Zeolite Association (IZA) has been most valuable. Composed of 16 experienced crystallographers, the Commission regularly scrutinizes proposed zeolite structures. Once a structure has been approved by the Commission, it is assigned a three-letter code (e.g. FAU for faujasite and zeolites X and Y; MTW for zeolite ZSM-12; MFI for zeolite ZSM-5 and its zeosil analogue silicalite-1; TON for zeolites Theta-1 and ZSM-22 which are isostructural) and included in the 'Atlas of Zeolite Structure Types'. Its latest edition appeared in 1996 [19] and embraces 98 structures. An additional 28 structures have since been published on the world wide web.

At this time (December 1999), there is hence a total of 126 approved zeolites structures. In Fig. 3, their range of crystallographic pore diameters is
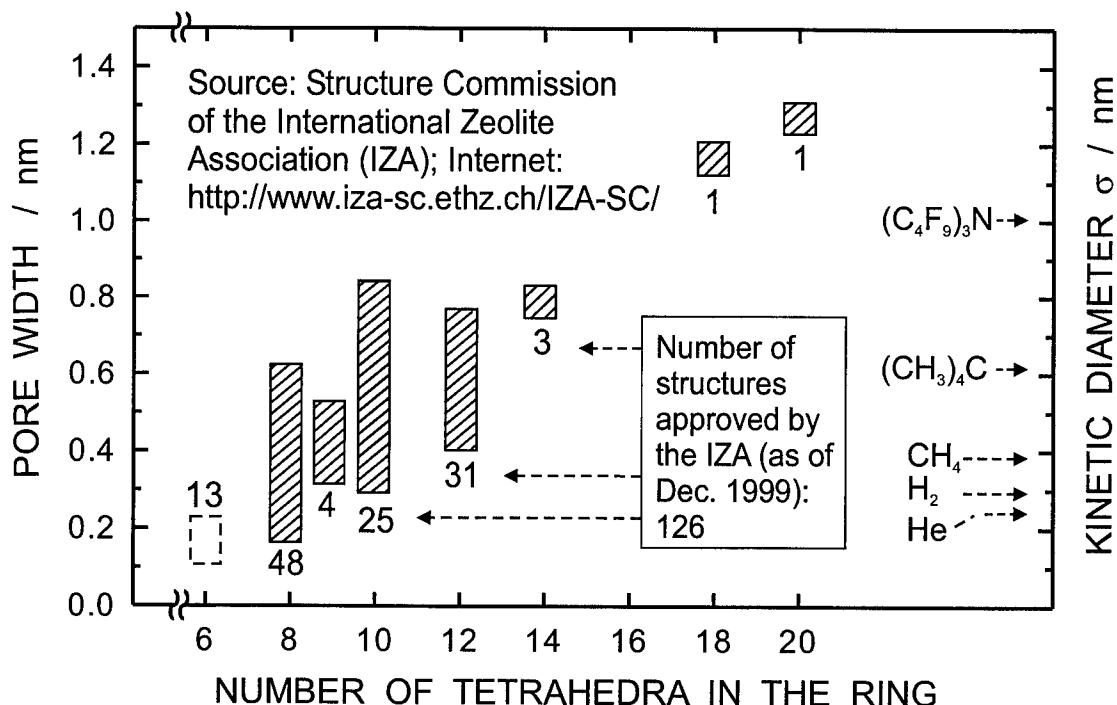
Fig. 3. Range of crystallographic pore diameters of zeolites approved by the Structure Commission of the International Zeolite Association (IZA). Sources: Ref. [19] and internet homepage of the IZA Structure Commission.

plotted versus the number of TO_4-tetrahedra circumscribing their pores. The largest, i.e. catalytically most relevant pores were chosen for those zeolites which possess more than one pore system. The kinetic diameters (σ in the Lennard–Jones model for intermolecular interactions) for a few selected molecules are also given in Fig. 3 for comparison. It is seen that there are 13 structurally different clathralites/clathrasils with six-membered-ring pores. Such pores are generally too narrow (around 0.2 nm) to admit the molecules involved in catalytic reactions. The remaining 113 zeolites span a range of pore widths which coincides with the range of dimensions of a very large number of molecules. It is furthermore seen from Fig. 3 that zeolites with eight-, ten- and 12-membered-ring pores for which, respectively, the terms small-pore, medium-pore and large-pore zeolites are customary, strongly predominate with a total of 104 structures, whereas the super-large-pore materials with pores formed by more than 12 TO_4-tetrahedra and materials with pores formed by an odd number of TO_4-tetrahedra are still scant.

The potential of zeolites with nine-membered-ring pores has so far hardly been explored. Zeolites with eight-membered-ring pores are good catalysts for a limited number of reactions involving small reactant and product molecules. Examples are the manufacture of mono- and dimethylamine from methanol and ammonia or the conversion of methanol to small olefins (MTO). For the majority of catalytic applications, medium- or large-pore zeolites will usually be preferred.

Fine-tuning and tailoring of the pore size of a given zeolite can be achieved by various post-synthesis modification techniques for which the generic term 'pore size engineering' has been coined [20]. Among these techniques are ion exchange and chemical vapor deposition (CVD). A frequently used class of CVD precursors are silanes and organosilanes, such as tetramethoxysilane or tetraethoxysilane.

3.2. Chemical composition

Many aluminosilicate zeolites can be synthesized over a range of aluminum contents, for example zeolite ZSM-5 from $n_{Si}/n_{Al} \approx 10$ to ∞. In addition, various techniques for the post-synthesis dealumination of the framework have been developed which can be classified into thermal treatments, hydrothermal treatments, extraction of framework aluminum with acid and replacement of framework aluminum with silicon by reaction with silicon halides or hexafluorosilicates [21]. Conversely, an insertion of aluminum into the zeolite framework can be achieved as well [21]. Among the properties which are affected by the framework aluminum content are the density of negative framework charges, the cation-exchange capacity, the density of Brønsted acid sites, their strength, the thermal stability, the hydrophilic or hydrophobic surface properties [22] and the unit cell dimensions.

As already mentioned, a number of elements other than silicon or aluminum can occur as T-atoms. Relevant to catalysis are silicoaluminophosphates, in part because some of these materials possess structures which do not exist for aluminosilicates, and in part because their acid strength is lower than the one of aluminosilicate zeolites. Materials containing titanium, vanadium, iron and other transition metals in the framework have recently attracted much interest as catalysts for selective oxidations [23]. The most prominent example is titanium silicalite-1 (TS-1, MFI structure) which is used on an industrial scale for the production of hydroquinone and catechol from phenol and hydrogen peroxide [24].

3.3. Ion exchange

With their negatively charged porous framework and the small and mobile cations sitting in the pores, zeolites are typical ion exchangers. In fact, zeolites are widely used as builders in laundry detergents where their role is to take up calcium and magnesium ions in exchange for sodium ions, thereby softening the washing water. Obviously, an as high as possible cation exchange capacity and, hence, the highest possible aluminum content in the framework ($n_{Si}/n_{Al} = 1$) are desired for this application. This is the domain of zeolite A, and as a whole, the use of zeolites as ion exchangers in detergents represents their largest market in terms of tonnage (not in terms of financial turnover) with a worldwide production rate close to 1 million t/annum.

In the manufacture of zeolite catalysts, ion exchange plays an outstanding role as well. For many catalytic applications, a Brønsted acid form of a zeolite is required. Brønsted acid sites in zeolites can

be readily generated by introducing ammonium ions followed by a heat treatment or by introducing multivalent metal cations, typically cations of the rare-earths, again followed by heat treatment (vide infra). In processes which work under hydrogen pressure, such as hydrocracking of heavy petroleum distillates or the isomerization of light gasoline, bifunctional catalysts are needed which contain both Brønsted acid sites and a component which activates hydrogen, typically a noble metal like palladium or platinum. These noble metals can again be easily introduced into the zeolite pores by ion exchange with cationic forms of such metals, e.g. $[Pd(NH_3)_4]^{2+}$ or $[Pt(NH_3)_4]^{2+}$, followed by thermal removal of the ammine ligands. More recently, the use of metal-containing zeolite catalysts for the selective reduction of nitrogen oxides with light hydrocarbons, e.g. in exhaust gases from diesel engines, has become a topic of worldwide research [25,26]. Here again, ion exchange is almost always applied to incorporate the frequently studied metals like Cu, Co, Pt or Pd into the zeolite.

Ion exchange is a very simple technique: The zeolite is suspended in an aqueous solution of a soluble salt containing the desired cation, preferentially under conditions which favor mass transfer, i.e. at elevated temperatures (ca. 90°C) under stirring. While this procedure is very versatile, it has its limitations: Sometimes, the cation with its hydrate shell is too bulky to enter the zeolite pores, or the salt with the cation in the desired valence state is unstable or insoluble in water. In these and other instances, the desired form of the zeolite can often be made by solid-state ion exchange: The zeolite, typically in its H^+-form, and a compound containing the in-going cation, e.g. a halide, are intimately mixed, whereupon this physical mixture of solids is heated in an inert gas stream. An excellent review on solid-state ion exchange with zeolites and its variants, viz. contact-induced solid-state ion exchange, vapor phase-mediated ion exchange and reductive solid-state ion exchange has recently been published by Karge [27].

3.4. Crystal size

The size of zeolite crystals is often in the order of one to several micrometers. A typical example is depicted in Fig. 4a which shows tablets of zeolite

ZSM-5 with dimensions of 1 to 3 μm. Some zeolites which are relevant to catalysis can, however, be synthesized in very small crystals with a size down to ca. 5 nm (such small crystals are X-ray-amorphous [28]) or in very large crystals up to ca. 100 μm or even 1 mm [29]. As an example, large crystals of zeolite ZSM-5 are shown in Fig. 4b. For catalytic applications, both a decreased and an increased crystal size can be desirable: Upon decreasing the crystal size, the diffusional paths of the reactant and product molecules inside the pores become shorter, and this can result in a reduction or elimination of undesired diffusional limitations of the reaction rate. However, while decreasing the crystal size, one must be careful, since below ca. 0.1 μm the external crystal surface begins to play a non-negligible role vis-à-vis the internal surface, and this is particularly undesirable if shape selectivity effects are to be exploited. Shape selectivity, which is a unique effect in zeolite catalysis, can only occur inside the channel and cage system (vide infra). Conversely, upon increasing the crystal size, the diffusional paths of the molecules inside the pores are lengthened, and this may, under certain circumstances, affect the selectivity in a desirable manner.

4. Acidity of zeolites

Among the most important properties of zeolites with respect to their use as catalysts is their surface acidity. To describe the acidity of zeolites in an adequate manner, it is mandatory to clearly distinguish between (i) the nature of the acid sites (i.e. Brønsted vs. Lewis acidity), (ii) the density or concentration of these sites, (iii) their strength or strength distribution and, last but not least, (iv) the precise location of the acid sites.

4.1. Nature of the acid sites

Both Brønsted and Lewis acid sites occur in zeolites. Brønsted acid sites are almost always generated by either of the procedures represented by Eqs. (2) and (3), where Z^- stands for the negatively charged framework:
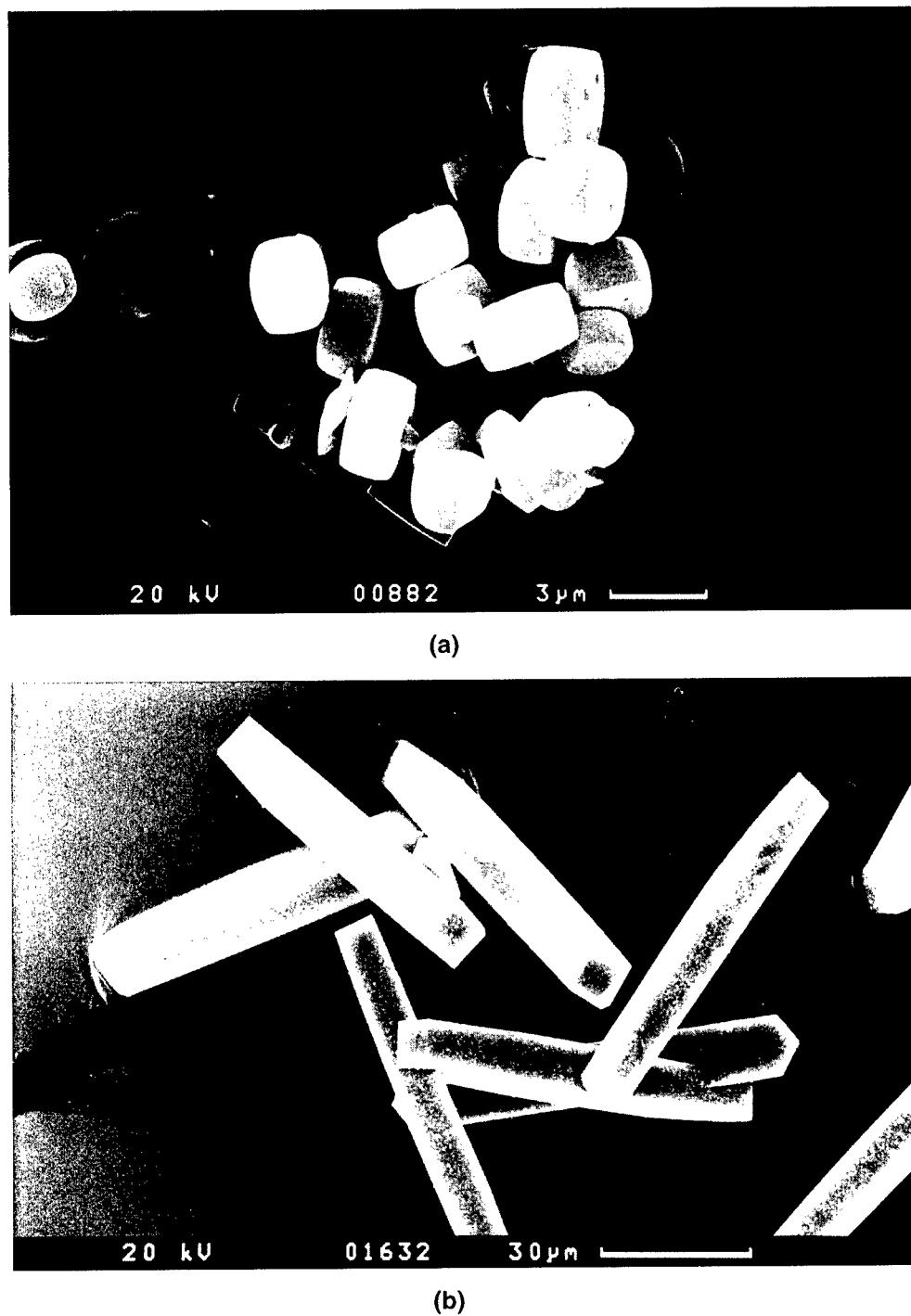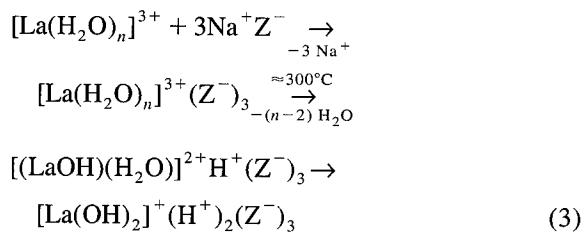
$$NH_4^+ + Na^+Z^- \xrightarrow[-Na^+]{} NH_4^+Z^- \xrightarrow[-NH_3]{\approx 300-400°C} H^+Z^- \qquad (2)$$

(a)

(b)
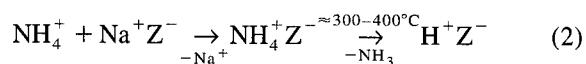
Fig. 4. Scanning electron micrographs showing crystals of zeolite ZSM-5. (a, top): Tablets of ca. $2 \times 2 \times 1$ μm; (b, bottom): Bars of ca. $80 \times 10 \times 10$ μm.

i.e. aqueous ion exchange with an ammonium salt followed by thermal decomposition of the ammonium ions inside the zeolite, or
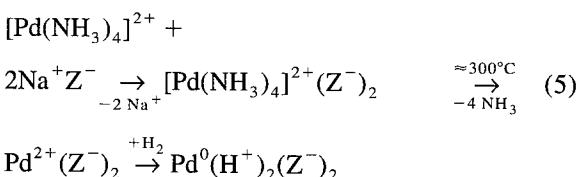
$$[La(H_2O)_n]^{3+} + 3Na^+Z^- \underset{-3\,Na^+}{\rightarrow}$$

$$[La(H_2O)_n]^{3+}(Z^-)_3 \underset{-(n-2)\,H_2O}{\overset{\approx 300°C}{\rightarrow}}$$

$$[(LaOH)(H_2O)]^{2+}H^+(Z^-)_3 \rightarrow$$

$$[La(OH)_2]^+(H^+)_2(Z^-)_3 \qquad (3)$$

i.e. aqueous ion exchange with the salt of a multivalent metal cation (often used are Mg^{2+}, Ca^{2+}, La^{3+} or mixed rare-earth cations) followed by thermal dehydration. The sequence of events in Eq. (3) is usually referred to as the Hirschler–Plank scheme: Upon removal of most of the water from the cation inside the zeolite pores, strong electrostatic fields build up, because the lanthanum ion has to neutralize three negative charges fixed in the framework at a significant distance from each other. Under the influence of these local electrostatic fields, remaining water molecules dissociate giving rise to a proton and an OH group which is non-acidic and bound to the metal cation. It is seen from Eq. (3) that a maximum of two Brønsted acid sites can be formed per La^{3+} ion introduced.

The direct ion exchange with mineral acids

$$H^+ + Na^+Z^- \underset{-Na^+}{\rightarrow} H^+Z^- \qquad (4)$$

is generally less favored, because an exposure of zeolites to such acids often leads to undesired effects like framework dealumination or, in the case of aluminum-rich zeolites, to a complete framework collapse.

Finally, Brønsted sites inevitably form, when cations of metals nobler than hydrogen are reduced by molecular hydrogen:

$$[Pd(NH_3)_4]^{2+} +$$

$$2Na^+Z^- \underset{-2\,Na^+}{\rightarrow} [Pd(NH_3)_4]^{2+}(Z^-)_2 \underset{-4\,NH_3}{\overset{\approx 300°C}{\rightarrow}} \qquad (5)$$

$$Pd^{2+}(Z^-)_2 \overset{+H_2}{\rightarrow} Pd^0(H^+)_2(Z^-)_2$$

Regardless of the method used for their generation [Eqs. (2)–(5)], the chemical nature of the Brønsted acid sites is the same, viz. bridging hydroxyl groups

formed by the proton and a framework oxygen in an AlO_4 tetrahedron.

Upon severe heat treatment ($\geq 500°C$), the Brønsted acid sites are degraded ('dehydroxylation'), water is split off with the concomitant formation of Lewis acid sites. Their precise chemical nature is less clear. For some time, they were looked upon as tricoordinated aluminum and/or tricoordinated, positively charged silicon in the framework. Kühl, however, was able to demonstrate [30] that silicon in dehydroxylated zeolites remains tetracoordinated and much of the aluminum is converted to octahedral rather than trigonal coordination. This led Kühl to conclude that $[(AlO)^+]_n^{n+}$ units removed from the zeolite framework act as true Lewis sites.

The Brønsted OH groups can be directly detected by solid-state IR (Fig. 5a) and ^{1}H-NMR (Fig. 5b) spectroscopy. In the OH-stretching region of the IR spectrum, acid faujasites (see Fig. 1, top line, for their structure) show essentially two bands appearing at ca. 3550 cm^{-1} and 3640 cm^{-1}. These bands are, respectively, due to bridging OH groups in the small sodalite cages and in the large supercages. In line with this assignment, the band at 3640 cm^{-1} disappears upon adsorption of the base pyridine, whereas the band at 3550 cm^{-1} does not. Obviously, the pyridine molecule is too bulky to penetrate the small cages. This is an example of a molecular sieve effect. In the region of ring deformation vibrations, new bands appear after adsorption of pyridine. The band around 1540 cm^{-1} is due to pyridinium ions chemisorbed on Brønsted acid sites, whereas the band at 1455 cm^{-1} is indicative of pyridine on Lewis acid sites. Note that the small band at ca. 3740 cm^{-1} originates from terminal, non-acidic OH bands either at the external surface of the crystals or at amorphous inclusions. It should also be mentioned that, unlike faujasite, most high-silica zeolites such as HZSM-5 show a single band in the OH-stretching region which appears close to 3600 cm^{-1}.

The ^{1}H-NMR spectrum of acid faujasite (Fig. 5b) consists of an intense signal at 3 to 6 ppm. After deconvolution, the signals for bridging OH groups in the large and in the small cages appear at 3.9 and 4.8 ppm, respectively. The combined application of solid-state IR and NMR spectroscopy has significantly contributed to our understanding of zeolite acidity, especially in relation to catalytic activity. An
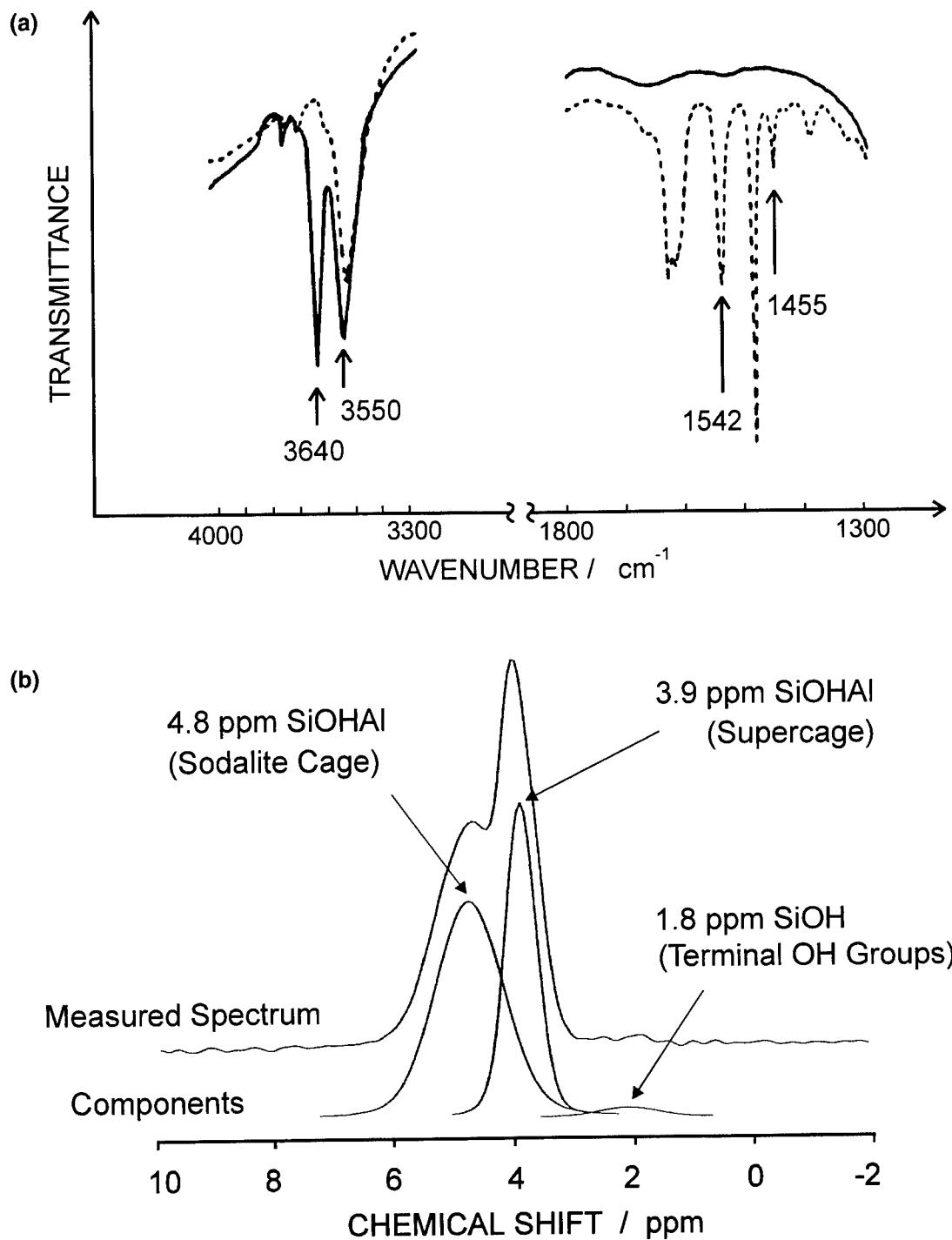
(a)

(b)

Fig. 5. (a, top): IR spectra of HY zeolite without (solid lines) and with (dotted lines) adsorbed pyridine; (b, bottom): ^{1}H-MAS-NMR spectrum of HY zeolite.

excellent account on solid-state IR and NMR spectroscopy and the information they furnish with respect to zeolite catalysis may be found in the recent literature [31].

It has been repeatedly found that the catalytic activity stems from the Brønsted rather than the Lewis acid sites. It is doubtful whether the Lewis sites play a role at all in acid-catalyzed reactions. It has been claimed [32] that, under certain circumstances, Lewis acid sites might enhance the strength of nearby Brønsted sites, thereby exerting an indirect influence on the catalytic activity.

4.2. Density and strength of acid sites

The density of Brønsted acid sites in a zeolite is obviously related to the framework aluminum content. Limiting cases are pure zeosils, which lack acidity, and aluminum-rich zeolites such as HY. Note that zeolite X which is even richer in aluminum is unstable in the H^+-form. The density of Brønsted sites can be measured by, e.g. ^{1}H-NMR spectroscopy or IR spectroscopy, either with or without adsorption of a base like pyridine, but the latter technique requires the knowledge of reliable extinction coefficients which are often difficult to find. Similarly, the density of Lewis acid sites is accessible through IR measurements using the 1455 cm^{-1} band after adsorption of pyridine (here again reliable extinction coefficients are needed). An alternative method is to measure the total number of acid sites by titration with a gaseous base like ammonia and to subtract the number of Brønsted acid sites which has to be determined separately.

Less readily obtained is the strength distribution of acid sites in zeolites. Calorimetric methods measuring the heat of adsorption of nitrogen bases probably give the most reliable results, but such experiments tend to be cumbersome and require very experienced experimentalists. Semi-quantitative results may be obtained by IR spectroscopy with bases like pyridine at a set of suitably selected temperatures. Temperature-programmed desorption of bases like ammonia or pyridine are most frequently employed, because the technique is simple and versatile. However, the results must be interpreted with care, since hindered diffusion of the desorbed base out of the pores and multiple adsorption/desorption may obscure the desired information.

All these techniques indicate that zeolites are significantly stronger acids than their forerunners in industrial catalysis, i.e. amorphous silica-aluminas, and it is in the first place this enhanced acid strength which made zeolites so valuable and successful in processes like catalytic cracking. The recently discovered mesoporous materials like MCM-41 do not possess the high acid strength of zeolites, and this is a major hurdle which, together with the relatively high cost of their manufacture, so far prevented them from being applied as catalysts in industrial processes.

It is well known and supported by quantum chemical calculations that, due to the higher electronegativity of silicon compared to aluminum, the strongest Brønsted acid sites in zeolites will occur on completely isolated AlO_4-tetrahedra, i.e. those which lack AlO_4-tetrahedra as next nearest neighbors. This is the reason why, upon dealumination of Y-zeolites with a typical n_{Si}/n_{Al} of 2.5, the catalytic activity generally *increases* up to $n_{Si}/n_{Al} \approx 10$. In this region, the gain in acid strength overcompensates the decrease in the density of Brønsted acid sites. From a certain n_{Si}/n_{Al} onwards (and with high-quality zeolite samples) the activity per acid site remains constant [32]. For a more detailed discussion of the important issue of zeolite acidity, the review by Rabo and Gajda [33] can be recommended.

4.3. Location of the acid sites

A complete description of zeolite acidity would include a detailed analysis of the location of the catalytically active sites. To what extent do these occur on the external surface of the crystals and inside the pores (only the internal surface can be expected to show shape selectivity, vide infra)? To what extent do the sites occur in large cavities, which are accessible for bulky reactant molecules, and in smaller cavities in which they are hidden for such molecules? Are the acid sites evenly distributed over the crystals, or are they concentrated in a shell near the external surface or, conversely, in the core of the crystals? More and more examples for surprising distributions of the location of acid sites are emerging in the literature. One example is the acid form of zeolite ferrierite which possesses both eight-membered-ring (dimensions: 0.35×0.48 nm) and ten-membered-ring (0.42×0.54 nm) pores. Interest-

ingly, about three quarters of the Brønsted acid sites are located in the eight-membered-ring pores and hence inaccessible to many potential reactant molecules [34,35].

5. Shape-selective catalysis in zeolites

The fact that the pores of zeolites and molecules interacting with the surface of zeolites have dimensions in the same order of magnitude (cf. Figs. 2 and 3), leads to unique effects in catalysis for which the generic term shape-selective catalysis is in use today. Shape-selective catalysis encompasses all effects in which the selectivity of the heterogeneously catalyzed reaction depends unambiguously on the pore width or pore architecture of the microporous catalyst [36].

Numerous such effects are known today. Almost always, they can be classified into one of the following categories:

(i) *Reactant shape selectivity*: There are at least two reactants with differences in their molecular dimensions. If the diffusion of the bulkier reactant molecules inside the pores is hindered, the less bulky molecules will react preferentially. The limiting case is a complete size exclusion of one reactant which leaves the catalytic reactor unconverted.

(ii) *Product shape selectivity*: At least two products with differences in their molecular dimensions may form in parallel or consecutive reactions. If the diffusion of the bulkier product molecules inside the pores is hindered, the less bulky molecules will be formed preferentially. The limiting case is a complete suppression of the formation of the bulkier molecules.

(iii) *Restricted transition state shape selectivity*: Neither the reactant nor the product molecules experience a hindered diffusion. However, out of at least two (parallel or consecutive) reactions, one is going via a bulky transition state or intermediate which cannot be accommodated inside the zeolite pores. In favorable cases, this reaction is entirely suppressed. The chances for achieving restricted transition state shape selectivity in a suitably selected zeolite are usually very good, if the same reactant can undergo a monomolecular and a bimolecular reaction.

Note that cases (i) and (ii) are identical in their nature and have their origin in mass transfer effects. If desired, these effects can be amplified (or weakened) by using larger (or smaller) crystals of the same zeolite, i.e. by lengthening (or shortening) the diffusional paths inside the pores, or by using another zeolite with slightly narrower (wider) pores. By contrast, case (iii) is an intrinsic chemical effect, and the selectivity will be independent of the crystal size.

Shape-selective catalysis in zeolites is already exploited in a number of large-scale processes [7]. In most cases, the observed selectivity effects can be rationalized satisfactorily in terms of the traditional classification outlined above. To account for more recent research results, however, a number of novel concepts for shape-selective catalysis in zeolites were advanced. Among these are cage or window effects, a directed (e.g. tip-on) adsorption of molecules at the active sites, secondary shape selectivity, inverse shape selectivity and pore mouth catalysis. For an adequate discussion of these and other concepts, the reader can be referred to Refs. [36,37].

6. Concluding remarks

Zeolite materials science is an advanced field, and the same is true for the use of zeolites in catalysis. Only a few fundamental aspects could be addressed in the present review, but the references cited offer the opportunity to the reader to acquire adequate, modern and in-depth information on a topic which is equally fascinating from a fundamental viewpoint and for industrial research. Zeolite catalysis is a good example for the impact and beneficial effects of novel materials on the performance and efficiency of industrial processes and, ultimately, the welfare of mankind. At the same time, zeolite catalysis is a truly interdisciplinary field which needs the expertise and ingenuity of mineralogists, crystallographers, chemists, physicists and engineers.

Catalysis is one of the most important fields of application of zeolites, but by no means the sole one. Zeolites are, besides, used on a large scale as ion exchangers in laundry detergents and for the clean-up of radioactive waste and as adsorbents for the purification and separation of numerous substances.

Large efforts are being undertaken worldwide to open the door to novel applications for zeolites, e.g. in electrochemistry, photochemistry, membrane science and technology, to enumerate only a few. Looking for such novel applications is equally fascinating as zeolite catalysis, but no doubt beyond the scope of this contribution.

Acknowledgements

References

[1] P.B. Venuto, E.T. Habib Jr., in: Fluid Catalytic Cracking With Zeolite Catalysts, Marcel Dekker, New York, Basel, 1979, 156 pp.

[2] R. von Ballmoos, D.H. Harris, J.S. Magee, in: G. Ertl, H. Knözinger, J. Weitkamp (Eds.), Handbook of Heterogeneous Catalysis, Vol. 4, Wiley–VCH, Weinheim, 1997, p. 1955.

[3] J.E. Naber, K.P. de Jong, W.H.J. Stork, H.P.C.E. Kuipers, M.F.M. Post, in: J. Weitkamp, H.G. Karge, H. Pfeifer, W. Hölderich (Eds.), Zeolites and Related Microporous Materials: State of the Art 1994, Studies in Surface Science and Catalysis, Vol. 84, Elsevier, Amsterdam, 1994, p. 2197, Part C.

[4] J. Scherzer, A.J. Gruia, in: Hydrocracking Science and Technology, Marcel Dekker, New York, Basel, Hong Kong, 1996, 305 pp.

[5] S.T. Sie, in: G. Ertl, H. Knözinger, J. Weitkamp (Eds.), Handbook of Heterogeneous Catalysis, Vol. 4, Wiley–VCH, Weinheim, 1997, p. 1998.

[6] F.G. Dwyer, in: W.R. Moser (Ed.), Catalysis of Organic Reactions, Marcel Dekker, New York, Basel, 1981, p. 39.

[7] N.Y. Chen, W.E. Garwood, F.G. Dwyer, in: Shape Selective Catalysis in Industrial Applications, Marcel Dekker, New York, Basel, 1989, p. 203.

[8] P.B. Venuto, Microporous Materials 2 (1994) 297.

[9] M.E. Davis, Microporous and Mesoporous Materials 21 (1998) 173.

[10] W. Löwenstein, Am. Mineralogist 39 (1954) 92.

[11] D.H. Everett, Pure Appl. Chem. 31 (1972) 585.

[12] J.C. Vartuli, W.J. Roth, J.S. Beck, S.B. McCullen, C.T. Kresge, in: H.G. Karge, J. Weitkamp (Eds.), Molecular Sieves — Science and Technology, Vol. 1, Springer Verlag, Berlin, Heidelberg, New York, 1998, p. 97.

[13] F. Liebau, in: Structural Chemistry of Silicates — Structure, Bonding and Classification, Springer Verlag, Berlin, Heidelberg, New York, Tokyo, 1985, 347 pp.

[14] F. Liebau, H. Gies, R.P. Gunawardane, B. Marler, Zeolites 6 (1986) 373.

[15] H. Gies, B. Marler, U. Werthmann, in: H.G. Karge, J. Weitkamp (Eds.), Molecular Sieves — Science and Technology, Vol. 1, Springer Verlag, Berlin, Heidelberg, New York, 1998, p. 35.

[16] A. Dyer, in: An Introduction to Zeolite Molecular Sieves, John Wiley and Sons, Chichester, 1988, p. 1.

[17] R. Szostak, in: H.G. Karge, J. Weitkamp (Eds.), Molecular Sieves — Science and Technology, Vol. 1, Springer Verlag, Berlin, Heidelberg, New York, 1998, p. 157.

[18] J.A. Martens, P.A. Jacobs, in: J. Weitkamp, L. Puppe (Eds.), Catalysis and Zeolites, Springer Verlag, Berlin, Heidelberg, New York, 1999, p. 53.

[19] W.M. Meier, D.H. Olson, Ch. Baerlocher, in: Atlas of Zeolite Structure Types, 4th Edition, Elsevier, London, 1996, 229 pp.

[20] E.F. Vansant, in: Pore Size Engineering in Zeolites, John Wiley–Salle-Sauerländer, Chichester–Aarau, 1990, p. 145.

[21] G. Kühl, in: J. Weitkamp, L. Puppe (Eds.), Catalysis and Zeolites, Springer Verlag, Berlin, Heidelberg, New York, 1999, p. 81.

[22] J. Weitkamp, P. Kleinschmit, A. Kiss, C.H. Berke, in: R. von Ballmoos, J.B. Higgins, M.M.J. Treacy (Eds.), Proceedings from the Ninth International Zeolite Conference, Vol. 2, Butterworth–Heinemann, Boston, 1993, p. 79.

[23] G. Perego, R. Millini, G. Bellussi, in: H.G. Karge, J. Weitkamp (Eds.), Molecular Sieves — Science and Technology, Vol. 1, Springer Verlag, Berlin, Heidelberg, New York, 1998, p. 187.

[24] G. Bellussi, C. Perego, in: G. Ertl, H. Knözinger, J. Weitkamp (Eds.), Handbook of Heterogeneous Catalysis, Vol. 5, Wiley–VCH, Weinheim, 1997, p. 2329.

[25] H.K. Shin, H. Hirabayashi, H. Yahiro, M. Watanabe, M. Iwamoto, Catal. Today 26 (1995) 13.

[26] A. Fritz, V. Pitchon, Appl. Catal. B: Environmental 13 (1997) 1.

[27] H.G. Karge, in: H. Chon, S.-K. Ihm, Y.S. Uh (Eds.), Progress in Zeolite and Microporous Materials, Studies in Surface Science and Catalysis, Vol. 105, Elsevier, Amsterdam, 1997, p. 1901, Part C.

[28] P.A. Jacobs, E.G. Derouane, J. Weitkamp, J. Chem. Soc. Chem. Comm. (1981) 591.

[29] E.N. Coker, J.C. Jansen, in: H.G. Karge, J. Weitkamp (Eds.), Molecular Sieves — Science and Technology, Vol. 1, Springer Verlag, Berlin, Heidelberg, New York, 1998, p. 121.

[30] G.H. Kühl, J. Phys. Chem. Solids 38 (1977) 1259.

[31] H.G. Karge, M. Hunger, H.K. Beyer, in: J. Weitkamp, L. Puppe (Eds.), Catalysis and Zeolites, Springer Verlag, Berlin, Heidelberg, New York, 1999, p. 198.

[32] R.M. Lago, W.O. Haag, R.J. Mikovsky, D.H. Olson, S.D. Hellring, K.D. Schmitt et al., in: Y. Murakami, A. Iijima, J.W. Ward (Eds.), New Developments in Zeolite Science and Technology, Studies in Surface Science and Technology, Vol. 28, Kodansha/Elsevier, Tokyo/Amsterdam, 1986, p. 677.

[33] J.A. Rabo, G.J. Gajda, in: D. Barthomeuf, E.G. Derouane, W. Hölderich (Eds.), Guidelines for Mastering the Properties of Molecular Sieves, NATO ASI Series B, Vol. 221, Plenum Press, New York, 1990, p. 273.

[34] V.L. Zholobenko, D.B. Lukyanov, J. Dwyer, W.J. Smith, J. Phys. Chem. B 102 (1998) 2715.

[35] J. Weitkamp, M. Breuninger, H.G. Karge, M. Hunger, in: M.M.J. Treacy, B.K. Marcus, M.E. Bisher, J.B. Higgins (Eds.), Proceedings of the 12th International Zeolite Conference, Materials Research Society, Warrendale, Pennsylvania, 1999, p. 2697, Part IV.

[36] J. Weitkamp, S. Ernst, L. Puppe, in: J. Weitkamp, L. Puppe (Eds.), Catalysis and Zeolites, Springer Verlag, Berlin, Heidelberg, New York, 1999, p. 327.

[37] P. Espeel, R. Parton, H. Toufar, J. Martens, W. Hölderich, P. Jacobs, in: J. Weitkamp, L. Puppe (Eds.), Catalysis and Zeolites, Springer Verlag, Berlin, Heidelberg, New York, 1999, p. 377.

The role of electrode microstructure on activation and concentration polarizations in solid oxide fuel cells[☆]

Anil V. Virkar[*], Jong Chen, Cameron W. Tanner, Jai-Woh Kim

University of Utah, Department of Materials Science & Engineering, 304 EMRO, 122 S. Central Campus Drive, Salt Lake City, UT 84112, USA

Abstract

Activation and concentration polarization effects in anode-supported solid oxide fuel cells (SOFC) were examined. The anode and the cathode consisted respectively of porous, composite, contiguous mixtures of Ni + yttria-stabilized zirconia (YSZ) and Sr-doped $LaMnO_3$ (LSM) + YSZ. The composite electrode provides parallel paths for oxygen ions (through YSZ), electrons (through the electronic conductor; Ni for the anode and LSM for the cathode), and gaseous species (through the pores) and thereby substantially decreases the activation polarization. The composite electrode effectively spreads the charge transfer reaction from the electrolyte/electrode interface into the electrode. At low current densities where the activation polarization can be approximated as being ohmic, an effective charge transfer resistance, R_{ct}^{eff}, is defined in terms of various parameters, including the intrinsic charge transfer resistance, R_{ct}, which is a characteristic of the electrocatalyst/electrolyte pair (e.g. LSM/YSZ), and the electrode thickness. It is shown that the R_{ct}^{eff} attains an asymptotic value at large electrode thicknesses. The limiting value of R_{ct}^{eff} can be either lower or higher than R_{ct} depending upon the magnitudes of the ionic conductivity, σ_i, of the composite electrode, the intrinsic charge transfer resistance, R_{ct}, and the grain size of the electrode. For an R_{ct} of 1.2 Ωcm^2, σ_i of 0.02 S/cm and an electrode grain size of 2 μm, the limiting value of R_{ct}^{eff} is 0.14 Ωcm^2 indicating almost an order of magnitude decrease in activation polarization. The experimental measurements on the cell resistance of anode-supported cells as a function of the cathode thickness are in accord with the theoretical model. The concentration polarization is analyzed by taking into account gas transport through porous electrodes. It is shown that the voltage, V, vs. current density, i, traces should be nonlinear and in anode-supported cells, the initial concave up curvature $(d^2V/di^2 \geq 0)$ has its origin in both activation and concentration polarizations. The experimental results are consistent with the theoretical model. © 2000 Elsevier Science B.V. All rights reserved.

Keywords: Electrode microstructure; Activation; Concentration polarization; Solid oxide; Fuel cell

1. Introduction

Solid state devices such as solid oxide fuel cells (SOFC) consist of a cathode, an electrolyte, and an anode. Two basic designs have been explored in the development of the SOFC; the electrolyte-supported

and the electrode-supported [1]. In the former, the electrolyte is the thickest component and is effectively the support structure. In electrolyte-supported cells, the thickness of the electrolyte, typically YSZ, is ≥ 150 μm with thin electrodes screen-printed on it [2,3]. In the latter, one of the two electrodes, either the cathode or the anode, is the thickest component and the support structure.

In electrolyte-supported cells the ohmic contribution is large due to high electrolyte resistivity. For this reason, such cells are being developed for operation at ~1000°C where the electrolyte resistivity is low, typically ~20 Ωcm. In cathode-supported cells, a 30–40 μm layer of YSZ is deposited on a porous LSM cathode of ~2 mm thickness [4]. Similarly, in anode-supported cells, a YSZ layer of 10–20 μm thickness is deposited on a relatively thick Ni + YSZ anode [1,5].

The overall performance of such devices is dictated by various polarizations; namely ohmic, activation, and concentration. The main contribution to the ohmic polarization is due to the electrolyte. A high ionic conductivity and a small electrolyte thickness are the desired characteristics of the solid electrolyte to minimize the ohmic contribution. Although various solid electrolytes with high ionic conductivities at moderate temperatures have been explored, yttria-stabilized zirconia (YSZ) is by far the most widely used solid electrolyte due to its excellent stability in both reducing and oxidizing environments, even though its conductivity is lower (resistivity is higher) than other materials such as ceria and Sr- and Mg-doped $LaGaO_3$ (LSGM). In electrolyte-supported cells, the typical YSZ membrane thickness is 150 μm. At 800°C, the resistivity of YSZ is about 50 Ωcm which translates into an area specific resistance (electrolyte contribution) of about 0.75 $Ωcm^2$. This value is very high with the result that the power density is rather low at temperatures below about 950°C. However, in electrode-supported cells, the YSZ electrolyte thickness need only be about 10 μm. With a 10 μm thick YSZ film as the electrolyte, the area specific resistance of the electrolyte is only about 0.05 $Ωcm^2$ at 800°C thus making an efficient operation of an SOFC at such a low temperature in principle possible. However, it is usually observed that despite a low ohmic contribution, the area

specific resistance of the cell as a whole may be several times larger. The reason is that activation and concentration polarizations can often outweigh the ohmic contribution. Thus, the minimization of the overall area specific resistance of cells requires an optimization of parameters which govern the activation and concentration polarization effects.

Activation polarization is related to charge transfer processes and thus depends upon the nature of electrode–electrolyte interfaces. In composite electrodes comprising a mixture of an ionic conductor and an electronic conductor, or in a single phase mixed ionic electronically conducting (MIEC) electrode, the process of charge transfer is expected to occur over some distance from the electrolyte/electrode interface into the electrode. That is, effectively the interface is diffuse insofar as the region over which charge transfer occurs. Concentration polarization is related to the transport of gaseous species through porous electrodes, and thus is related to the microstructure of the electrodes; specifically the volume percent porosity, the pore size, and the tortuosity factor. It is thus clear that a reduction in the overall area specific resistance of cells and a concomitant improvement in cell performance can be achieved only through a reduction in these two polarization effects. Indeed, recent work has shown that an area specific resistance less than 0.15 $Ωcm^2$ can be realized in anode-supported cells at 800°C with a maximum power density in excess of 1.8 $Ω/cm^2$ [6]. This was achieved by minimizing both activation and concentration polarizations. Effectively, the microstructures of the electrodes and the electrolyte/electrode interfaces were tailored to minimize these polarization effects. In this paper, these two polarization effects are examined in light of anode-supported SOFCs.

2. Activation polarization

The role of composite electrodes, comprising a mixture of a solid electrolyte and an electronic conductor, or a mixed ionic–electronically conducting (MIEC) material, on electrode kinetics has been examined by a number of researchers [7–11]. The rationale for the use of a composite or an MIEC

electrode is that it allows a spreading of the reaction zone from the electrolyte/electrode interface into the electrode. That is, effectively it results in a sort of a diffuse electrolyte/electrode interface wherein the charge transfer reaction occurs. Even though it has been proposed by some that in a mixed conducting material as an electrode the charge transfer reaction can occur over the entire surface, it is generally thought to occur at electrolyte–electrocatalyst–gas three phase boundaries (TPB), which are also high energy sites. In a single phase MIEC electrode, the charge transfer may predominantly occur at high energy sites such as grain boundaries and defects in the MIEC at the MIEC/gas phase interface. Tanner et al. [11] examined charge transfer reactions in a composite electrode. For the case of SOFC, for example, the analysis is applicable to Ni+YSZ anode and to LSM+YSZ cathode. It is known that the electrode overpotential at a Ni+YSZ electrode is usually negligible and much of the activation polarization can be attributed to the cathode. In this context, the following discussion is particularly applicable to Sr-doped LaMnO$_3$ (LSM)+YSZ cathode. The electrocatalytic properties of LSM over YSZ can in principle be described in terms of a phenomenological model such as the Butler–Volmer equation which relates the current density, i, to the activation overpotential, η_{act}, by

$$i = i_o \left\{ \exp\left(\frac{\alpha z F \eta_{act}}{RT} \right) - \exp\left(\frac{-(1-\alpha)zF\eta_{act}}{RT} \right) \right\}$$

(1)

where i_o is the exchange current density, α is the transfer coefficient, z is the number of electrons participating in the electrode reaction, F is the Faraday constant, R is the gas constant, and T is the temperature. In the low current density regime,

$$\eta_{act} \approx \frac{RT}{zFi_o} i = R_{ct} i$$

(2)

where R_{ct} given by

$$R_{ct} = \frac{RT}{zFi_o}$$

(3)

is the intrinsic charge transfer resistance in Ωcm^2. It is a function of the electrochemical properties of the electrocatalyst/electrolyte pair (LSM/YSZ here), and also a function of the TPB line length. Thus, it is a function of the particle size of LSM and the amount of LSM per unit area of YSZ. In what follows, R_{ct} will be treated as an empirical parameter, determined experimentally for a given electrocatalyst/electrolyte pair. In composite electrodes comprising a mixture of LSM+YSZ for instance, the reaction zone, that is the region over which the process of charge transfer occurs, is spread out from the electrolyte/electrode interface into the electrode. In such a case, it is expected that the activation overpotential, η_{act}, may be lower than that given by Eq. (2). Tanner et al. [11] defined an effective charge transfer resistance, R_{ct}^{eff}, given by

$$\eta_{act} \approx R_{ct}^{eff} i$$

(4)

Using this as a parameter for the design of composite electrodes, Tanner et al. [11] derived an expression for R_{ct}^{eff} terms of R_{ct} and the ionic conductivity of the electrode, σ_i, which describe the properties of the electrode/electrolyte interface and the electrolyte, respectively, and microstructural parameters of the electrode, namely the grain size and porosity. This equation is given by [11]

$$R_{ct}^{eff} = \frac{BR_{ct}}{B\left(\dfrac{1+\beta}{1+\beta \exp\left(-\dfrac{2h}{\lambda} \right)} \right)(1-V_\nu)\exp\left(-\dfrac{h}{\lambda} \right) + \left(\dfrac{1+\beta \exp\left(-\dfrac{h}{\lambda} \right)}{1+\beta \exp\left(-\dfrac{2h}{\lambda} \right)} \right)\lambda\left(1 - \exp\left(-\dfrac{h}{\lambda} \right) \right) + bV_\nu}$$

(5)

where

$$\lambda = \sqrt{\sigma_i B (1 - V_\nu) R_{ct}} \quad \text{and} \quad \beta = \frac{\sigma_i R_{ct} - \lambda}{\sigma_i R_{ct} + \lambda} \qquad (6)$$

in which B is the grain size of the electrolyte in the composite electrode, V_ν denotes the fractional porosity, and h is the electrode thickness. It is to be emphasized that the ionic conductivity of the electrode, σ_i in general may be different from that of the dense electrolyte membrane. For example, the electrolyte membrane may be of say YSZ but the electrode may contain doped ceria. The analysis assumes that the electronic conductivity of the electrode is much larger than the ionic conductivity, and gas transport through the electrode is not rate-limiting. Eq. (5) shows that the effective charge transfer resistance, R_{ct}^{eff} approaches R_{ct} as $h \rightarrow 0$, and achieves an asymptotic value with an increasing electrode thickness. It can be shown that as $h \rightarrow \infty$, the R_{ct}^{eff} is given by [11]

$$R_{ct}^{eff} \approx \sqrt{\frac{B R_{ct}}{\sigma_i (1 - V_\nu)}} \qquad (7)$$

as long as σ_i is not too small. As $\sigma_i \rightarrow 0$, the asymptotic value of R_{ct}^{eff} is given by

$$R_{ct}^{eff} \approx \frac{R_{ct}}{V_\nu} \qquad (8)$$

If $\sigma_i \rightarrow 0$, it means that only the three phase boundary (TPB) at the surface of the electrocatalyst/dense electrolyte membrane (e.g. LSM and the dense YSZ membrane) contributes to the charge transfer reaction; hence the presence of V_ν in the denominator of Eq. (8). Eqs. (6) and (7) also show the effect of the microstructural dimension, B, which is essentially the grain size of YSZ in the electrode. As an illustration, let us choose the following values: $R_{ct} = 1.2$ Ωcm^2, $\sigma_i = 0.02$ S/cm, $B = 2$ μm, and $= V_\nu = 0.35$. Then, the estimated value of the effective charge transfer resistance R_{ct}^{eff} is 0.14 Ωcm^2, almost an order of magnitude decrease in the charge transfer resistance, or an order of magnitude increase in the effective exchange current density, $i_{o(eff)}$. This shows the profound effect of composite, mixed conducting electrodes on electrode kinetics.

Eq. (7) shows that the effect of composite elec-

trode need not always be an enhancement in electrode kinetics. Indeed, Eq. (7) shows that

$$R_{ct}^{eff} \leq R_{ct} \quad \text{if} \quad \frac{B}{\sigma_i (1 - V_\nu)} \leq R_{ct}$$

However,

$$\frac{R_{ct}}{V_\nu} \geq R_{ct}^{eff} \geq R_{ct} \quad \text{if} \quad \frac{B}{\sigma_i (1 - V_\nu)} \geq R_{ct}$$

That is, the electrode kinetics could actually be suppressed if the electrode parameters are unfavorable; e.g. too coarse a microstructure (large B) and/or too low an ionic conductivity, σ_i, of the electrolyte material in the electrode (or too low an ionic conductivity of a single phase MIEC electrode). As an example, a suppression of the electrode kinetics would occur if an SOFC anode is made of Ni + an inert material, such as α-alumina. Since α-alumina is not an oxygen ion conductor, its σ_i is essentially zero. In such a case, the electrode polarization should actually increase when using such a composite electrode. Fig. 1 shows plots of R_{ct}^{eff} vs. log h (Eq. (5)) for various values of σ_i. Note that the R_{ct}^{eff} can either decrease or increase depending upon the value of σ_i for given values of R_{ct}, B and V_ν. The experimental results of Kenjo et al. [7] on composite electrodes showed that in some cases, the polarization resistance decreased with an increasing electrode thickness, while in other cases there appeared to be no effect of the thickness. These observations are at variance with the predictions of the model by Kenjo et al. [7]. However, their results are entirely consistent with the model presented by Tanner et al. [11].

Eq. (5) shows the dependence of R_{ct}^{eff} on h. For values of h greater than the critical value, R_{ct}^{eff} achieves an asymptotic value given by Eq. (7). An experimental verification of the dependence of the asymptotic value of R_{ct}^{eff} on electrode thickness was obtained on anode-supported solid oxide fuel cells with a varying cathode thickness. The anode (Ni + YSZ) thickness was typically 1 mm with an electrolyte (YSZ) thickness of ~20 μm. The cathode thickness was varied over a range between ~0 to ~85 μm. The cathode was prepared by first forming a porous layer of YSZ on the dense YSZ electrolyte layer, and then infiltrating an aqueous solution of
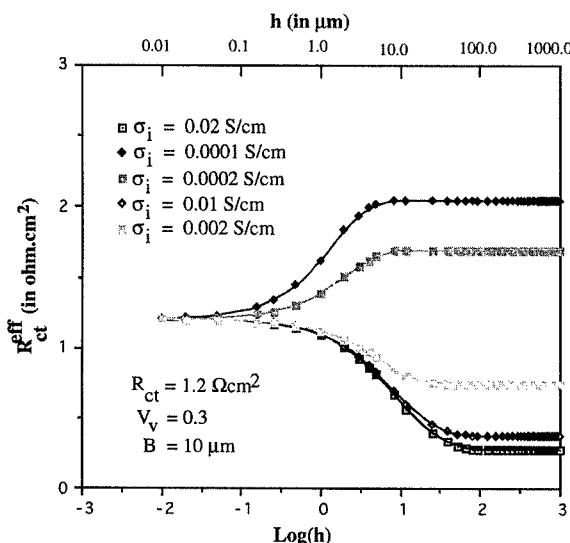
Fig. 1. Theoretically calculated values of the effective charge transfer resistance, R_{ct}^{eff}, for an intrinsic charge transfer resistance, R_{ct}, of 1.2 Ωcm^2 for several values of the ionic conductivity, σ_i, of the composite electrode. At high values of σ_i, the R_{ct}^{eff} decreases with an increasing electrode thickness, h, and achieves a limiting value. However, it is seen that for low values of σ_i, the R_{ct}^{eff} actually increases with the electrode thickness, h. That is, under such conditions, the composite electrode may actually suppress electrode kinetics (enhance electrode polarization).

La-nitrate, Sr-nitrate, and Mn-nitrate. After salt infiltration, the cells were heated to 1000°C to decompose the salts and form LSM. The voltage, V, vs. current density, i, performance curves were measured at 800°C with humidified hydrogen as the fuel and air as the oxidant. Fig. 2 shows the voltage vs. current density polarization curves for a number of cells for different cathode thicknesses. It is clearly seen that the performance increases with an increasing cathode thickness up to ~45 μm. For the cell with a cathode thickness of ~85 μm, the performance is somewhat lower than for the cell with a ~45 μm cathode. This is attributed to three possible reasons: (a) The method of deposition of the porous YSZ layer of the cathode was not optimized which led to a highly tortuous path for the transport of gaseous species. This presumably led to a significant concentration polarization, especially at larger cathode thicknesses. (b) In this nonoptimized method for the preparation of the cathode layer, some cracking of the layer with cracks parallel to the
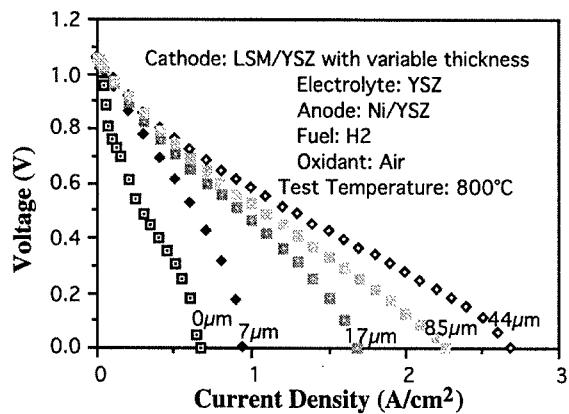
Fig. 2. The experimentally measured voltage, V, vs. current density, i, traces for anode-supported cells with varying cathode thicknesses. Note that, in general, the performance increases with an increase in cathode thickness.

electrolyte/cathode interface is possible. This may have led to some increase in the resistance. (c) The method of introducing the salt solutions was not optimized which may have led to a nonuniform distribution of the subsequent LSM formed after calcination. It is nevertheless clear that the cell performance indeed increases with an increasing cathode thickness. From the near linear regions of the voltage vs. current density traces, the cell resistance was measured. From this, the electrolyte area specific resistance, R_i, calculated using independently measured σ_i and the electrolyte thickness, was subtracted. Neglecting concentration polarization, this gives an approximate estimate of the effective charge transfer resistance, R_{ct}^{eff}. Fig. 3 shows the estimated (experimental) R_{ct}^{eff} vs. the cathode thickness (on a log scale). Also shown is a plot of R_{ct}^{eff} calculated using Eq. (5) with $R_{ct} = 1.2$ Ωcm^2, $\sigma_i = 0.02$ S/cm, $B = 5$ μm, and $V_v = 0.3$. Note that the agreement between the experimental data and the model is good.

The preceding discussion assumes the activation polarization to be ohmic; i.e. η_{act} being linearly proportional to the current density, i, which is applicable for current densities less than the exchange current density, i_o. The composite electrode thus increases the exchange current density, which may be termed the effective exchange current density, $i_{o(eff)}$, given by
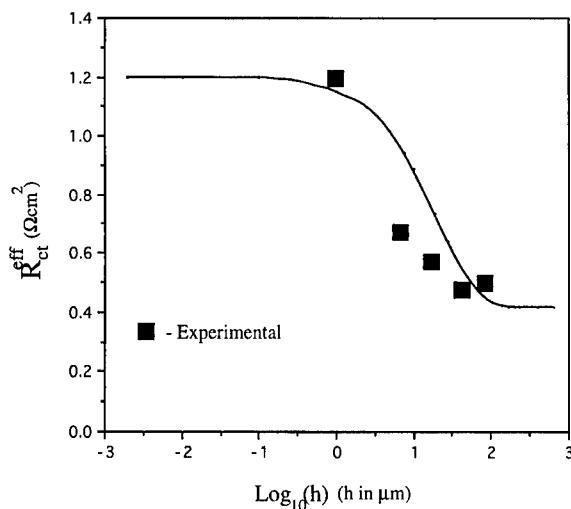
Fig. 3. A plot of R_{ct}^{eff} vs. cathode thickness, h (log scale), calculated using $R_{ct} = 1.2$ Ωcm^2, $\sigma_i = 0.02$ S/cm, and the grain size of YSZ in the cathode $= 5$ μm. Also plotted are the experimentally estimated (approximate, because the V vs. i traces are nonlinear) R_{ct}^{eff} from the data in Fig. 2. The data point corresponding to zero cathode thickness is that corresponding to the LSM paste directly applied on the dense YSZ layer, without a porous YSZ layer. Since the data point corresponding to zero cathode thickness actually represents that for a small but a nonzero thickness, and that zero thickness can not be shown on a log scale, this data point is shown at $h = 1$ μm.

$$i_{o(eff)} \approx \frac{RT}{zFR_{ct}^{eff}} \quad (9)$$

However, at large current densities, either the Butler–Volmer or the Tafel equation will be applicable. Preliminary calculations have shown that the composite electrode can be effective in decreasing the η_{act} in a similar manner, although an explicit analytical form is not available. In the Tafel limit, the η_{act} may be given by

$$\eta_{act} \approx a + b \ln i \quad (10)$$

where the parameters a and b are influenced by the electrode microstructure and the thickness. In what follows, it will be assumed that the activation polarization is adequately described by the Tafel equation and it will be incorporated into the analysis

of the voltage vs. current density traces of cells. Thus, it is tacitly assumed that the composite electrode modifies a and b such that $i_{o(eff)}$ is much larger than i_o.

3. Concentration polarization

Fig. 4 shows schematics of cathode-supported and anode-supported cells. In the former, the cathode is the thickest component of the cell and in the latter the anode is the thickest component. Fig. 4 also shows schematic variations of the partial pressures of the various gaseous species. The analysis of concentration polarization thus should begin with the analysis of the transport of gases through porous electrodes. In the anode, the principal gaseous species are H_2 and H_2O, and in the cathode they are O_2 and N_2. The basic equations describing an isothermal transport of gaseous species through porous electrodes for a mixture of two gases, A and B, are given by [12,13]

$$J_A = -D_A \nabla n_A + X_A \delta_A J - X_A \gamma_A \left(\frac{nB_o}{\mu}\right) \nabla p \quad (11)$$

$$J_B = -D_B \nabla n_B + X_B \delta_B J - X_B \gamma_B \left(\frac{nB_o}{\mu}\right) \nabla p \quad (12)$$

where
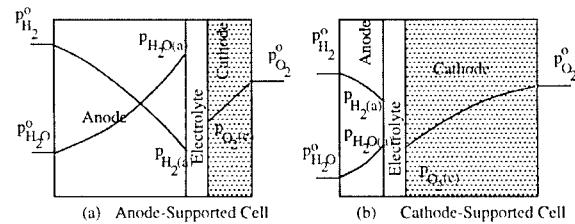
Fig. 4. Schematics showing the variation of partial pressures of hydrogen, p_{H_2}, and water vapor, p_{H_2O}, through the anode, and oxygen, p_{O_2}, through the cathode of: (a) an anode-supported cell, and (b) a cathode-supported cell.

$$\frac{1}{D_A} = \frac{1}{D_{AK(eff)}} + \frac{1}{D_{AB(eff)}}$$

$$\delta_A = \frac{D_{AK(eff)}}{D_{AK(eff)} + D_{AB(eff)}} \qquad \gamma_A = \frac{D_{B(eff)}}{D_{AK(eff)} + D_{AB(eff)}}$$

$$\frac{1}{D_B} = \frac{1}{D_{BK(eff)}} + \frac{1}{D_{AB(eff)}}$$

$$\delta_B = \frac{D_{BK(eff)}}{D_{BK(eff)} + D_{AB(eff)}} \qquad \gamma_B$$

$$= \frac{D_{AB(eff)}}{D_{BK(eff)} + D_{AB(eff)}} \tag{13}$$

In Eqs. (11) and (12), the fluxes of A and B are given by J_A and J_B, respectively, $D_{AB(eff)}$ is the effective binary diffusivity (taking into account the porosity and the tortuosity factor), $D_{AK(eff)}$ & $D_{BK(eff)}$ are the effective Knudsen diffusivities, n_A & n_B are the concentrations of A & B ($\#/cm^3$), respectively, $n = (n_A + n_B)$, X_A & X_B are the mole fractions, B_o is the permeability through the porous electrode, μ is the viscosity, p is the total pressure, and J is the total flux. The effective diffusivities are given by the intrinsic diffusivities multiplied by the porosity, V_v, and divided by the tortuosity factor, τ [12–14]. The parameters δ_A & δ_B, and γ_A & γ_B are as defined above. Eqs. (11) and (12) include two flux contributions; a diffusive flux and a viscous flux. The diffusive contribution consists of two terms; a free molecule or Knudsen flow (the terms containing $D_{AK(eff)}$ & $D_{BK(eff)}$), and a continuum part (the terms containing the effective binary diffusivities). The typical total pressure on the anodic and the cathodic sides is on the order of 1 atm or greater, and the typical pore size is ≥ 1 μm. Thus, in general it may be assumed that $D_{AK(eff)}$ & $D_{BK(eff)} \gg D_{AB(eff)}$. Thus, it will be assumed that D_A & D_B can be replaced by $D_{AB(eff)}$ [12]. That is, at high pressures, such as those of interest here, both D_A & D_B approach $D_{AB(eff)}$, the effective binary diffusion coefficient, and δ_A & $\delta_B \rightarrow 1$, and γ_A & $\gamma_B \rightarrow 0$. For the cathode, the D_{AB} is the binary diffusion coefficient for a mixture of oxygen, O_2, and nitrogen, N_2. For the anode, the binary diffusion coefficient is that for H_2 and H_2O. At room temperature, $D_{O_2-N_2} \approx$ 0.22 cm²/s and $D_{H_2-H_2O} \approx 0.91$ cm²/s [13]. If the fuel also contains CO and CO_2, then their transport

must also be accounted for. The dependence of diffusion coefficient on temperature is not very strong and to a first approximation it may be modified using the kinetic theory of gases. This suggests that for comparable porosities and electrode thicknesses, the concentration polarization effects in general should be less on the anode side.

If the electrode porosity and microstructure are functions of position, and/or $D_{B(eff)}$ is composition-dependent, the variation of partial pressures of the various species with position will not be linear. For this reason, the schematics given in Fig. 4 show nonlinear variations of partial pressures.

In a steady state, the equality

$$|j_{H_2}| = |j_{H_2O}| = 2|j_{O_2}| = \frac{iN_A}{2F} \tag{14}$$

must hold, where j_{H_2}, j_{H_2O} and j_{O_2} are respectively the fluxes of hydrogen through the porous anode, of water vapor through the porous anode and of oxygen through the porous cathode, and N_A is the Avogadro number. The flux equations were solved for the steady state, subject to the above flux equality requirement [6]. By incorporating the activation polarization (using the Tafel equation) and the concentration polarization (by solving the flux equations for transport through porous electrodes), it was shown that the voltage vs. current density behavior can be adequately described by [6]

$$V(i) = E_o - iR_i - a - b \ln i + \frac{RT}{4F} \ln \left(1 - \frac{i}{i_{cs}}\right)$$

$$+ \frac{RT}{2F} \ln \left(1 - \frac{i}{i_{as}}\right) - \frac{RT}{2F} \ln \left(1 + \frac{p_{H_2}^i i}{p_{H_2O}^o i_{as}}\right) \tag{15}$$

where E_o is the open circuit voltage (V), R_i is the area specific resistance (ohmic) of the cell (Ωcm^2), $p_{H_2}^o$ is the partial pressure of hydrogen in the fuel (outside of the anode), $p_{H_2O}^o$ is the partial pressure of water vapor in the fuel (outside of the anode), i_{as} is the anode-limiting current density (a current density at which the partial pressure of hydrogen at the anode/electrolyte interface is nearly zero), Amp/cm², and i_{cs} is the cathode-limiting current density (a current density at which the partial pressure of
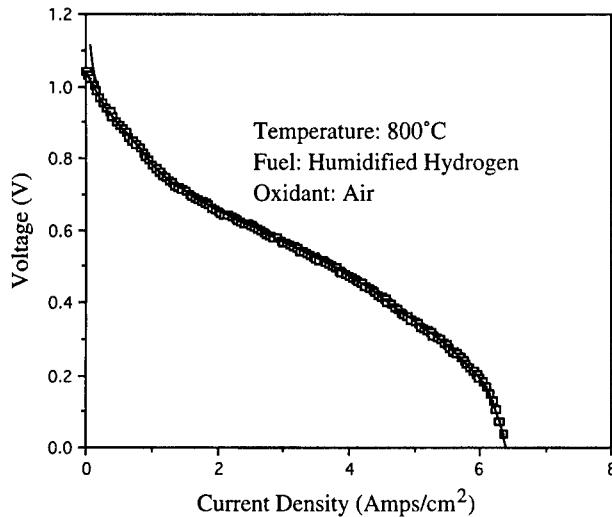
Fig. 5. The voltage, V, vs. current density, i, trace for an improved anode-supported cell tested at 800°C with humidified hydrogen as the fuel and air as the oxidant. The anode thickness was ~1.04 mm and the electrolyte (YSZ) thickness was ~10 μm. The symbols are the experimental data points while the curve is the best fit to Eq. (15). The parameters corresponding to the best fit are given in Table 1.

oxygen at the cathode/electrolyte interface is nearly zero), Amp/cm². The i_{as} and the i_{cs} can be given in terms of the respective electrode thicknesses, the respective effective binary diffusivities (which include the porosity and the tortuosity factors), and $p^o_{H_2}$ and $p^o_{O_2}$, respectively, where $p^o_{O_2}$ is the partial pressure of oxygen in the oxidant (0.21 atm for air as the oxidant) [6].

The data given in Fig. 2 are on some early cells wherein the porous YSZ layer for the prospective cathode was first deposited followed by the introduction of an aqueous salt solution of the cathode precursor. The microstructure in such cathodes was however rather coarse. Eq. (7) shows that the grain size of the YSZ in the cathode should be as small as possible. Thus, in later cells, a much finer cathode microstructure was developed. Also, in these cells, the YSZ electrolyte was typically about 10 μm in thickness; about half as thick as in cells for which the performance data are given in Fig. 2.

Fig. 5 shows a plot of V vs. i for an improved anode-supported cell tested at 800°C with humidified hydrogen as the fuel and air as the oxidant. The electrolyte thickness was about 10 μm and the anode thickness was about 1 mm. The corresponding power density vs. current density plot is shown in Fig. 6. As seen in Fig. 6, a power density as high as 1.9 Ω/cm²

was measured. Such a high power density was achieved by minimizing both activation and concentration polarizations through an optimization of the electrode microstructure. The symbols in Fig. 5 are the experimental data points and the curve is the best fit to Eq. (15). For an anode-supported cell, the
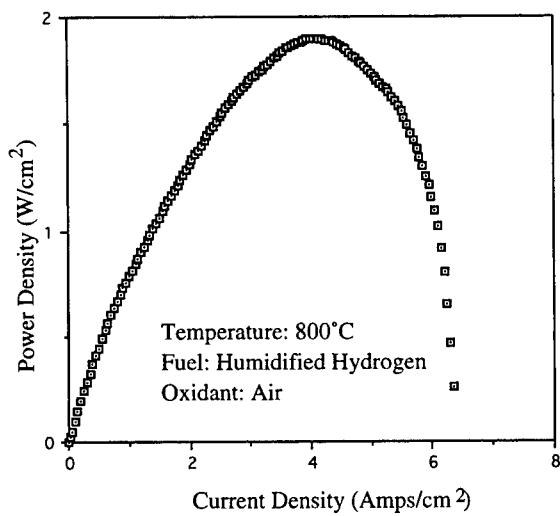
Fig. 6. The power density vs. current density, i, trace for the cell in Fig. 5. The maximum power density measured is ~1.9 Ω/cm².

anode thickness, l_a, is much greater than the cathode thickness, l_c, with the result that $i_{as} \ll i_{cs}$. Thus, the term containing i_{cs} from Eq. (15) can be neglected. Table 1 gives the parameters corresponding to the best fit to Eq. (15), as well as some of the experimentally measured parameters. The effective exchange current density, $i_{o(eff)}$, was estimated to be ~110 mA/cm^2, which is more than an order of magnitude higher than that corresponding to LSM on YSZ at 800°C. The electrolyte area specific resistance, R_i, from the best fit was estimated to be ~0.046 Ωcm^2. The electrolyte thickness was about 10 μm. With the resistivity of YSZ as ~50 Ωcm at 800°C, the estimated value of R_i is about ~0.05 Ωcm^2, in good agreement with the value obtained from the curve fit. Finally, the estimated value of the effective binary diffusivity on the anode side, $D_{a(eff)}$, is about 0.31 cm^2/s This value is reasonable when the porosity and the tortuosity factor are taken into account.

The theoretical analysis predicts that the initial concave-up curvature ($d^2V/di^2 \geq 0$) in V vs. i traces in anode-supported cells is due to two reasons [6]: (a) An activation polarization that is nonohmic (e.g. Tafel). (b) A concentration polarization that is

Table 1
Experimentally measured and curve-fitted parameters for the voltage vs. current density trace shown in Fig. 5

Parameter (description)	Parameter (symbol)	Measured	From the curve fit to the V vs. i
Anode thickness	i_a	1.04 mm	
Tafel coefficient	a		0.115
Tafel coefficient	b		0.0552
Effective exchange Current density	$i_{o(eff)}$		110 mA/cm^2
Cell area Specific Resistance (Ohmic)	R_i		0.046 Ωcm^2
Short circuit Current density	i_s	6.35 A/cm^2	
Anode limited Short circuit Current density	i_{as}		6.35 A/cm^2
Anode effective Binary diffusion Coefficient	$D_{a(eff)}$		0.31 cm^2/s
Maximum power Density		1.9 W/cm^2	

associated with too low a partial pressure of water vapor, embodied in the last term of Eq. (15). By contrast, any initial concave-up curvature ($d^2V/di^2 \geq 0$) in cathode-supported cells must entirely be due to a nonohmic activation polarization. The analytical form of the effect of concentration polarization in cathode-supported cells is such as to impart a convex-up curvature ($d^2V/di^2 \leq 0$) over the entire range of current densities [6]. Thus, if the activation polarization is ohmic, the curvature of V vs. i in cathode-supported cells must be convex-up ($d^2V/di^2 \leq 0$) over the entire range of current densities. Indeed, this has been observed in cathode-supported cells at 1000°C. In anode-supported cells, however, the initial curvature is expected to be concave-up ($d^2V/di^2 \geq 0$) even when the activation polarization is ohmic.

4. Summary

The present work has shown that the principal losses in SOFC are attributed to activation and concentration polarizations, especially when the electrolyte is a thin film supported on an electrode. Power densities as high as 1.9 Ω/cm^2 at 800°C were obtained with a thin film (~10 μm) of YSZ deposited on a relatively thick (1 mm), porous Ni + YSZ anode. The activation polarization on the cathode side can be substantially decreased by using a composite electrode comprising a mixture of an electrocatalyst, such as LSM, and an oxygen ion conductor, such as YSZ. The theoretical analysis predicts that activation polarization, as defined in terms of an effective charge transfer resistance, R_{ct}^{eff}, can decrease or increase with an increasing cathode thickness and attain a limiting value. For the set of parameters applicable to LSM as the electrocatalyst and YSZ as the oxygen ion conductor, the experimental results show that R_{ct}^{eff} decreases with an increase in the cathode thickness. Thus, a composite electrode of LSM + YSZ is very effective in lowering the activation polarization. It is known that activation polarization at the Ni + YSZ anode is generally much smaller than at the cathode. This suggests that R_{ct}^{eff} at the Ni + YSZ anode must be very small and that a composite electrode of Ni + YSZ is very effective in lowering the activation polarization at the anode. The

analysis of gas transport through a relatively thick anode shows that the V vs. i traces are expected to be nonlinear, in accord with the experimental results. Further, the analysis also shows that the initial concave-up curvature ($d^2V/di^2 \geq 0$) in anode-supported cells has its origin in both activation as well as concentration polarizations. The present results show that the polarization effects in SOFC can be minimized through a microstructural optimization of the electrodes. As far as the activation polarization is concerned, the use of composite electrodes spreads the reaction zone from the electrolyte/electrode interface some distance into the electrode. In this sense, the electrolyte/electrode interface is a functionally diffuse interface.

Acknowledgements

References

[1] N.Q. Minh, J. Am. Ceram. Soc. 76 (1993) 563.

[2] N. Hisatome, K. Nagata, S. Kakigami, H. Omura, in: Fuel Cell Seminar Program and Abstracts, 1996 Fuel Cell Seminar, Orlando, FL, November 17–20, 1996, p. 194.

[3] Y. Miyake, M. Kadowaki, Y. Akiyama, T. Yasuo, S. Taniguchi, K. Nishio, in: Fuel Cell Seminar Program and Abstracts, 1996 Fuel Cell Seminar, Orlando, FL, November 17–20, 1996, p. 28.

[4] S.C. Singhal, in: Meeting Abstract of the Third International Symposium on Ionic and Mixed Conducting Ceramics, the 1997 Joint International Meeting, the Electrochemical Society and the International Society of Electrochemistry, Paris, France, August 31–September 5, 1997, p. 2498.

[5] H.P. Buchkremer, U. Diekmann, L.G.J. de Haart, H. Kabs, U. Stimming, D. Stover, in: 1996 Fuel Cell Seminar, sponsored by the Fuel Cell Organizing Committee, Washington DC, 1996, pp. 175–178.

[6] J.-W. Kim, A.V. Virkar, K.-Z. Fung, K. Mehta, S.C. Singhal, J. Electrochem. Soc. 146 (1) (1999) 69–78.

[7] T. Kenjo, S. Osawa, K. Fujikawa, J. Electrochem. Soc. 138 (1991) 349.

[8] T. Kenjo, M. Nishiya, Solid State Ionics 57 (1992) 295.

[9] H. Deng, M. Zhou, B. Abeles, Solid State Ionics 74 (1994) 75.

[10] T. Kenjo, Y. Yamakoshi, Bull. Chem. Soc. Jpn. 65 (1992) 995–1001.

[11] C.W. Tanner, K.-Z. Fung, A.V. Virkar, J. Electrochem. Soc. 144 (1) (1997) 21–30.

[12] E.A. Mason, A.P. Malinauskas, Gas Transport in Porous Media: The Dusty Gas Model, Elsevier, Amsterdam, 1983.

[13] R. Jackson, Transport in Porous Catalysts, Elsevier, Amsterdam, 1977.

[14] E.L. Cussler, Diffusion: Mass Transfer in Fluid Systems, Cambridge University Press, Cambridge, 1995.

A novel technique for imaging electrochemical reaction sites on a solid oxide electrolyte

T. Kawada[a,*], T. Horita[b], N. Sakai[b], H. Yokokawa[b], M. Dokiya[c], J. Mizusaki[a]

[a]Research Institute for Scientific Measurements, Tohoku University 2-1-1, Katahira, Aoba-ku, Sendai 980-8577 Japan
[b]National Institute of Materials and Chemical Research, Tsukuba Research Center, Ibaraki 305, Japan
[c]Institute of Environmental Science and Technology, Yokohama National University, Tokiwadai, Hodogaya-ku, Yokohama 240, Japan

Abstract

Oxygen isotope was used to investigate the active electrochemical reaction site on a solid oxide electrolyte. The isotope exchange reaction was performed under current flow, and the distribution of the incorporated isotope was analyzed by a secondary ion mass spectrometer. The results were compared with calculations using a simple model. The lateral resolution of the present method was estimated to be around 1 μm. The quenching process and the imaging resolution should be improved to investigate further details. © 2000 Elsevier Science B.V. All rights reserved.

Keywords: Electrochemical reaction site; $^{18}O/^{16}O$; Isotope exchange; SIMS

Materials: Platinum; Yttria stabilized zirconia; Oxygen

1. Introduction

Kinetics of electrochemical reactions on a solid oxide electrolyte have been widely investigated by many researchers not only from scientific interest but also from technological requirements. The improvement of the electrodes can often be a key technology in a practical application such as gas sensors, solid oxide fuel cells, or oxygen separation membranes. Although much effort has been made to understand the electrode reaction process, there still remain many unsolved problems. Among them, one of the most essential question is "where in the electrode does the electrochemical reaction take place?". In a gas/porous electrode/oxide electrolyte system, the most preferable electrochemical reaction site is undoubtedly a triple phase boundary (TPB) of electrode/electrolyte/gas, where electron, oxide ion and the gaseous species meet together [1]. In some cases, however, the active reaction area extends to the electrode surface, to the free electrolyte surface or to the electrode/electrolyte two phase boundaries. Since the extension of the reaction site is related to the kinetic parameters, misunderstanding will lead to a wrong interpretation of the experimental data as pointed out by several authors [2–4]. The knowledge of the active reaction site is thus essential for the basic kinetic analysis of the experimental data.

---

*Corresponding author. Tel.: +81-22-217-5341; fax: +81-22-217-5343.
E-mail address: kawada@rism.tohoku.ac.jp (T. Kawada)

Similarly, in designing a practical electrode, knowledge on both microscopic and macroscopic current distribution is necessary. The microscopic distribution is related to the reaction kinetics as mentioned above and is important for the design of the electrode material and microstructure. The macroscopic current distribution is important in improvement of current collection. The both will seriously affect the electrode performance.

Regardless of the importance, an experimental technique has never been developed for getting direct information on the electrode reaction site. So far, the research works have been performed only with indirect experiments, e.g. measurement of I–V curve or ac impedance responses as a function of the electrode morphology. One of the ideas to get direct information on the reaction site is to observe the trace of the oxide ion migration in the electrolyte. This may be possible by using an oxygen isotope, $^{18}O_2$, and secondary ion mass spectrometer (SIMS) with imaging capability. The similar technique has been successfully applied in the investigation of diffusion coefficients or fast diffusion paths in ceramics [5–7] or preferable oxidation sites in metals.

The authors have been trying to develop an experimental technique to visualize the active reaction site on a solid oxide electrolyte with a porous platinum electrode [8] and with a patterned $(La,Sr)MNO_3$ electrode [9]. In this paper, the experimental procedure for the isotope imaging is reported in detail. A numerical calculation is performed to evaluate the preferable experimental condition for the active site imaging. The experimental result with a porous Pt electrode will be compared with the calculation. The merit and the limitation of this method will be discussed.

2. The method for imaging the active site

2.1. Experimental procedure

Fig. 1 outlines the experimental procedure for determining the active reaction site on a solid oxide electrolyte. The sample is first equilibrated in a certain atmosphere, and then exposed to ^{18}O enriched gas of the same oxygen potential. After a
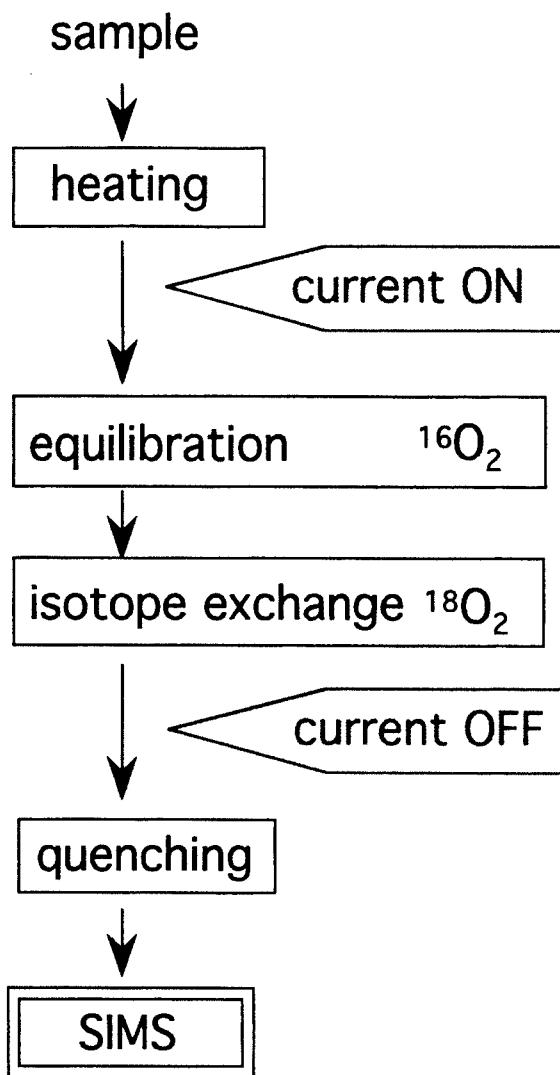
Fig. 1. Schematic diagram of the experimental procedure for imaging electrochemical active sites on a solid oxide electrolyte.

period the sample is quenched and the isotope distribution is measured by SIMS. This sequence is quite similar to that used for determining oxygen isotope diffusion coefficient [7]. The only difference is that the sample has electrodes and oxide ionic current is flowing during the equilibration and the isotope exchange processes. If the cathodic current is applied to the electrode, the isotope enriched oxygen will be incorporated from the active electrochemical reaction site, and the resulting isotope distribution in the quenched sample will give information on the

active reaction site. In principle, the anodic reaction can also be imaged by comparing the isotope profiles with and without electrical current. For such an analysis, however, a well defined electrode and highly reproducible experiments are required, which are technologically difficult in our present equipment. In this report, only cathodic reaction is considered.

2.2. Required conditions

The isotope mapping of the active reaction site is not always possible. This is because the isotope exchange reaction takes place not only by the electrochemical oxygen incorporation at the active site but also by the exchange of neutral oxygen on the free electrolyte surface. If the surface exchange process is too fast, the isotope concentration becomes high at the surface and will hide the trace of the electrochemically incorporated isotope. The surface isotope concentration is determined by the ratio of the surface reaction rate k^* and the isotope diffusion coefficient D^*. When k^* is much larger than D^*, the isotope concentration on the sample surface is close to that in the gas phase. In such a case, the electrochemical incorporation of the isotope is not detectable. The atmosphere, temperature and annealing time in the experiment must be chosen to accomplish that k^* is sufficiently smaller than D^*. The other requirement is fast quenching. Otherwise, the isotope distribution pattern will diffuse away in the quenching procedure. In case of YSZ electrolyte, oxygen isotope diffuses several microns if it is kept for 10 s at 1000 K. Thus, the sample temperature must decrease below 1000 K in less than a second to get the imaging resolution higher than 1 μm.

2.3. Numerical calculation

Numerical calculations were performed to predict the isotope distribution pattern around the active reaction site. The differential equation of Fick's second law was solved using a finite element method ('MARC K-6', Nippon Marc Co.). A simple model of a stripe shaped electrode was defined as shown in Fig. 2. For simplicity, the following boundary conditions were used:
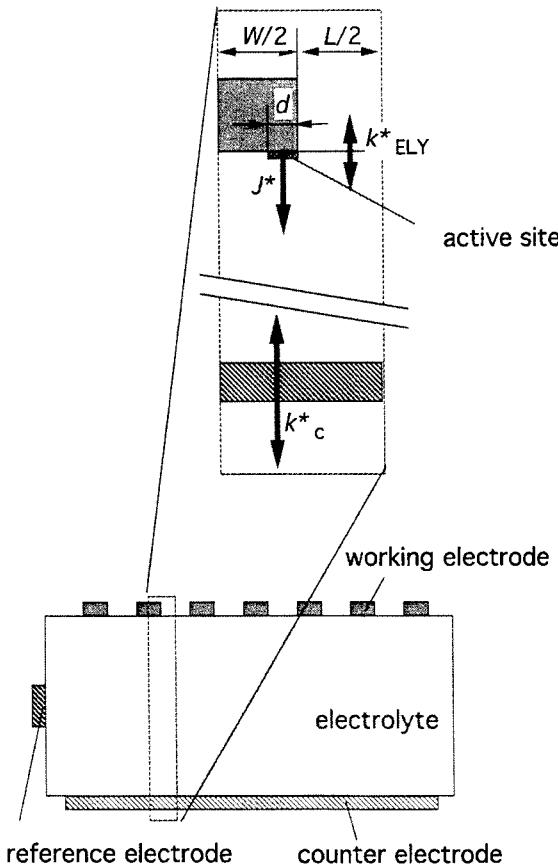
Fig. 2. A two dimensional electrode model to simulate the isotope distribution pattern. The working electrode is stripe shaped. The calculation was done for the unit cycle surrounded by the square in the figure. The parameters used for the calculation are listed in Table 1.

1. The isotope flux is zero on the electrode/electrolyte two phase boundary except for the electrochemical reaction site.
2. The active electrochemical reaction site has a limited width around the TPB, and the oxide ion (isotope) flux is homogeneous inside this area.
3. Only isotope diffusion is considered inside the electrolyte. Migration of the oxide ion under the electrical field is neglected. The effect of the electrical current is included in the calculation as the increase of isotope incorporation flux at the active reaction site.
4. The ionic flux density at the reaction site was estimated by dividing the apparent current density by the total TPB length in unit area.

5. The oxygen isotope diffusion coefficient in the electrolyte and the surface exchange coefficient on the free electrolyte surface were estimated from a separate isotope diffusion experiment.
6. The surface exchange rate at the counter electrode was assumed to be infinity.

The parameters used in the calculation are listed in Table 1.

Fig. 3 shows the calculated isotope concentration

Table 1
The parameters used in the calculation of isotope distribution

Electrode pattern width	W	5 μm
Electrode pattern distance	L	5 μm
Active reaction site width	d	0.0625 to 1 μm
Temperature	T	973 K
Isotope diffusion coefficient	D^*	5.7×10^{-8} cm^2 s^{-1}
Surface exchange coefficient	k^*	3.0×10^{-8} cm s^{-1}
Apparent current density	J	0.15–15 mA cm^{-2}
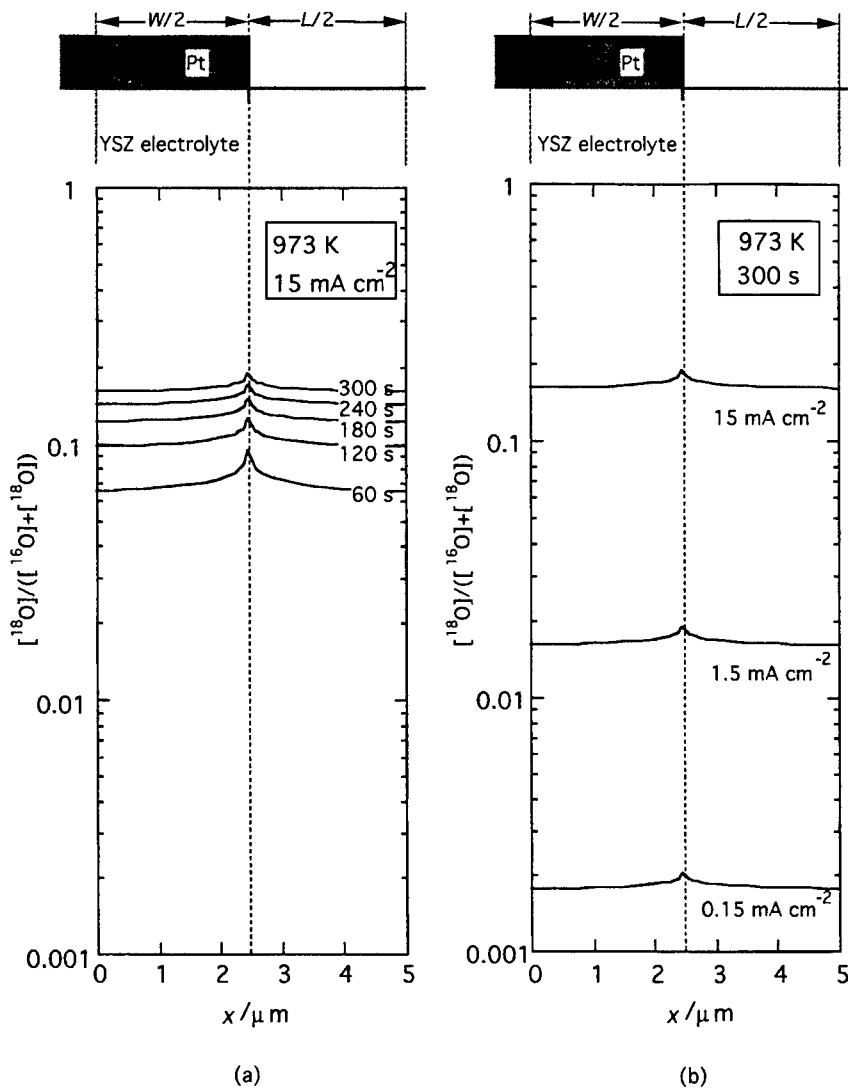
Fig. 3. Dependence of the calculated isotope concentration profile on reaction time (a) and ionic current density (b). The parameters in the standard condition are listed in Table 1.
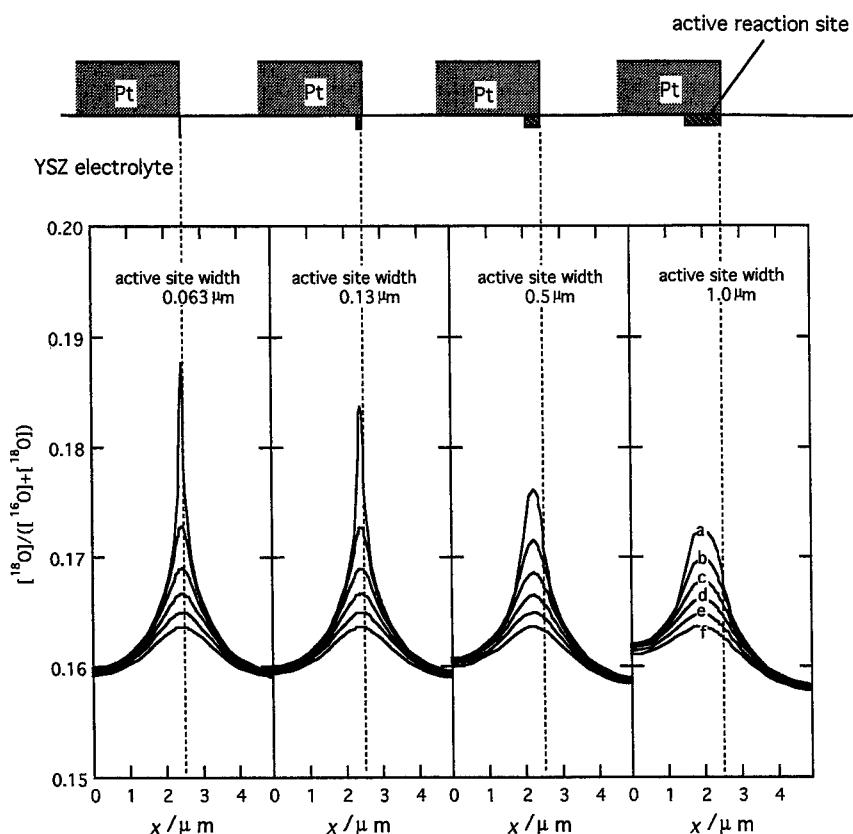
Fig. 4. Dependence of calculated isotope distribution on the active site width. The curves are isotope concentration profile in the depth of the electrolyte (a) 0 μm (b) 0.031 μm, (c) 0.063 μm, (d) 0.09375 μm, (e) 0.125 μm and (f) 0.15625 μm.

profile at the surface of the electrolyte as functions of (a) the reaction time and (b) the ionic current density. The active reaction site is assumed to extend 0.063 μm from TPB into the electrode/electrolyte two phase boundary. Since the diffusion coefficient is high, the incorporated isotope diffuses quickly into the whole surface of the electrolyte. In the vicinity of TPB, however, the peak of the isotope concentration remains distinguishable from the other parts. If the peak is detected by the SIMS analysis, the information on the reaction site will be obtained. For getting a clearer contrast, shorter reaction time and larger current density are preferred in principle but with small difference.

Fig. 4 compares the calculated profiles with different active site width. The curves in each graph represent the equi-depth isotope concentration profile in the electrolyte which corresponds to the ex-

perimental data obtained by successive sputtering and line scanning with SIMS. The high isotope concentration site is observed in the vicinity of the TPB at the surface. The intensity of the isotope fades rapidly with depth in the electrolyte. The peak of the isotope concentration is higher and sharper when the active reaction site is narrower. The resolution of the measurement depends on the lateral resolution of the SIMS equipment. It depends also on the quenching rate which must be fast enough to keep the original distribution of the isotope.

3. Experimental details

3.1. Sample preparation

Commercially available YSZ powder (Y_2O_3 8

mol% doped ZrO_2: TOSOH TZ8Y) was used for preparation of the electrolyte. The powder was pressed into a pellet and sintered at 1780 K for 5 h. The relative density was higher than 99%. The pellet was cut into 5 mm×5 mm×0.3 mm, and the surfaces were polished with diamond paste down to 1/4 micron.

Two platinum electrodes were applied to both surfaces of the sample with an area of 3 mm×3 mm as a working and a counter electrodes. A reference electrode of a smaller size was applied at the periphery of the sample. Each electrode was applied by painting an appropriate amount of platinum paste (Tanaka, TR7905). After heating at 1400 K for 5 h, grain growth of platinum occurred keeping the two dimensional network. The optical photograph of the surface of the sample is shown in Fig. 5. The platinum grains and the bare surface of the YSZ are

Fig. 5. Optical photograph of the Pt/YSZ surface. Brighter parts are the platinum electrode particles.

both visible from the surface. The line between those two parts corresponds to the TPB.

3.2. Isotope exchange

Fig. 6 shows the isotope exchange apparatus. The gas circulation chamber consisted of two parts. The left hand side in Fig. 6 is the circulation loop for normal oxygen (natural isotope abundance), and the right hand side is for $^{18}O_2$ enriched (97%) gas. The oxygen pressure in the both loops are adjusted to be same by using a pressure gauge. The sample chamber was connected to the circulation loops via a six-way valve which can choose one of the gases to flow over the sample. As is shown in Fig. 7, three lead wires and a thermocouple were connected to the electrical apparatus through the top part of the cell. Separable connectors ('Quick connects', Swagelock Co.) were used so that the sample chamber was able to be disconnected after isotope exchange operation. An infra-red furnace was used for heating the sample. Gas flowed from the inner tube through the outer tube.

At first, the sample was exposed to the normal oxygen gas and was heated up to a certain temperature (773–1173 K). A potentiostat (TOHO GIKEN 2020) was used to supply current to the sample keeping a constant voltage between the working and the reference electrodes. After a steady state current was reached, the gas was changed abruptly to the $^{18}O_2$ enriched one by the six-way valve. After annealing in $^{18}O_2$, the sample chamber was disconnected from the gas circulation chamber. At the same time, the sample was brought out of the focus of the infra-red furnace, and immediately cooled by blowing cooling gas against the wall of the sample tube. The sample was cooled from 1000 K to 700 K in less than 5 s, and to room temperature in 15 s.

3.3. SIMS analysis

Measurements of the isotope ratio were carried out with a CAMECA ims-5f SIMS equipment. A cesium primary ion beam (Cs^+) was bombarded on the sample at 14.5 keV. The negative secondary ion beam was accelerated at -4.5 keV and analyzed in the mass spectrometer with electronic and magnetic
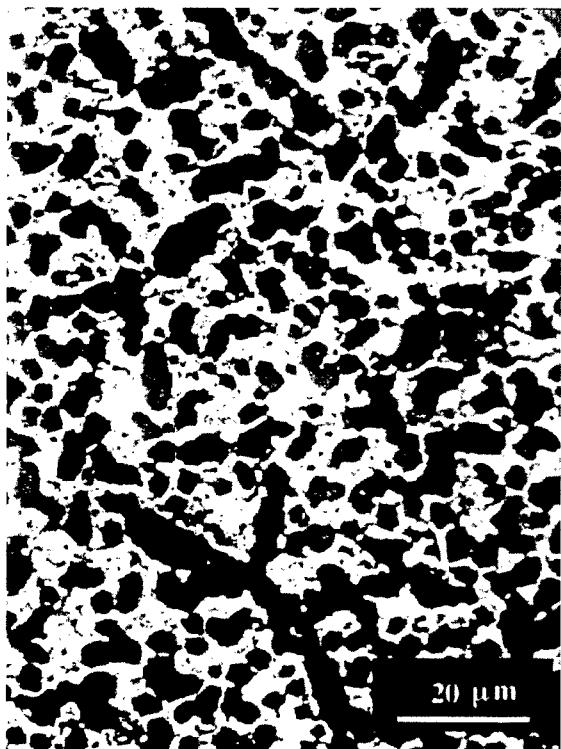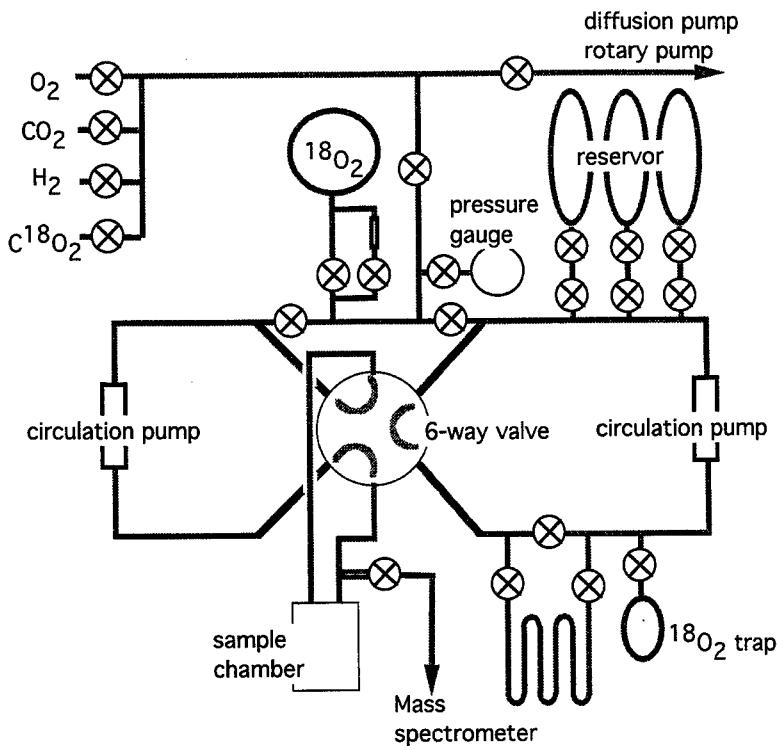
Fig. 6. Schematic view of the isotope exchange equipment (gas circulation system).

sectors. The mass resolution $M/\Delta M$ was about 300 in a normal operation mode, and higher than 7000 in a 'high resolution' operation mode. To distinguish $^{18}O^-$ from $H_2^{16}O^-$, high mass resolution measurements were performed. In all the cases, the signal of $H_2^{16}O^-$ was found to be much smaller than that of $^{18}O^-$. Thus, the imaging experiments were performed in the normal resolution. Since YSZ is an insulator at low temperature, a gold mesh of 250 μm pitch was placed on the sample, and an electron gun was used to compensate for the electric charge.

Two different imaging methods ('microscope' mode and 'micro-probe' mode) were applied to observe the distribution of a selected mass on the sample surface. In the microscope mode, the secondary ion image was focused on a channel plate and observed directly on the screen. The digital image was acquired with a position sensitive detector. The lateral resolution in this mode was about 1 to 2 μm. For a higher resolution image, the micro-probe mode

was used, in which the primary beam was focused and scanned on the sample. The lateral resolution depends on the size of the focused primary ion beam, which was around 0.2 μm in our equipment.

4. Results and discussion

4.1. Polarization behavior at 973 K

Fig. 8 shows a steady state polarization curve at 973 K in 0.2 bar oxygen. It showed a characteristic behavior of a Pt electrode on a YSZ electrolyte as reported by Mizusaki et al. [2]. The isotope exchange experiment was performed at the polarization voltage of -0.5 V vs. the reference electrode. The apparent current density over the total electrode area was about -1.5 mA cm^{-2}. After keeping the voltage for 1 h, the $^{18}O_2$ enriched gas was introduced by the six-way valve. The change in the current density was
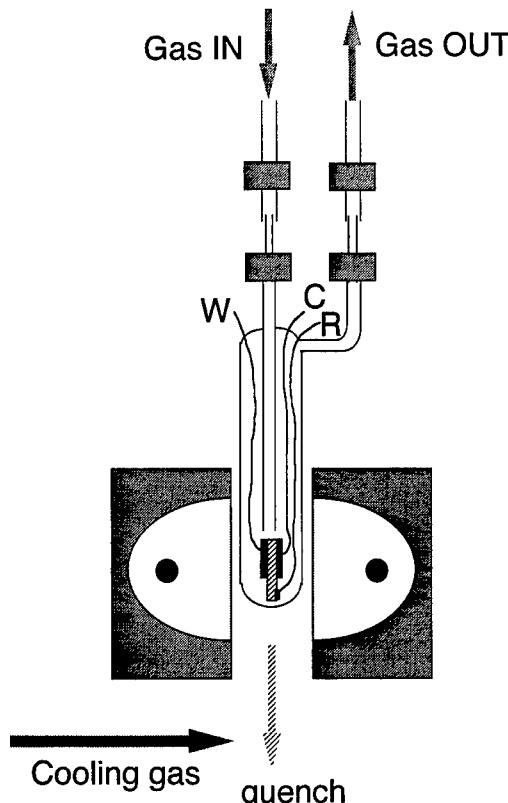
Fig. 7. Sample chamber for the isotope exchange with applying current. The lead wires W, C, R are connected to the working, the counter, and the reference electrodes, respectively.

Fig. 8. Steady state polarization curve for Pt/YSZ sample at 973 K in 0.2 bar oxygen.

less than 5% before and after the isotope exchange. The sample was kept for 5 min in $^{18}O_2$, and then, quenched and transferred to SIMS analysis.

4.2. Isotope distribution mapping

Fig. 9(a) shows the $^{16}O^-$ and $^{18}O^-$ secondary ion distribution at the surface of the sample measured by SIMS in the 'microprobe' mode. The brighter spot in the figure represents the higher secondary ion signal. The dark parts correspond to the platinum particles which cover the oxide electrolyte surface. What should be noted in Fig. 9(a) is that the signal of $^{16}O^-$ came homogeneously from the electrolyte part, whereas that of $^{18}O^-$ was localized along the edge of the electrolyte area, i.e. on the triple phase boundaries (TPB).

In Fig. 9(a), not all of the TPB lines were visible

because some are behind the platinum particles and could not be hit by the primary ion beam of which the incident angle was 30° to the normal. In order to observe the whole TPB lines, the platinum particles were removed by sputtering with a larger primary ion beam $(1 \times 10^{-8} A)$. After 2 min of sputtering, the primary beam current was reduced ($<1 \times 10^{-10}$ A) and focused again, and the image was acquired. The sputtering and data acquisition cycle was repeated several times. Fig. 9(b)–(d) show the sequential images of the isotope distribution aligned in the order of the sputtering time. By removing the platinum electrode, all of the TPB lines appeared gradually. In the $^{18}O^-$ image, the high intensity sites in the first figure disappeared with sputtering, and new high intensity sites came out around the sputtered edges of the Pt particles. They disappeared by further sputtering. This means that the active reaction site is actually localized around TPB lines.

For quantitative representation, the data in Fig. 9 were scanned on the line A–B, and plotted in terms of total oxygen intensity and the isotope ratio in Fig. 10. Several peaks were observed in the isotope ratio plot. Among them, some peaks were located where the total oxygen intensity is small; i.e. on the platinum particles. Those peaks disappeared much faster than the others by sputtering. They probably came from any contamination on the Pt electrode.
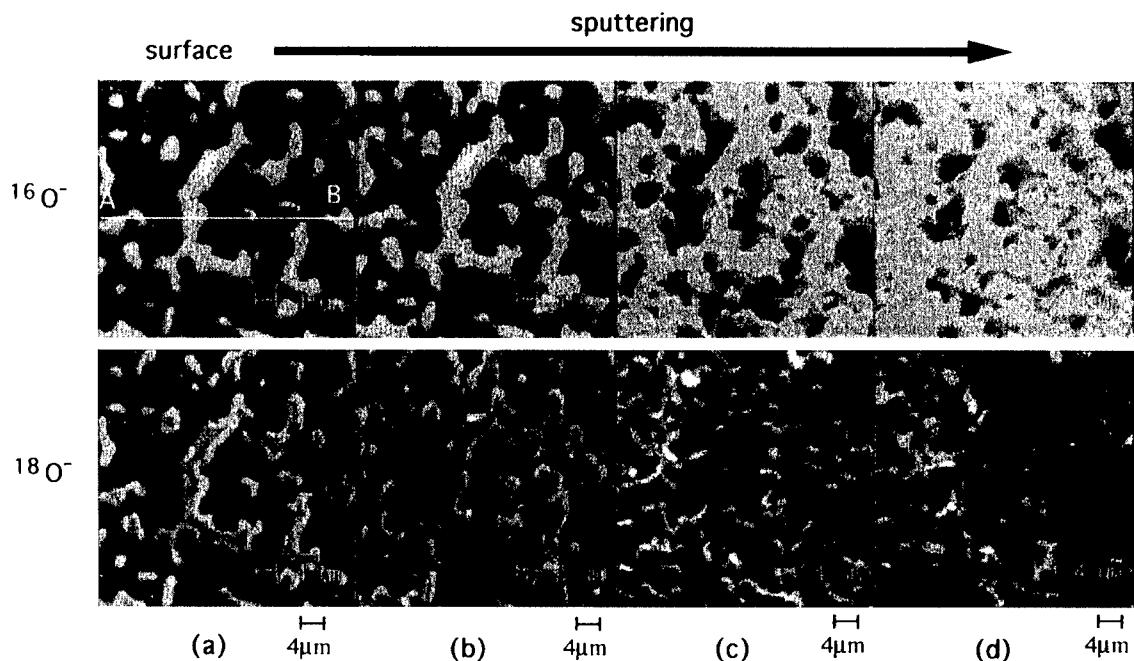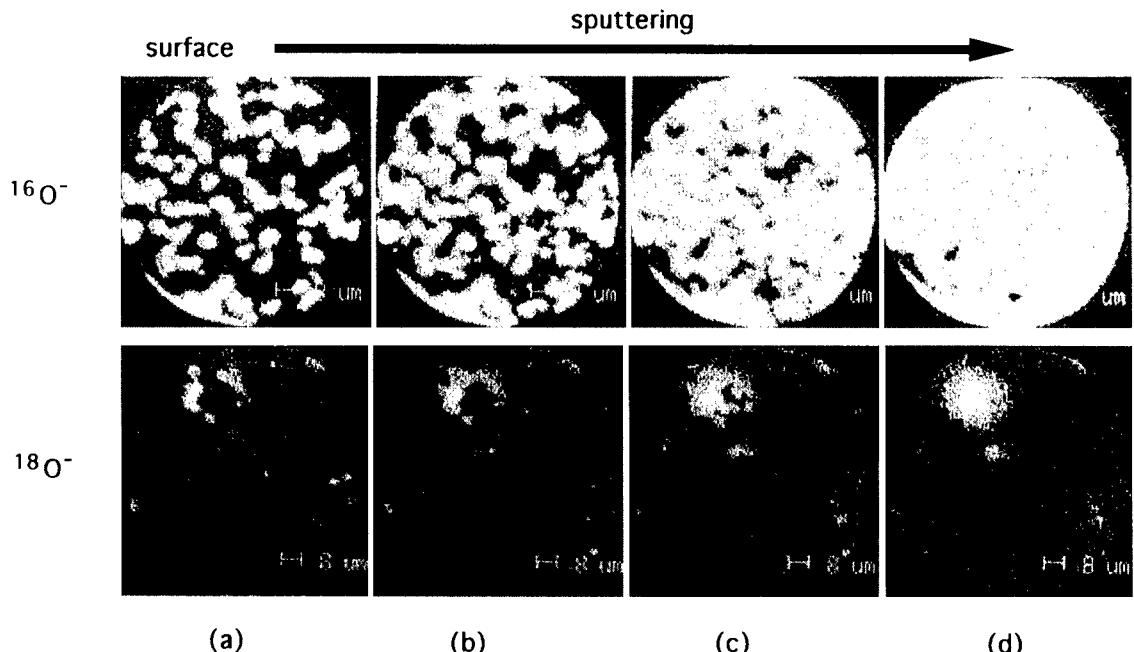
Fig. 9. ^{16}O and ^{18}O distribution in the sample treated at 973 K in 0.2 bar oxygen ^{18}O under cathodic polarization (−0.5 V) for 5 min. Images were taken at the surface (a); after sputtering 2 min. (b); 4 min. (c); and 6 min. (d).

The other peaks were all located around the TPB lines. They are the trace of the electrochemical oxygen incorporation.

The observed isotope profile can be compared with those of the model calculation shown in Fig. 4. The isotope concentration at the surface was around 0.2 at the peaks and 0.05 to 0.1 at the valleys. Most of the peaks disappeared at the last sputtering cycle. Though the exact depth of one sputtering cycle was not clear, it is roughly estimated to be 10–100 nm. From those data, the active reaction site width is estimated to be less than 1 μm. However, the detail of the observed profile is different from the calculation. The further discussion is difficult in the present experiment. In order to determine the reaction site extension in more detail, the electrode of a well defined morphology should be tested, and the quenching speed and the lateral imaging resolution must be improved. Also, the calculation may have to include the effect of oxide ion migration under the electrical field. Due to those limitations, the resolution of the active site imaging in the present experiment may be around 1 μm.

4.3. Reaction site expansion at lower temperature (773 K)

Fig. 11 shows the $^{16}O^-$ and $^{18}O^-$ images of the sample treated under current flow at 773 K. The images were taken in the microscope mode. Unlike the results at 973 K, the $^{18}O^-$ isotope did not distribute along every TPB line. Some 'hot spots' were observed for the isotope incorporation reaction. The existence of the hot spot is an important problem in a practical application. The hot spot generation can be initiated by the existence of any inhomogeneity in morphology of the electrode particles. Current and mass flow may favor extraordinary points such as a valley or a bay of the electrode particles. The existence of any impurity or defect may cause the inhomogeneity of the reaction rate as well. When a hot spot of the reaction is generated, the temperature will increase around those sites and the reaction site becomes further inhomogeneous.

On those hot spots, the active reaction site extended under the platinum electrode particles. When the sputtering process proceeds, the high intensity parts
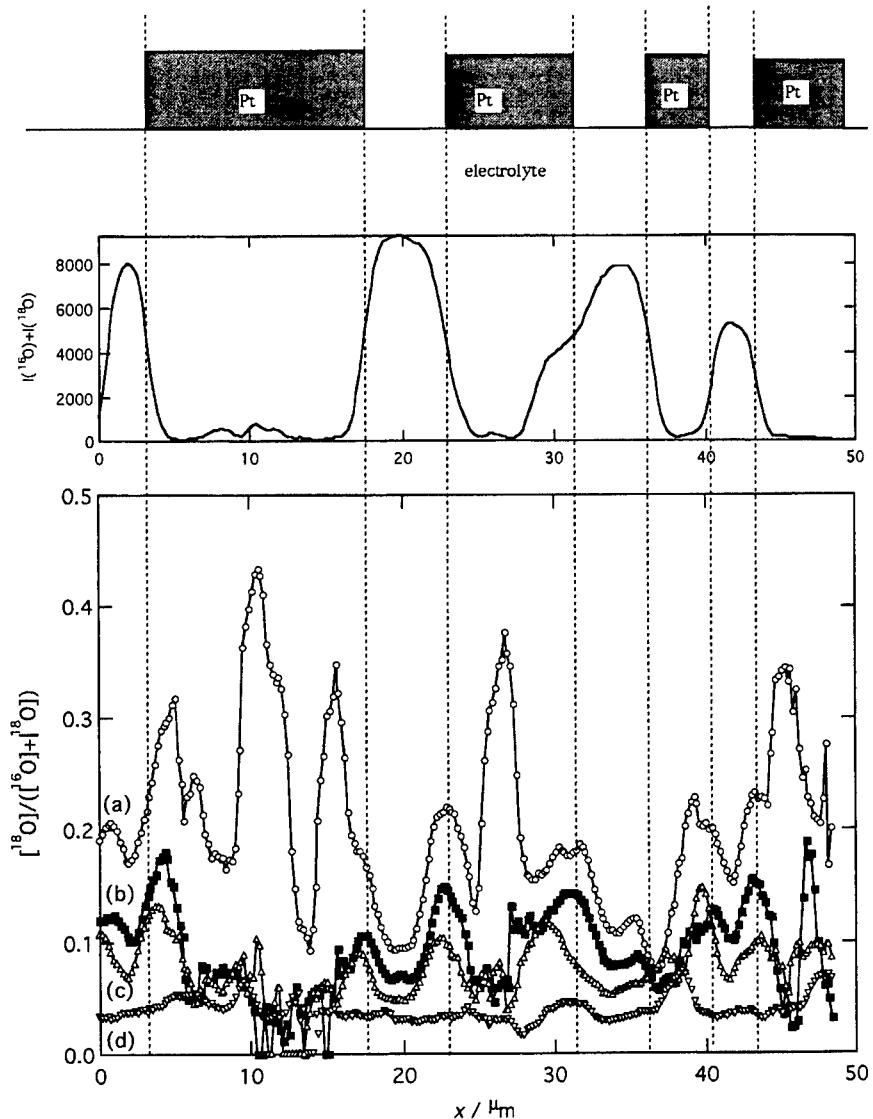
Fig. 10. Total oxygen and isotope concentration profile on the line A–B in Fig. 9. The total oxygen profile is the sum of the ^{16}O and ^{18}O signals in Fig. 9(a).

in $^{18}O^-$ image appeared under the platinum electrode. For example, the two bright spots in Fig. 11(a) became connected after sputtering Pt electrode. The isotope distribution in Fig. 11(d) is rather broad under platinum electrode particles, which suggested that the extension of the active reaction site was large into the platinum/electrolyte two phase boundaries in this experimental condition. The extension can be estimated to be several microns.

4.4. Measurements with the sample treated at higher temperature (1173 K)

Though the same experiments were attempted at 1173 K, no contrast was observed in the isotope distribution. It is probably because the diffusion rate was too large, and the difference of the surface reaction rate was not kept in the profile during the quenching process. Shorter annealing time and faster

Fig. 11. ^{16}O and ^{18}O distribution in the sample treated at 773 K in 0.2 bar oxygen ^{18}O under cathodic polarization (−0.5 V) for 5 min. Images were taken at the surface (a); after sputtering 2 min. (b); 4 min. (c); and 6 min. (d).

quenching will be necessary for the isotope imaging at higher temperature.

5. Conclusion

The proposed method was found to be applicable for the investigation of active electrochemical reaction sites in limited experimental conditions. The lateral resolution of the active site imaging with the present equipment was around 1 μm when the sample was treated at 973 K. The largest factor to determine the resolution was the quenching rate. It was difficult to visualize the reaction site when YSZ was treated at 973 K due to the difficulty in quenching. In the present equipment, the sample can not be cooled directly. The improvement is necessary for the study in further detail. Also, the electrode should be prepared in a well defined structure for more quantitative analysis.

The existence of 'hot spots' could be shown for the low temperature electrode reaction. From a view point of designing a practical electrode, the inhomo-

geneity of the current distribution is a serious problem. The isotope imaging method can be a useful technique to investigate rather macroscopic distributions of the reaction sites.

References

[1] J. Mizusaki, K. Amano, S. Yamauchi, K. Fueki, Solid State Ionics 22 (1987) 313.

[2] M. Kleitz, L. Dessemond, T. Kloidt, Space Expansions of the Regular Oxygen Electrode Reaction on YSZ, abstract 110A p. 35 in Extended Abstracts of the 3rd Symp. on Solid Oxide Fuel Cells in Japan, Tokyo, 1994.

[3] J. Fleig, J. Maier, J. Electrochem. Soc. 144 (1997) L302.

[4] K. Kawada, A. Masuda, K. Kaimai et al., in: A.J. McEvoy, K. Nisancioglu (Eds.), Proc. 10th SOFC Workshop, IEA Programme of R, D&D on Advanced Fuel Cells, 28–31 January 1997, Les Diablerets, CH, International Energy Agency, 1997, p. 146.

[5] R.J. Chater, S. Carter, J.A. Kilner, B.C.H. Steele, Solid State Ionics 53–56 (1992) 859.

[6] H. Haneda, C. Monty, J. Am. Ceram. Soc. 72 (1989) 1153.

[7] T. Kawada, T. Horita, N. Sakai, H. Yokokawa, M. Dokiya, Solid State Ionics 79 (1995) 201.

[8] T. Kawada, T. Horita, N. Sakai, H. Yokokowa, M. Dokiya, J. Mizusaki, Proc. the 2nd Intern. Meeting of Pacific Rim Ceramic Societies (PacRim-2), 15–17 July 1996, Cairns, Australia, pp. 543–565.

[9] T. Horita, K. Yamaji, M. Ishikawa, N. Sakai, H. Yokokawa, T. Kawada, T. Kato, J. Electrochem. Soc. 145 (9) (1998) 3196.

Author index to volume 131 Nos. 1 and 2

Subject index to volume 131 Nos. 1 and 2